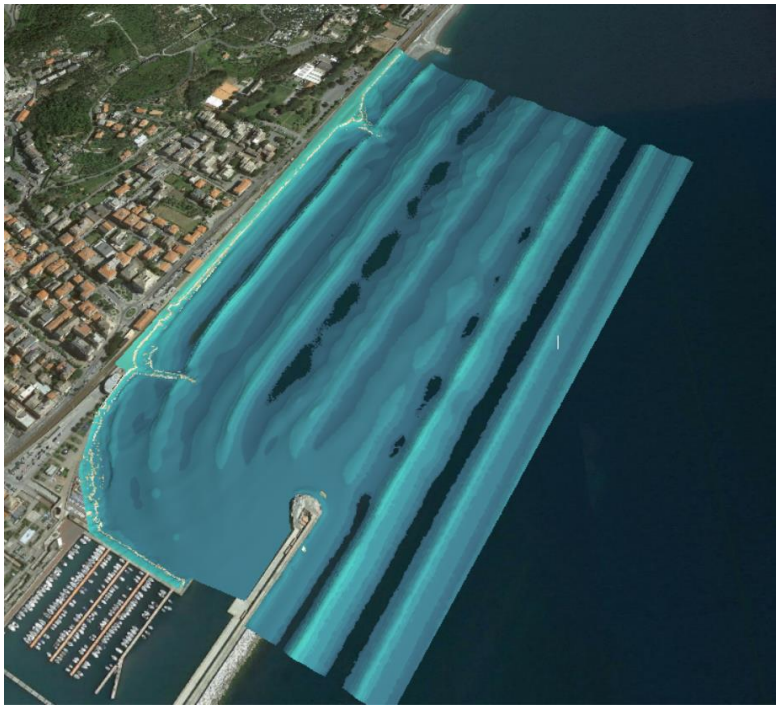
Attività di studio e modellazione numerica a supporto della progettazione degli interventi di ripascimento strutturale del litorale di Lavagna-Cavi

Relazione tecnica



Comune di Lavagna

The expert in WATER ENVIRONMENTS

Febbraio 2022

This report has been prepared under the DHI Business Management System certified by Bureau Veritas to comply with ISO 9001 (Quality Management)



Attività di studio e modellazione numerica a supporto della progettazione degli interventi di ripascimento strutturale del litorale di Lavagna-Cavi

Relazione tecnica

Committente	Comune di Lavagna
Referente del Committente	dott. Lorella Cella, p.i.Giampiero Donati, geom. Sonia Cugnata



Visualizzazione tridimensionale della mappa di surface elevation

Project manager	Silvia Torretta
Quality supervisor	Andrea Pedroncini
Autore	Silvia Torretta

Codice progetto - elaborato	22803664-01-00100
Data di approvazione	28.02.2022
Emissione	1.0
Classificazione	Aperta

DHI S.r.l. a socio unico• Via Bombrini 11/12• 10149 Genova• Italy•
Telefono: +39 010 8481220 • dhi-italia@dhigroup.com • www.dhigroup.com

INDICE

1 Premessa 1

2 Inquadramento del sito 2

3 Dati disponibili 2
3.1 Dati meteomarini 2
3.1.1 Dati di vento 5
3.1.2 Dati di moto ondoso 8
3.2 Dati batimetrici 11
3.3 Dati sedimentologici 12

4 Propagazione delle onde dal largo a costa 13
4.1 Condizioni d'onda 13
4.2 Batimetria e dominio di calcolo 13
4.3 Risultati del modello di propagazione delle onde dal largo a costa 15

5 Modellazione di dettaglio del moto ondoso nella configurazione attuale e nelle due ipotesi di progetto 20
5.1 Dominio di calcolo, batimetria 21
5.2 Selezione delle mareggiate rappresentative 28
5.3 Risultati del modello d'onda di dettaglio 30
5.3.1 Configurazione di stato attuale 31
5.3.2 Configurazione di progetto A 39
5.3.3 Configurazione di progetto B 47
5.3.4 Sintesi dei risultati del modello 54

6 Modellazione del trasporto litoraneo 55
6.1 Clima ondoso sottocosta 56
6.2 Risultati del modello e calcolo della profondità di chiusura 57
6.3 Orientazione di equilibrio 58

7 Simulazione delle dinamiche costiere con modellazione 2D 59
7.1 Dominio di calcolo, batimetria 60
7.2 Selezione delle condizioni d'onda rappresentative 61
7.3 Simulazione della circolazione nella configurazione di stato attuale 62

8 Analisi della capacità di trasporto sedimentario 65

9 Valutazioni su un'ulteriore configurazione di ripascimento 73

10 Conclusioni 77

11 Riferimenti 79

ALLEGATI

ALLEGATO A
Mediterranean Wind Wave Model (MWM)

ALLEGATO B
MIKE 21 Spectral Waves (SW)

ALLEGATO C
MIKE 3 Wave FM MIKE 3 Wave FM

ALLEGATO D
Littoral Process (LitDrift)

ALLEGATO E
MIKE 21 Hydrodynamics (HD) MIKE 21 Hydrodynamics (HD)

1 Premessa

La mareggiata che ha colpito la costa ligure nei giorni 29 e 30 Ottobre 2018 ha causato ingenti danni all'intero litorale regionale e anche nel Comune di Lavagna si sono riscontrati danneggiamenti alle opere e alle strutture di difesa. Nell'immediato, l'Amministrazione Comunale aveva individuato una serie di interventi urgenti necessari al rifiorimento e consolidamento delle opere marittime di difesa del litorale (pennelli e scogliere) significativamente danneggiate, e ha successivamente proseguito con la pianificazione di uno schema di difesa costiera finalizzato all'aumento della resilienza della lunga spiaggia di Lavagna-Cavi.

Fin dalle prime fasi di progettazione e monitoraggio degli interventi era risultato evidente come una delle aree maggiormente colpite durante l'evento fosse la prima "cella" a ponente, contigua al porticciolo turistico, che presentava oltre ad ingenti danni alle strutture di difesa, anche una significativa erosione dell'arenile, che da allora risulta insufficiente alla protezione delle retrostanti infrastrutture pubbliche, anche in occasione di eventi meteo-marini di minore intensità.

Il presente elaborato illustra una serie di attività di analisi e di modellazione numerica predisposte a supporto della progettazione di interventi di difesa della costa per quella specifica cella.

Per la **caratterizzazione del clima ondoso al largo** si è fatto riferimento al database Mediterranean Wind Wave Model (MWM) [1], un complesso dataset che fornisce la ricostruzione modellistica di 42 anni di dati di vento ed onda ad elevata risoluzione sull'intero bacino del Mar Mediterraneo, prodotto da DHI in collaborazione con HyMO*Lab* (Hydrodynamics and Met-Ocean Laboratory), struttura del Dipartimento di Ingegneria e Architettura dell''Università di Trieste. Tali dati sono stati opportunamente propagati sottocosta attraverso la predisposizione di un modello d'onda a maggior risoluzione, che ha permesso di simulare la trasformazione delle caratteristiche dell'onda nella sua propagazione verso l'area di studio (principalmente ad opera di rifrazione, shoaling, attrito col fondo e frangimento).

Sulla base dei risultati della propagazione della serie ultra-quarantennale, sono stati quindi selezionati alcuni eventi rappresentativi, in termini di altezza d'onda significativa e direzione media di propagazione, che sono stati simulati mediante un ulteriore modello di dettaglio, un tridimensionale pienamente non lineare, "*phase resolving*", su maglia non strutturata. Il modello, implementato con il codice di calcolo MIKE 3 WAVE FM [2], ha permesso di individuare le dinamiche attuali, di riprodurre i fenomeni di frangimento, *runup* ed *overtopping* per la cella oggetto di studio. Mediante la ricostruzione della distribuzione dell'onda e delle correnti locali è stato possibile evidenziare l'efficacia degli interventi di solo ripascimento (Configurazione di Progetto A, già approvato ed in fase di realizzazione) e di ripascimento comprensivo di protezione in massi al limite della cella (Configurazione di Progetto B), in analogia con la tipologia di intervento già attuato nelle altre spiagge del lungo litorale.

Per supportare l'indivudazione della configurazione progettuale ottimale sono state predisposte simulazioni numeriche anche del **trasporto sedimentario longitudinale (*long-shore*)**, con il codice LitDrift della suite Littoral Process [3], che hanno permesso la definizione della "profondità di chiusura" e l'orientazione di equilibrio della spiaggia nel tratto in esame.

A seguire si illustrano in dettaglio i dati utilizzati, la metodologia adottata, le impostazioni dei modelli numerici ed i risultati ottenuti. Si precisa che le attività sono state effettuate in stretta collaborazione con i professionisti incaricati della progettazione degli interventi ed hanno previsto una condivisione dei risultati preliminari con i tecnici del Comune di Lavagna.

2 Inquadramento del sito

Il paraggio di Lavagna è costituito in prevalenza da una lunga spiaggia pressochè rettilinea che ha origine dal molo sottoflutto del porto turistico e si protende a levante fino alla punta del Cigno, in corrispondenza di un pennello trasversale, che interrompe la continuità dell'arenile prima delle Rocche di Sant'Anna.

La spiaggia misura circa 3'500 metri di lunghezza ed è attualmente suddivisa in 13 celle delimitate da altrettanti pennelli ortogonali alla riva, sostanzialmente equidistanti tranne all'estremità di ponente, dove la spiaggia assume una falcatura decisamente arcuata indotta dalla presenza della diga foranea del porto di Lavagna. Proprio quest'area è oggetto del presente studio di approfondimento delle attuali dinamiche e dell'efficacia dell'intervento in progetto (Figura 2-1).



Figura 2-1 Inquadramento del litorale di Lavagna, con evidenziata in rosso la zona oggetto di studio

3 Dati disponibili

Tra le prime attività necessarie negli studi di dinamica costiera, vi è la definizione delle condizioni meteomarine di riferimento al largo del tratto di costa interessato, con particolare riferimento al moto ondoso, nonché la caratterizzazione del sito dal punto di vista batimetrico e dei sedimenti.

Nelle sezioni a seguire sono descritti ed analizzati i dataset utilizzati per questa caratterizzazione.

3.1 Dati meteomarini

Per quanto riguarda la disponibilità di registrazioni di moto ondoso, la principale fonte di riferimento nel nostro paese è la Rete Ondametrica Nazionale (RON) gestita dall'ISPRA (Istituto Superiore per la Protezione e la Ricerca Ambientale). I dati di boa possono essere utilizzati come riferimento anche ad una certa distanza dal sito di interesse, qualora l'esposizione alle mareggiate per i diversi settori direzionali possa essere considerata simile tra il sito in esame ed il sito che ospita la boa ondametrica. Frequentemente, tuttavia, per la caratterizzazione meteomarina di un sito non è possibile fare affidamento alle misure. Questo avviene o perché i dati sono troppo

frammentati a causa di malfunzionamenti dello strumento o periodi di manutenzione dello stesso, o perché le serie temporali disponibili coprono solo pochi anni (5÷10) oppure ancora perché per il paraggio in esame la boa non è disponibile o non è sufficientemente rappresentativa.

Sempre più spesso, pertanto, si fa ricorso ad una ricostruzione storica delle condizioni meteomarine attraverso modellistica numerica. Tale approccio, comunemente definito come "*wave hindcast*" permette di disporre di serie temporali, tra l'altro, di altezza d'onda, periodo e direzione, nel punto desiderato.

Se da un lato la possibilità di disporre di ricostruzioni di condizioni meteomarine pregresse attraverso un approccio modellistico rappresenta oggi un formidabile supporto nell'ingegneria costiera ed offshore, dall'altro va sottolineata l'importanza di disporre di ricostruzioni modellistiche robuste, accurate e validate.

Tra i database disponibili, un esempio di ricostruzione storica di vento e moto ondoso per l'intero bacino del Mediterraneo è costituito dal database Mediterranean Wind Wave Model (MWM) [1], prodotto da DHI in collaborazione con HyMO*Lab* (Hydrodynamics and Met-Ocean Laboratory), struttura del Dipartimento di Ingegneria e Architettura dell'Università di Trieste. Il database MWM deriva dall'implementazione di una catena modellistica che beneficia di due modelli che rappresentano lo stato dell'arte rispettivamente nell'ambito della modellazione atmosferica (WRF-ARW) e della modellazione del moto ondoso (MIKE 21 SW di DHI) [6].

In Figura 3-1 e Figura 3-2 sono riportate rispettivamente la batimetria di riferimento per la componente modellistica di moto ondoso ed un dettaglio della "mesh" di calcolo adottata. La risoluzione del modello d'onda è variabile da circa 10 km al largo fino a circa 3 km sottocosta. I dati sono stati estensivamente validati con confronti con anemometri, boe, nonché con le stime di intensità del vento e altezza d'onda da satellite.

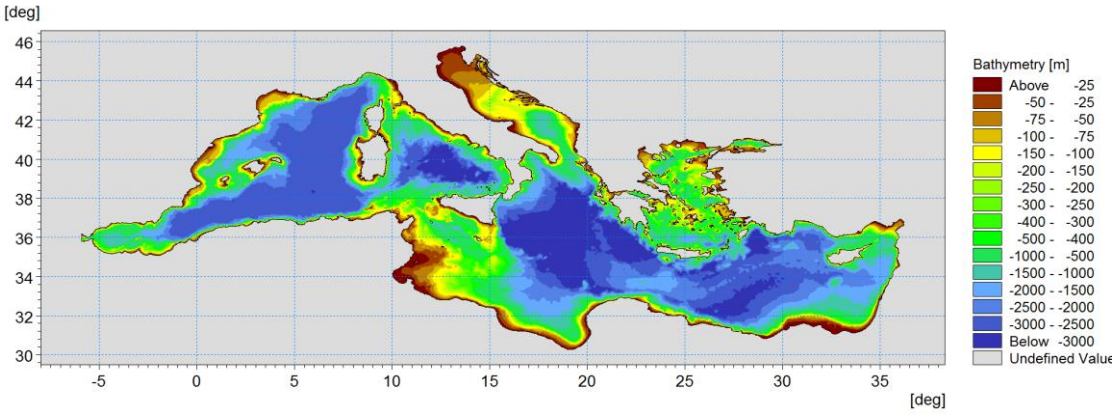


Figura 3-1 Batimetria di riferimento per la componente "onda" del database MWM

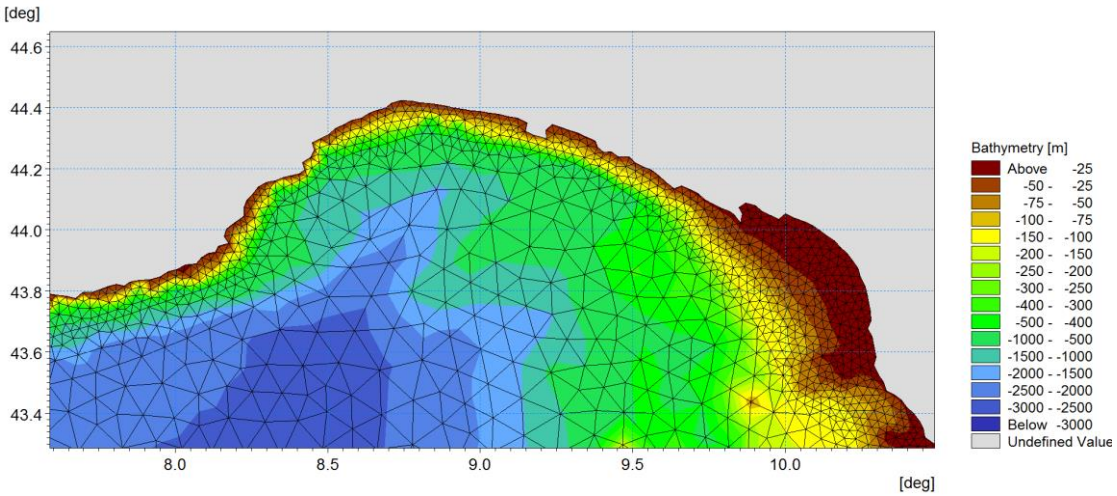


Figura 3-2 Batimetria di riferimento per la componente “onda” del dataset MWM – dettaglio sul Mar Ligure

Il database Mediterranean Wind Wave Model (MWM), descritto diffusamente in Allegato A al presente documento, è stato pertanto preso a riferimento per la caratterizzazione meteomarina al largo del sito oggetto di studio.

La selezione della cella del database MWM più adeguata a rappresentare il clima meteomarino al largo di Lavagna è stata effettuata tenendo in considerazione diversi aspetti:

- il punto deve essere ben rappresentativo dell’esposizione del sito alle onde;
- in virtù della risoluzione del database MWM (circa 4 km), il punto deve essere collocato ad una profondità alla quale possa essere ritenuta trascurabile l’interazione dell’onda con il fondale, che viene pertanto demandata al modello di propagazione largo-costa descritto in seguito;
- la localizzazione del punto non deve essere troppo lontana dalla costa, in modo che il modello di propagazione largo-costa non presenti un dominio troppo ampio, con tempi di calcolo troppo onerosi.

Sulla base di tali prescrizioni e della risoluzione spaziale del database MWM è stato selezionato un punto per la caratterizzazione dei parametri d’onda relativamente ai 42 anni (1979-2020) di ricostruzione storica (modalità *hindcast*) delle serie orarie.

A seguire si riportano l’ubicazione grafica e le coordinate del punto selezionato, ubicato a circa 9 km dal litorale in esame.

Tabella 3-1 Coordinate del punto selezionato dal dataset di MWM per la caratterizzazione meteomarina del sito

Punto	Lon [°E]	Lat [°N]	Prof. [m]
MWM	9.328	44.22	130

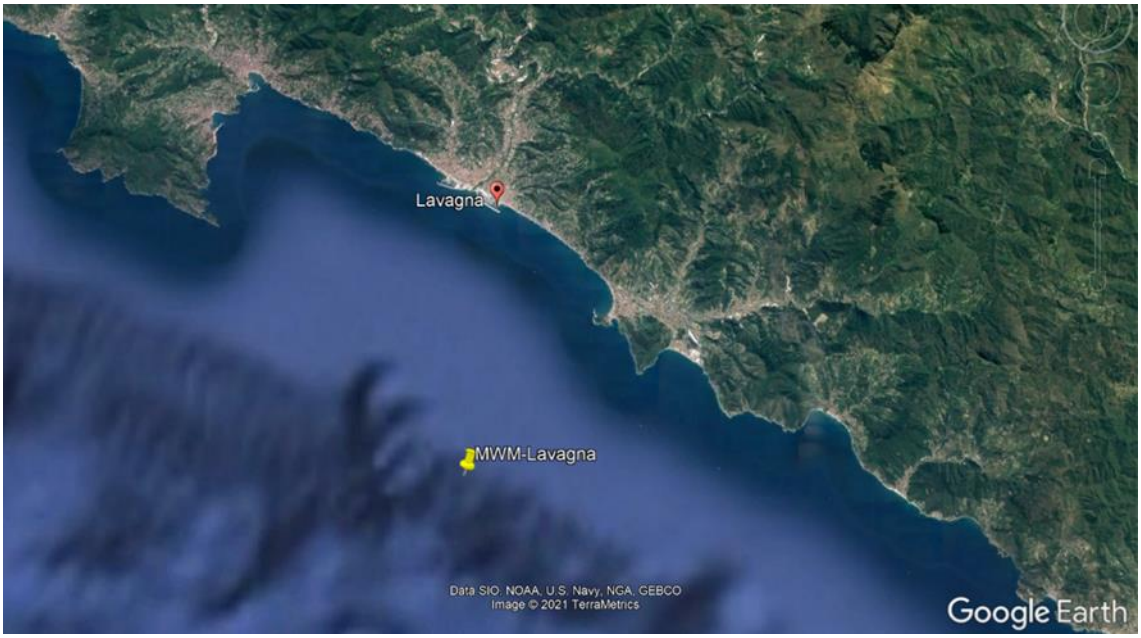


Figura 3-3 Ubicazione del punto di estrazione da MWM (LON 9.328°E, LAT 44.220°N) i cui dati dal 1979 al 2020 sono stati utilizzati per la caratterizzazione del moto ondoso al largo

3.1.1 Dati di vento

In Figura 3-4 e Tabella 3-2 si riportano rispettivamente la rappresentazione in forma di rosa della serie di intensità e direzione del vento e la frequenza delle classi di intensità del vento in funzione della direzione per il punto MWM selezionato.

Come si può osservare, nel periodo dei 42 anni considerati si raggiungono valori massimi di velocità del vento fino a oltre 26 m/s. Dall'analisi della rosa del vento si evince che il settore dominante, ossia caratterizzato dai venti più intensi, è quello da Nord-Est, in particolare le direzioni comprese tra 30°N e 60°N, che presentano una frequenza di circa il 19%, pari a poco più di 2 mesi all'anno in media.

Altrettanto frequenti, ma caratterizzati da velocità inferiori, sono i venti provenienti da Sud-Est, in particolare dal settore compreso tra 120°N e 165°N. Da questo settore direzionale i venti si presentano con una frequenza media di circa 17.8%, corrispondente a circa 2 mesi all'anno in media.

La condizione di calma, qui associata ad intensità del vento inferiore a 2 m/s, si verifica mediamente per il 24.5% del tempo, ovvero per circa 3 mesi all'anno.

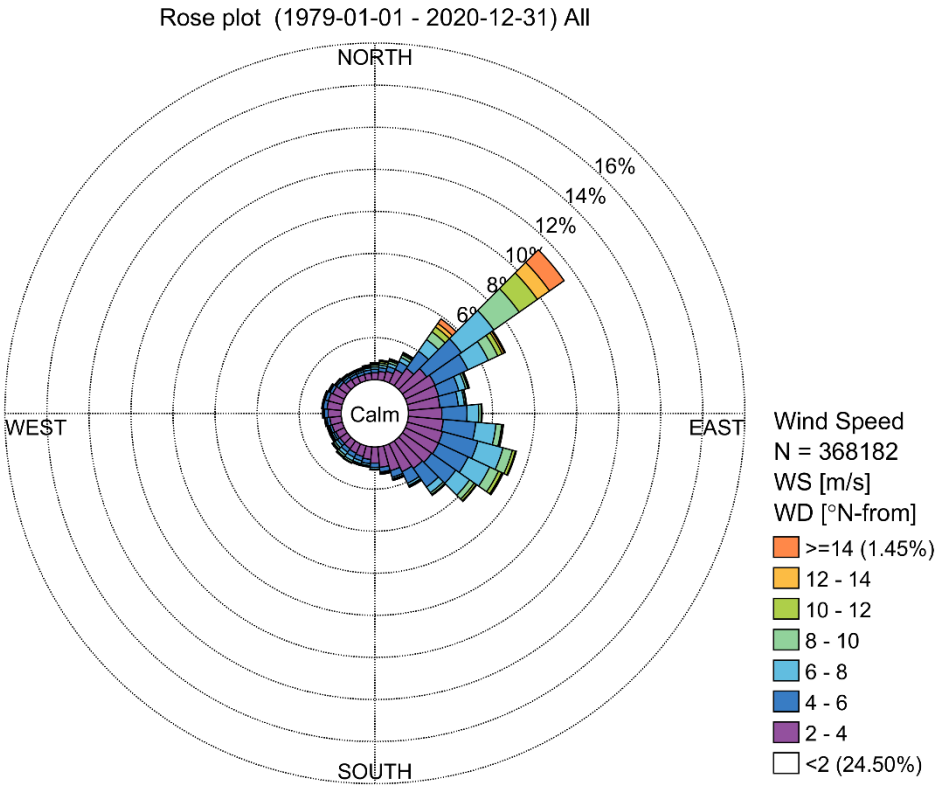


Figura 3-4 Rosa del vento per il punto MWM (LON 9.328°E, LAT 44.220°N) per il periodo 1979-2020. La calma è qui associata a venti con velocità inferiori a 2 m/s

Tabella 3-2 Numero di eventi per classi di intensità del vento WS (colonne) e direzione media WD (righe) per il punto MWM (LON 9.328°E, LAT 44.220°N) per l'intero periodo 1979 – 2020

Lavagna (9.33E;44.22N;-130.00mMSL)
Number of Occurrences (1979-01-01 - 2020-12-31) All
WS [m/s] - Wind Speed

WD [°N-from] - Wind Direction

	[2-4[	[4-6[	[6-8[	[8-10[	[10-12[	[12-14[	[14-16[	[16-18[	[18-20[	[20-22[	[22-24[	[24-26[	[26-28[	[28-30[	Total	Accum
[330-345[	1718	787	452	314	168	101	43	5	4	-	-	-	-	-	3592	277955
[315-330[	1951	771	470	308	153	58	6	1	-	-	-	-	-	-	3718	274363
[300-315[	2891	727	379	174	71	22	9	4	1	-	-	-	-	-	4278	270645
[285-300[	3689	886	340	96	26	10	-	-	-	-	-	-	-	-	5047	266370
[270-285[	3692	1002	302	110	34	4	1	1	-	-	-	-	-	-	5146	261323
[255-270[	3113	825	363	167	62	21	7	1	1	-	-	-	-	-	4560	256177
[240-255[	2673	571	342	198	130	105	55	19	11	1	1	-	-	-	4106	251617
[225-240[	2406	797	683	440	246	150	67	17	7	-	-	-	-	-	4813	247511
[210-225[	2556	1181	933	568	215	71	15	3	1	-	-	-	-	-	5543	242698
[195-210[	2848	1147	831	398	152	46	8	-	-	-	-	-	-	-	5430	237155
[180-195[	3484	1124	496	224	87	42	15	6	-	-	-	-	-	-	5478	231725
[165-180[	5102	1193	352	164	79	37	21	5	3	1	-	-	-	-	6957	226247
[150-165[	7108	2113	475	219	121	57	44	13	1	-	-	-	-	-	10151	219290
[135-150[	8634	5296	1458	496	193	56	15	9	1	-	-	-	-	-	16158	209139
[120-135[	9441	7986	4988	1776	708	229	54	11	1	-	-	-	-	-	25194	192981
[105-120[	9601	9305	6705	2602	877	250	58	8	-	-	-	-	-	-	29406	167787
[90-105[	9210	8078	4703	1290	301	76	7	1	-	-	-	-	-	-	23666	138381
[75-90[	8329	5273	1950	460	146	37	19	1	-	-	-	-	-	-	16215	114715
[60-75[	8532	6280	2667	941	395	168	62	31	7	1	-	-	-	-	19084	98500
[45-60[	8096	11110	9484	6709	4503	2865	1595	959	499	197	61	3	-	-	46081	79416
[30-45[	5117	4592	2930	1920	1199	793	493	294	158	80	17	-	1	-	17594	33335
[15-30[	2930	1478	941	629	367	159	64	21	4	1	-	-	-	-	6594	15741
[0-15[	2111	964	648	542	409	248	79	23	7	2	-	-	-	-	6033	9147
[-30-0[	1762	856	557	384	286	170	74	19	6	-	-	-	-	-	4114	4114
Total	116994	74342	43449	21129	10928	5775	2811	1452	712	283	79	3	1	-	277955	-
Accum	116994	191336	234785	255914	266842	272617	275428	276880	277592	277875	277954	277957	277958	277958	-	-

3.1.2 Dati di moto ondoso

Dall'analisi della rosa del clima ondoso (Figura 3-5) e della tabella delle frequenze di occorrenza (Tabella 3-3) risultanti dalla serie storica oraria di 42 anni estratta dal database MWM, si evince che le ondazioni più frequenti e più intense provengono da Sud-Ovest (Libeccio), con particolare riferimento alle direzioni comprese tra 205°N e 235°N. Complessivamente, tale settore racchiude circa il 33% delle onde totali, corrispondente in media a circa 4 mesi all'anno. In questo settore direzionale l'onda raggiunge un'altezza significativa massima di circa 8 m.

Significative per frequenza di occorrenza (25%), ma caratterizzate da altezze significative inferiori ai 5.5 m, sono le onde provenienti da Sud-Est (Scirocco), in particolare dal settore compreso tra 145°N e 175°N.

La condizione di calma, qui associata ad una altezza d'onda significativa inferiore a 0.5 m, si verifica mediamente per circa il 46% del tempo, corrispondente a poco meno di 6 mesi all'anno.

Il valore di altezza d'onda significativa più elevato presente nella serie risulta associato alla mareggiata del 28 Dicembre 1999 (Hs al picco pari a circa 8.1 m), seguito da quella del 16 Dicembre 2011 (Hs al picco pari a circa 8.0 m). La più recente mareggiata del 29-30 Ottobre 2018, che ha colpito pesantemente l'intero litorale ligure come descritto in premessa, presenta nel punto MWM selezionato immediatamente al largo di Lavagna un valore di altezza significativa al picco pari a circa 6.9 m (Figura 3-6).

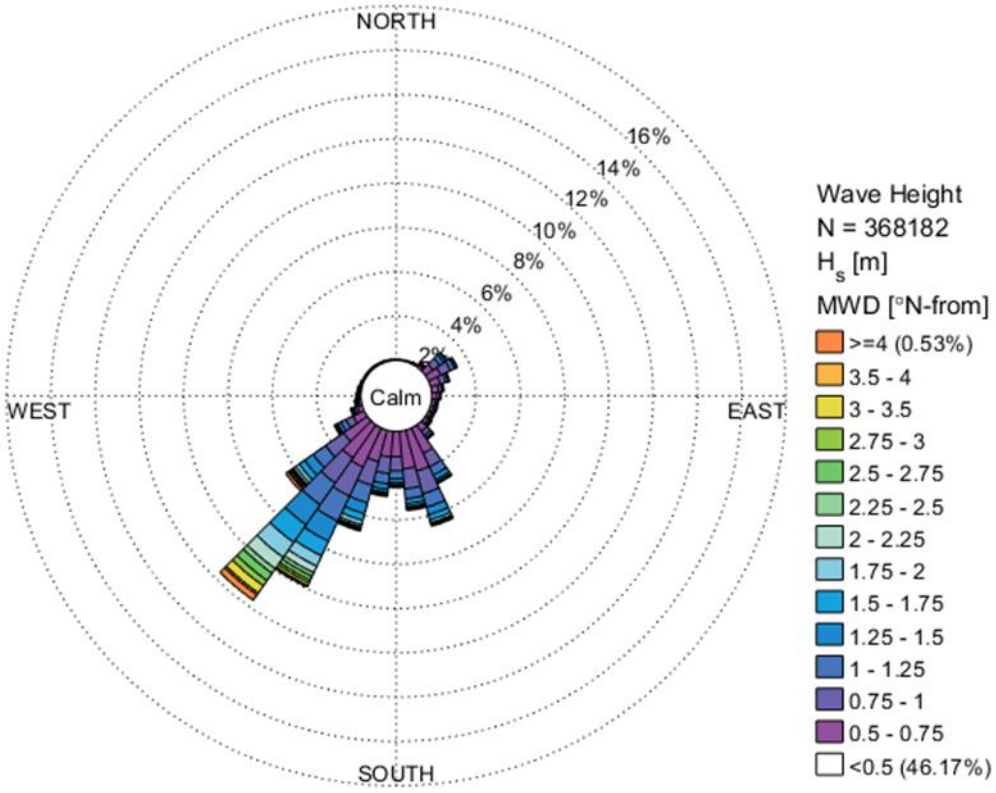


Figura 3-5 Rosa del clima ondoso al largo per il punto MWM (LON 9.328°E, LAT 44.220°N) per il periodo 1979 – 2020 su base annuale. La calma è qui associata a onde con H_s inferiori a 0.5 m

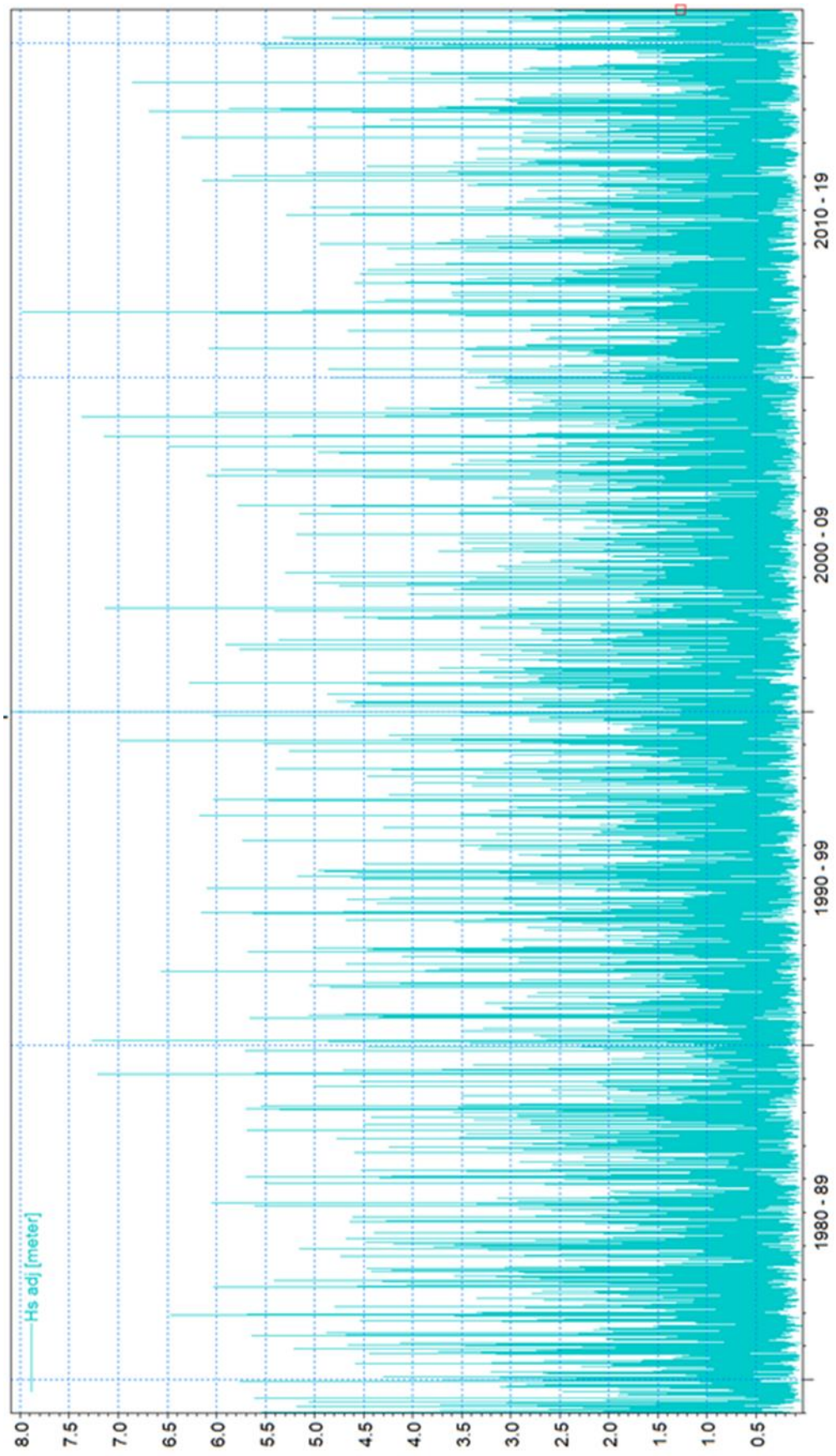


Figura 3-6 Serie storica di altezza d'onda significativa Hs estratta nel punto MWM (LON 9.328°E, LAT 44.220°N) per il periodo 1979 – 2020

Tabella 3-3 Numero di eventi per classi di altezza d'onda significativa Hs in funzione della direzione media di provenienza MWD per il punto MWM calcolata sul periodo 1979 – 2020

Lavagna (476111.00E;4915838.00N;-50.00mMSL)
Number of Occurrences (1979-01-01 - 2020-12-31) All
H_[m] - Wave Height

MWD [°N-from] - Mean Wave Direction

	[0-0.25[	[0.25-0.5[	[0.5-1[	[1-1.5[	[1.5-2[	[2-2.5[	[2.5-3[	[3-3.5[	[3.5-4[	[4-4.5[	[4.5-5[	[5-5.5[	[5.5-6[	[6-6.5[	[6.5-7[	[7-7.5[	[7.5-8[	[8-8.5[	[8.5-9[	Total	Accum
[345-355[	17	183	221	35	1	-	-	-	-	-	-	-	-	-	-	-	-	-	-	457	368182
[335-345[	26	198	242	57	4	-	-	-	-	-	-	-	-	-	-	-	-	-	-	527	367725
[325-335[	27	170	221	74	2	-	-	-	-	-	-	-	-	-	-	-	-	-	-	494	367198
[315-325[	32	200	229	114	9	-	-	-	-	-	-	-	-	-	-	-	-	-	-	584	366704
[305-315[	53	211	247	95	16	-	-	-	-	-	-	-	-	-	-	-	-	-	-	621	366120
[295-305[	63	235	217	111	13	-	-	-	-	-	-	-	-	-	-	-	-	-	-	639	365499
[285-295[	197	354	311	139	20	-	-	-	-	-	-	-	-	-	-	-	-	-	-	1021	364860
[275-285[	847	829	424	187	50	2	-	-	-	-	-	-	-	-	-	-	-	-	-	2339	363839
[265-275[	1171	965	517	242	73	2	-	-	-	-	-	-	-	-	-	-	-	-	-	2990	361500
[255-265[	1267	1135	696	305	137	21	-	-	-	-	-	-	-	-	-	-	-	-	-	3561	358510
[245-255[	1616	1696	1231	561	197	51	4	1	-	-	-	-	-	-	-	-	-	-	-	5357	354949
[235-245[	3566	3919	3360	1513	442	134	76	10	1	1	1	-	-	-	-	-	-	-	-	13023	349592
[225-235[	6378	7626	8482	4264	1767	611	421	323	163	136	154	110	57	36	14	10	3	2	-	30767	336569
[215-225[	6397	10110	11806	8466	6617	3214	2561	1445	387	411	338	175	96	35	17	14	1	-	-	52090	305802
[205-215[	5400	9601	12491	8268	4582	1864	1166	504	110	131	40	17	8	4	6	1	-	-	-	44193	253712
[195-205[	4903	7292	9487	4893	1914	616	259	104	37	33	12	7	3	4	1	-	-	-	-	29565	209519
[185-195[	5290	6737	7084	2696	736	277	115	37	26	18	19	2	1	1	-	-	-	-	-	22939	179954
[175-185[	6253	8015	6575	1956	514	150	90	33	21	16	11	2	-	-	-	-	-	-	-	23636	157015
[165-175[	8167	11788	9623	2494	684	232	127	34	29	9	4	-	-	-	-	-	-	-	-	33191	133379
[155-165[	8697	13024	10951	3612	1365	423	140	38	7	-	-	-	-	-	-	-	-	-	-	38227	100188
[145-155[	3837	6921	7103	2373	557	136	24	1	-	-	-	-	-	-	-	-	-	-	-	20952	61961
[135-145[	370	1386	2127	709	127	13	-	-	-	-	-	-	-	-	-	-	-	-	-	4712	41009
[125-135[	201	833	1011	327	40	2	-	-	-	-	-	-	-	-	-	-	-	-	-	2414	36297
[115-125[	154	693	833	289	18	1	-	-	-	-	-	-	-	-	-	-	-	-	-	1988	33883
[105-115[	195	774	945	218	26	-	-	-	-	-	-	-	-	-	-	-	-	-	-	2158	31895
[95-105[	175	824	976	185	19	-	-	-	-	-	-	-	-	-	-	-	-	-	-	2179	29737
[85-95[	204	1040	1327	213	13	-	-	-	-	-	-	-	-	-	-	-	-	-	-	2797	27558
[75-85[	190	1252	1733	330	33	-	-	-	-	-	-	-	-	-	-	-	-	-	-	3538	24761
[65-75[	181	1524	2638	621	61	-	-	-	-	-	-	-	-	-	-	-	-	-	-	5025	21223
[55-65[	124	1505	4014	1190	125	1	-	-	-	-	-	-	-	-	-	-	-	-	-	6959	16198
[45-55[	77	883	2924	1264	202	2	-	-	-	-	-	-	-	-	-	-	-	-	-	5352	9239
[35-45[	83	529	766	195	29	-	-	-	-	-	-	-	-	-	-	-	-	-	-	1602	3887
[25-35[	53	356	344	29	3	-	-	-	-	-	-	-	-	-	-	-	-	-	-	785	2285
[15-25[	45	259	228	23	2	-	-	-	-	-	-	-	-	-	-	-	-	-	-	557	1500
[5-15[	41	227	178	19	2	-	-	-	-	-	-	-	-	-	-	-	-	-	-	467	943
[-5-5[	44	203	205	24	-	-	-	-	-	-	-	-	-	-	-	-	-	-	-	476	476
Total	66311	103997	111767	47981	20419	7752	4983	2530	781	755	579	313	165	80	38	25	4	2	-	368182	-
Accum	66311	170008	281775	329756	350175	357927	362910	365440	366221	366976	367555	367868	368033	368113	368151	368176	368180	368182	368182	-	-

3.2 Dati batimetrici

Per la caratterizzazione topo-batimetrica della spiaggia di Lavagna si è fatto riferimento al rilievo di dettaglio dell'area, predisposto da Drafinsub nel Luglio 2021 (Figura 3-7).

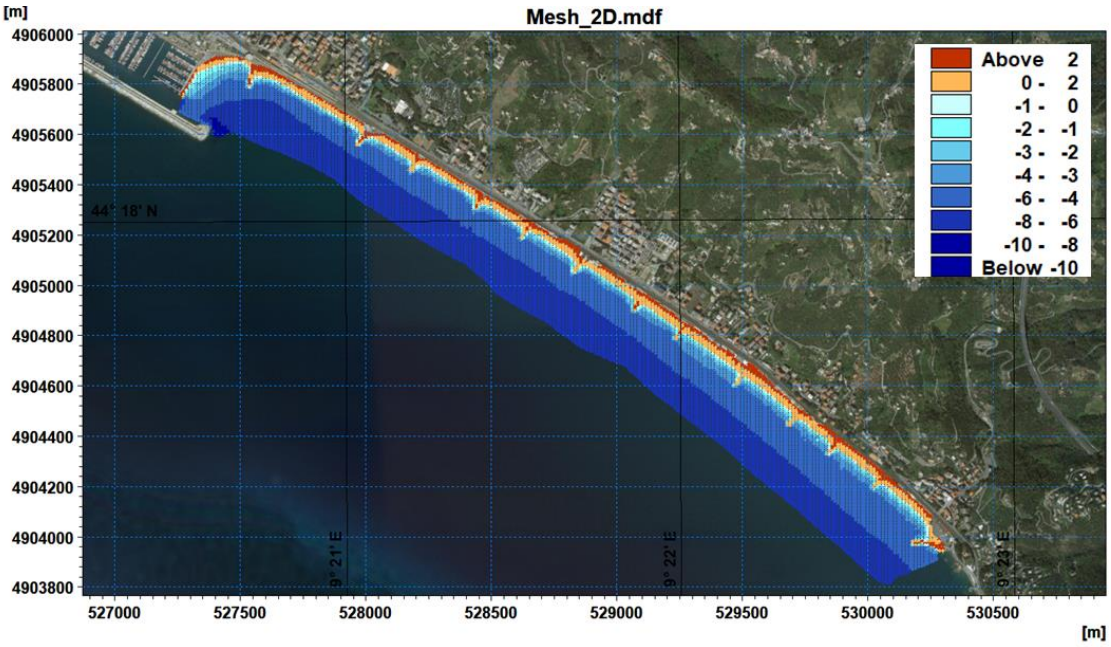


Figura 3-7 Rilievo di dettaglio della spiaggia di Lavagna (Drafinsub, Luglio 2021)

Le dimensioni del dominio di calcolo del modello numerico implementato sono tuttavia più estese rispetto all'area per la quale risulta disponibile tale rilievo. A integrazione dei recenti dati locali, sono state pertanto utilizzate le batimetrie provenienti dalle carte nautiche digitali appartenenti al database CM-93 [4] di C-MAP [5], un database globale di cartografia nautica in formato digitale, creato e continuamente aggiornato da Jeppesen (Figura 3-8).

I dati forniti da questo database sono direttamente importabili nell'ambiente di lavoro dei codici di calcolo di DHI, consentendo quindi una rapida caratterizzazione batimetrica dell'area.

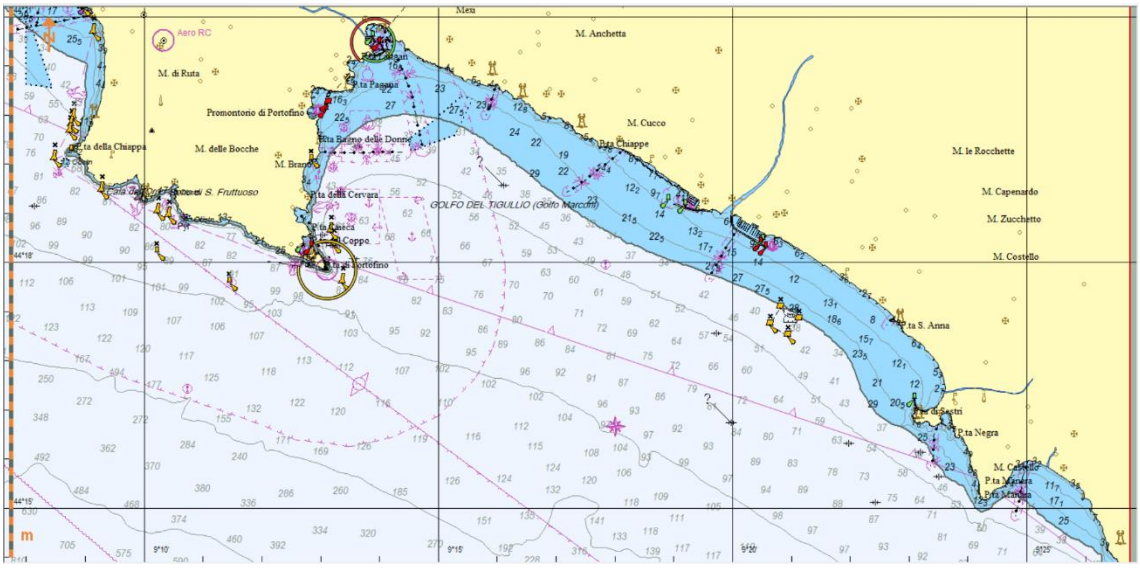


Figura 3-8 Rappresentazione della cartografia nautica digitale per il Golfo del Tigullio, database CM-93 di C-MAP

3.3 Dati sedimentologici

Per la caratterizzazione sedimentologica del sito si è fatto riferimento alle analisi granulometriche effettuate nel Marzo 2021 da Rina Consulting per il Porto di Lavagna e messe a disposizione dal Comune (Figura 3-9).

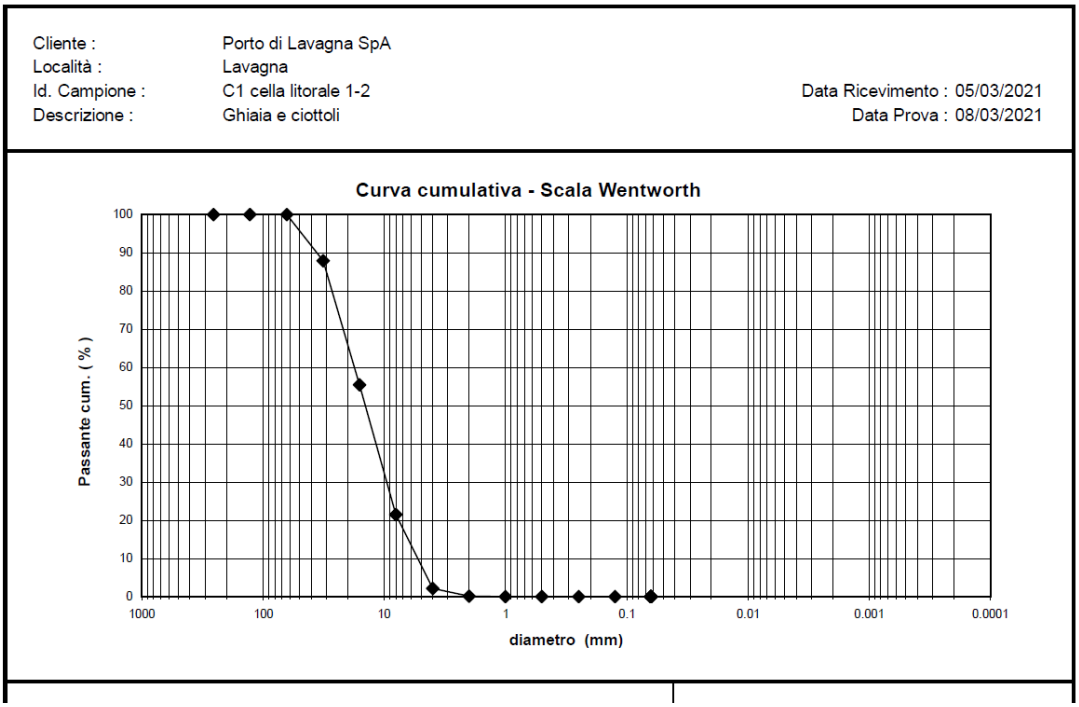


Figura 3-9 Analisi granulometriche del campione prelevato nella cella 1 di Lavagna (Rina Consulting 5 Marzo 2021)

4 Propagazione delle onde dal largo a costa

Al fine di propagare l'intera serie ultra-quarantennale di moto ondoso da largo sino al litorale di Lavagna è stato implementato il modulo MIKE 21 SW - Spectral Waves di DHI [6], un modello spettrale per vento ed onde di terza generazione, basato su una griglia non strutturata in grado di simulare la trasformazione di onde generate dal vento ed onde di *swell* sia offshore, sia in aree costiere.

Tale modello, a maglia triangolare "flessibile", permette di utilizzare una risoluzione spaziale variabile, più elevata nelle aree per le quali si richiede un maggior dettaglio, laddove rifrazione, *shoaling*, attrito con il fondo e frangimento determinano una forte trasformazione delle caratteristiche dell'onda incidente su distanze relativamente limitate.

I fenomeni fisici che sono modellati con MIKE 21 SW sono i seguenti:

- generazione dell'onda ad opera del vento;
- interazione non lineare onda-onda;
- dissipazione dovuta al cosiddetto "*white capping";*
- dissipazione dovuta all'attrito con il fondo;
- dissipazione dovuta al frangimento;
- rifrazione e *shoaling* dovuti alle variazioni del fondale;
- interazione onde-correnti;
- diffrazione;
- riflessione.

Un'accurata descrizione del modulo MIKE 21 SW è riportata nell'Allegato B al presente elaborato.

I dati di input da inserire nel modello possono essere raggruppati in differenti categorie, ovvero:

- parametri di base (es. mesh di calcolo, durata della simulazione);
- tipo di formulazione, discretizzazione nel dominio delle frequenze e delle direzioni, tecniche di soluzione;
- forzanti (livelli, vento, correnti);
- parametri di dissipazione (frangimento, *white-capping*, attrito al fondo);
- condizioni iniziali (stato di mare iniziale);
- condizioni al contorno (onde al largo o alternativamente contorno chiuso).

I risultati ottenuti, per ognuno degli elementi della *mesh*, sono costituiti essenzialmente dai parametri caratteristici dell'onda: altezza d'onda significativa, periodo, direzione media, *radiation stress*.

4.1 Condizioni d'onda

Il modello d'onda MIKE 21 SW è stato implementato applicando come condizioni lungo il contorno aperto posto al largo del dominio di calcolo l'intera serie oraria di 42 anni di dati d'onda ricavati dal modello a larga scala MWM.

4.2 Batimetria e dominio di calcolo

Sulla base dei dati disponibili, descritti alla sezione 3.2, è stata predisposta una batimetria di calcolo a maglia triangolare le cui dimensioni e risoluzioni sono state individuate al fine di rappresentare al meglio tutti i fenomeni che intervengono nella propagazione dell'onda da largo verso costa, ottimizzando al contempo i tempi di calcolo.

Il dominio di calcolo si estende per circa 15.4 km in direzione parallela a costa, comprendendo l'interno Golfo del Tigullio, tra il promontorio di Portofino ad Ovest ed il promontorio di Punta Manara ad Est; trasversalmente a costa esso si estende per circa 9 km, fino a raggiungere il punto di estrazione dei dati del clima ondoso del database MWM.

La batimetria del modello è stata costruita utilizzando un approccio a maglia flessibile: la risoluzione spaziale al largo (lunghezza media dei lati dei triangoli) è di circa 270 m, ed aumenta progressivamente fino a 30 m (Figura 4-1).

Complessivamente, la *mesh* di calcolo è costituita da circa 11'600 elementi.

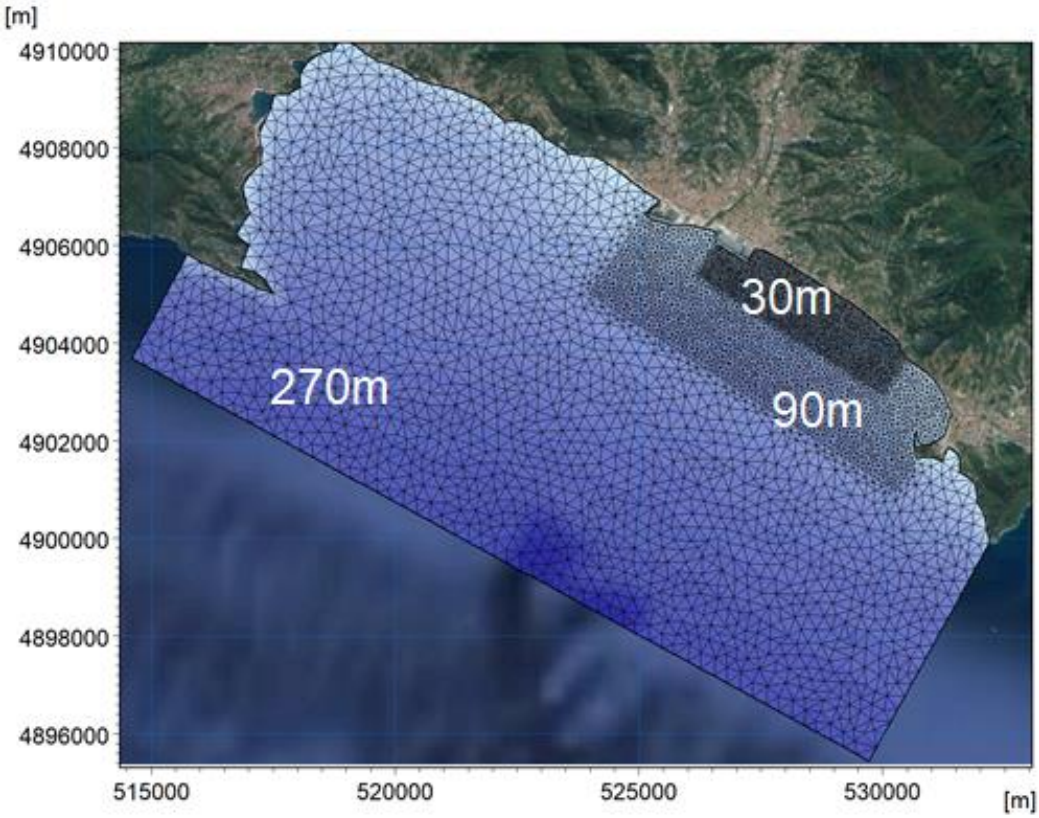


Figura 4-1 Rappresentazione della differente risoluzione della *mesh* di calcolo utilizzata nel modello di propagazione del moto ondoso

Per la caratterizzazione batimetrica dell'area oggetto di studio, come detto, si è fatto riferimento al database di carte nautiche digitalizzate CM-93 di CMAP e al rilievo batimetrico di dettaglio a disposizione.

Il risultato finale del processamento dei dati batimetrici a disposizione è mostrato in Figura 4-2, in cui sono rappresentate l'estensione del modello e la batimetria di calcolo.

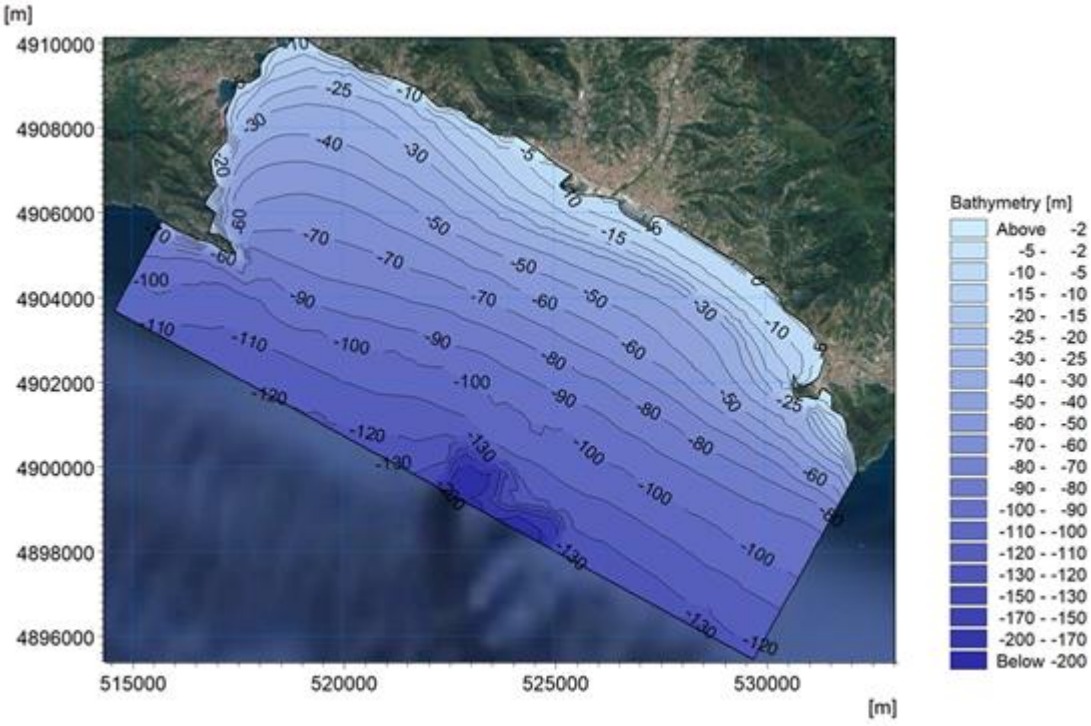


Figura 4-2 Batimetria ottenuta dal processamento dei dati a disposizione

4.3 Risultati del modello di propagazione delle onde dal largo a costa

La propagazione dell'intera serie di dati orari estratti dal dataset MWM ha permesso di ottenere la distribuzione delle principali grandezze di moto ondoso (altezza d'onda significativa, periodo medio e di picco e direzione media di propagazione) in tutti i punti del dominio di calcolo, rendendo pertanto possibile estrarre la serie in qualsiasi punto sottocosta.

Nelle immagini a seguire è riportata la distribuzione spaziale dell'altezza d'onda significativa in riferimento ad alcuni eventi intensi e provenienti dai principali settori direzionali: un evento da Scirocco (Figura 4-3), un evento da Mezzogiorno (Figura 4-4) e uno, il più intenso, da Libeccio (Figura 4-5). In queste mappe la scala cromatica e la lunghezza dei vettori, proporzionale in ogni punto all'altezza d'onda e con direzione coincidente con la direzione media di propagazione, mostrano in maniera efficace le trasformazioni che l'onda subisce nella sua propagazione da largo verso costa.

In particolare, si osserva che il promontorio di Portofino induce un'importante attenuazione delle altezze per le onde provenienti da Libeccio; l'effetto schermante, che interessa principalmente la parte occidentale del Golfo del Tigullio e non raggiunge il litorale di Lavagna, si attenua progressivamente per direzioni di provenienza via via meno inclinate rispetto all'allineamento della costa. La scala cromatica mette bene in evidenza anche la protezione offerta dal promontorio di Punta Manara per le onde con direzione di provenienza da Scirocco, anche se il minore aggetto del promontorio rispetto a quello di Portofino determina una zona d'ombra significativamente più ristretta.

La fascia dei frangenti, ossia la zona dove l'onda subisce la massima dissipazione energetica nella propagazione verso riva, è evidenziata nelle mappe dalla variazione cromatica rapida.



Figura 4-3 Distribuzione dell'altezza d'onda significativa nel dominio di calcolo per un'onda da Scirocco (dati di onda del 14 Novembre 2019 ore 22. Dati al largo: Hs=2.6 m, Tp=6.1 s, MWD=149°N)

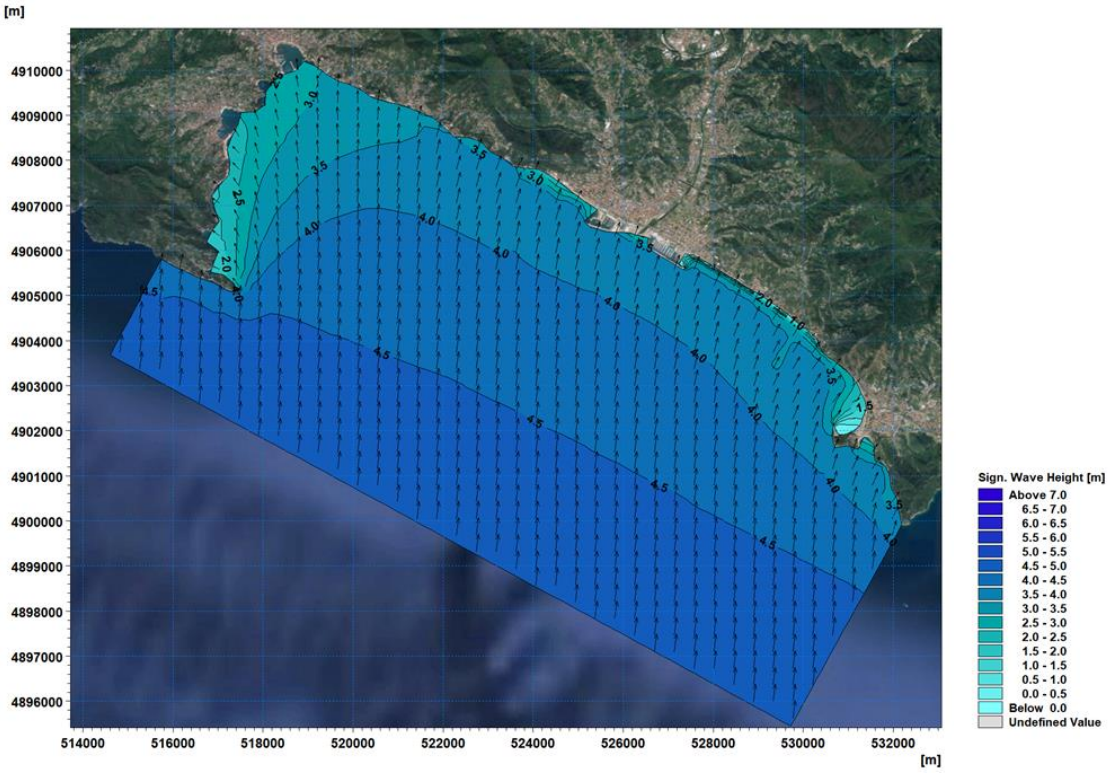


Figura 4-4 Distribuzione dell'altezza d'onda significativa nel dominio di calcolo per un'onda da Mezzogiorno (dati di onda del 29 Ottobre 2018 ore 19. Dati al largo: Hs=4.6 m, Tp=10.9 s, MWD=186°N)

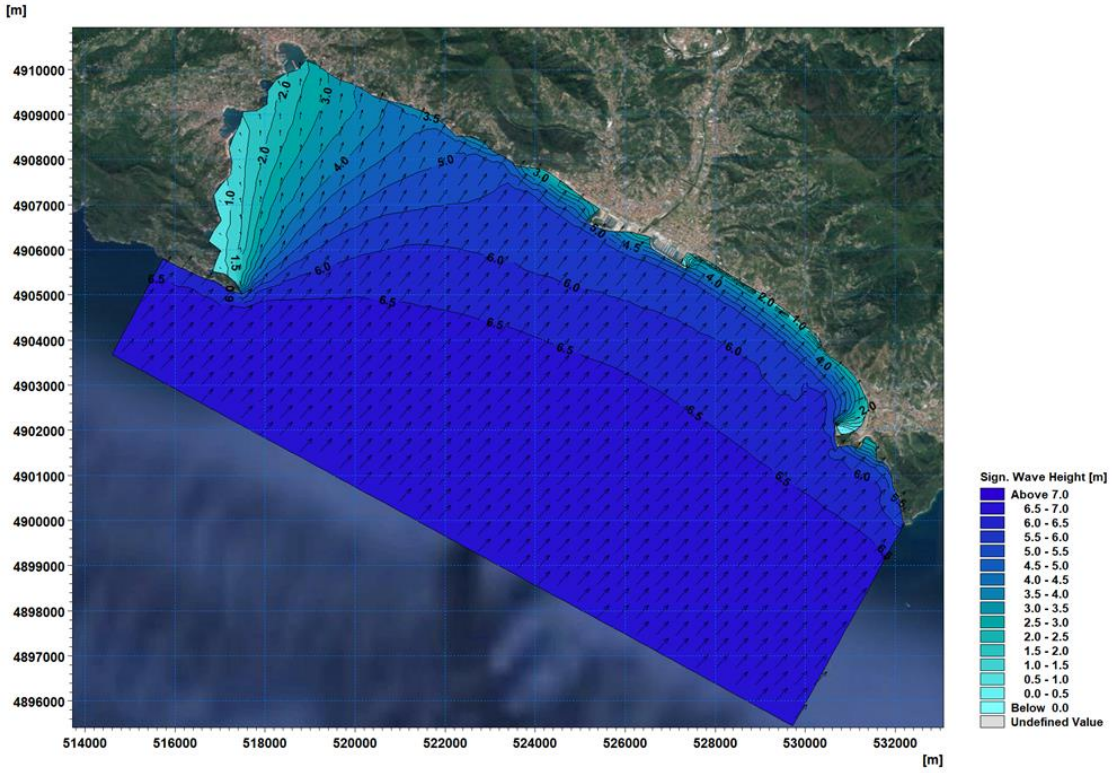


Figura 4-5 Distribuzione dell'altezza d'onda significativa nel dominio di calcolo per un'onda da Libeccio (dati del 16 Dicembre 2011 ore 21. Dati al largo: Hs=6.7 m, Tp=10.7 s, MWD=223°N)

I risultati della propagazione del moto ondoso mostrano una distribuzione delle altezze piuttosto regolare con l'andamento dei fondali: la variazione di pendenza determina infatti una graduale dissipazione dell'energia ondosa con la propagazione verso costa.

La variazione dell'orientazione dei vettori nell'avvicinamento a costa, che tendono a disporsi perpendicolarmente alle isobate, mette in evidenza il verificarsi del fenomeno della rifrazione, che è tanto più marcato quanto più la direzione di provenienza delle onde al largo è inclinata rispetto alla perpendicolare a costa.

Per completezza di analisi, sono state rappresentate la rosa (Figura 4-7) e la tabella di frequenza (Tabella 4-1) annuali del clima ondoso in un punto, denominato "P" (527626m E, 4905449m N), ubicato ad una distanza di circa 350 m da costa, in posizione centrale rispetto al tratto di litorale oggetto di studio, ad una profondità di circa 8 m.

L'analisi della rappresentazione del moto ondoso in forma di rosa nel punto "P" evidenzia, nel confronto con la rosa al largo (Figura 3-5), un significativo restringimento del settore di provenienza delle onde stesse, particolarmente evidente per gli eventi con direzione media di provenienza da Scirocco.

Alla profondità di 8 m del punto P la rifrazione comporta infatti la rotazione delle onde più oblique, restringendo di fatto il settore di provenienza alle direzioni comprese tra 165°N e 235°N. In particolare, solo un quarto circa delle onde provengono dal secondo settore e tre quarti circa sono caratterizzate da direzioni appartenenti al terzo settore.

Il settore prevalente, ossia con gli eventi più alti e più frequenti, risulta sempre essere compreso tra 205°N e 225°N, come evidenziato nell'analisi dei dati al largo, in quanto per queste direzioni, pressoché perpendicolari a costa, non subiscono significative riduzioni dal punto di vista energetico.



Figura 4-6 Ubicazione del punto P di estrazione dei parametri d'onda sottocosta (coordinate 527626m E, 4905449m N)

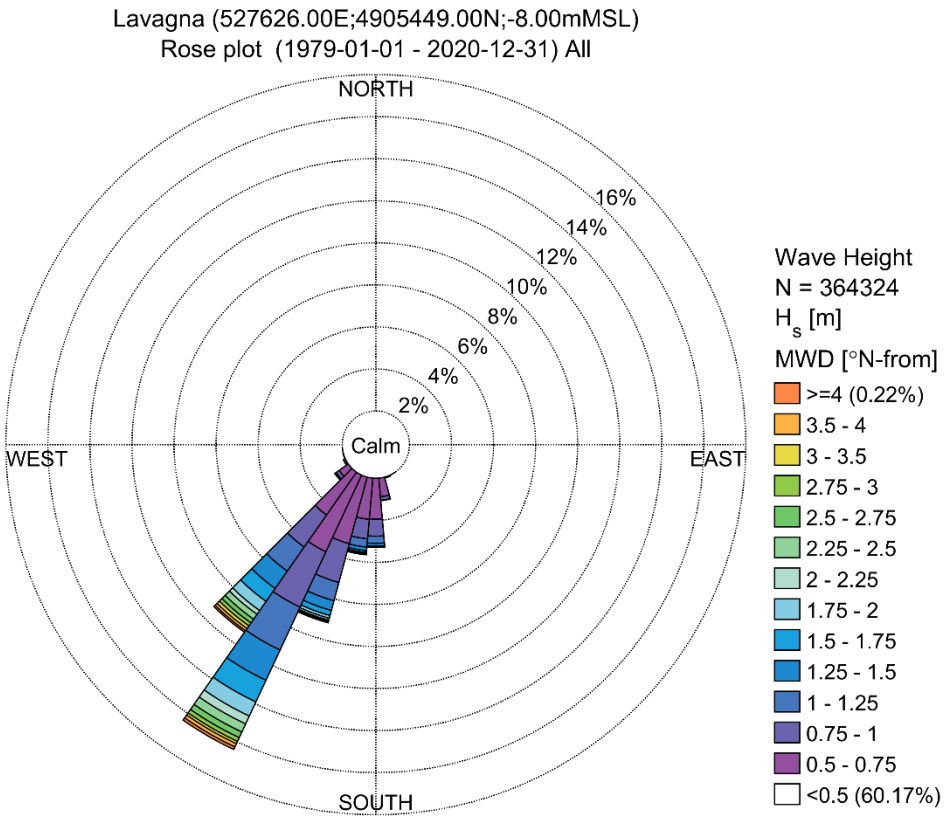
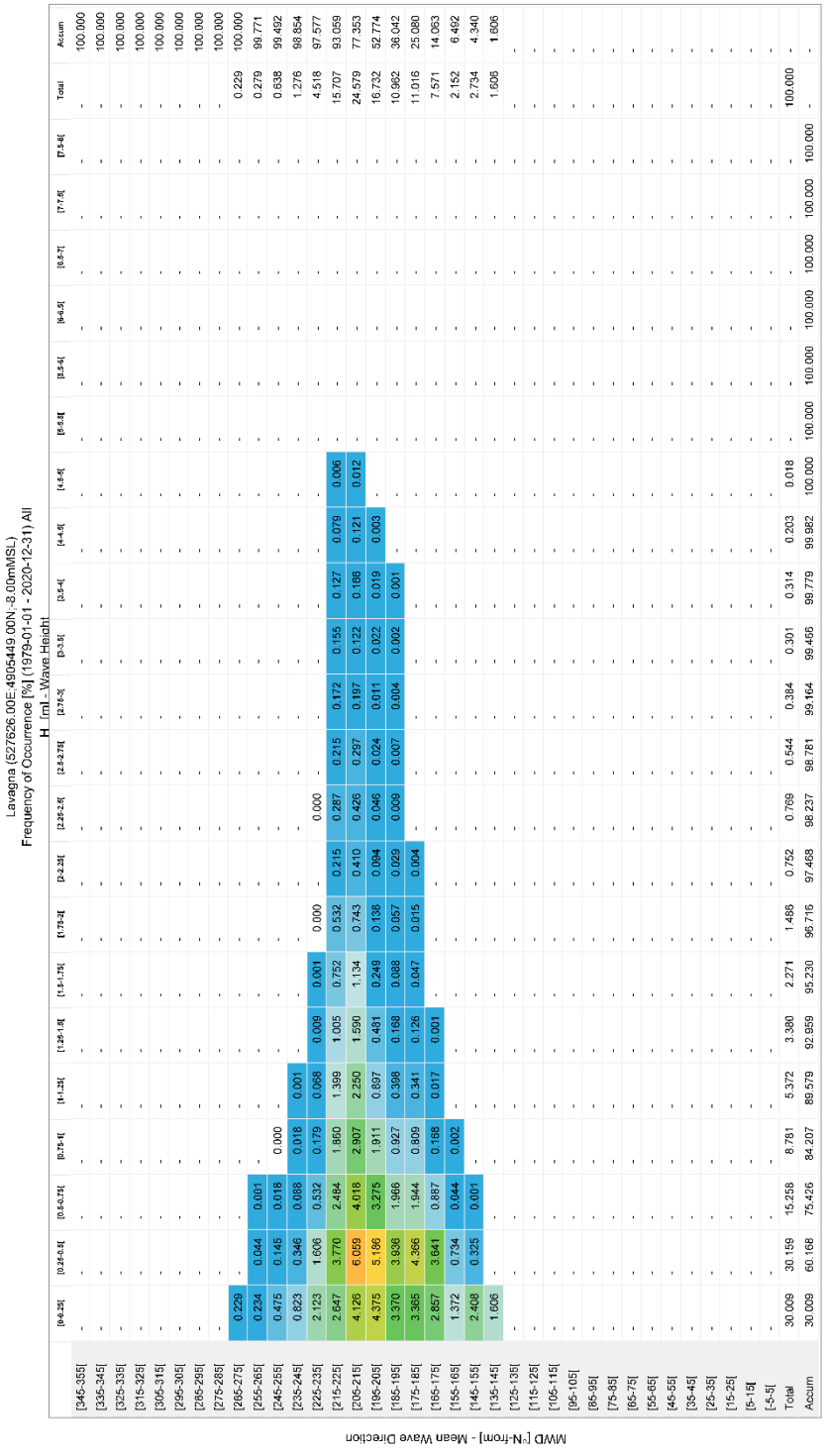


Figura 4-7 Rosa del clima ondoso per il punto P sottocosta (527626m E, 4905449m N) calcolata sul periodo 1979 – 2020. La calma è riferita ad onde con Hs inferiori a 0.5 m

Tabella 4-1 Numero di eventi per classi di altezza d'onda significativa Hs in funzione della direzione media di provenienza MWD per il punto P sottocosta (527626m E, 4905449m N) calcolata sul periodo 1979 – 2020



5 Modellazione di dettaglio del moto ondoso nella configurazione attuale e nelle due ipotesi di progetto

Al fine di raggiungere gli obiettivi dello studio, con particolare riferimento alla verifica dell'adeguatezza del ripascimento previsto ai fini di un'efficace difesa dalla risalita del moto ondoso sulla battigia e alla quantificazione dei benefici della possibile realizzazione di una protezione in massi a chiusura della cella, è stato utilizzato il nuovo modulo MIKE 3 WAVE FM di DHI [2].

Escludendo i modelli di fluidodinamica computazionale (CFD), non applicabili alle scale spaziali in oggetto, MIKE 3 WAVE FM è il modello d'onda più avanzato tra quelli disponibili sul mercato. È un modello 3D pienamente non lineare, "*phase resolving*", su maglia non strutturata. L'utilizzo del modello ha permesso di simulare le dinamiche di frangimento, run-up ed overtopping per un dominio di calcolo comprensivo della cella oggetto degli interventi, sia nella configurazione di stato attuale che in quelle di progetto.

Il codice MIKE 3 Waves viene abitualmente utilizzato per studi inerenti:

- Porti e Terminal: sia per lo studio dell'agitazione ondosa indotta da onde corte e lunghe, sia per la definizione delle caratteristiche degli input necessari agli studi di ormeggio;
- Studi costieri: per la propagazione non lineare dell'onda, per la dinamica alle basse profondità, per lo studio del frangimento e della risalita dell'onda sulla spiaggia, per l'analisi di allagamenti costieri fino alla riproduzione di tsunami;
- Strutture costiere, per lo studio dell'overtopping, della trasmissione e riflessione dell'onda su strutture porose.

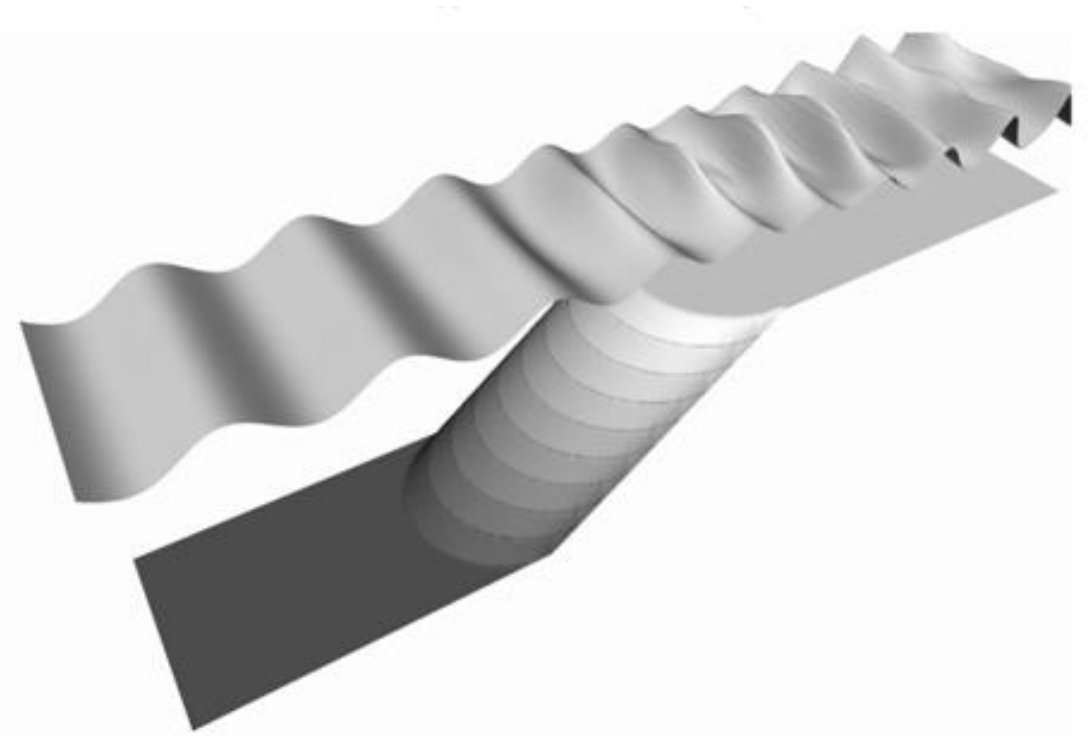


Figura 5-1 Esempio di mappa istantanea della superficie libera del mare riprodotta con MIKE 3 Wave

Il modello è basato sulla soluzione numerica delle equazioni tridimensionali incomprimibili di Navier-Stokes mediate (Reynolds Averaged Navier-Stokes equations) ed in condizioni di pressione non idrostatica. La discretizzazione spaziale viene eseguita utilizzando un metodo a volumi finiti, centrato sulla cella, mentre l'integrazione temporale viene eseguita utilizzando uno

schema semi-implicito. I termini convettivi verticali e di diffusione sono discretizzati utilizzando uno schema implicito per rimuovere i limiti di stabilità associati alla risoluzione verticale. I restanti termini sono discretizzati utilizzando uno schema Runge-Kutta esplicito del secondo ordine. I flussi convettivi dell'interfaccia vengono calcolati utilizzando un solutore Riemann approssimato HLLC. Questo schema consente una simulazione robusta e stabile di flussi anche in presenza di salti e/o discontinuità geometriche, essenziale per la modellazione delle onde nella zona di rottura o nelle strutture porose. La dissipazione numerica tiene conto della dissipazione nelle onde frangenti.

Nella dimensione orizzontale è utilizzata una maglia non strutturata costituita da triangoli o quadrilateri, mentre per la dimensione verticale si può utilizzare sia l'approccio di discretizzazione della colonna d'acqua secondo i cosiddetti livelli σ (strati di spessore variabile in funzione della profondità locale), che un approccio basato su livelli orizzontali "z" (strati orizzontali di spessore costante) sia, infine, un approccio combinato sigma-zeta.

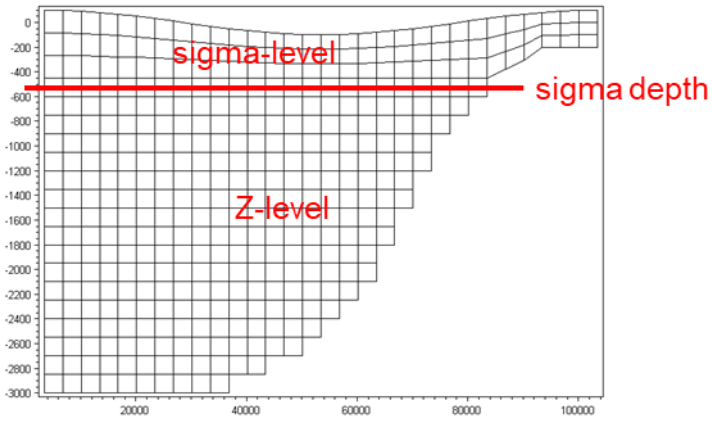


Figura 5-2 Possibili tipologie di discretizzazione della colonna d'acqua: con livelli di spessore variabile in funzione della profondità locale (sigma-layer), oppure con livelli orizzontali (z-layer)

Una descrizione tecnica del codice di calcolo è riportata in Allegato C.

5.1 Dominio di calcolo, batimetria

Il modello è stato implementato su un dominio di calcolo incentrato sull'area di interesse e risulta esteso lungo costa per circa 1 km e verso il largo per circa 0.6 km.

Al fine di rappresentare opportunamente i fenomeni non lineari, è stato necessario utilizzare una risoluzione elevata; l'area è stata quindi suddivisa in differenti sottodomini, ognuno caratterizzato da forma degli elementi e risoluzione differente: la risoluzione spaziale (lunghezza media dei lati dei triangoli) nella zona di mare più esterna è di circa 4 m, con una zona intermedia caratterizzata da elementi con lato 2 m, sino all'area della cella di interesse, compresa tra il pennello P1 e il pennello P2 (Figura 5-3), ove gli elementi sono quadrangolari e di lato 2 m (nella direzione di propagazione dell'onda).

La scelta di aumento incrementale di risoluzione verso costa consente di riprodurre le dinamiche prettamente costiere (frangimento, rifrazione, *shoaling*, attrito con il fondo) ad un grado di dettaglio adeguato agli obiettivi del presente lavoro.

In Figura 5-4 è illustrata la risoluzione orizzontale della mesh di calcolo del modello, complessivamente costituita da circa 160'000 elementi orizzontali.

Il risultato finale di interpolazione dei dati batimetrici a disposizione (par. 3.2) è mostrato nell'immagine a seguire, in cui sono rappresentate l'estensione del modello e la batimetria di calcolo per lo stato attuale.

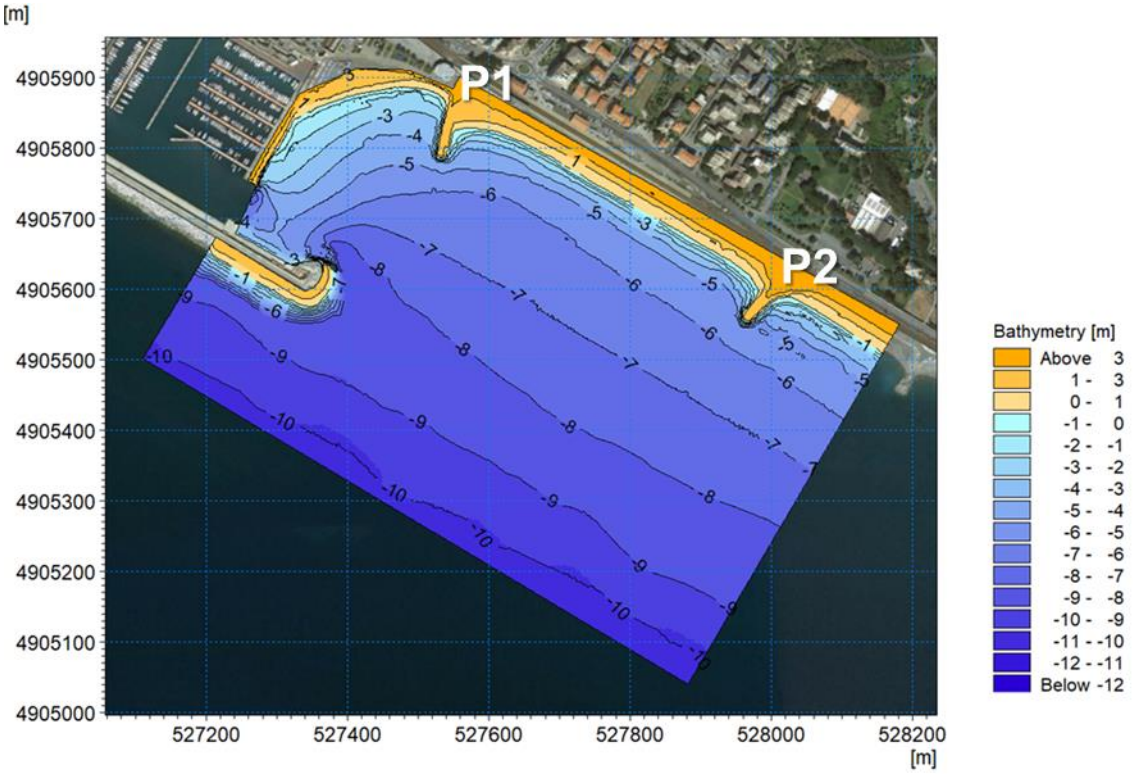


Figura 5-3 Batimetria del modello di dettaglio per la configurazione di stato attuale, ottenuta dal processamento dei dati a disposizione

L'andamento delle isobate risulta regolare e parallelo alla costa ad eccezione dell'area protetta dal molo di sopraflutto del porto di Lavagna, dove si osserva una graduale e significativa rotazione in senso antiorario delle isolinee.

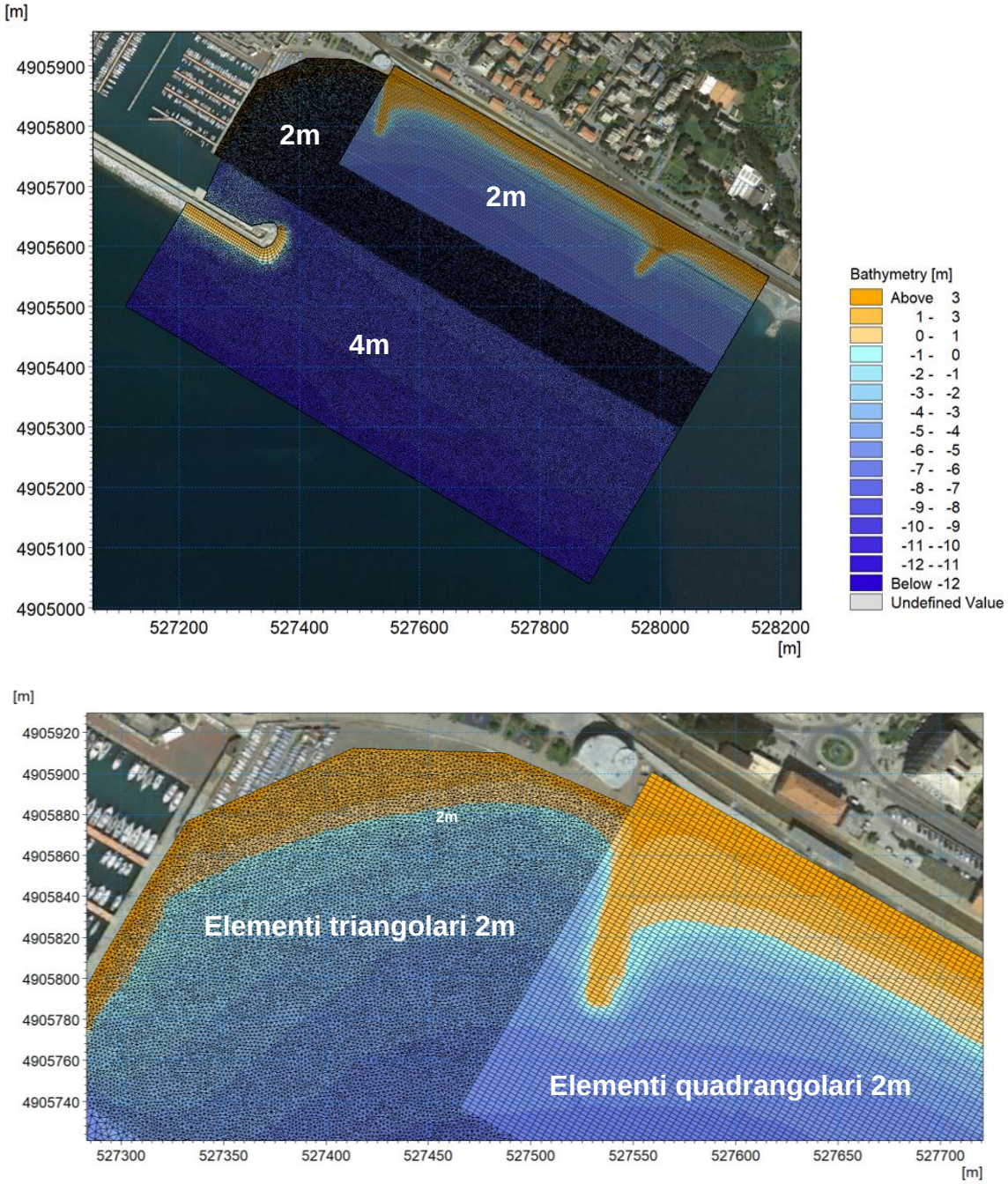


Figura 5-4 Risoluzione della mesh di calcolo del modello per l'intero dominio (in alto) e per un dettaglio (in basso)

Per la discretizzazione verticale sono stati utilizzati sei livelli di tipo sigma, con spessore variabile all'aumentare della profondità e tra i diversi layers. La Figura 5-5 illustra un esempio di rappresentazione di una sezione trasversale centrale alla cella di studio.

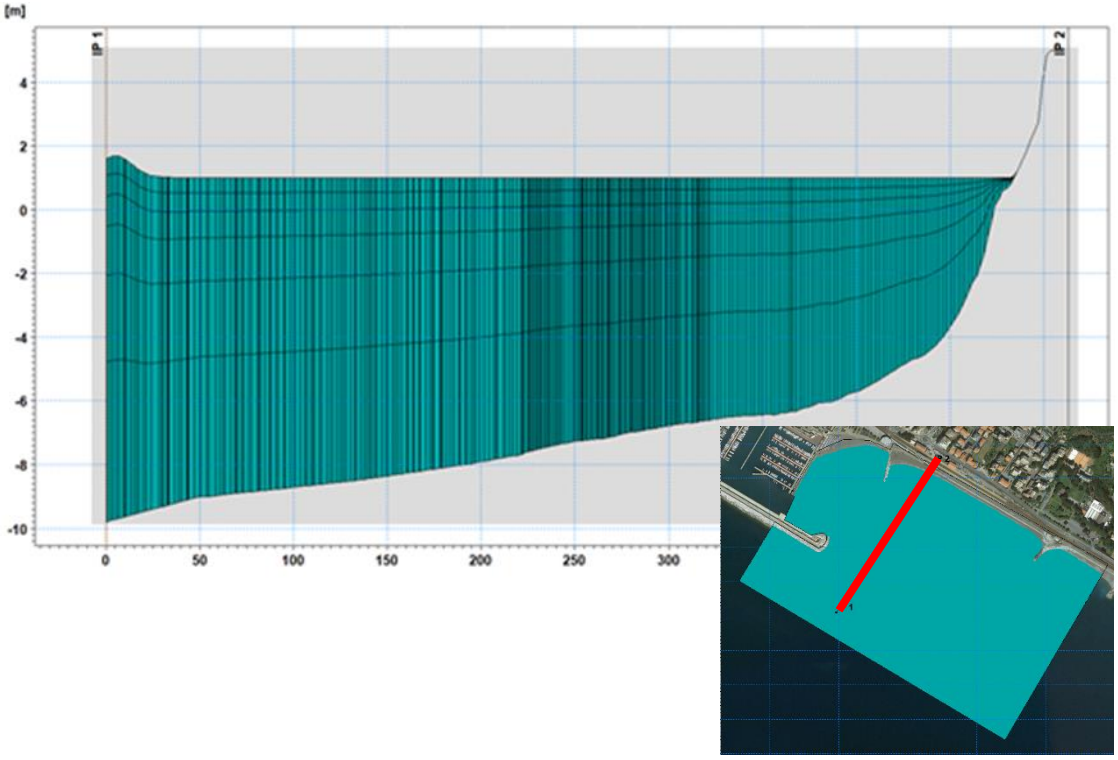


Figura 5-5 Esempio di discretizzazione della colonna d'acqua in layers sigma. Nell'immagine in basso a destra la linea in rosso indica la traccia della sezione

La dimensione del dominio e la relativa risoluzione, nei vari sottodomini, è stata mantenuta eguale anche per le configurazioni progettuali.

Come anticipato in premessa le alternative progettuali analizzate sono due:

- Configurazione di Progetto A: comprensiva dell'intervento di ripascimento, (19'480m^3 di sedimenti provenienti dalla barra fociva del fiume Entella), ha previsto un'opportuna modifica delle quote e delle pendenze del fondale nella fascia compresa tra l'isobata -4 m e la quota di +2 m, come da specifiche progettuali;
- Configurazione di Progetto B: comprensiva dell'intervento di ripascimento come sopra, ha previsto l'integrazione dell'intervento con l'inserimento di un'opera in massi (12'100t di massi naturali) alla profondità di circa 5.8 m, con berma posta a -4 m, in analogia alla tipologia di opere già realizzate nelle celle litorali adiacenti.

Si riporta nell'immagine a seguire lo schema planimetrico della configurazione proposta, rimandando agli elaborati progettuali dedicati per i dettagli.

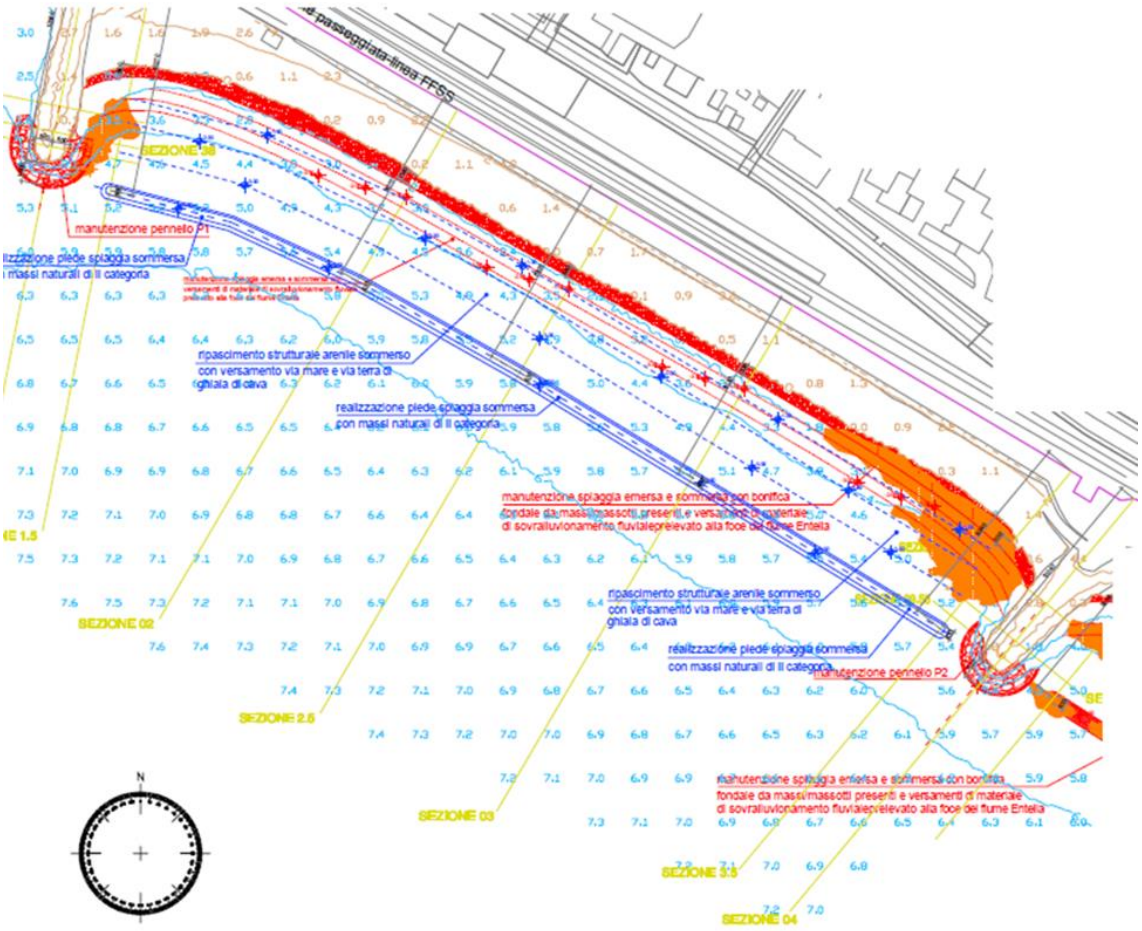


Figura 5-6 Schema planimetrico progettuale, con in colore rosso la configurazione A, comprensiva di riprofilatura dei fondali, rifioritura delle testate dei pennelli e, in arancione, dello sbancamento di una porzione rocciosa; in colore blu, alla profondità a cui sono imbasate le testate dei pennelli, è inserita l'opera in massi (configurazione B)

In Figura 5-7 viene riportata la batimetria risultante per la configurazione di Progetto A mentre in Figura 5-8 è rappresentata la configurazione di Progetto B, con un dettaglio sulla zona dell'opera a chiusura della cella.

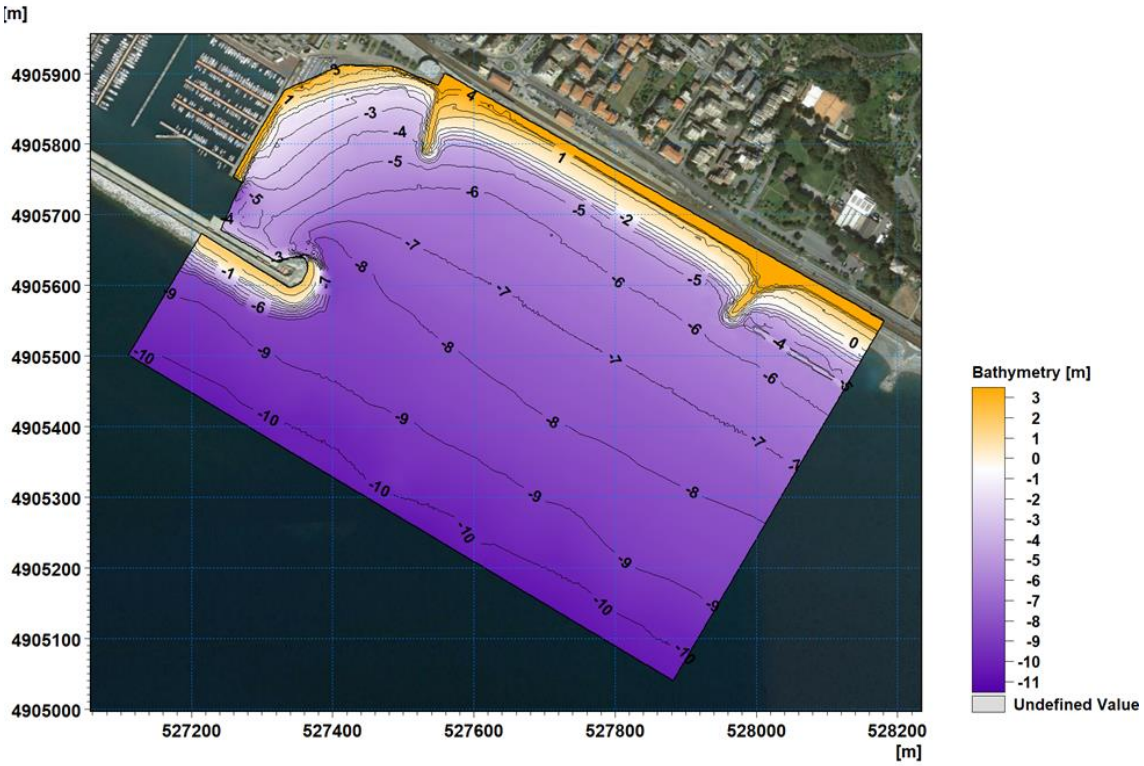


Figura 5-7 Batimetria del modello di dettaglio per la configurazione A, ottenuta dal processamento dei dati a disposizione secondo le indicazioni progettuali sul ripascimento previsto

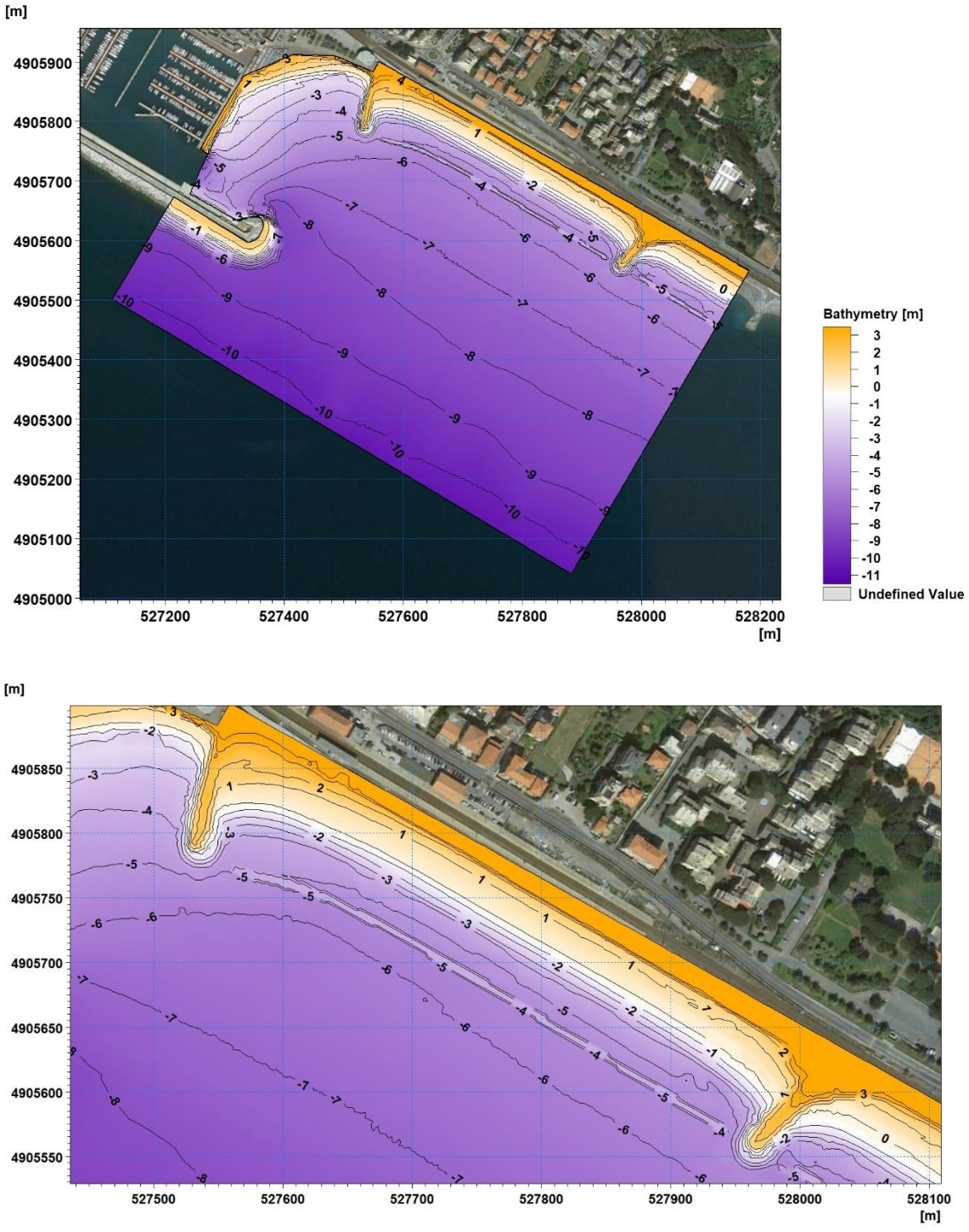


Figura 5-8 Batimetria del modello di dettaglio per la configurazione B, comprensiva sia dell'intervento di ripascimento che dell'opera in massi al limite della cella. In alto la rappresentazione per l'intero dominio di calcolo, in basso un dettaglio sulla cella oggetto degli interventi

5.2 Selezione delle mareggiate rappresentative

Il modello MIKE 3 Wave, come anticipato, è stato utilizzato per l'identificazione e l'analisi delle principali dinamiche sottocosta in prossimità del litorale di Lavagna.

A tal fine è stato preliminarmente necessario selezionare una serie di condizioni d'onda rappresentative. Sulla base dell'analisi dei risultati della propagazione della serie ultra-quarantennale dei dati d'onda (capitolo 4), estratti sottocosta nel punto P (Figura 4-6), si è assunto di selezionare per i successivi approfondimenti modellistici tre eventi rappresentativi, variabili sia per direzione di provenienza, sia per altezza d'onda al picco della mareggiata. L'analisi ha evidenziato che, sottocosta, i settori direzionali di provenienza del moto ondoso siano sostanzialmente limitati a Libeccio e Mezzogiorno. Le onde che al largo si presentano da SE (Scirocco) tendono infatti a ruotare significativamente sottocosta per rifrazione e a disporsi da S (Mezzogiorno).

Per il settore di Libeccio, regnante e dominante, è stata selezionata la mareggiata più intensa in riferimento agli ultimi anni, ovvero quella del 30 Ottobre 2018, caratterizzata da una altezza d'onda Hs al picco pari a 4.53 m (Figura 5-9). Per tale evento è stato possibile reperire anche importanti testimonianze fotografiche (riportate negli elaborati progettuali) e video che hanno permesso di valutare la corretta ricostruzione modellistica dell'ondazione.

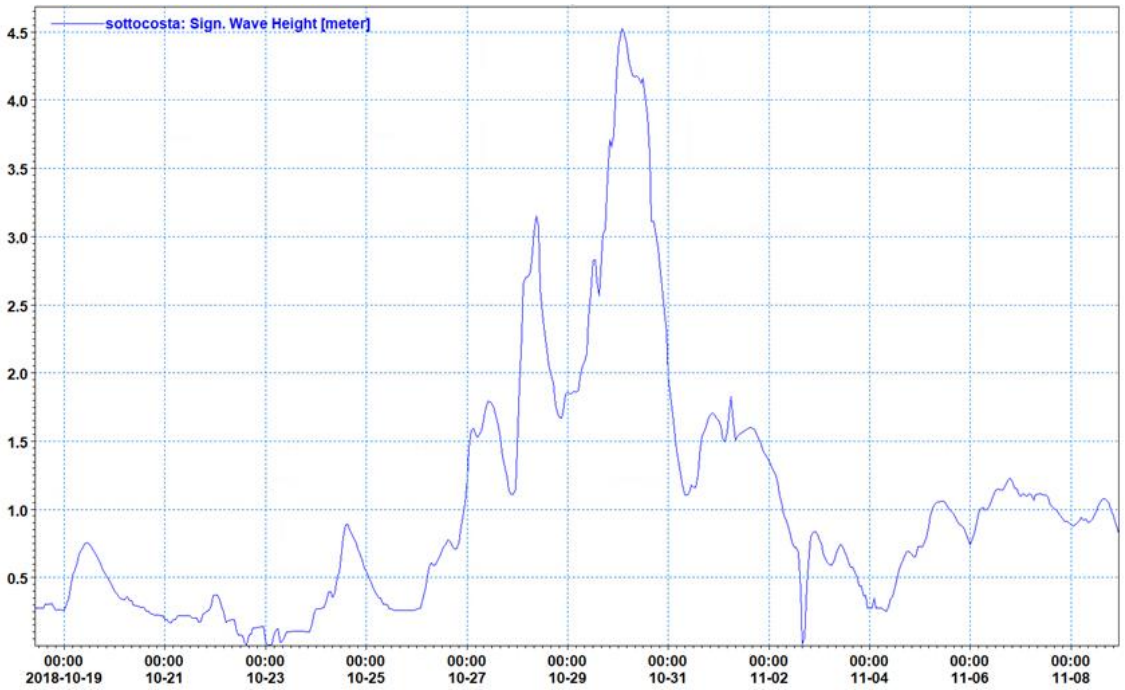


Figura 5-9 Serie di altezza d'onda significativa Hs, comprensiva dell'evento del 30 Ottobre 2018, estratta sottocosta nel punto P. Le condizioni d'onda al picco sono state prese a riferimento per la simulazione tridimensionale di dettaglio

La seconda mareggiata è stata selezionata in riferimento alla direzione media di provenienza da Mezzogiorno (evento del 26 Dicembre 2013, Hs al picco pari a 3.87 m, Figura 5-10).

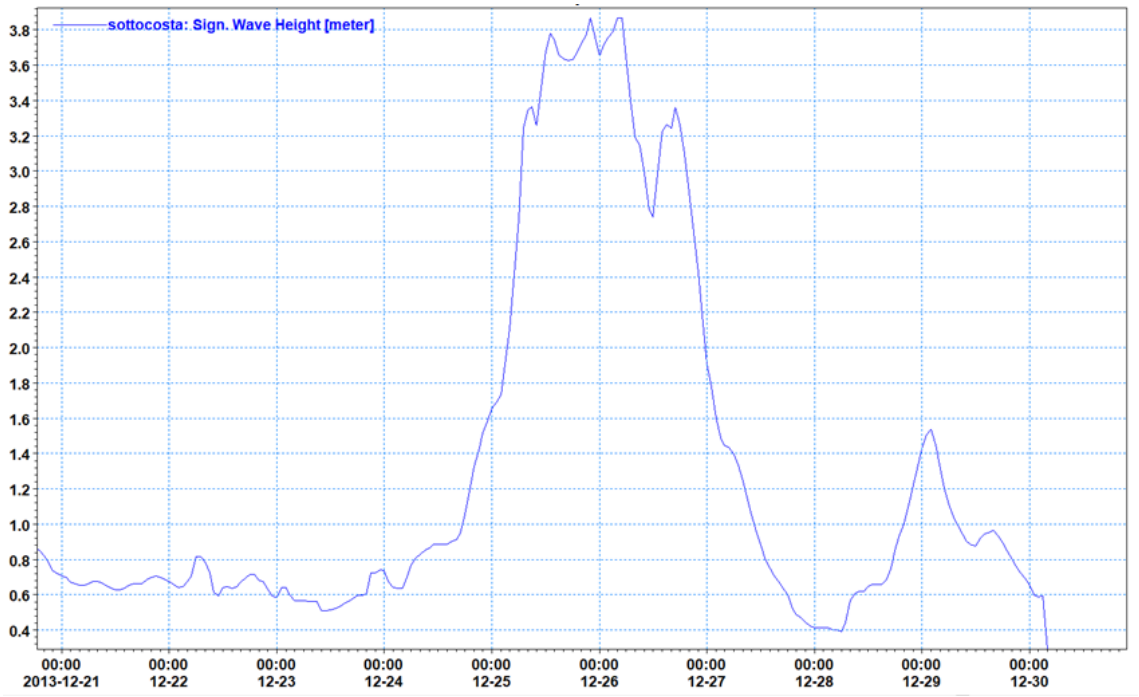


Figura 5-10 Serie di altezza d'onda significativa Hs comprensiva dell'evento del 26 Dicembre 2013, estratta sottocosta nel punto P. Le condizioni d'onda al picco sono state prese a riferimento per la simulazione tridimensionale di dettaglio

Per completare l'analisi è stata selezionata un'ulteriore onda da Libeccio, caratterizzata da un'altezza d'onda significativa al picco molto inferiore a quella del 30 Ottobre 2018. In particolare è stato selezionato l'evento del 6 Marzo 2020 (Figura 5-11) che presenta una Hs al picco pari a 1.98 m.

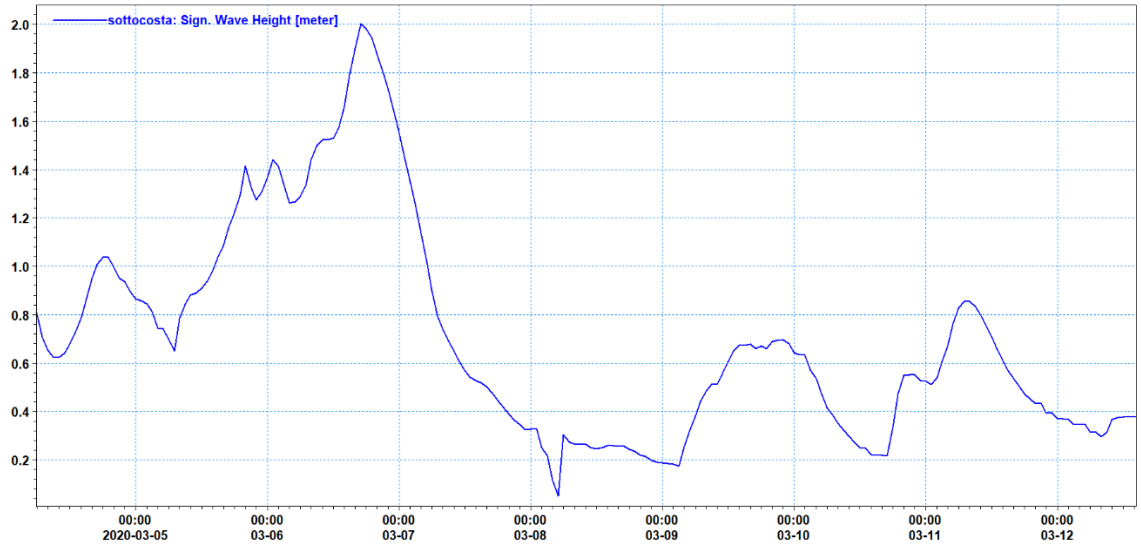


Figura 5-11 Serie di altezza d'onda significativa Hs comprensiva dell'evento del 6 Marzo 2020, estratta sottocosta nel punto P. Le condizioni d'onda al picco sono state prese a riferimento per la simulazione tridimensionale di dettaglio

Le caratteristiche delle tre onde prese a riferimento per le simulazioni sono riassunte in Tabella 5-1.

Tabella 5-1 Elenco delle condizioni d'onda selezionate per la modellazione di dettaglio (onda e conseguente circolazione locale). I dati si riferiscono al picco di mareggiata

Evento di mareggiata	Hs [m]	Tp [s]	MWD [°N]
30 Ottobre 2018	4.53	10.8	209
26 Dicembre 2013	3.87	10.7	198
6 Marzo 2020	1.98	8.9	216

Si precisa che alle condizioni d'onda sopra riportate, nelle simulazioni modellistiche descritte in dettaglio nel seguito, è stato cautelativamente associato un livello del mare di riferimento pari a 1 m per gli eventi più intensi (Ottobre 2018 e Dicembre 2013) e pari a 0.5 m per la mareggiata del Marzo 2020.

5.3 Risultati del modello d'onda di dettaglio

Le simulazioni condotte hanno permesso di ottenere, per ciascuna delle tre configurazioni geometriche descritte e per le tre condizioni d'onda selezionate, i risultati delle principali grandezze di moto ondoso ed idrodinamiche, in tutti i punti del dominio di calcolo.

Nei paragrafi a seguire si riportano i risultati in termini di:

- mappe di altezza d'onda significativa e direzione di provenienza;
- mappe di elevazione della superficie libera;
- andamento dell'onda per 3 transetti rappresentativi interni alla cella.

Nell'immagine a seguire è riportata l'ubicazione dei transetti A, B e C selezionati per analizzare la risalita dell'onda sulla spiaggia in determinati istanti degli eventi simulati.



Figura 5-12 Ubicazione dei 3 transetti rappresentativi A, B e C

5.3.1 Configurazione di stato attuale

Il principale obiettivo delle simulazioni della configurazione di stato attuale è, attraverso il confronto con i risultati delle configurazioni di progetto, quantificare l'efficacia degli interventi proposti, con particolare riferimento alla risalita dell'onda sull'arenile (runup).

Al fine di agevolare la comparazione dei risultati si è proceduto riportando le medesime tipologie di mappe, nei medesimi istanti delle simulazioni, suddivisi per ondazione di riferimento.

Mareggiata 2018

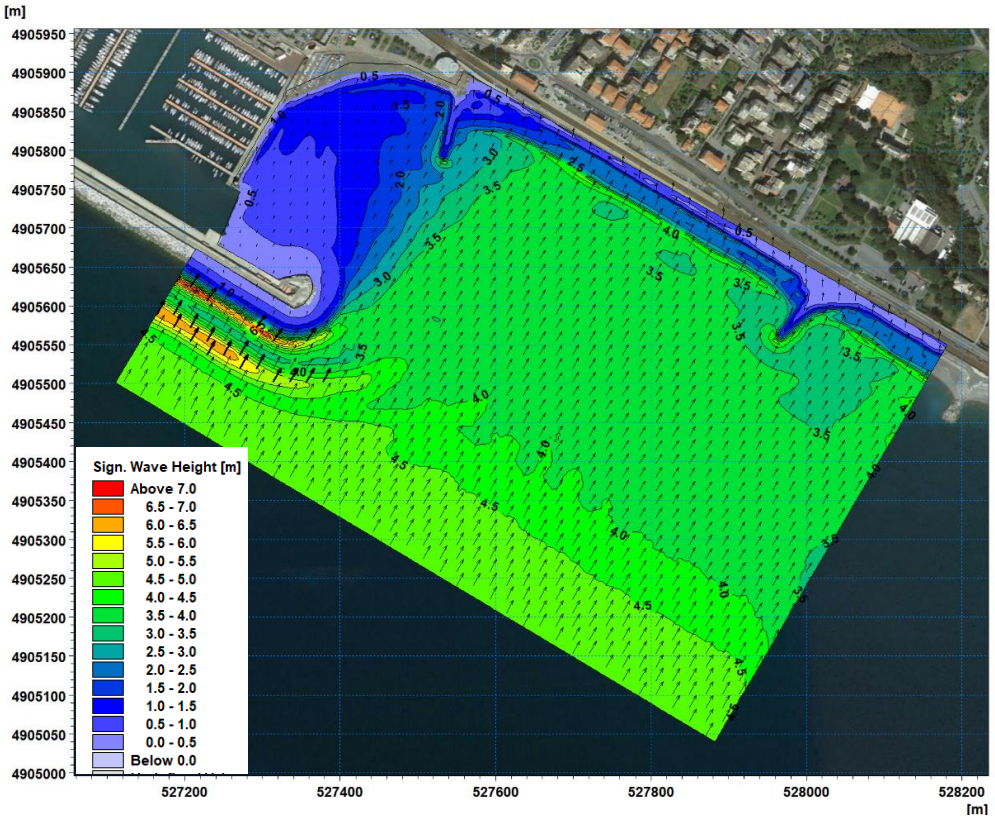


Figura 5-13 Configurazione di stato attuale / picco di mareggiata del 30 Ottobre 2018: mappa di distribuzione dell'altezza d'onda significativa Hs

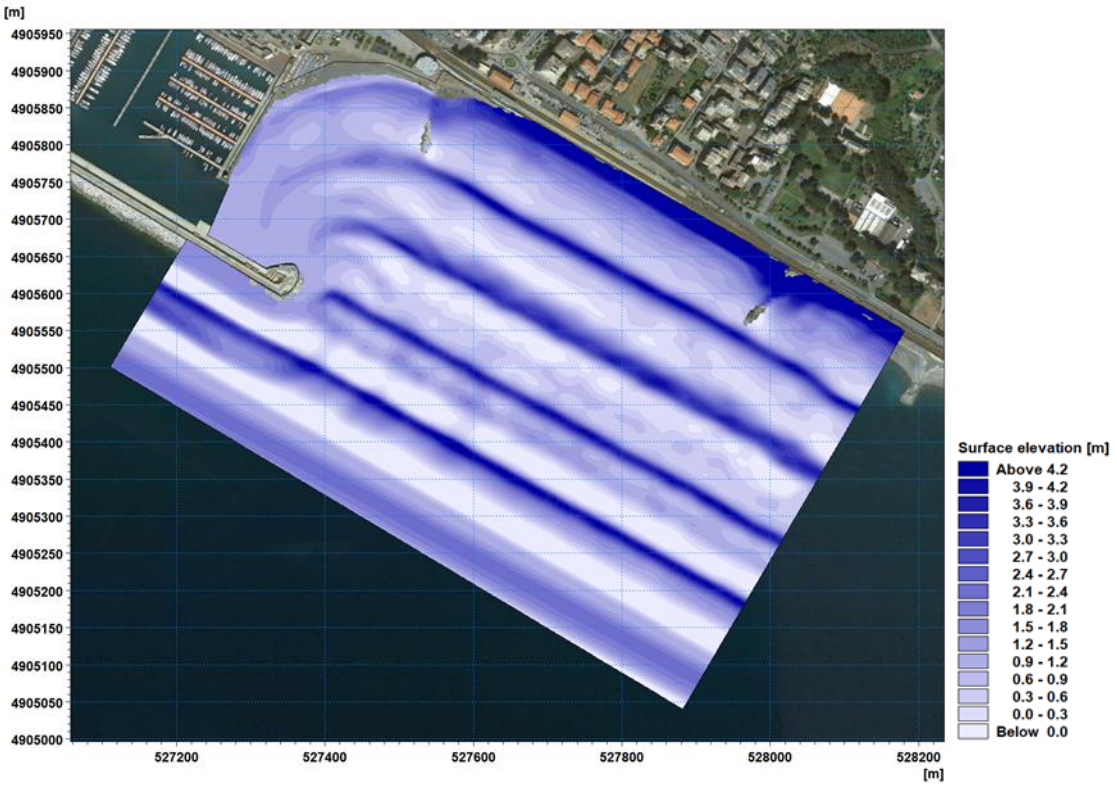


Figura 5-14 Configurazione di stato attuale / picco di mareggiata del 30 Ottobre 2018: distribuzione dell'elevazione della superficie libera durante l'evento

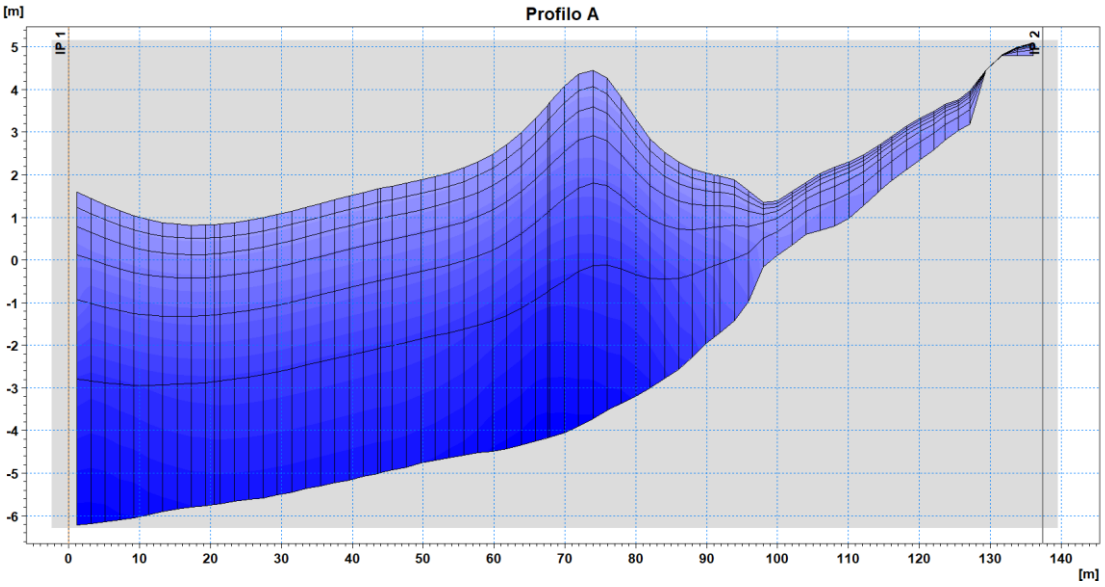


Figura 5-15 Configurazione di stato attuale: esempio di risalita dell'onda lungo il profilo A in un istante della mareggiata del 30 Ottobre 2018 (Time Step 1827)

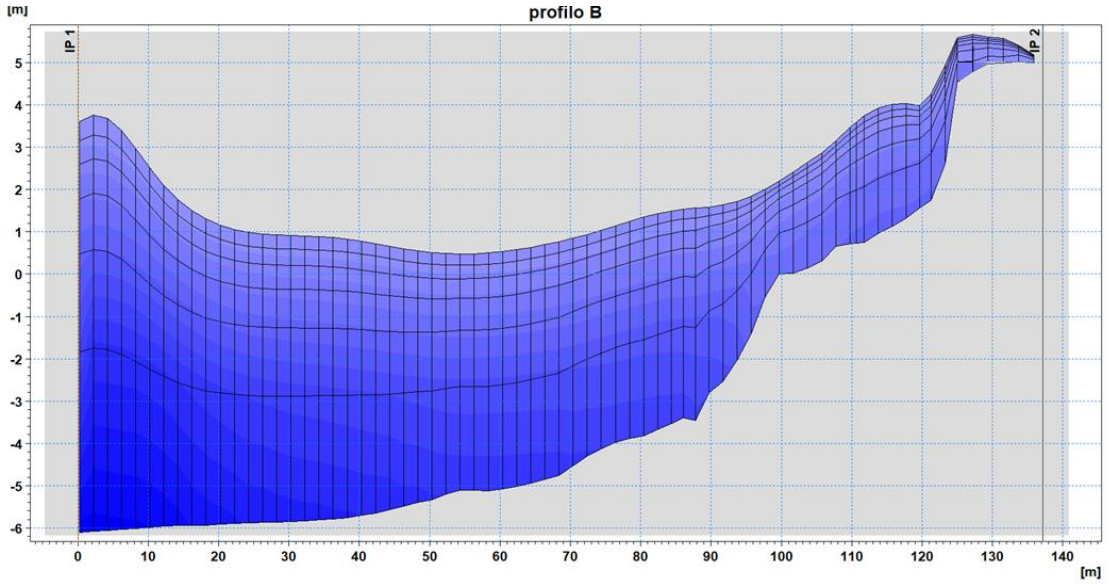


Figura 5-16 Configurazione di stato attuale: esempio di risalita dell'onda lungo il profilo B in un istante della mareggiata del 30 Ottobre 2018 (Time Step 2753)

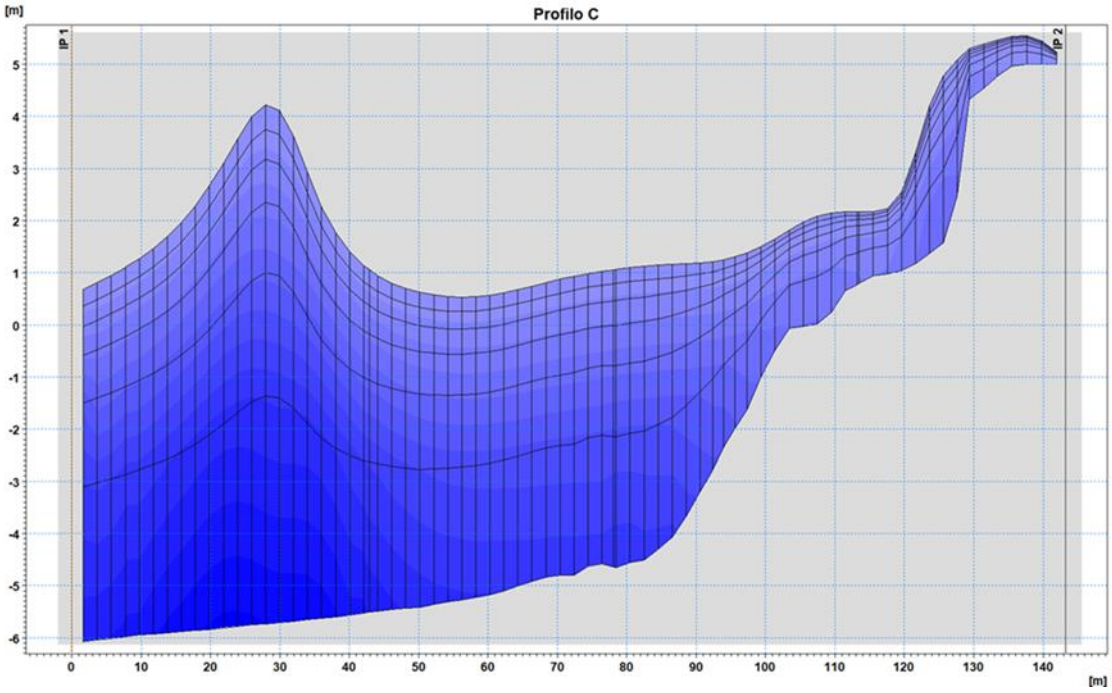


Figura 5-17 Configurazione di stato attuale: esempio di risalita dell'onda lungo il profilo C in un istante della mareggiata del 30 Ottobre 2018 (Time Step 3105)

Mareggiata 2013

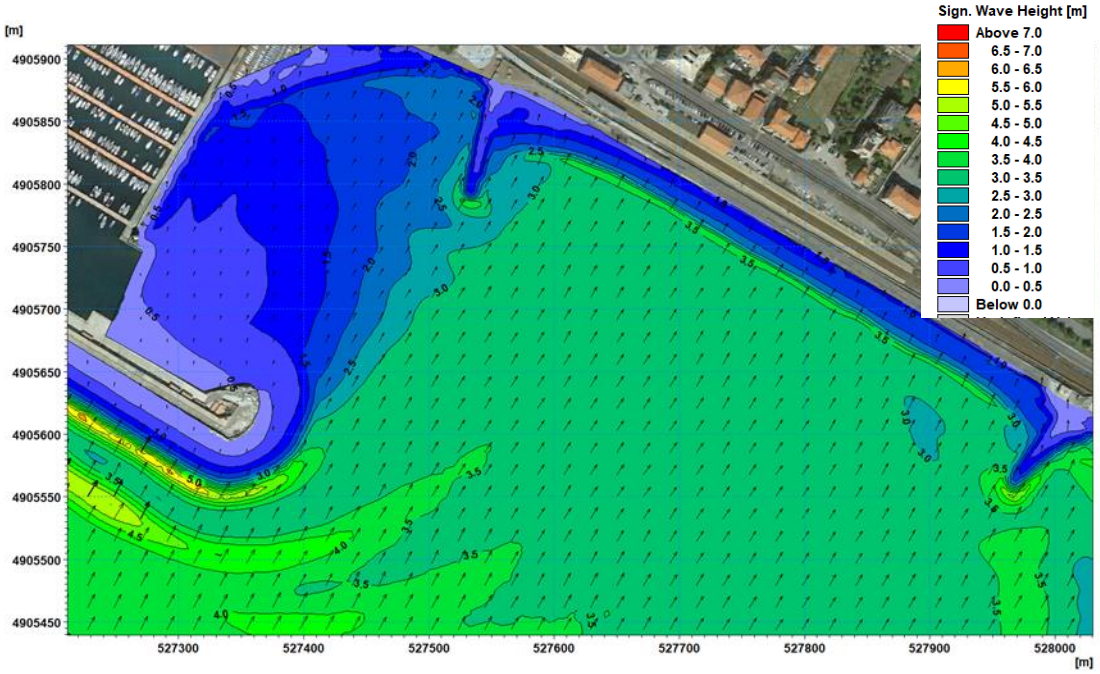


Figura 5-18 Configurazione di stato attuale / picco di mareggiata del 26 Dicembre 2013: dettaglio della mappa di distribuzione dell'altezza d'onda significativa Hs

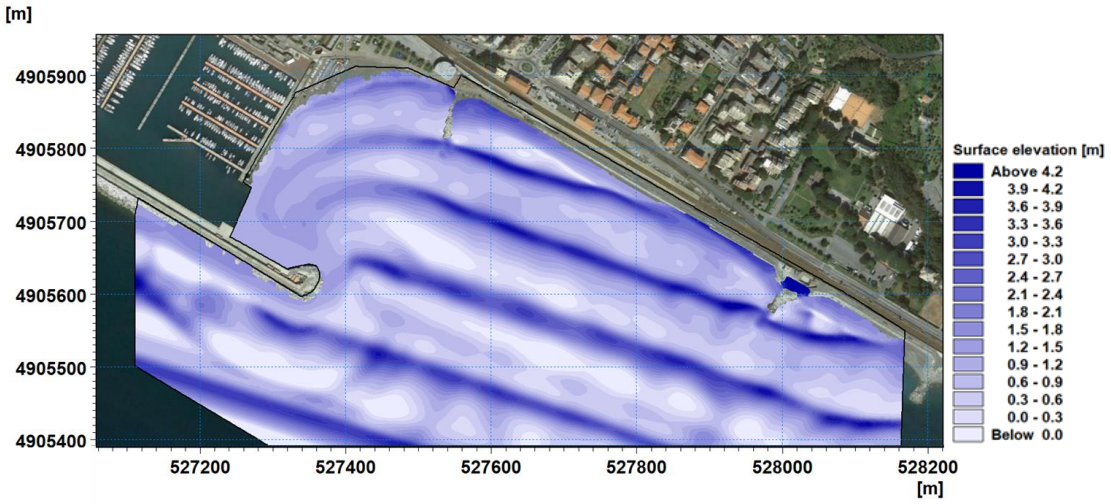


Figura 5-19 Configurazione di stato attuale / picco di mareggiata del 26 Dicembre 2013: esempio di distribuzione dell'elevazione della superficie libera durante l'evento

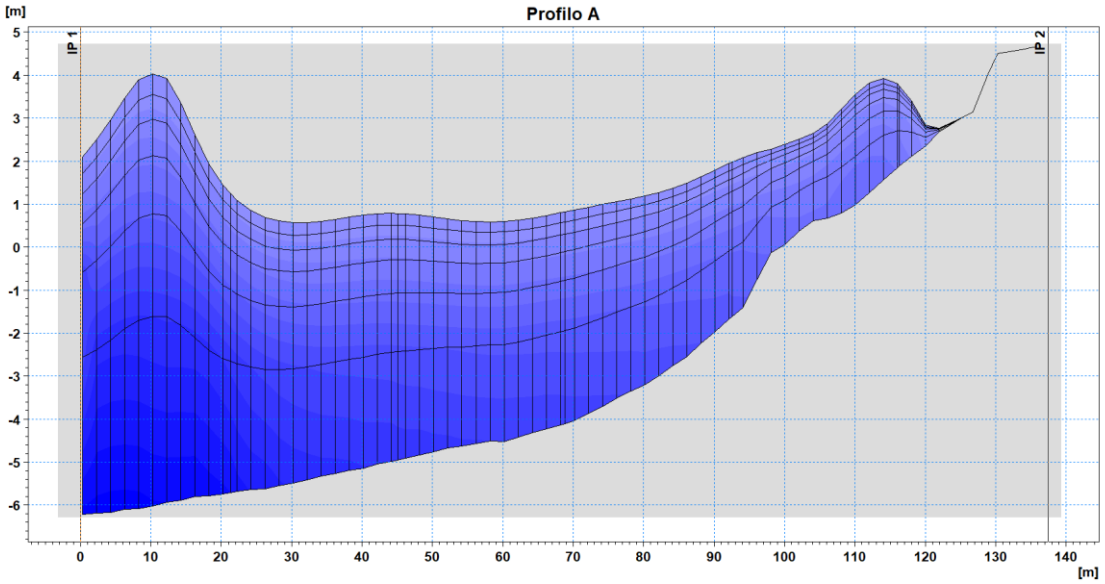


Figura 5-20 Configurazione di stato attuale: esempio di risalita dell'onda lungo il profilo A in un istante della mareggiata del 26 Dicembre 2013 (Time Step 291)

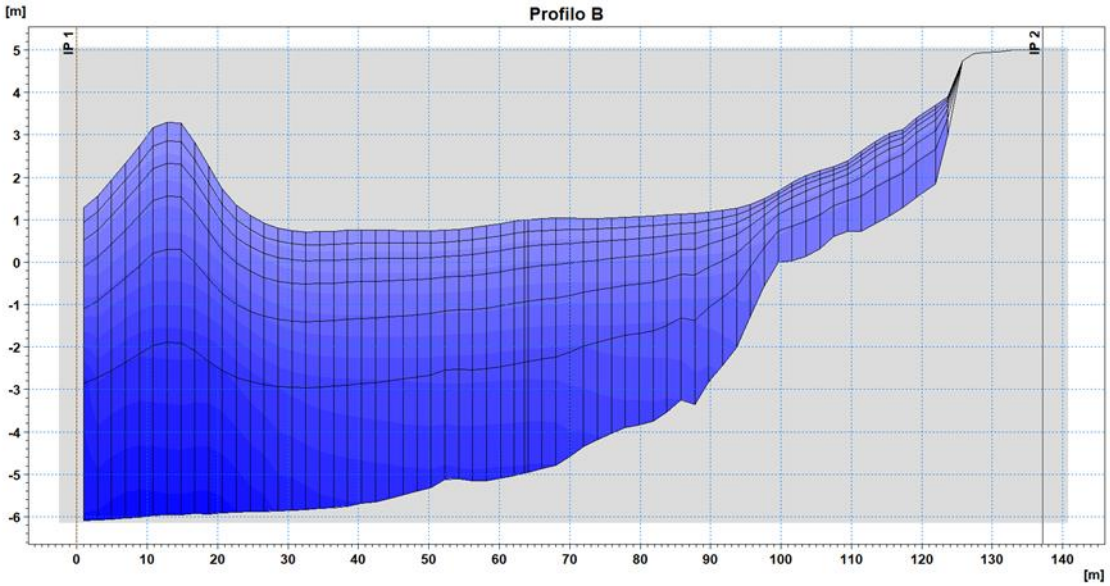


Figura 5-21 Configurazione di stato attuale: esempio di risalita dell'onda lungo il profilo B in un istante della mareggiata del 26 Dicembre 2013 (Time Step 102)

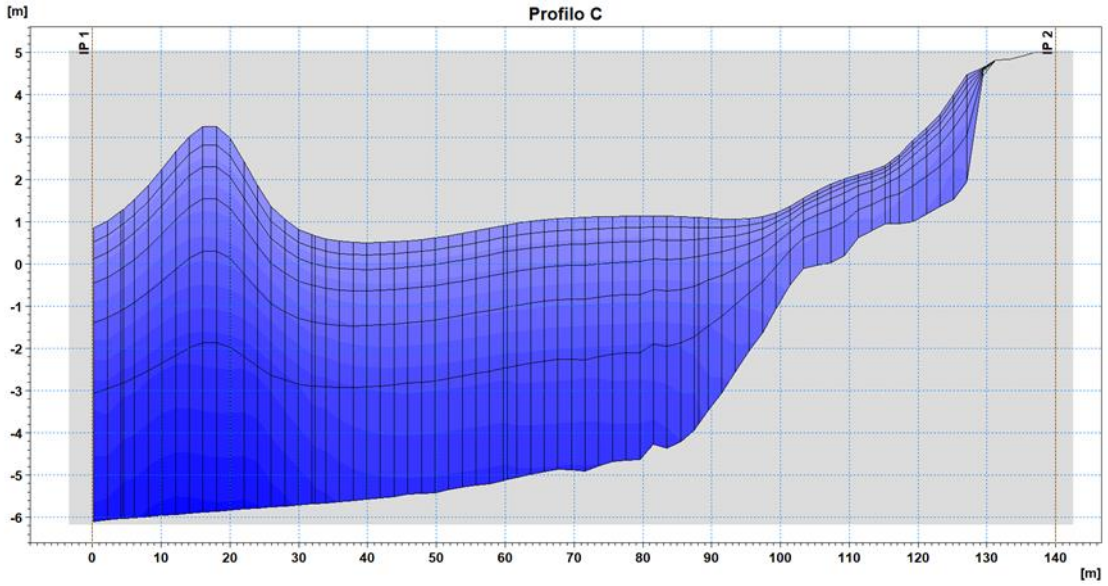


Figura 5-22 Configurazione di stato attuale: esempio di risalita dell'onda lungo il profilo C in un istante della mareggiata del 26 Dicembre 2013 (Time Step 98)

Mareggiata 2020

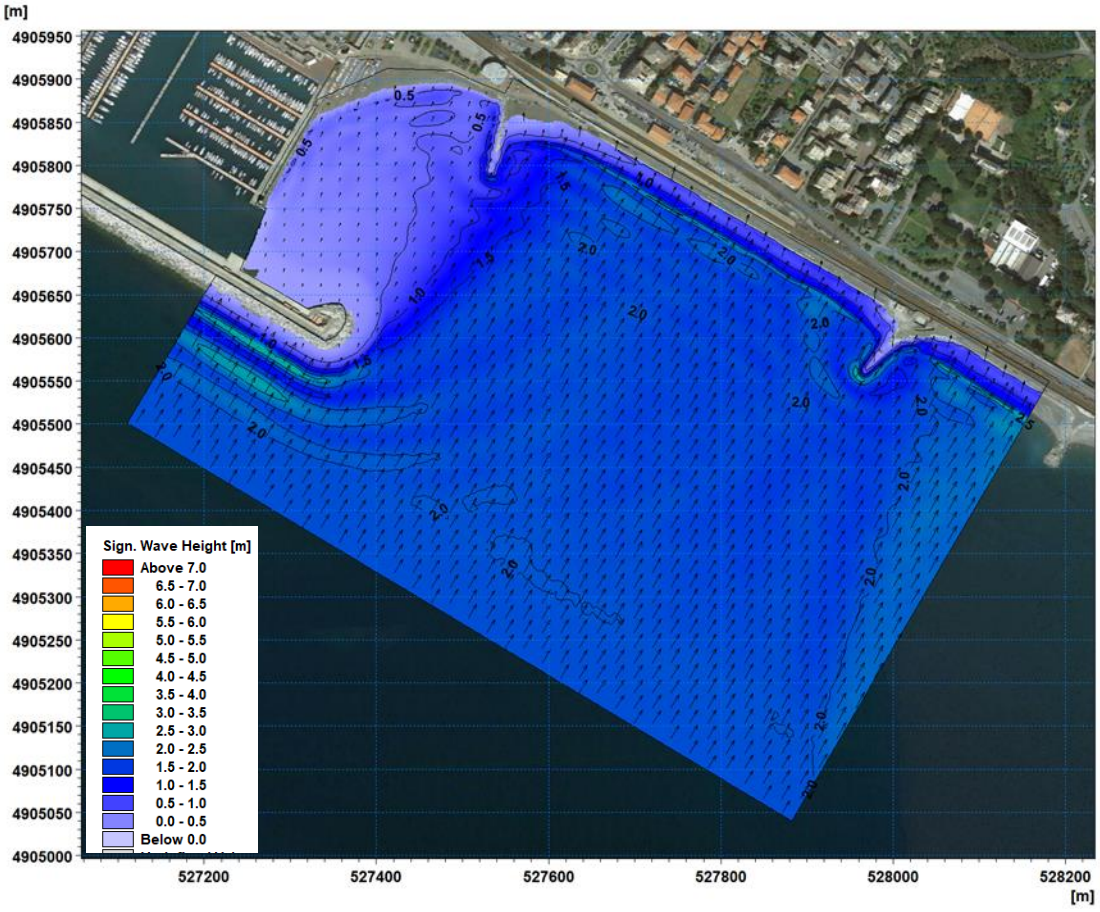


Figura 5-23 Configurazione di stato attuale / picco di mareggiata del 6 Marzo 2020: mappa di distribuzione dell'altezza d'onda significativa Hs

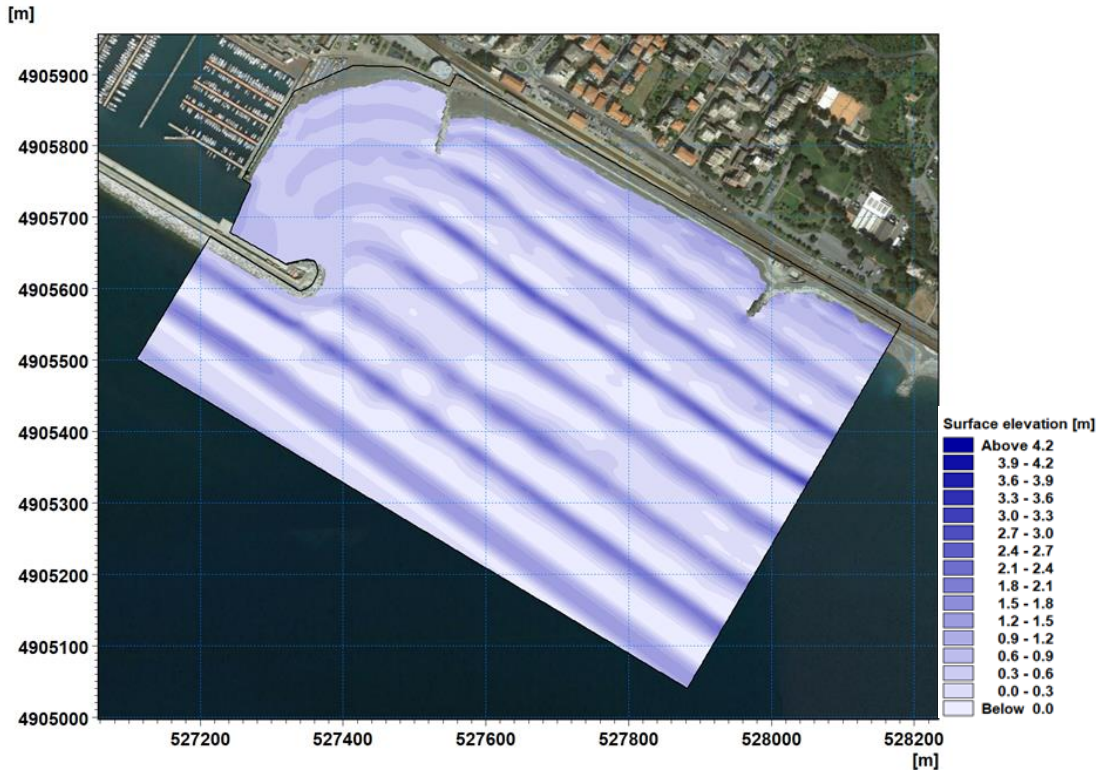


Figura 5-24 Configurazione di stato attuale / picco di mareggiata del 6 Marzo 2020: esempio di distribuzione dell'elevazione della superficie libera durante l'evento

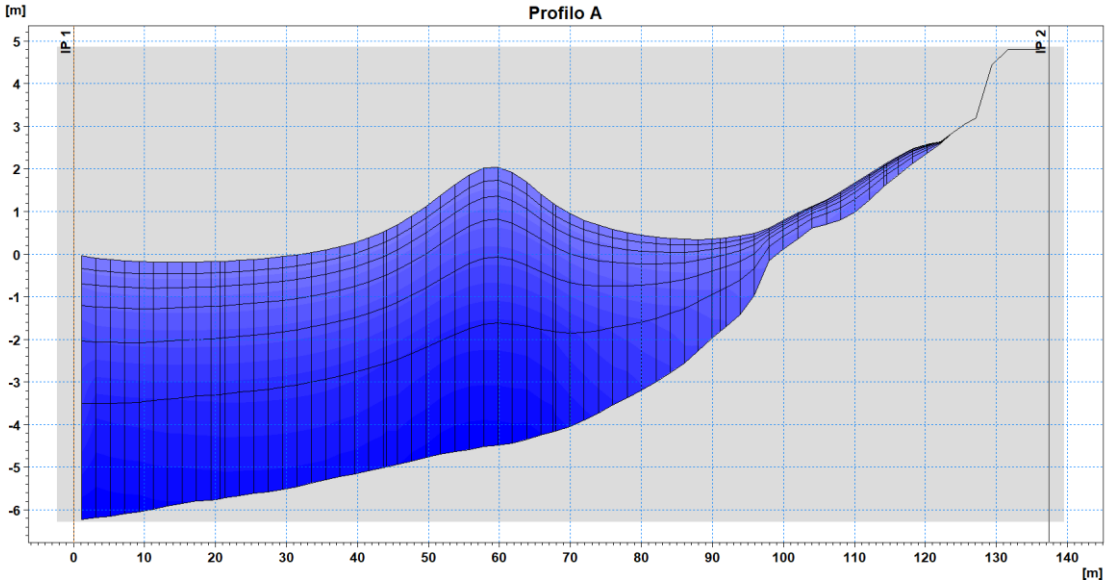


Figura 5-25 Configurazione di stato attuale: esempio di risalita dell'onda lungo il profilo A in un istante della mareggiata del 6 Marzo 2020 (Time Step 1038)

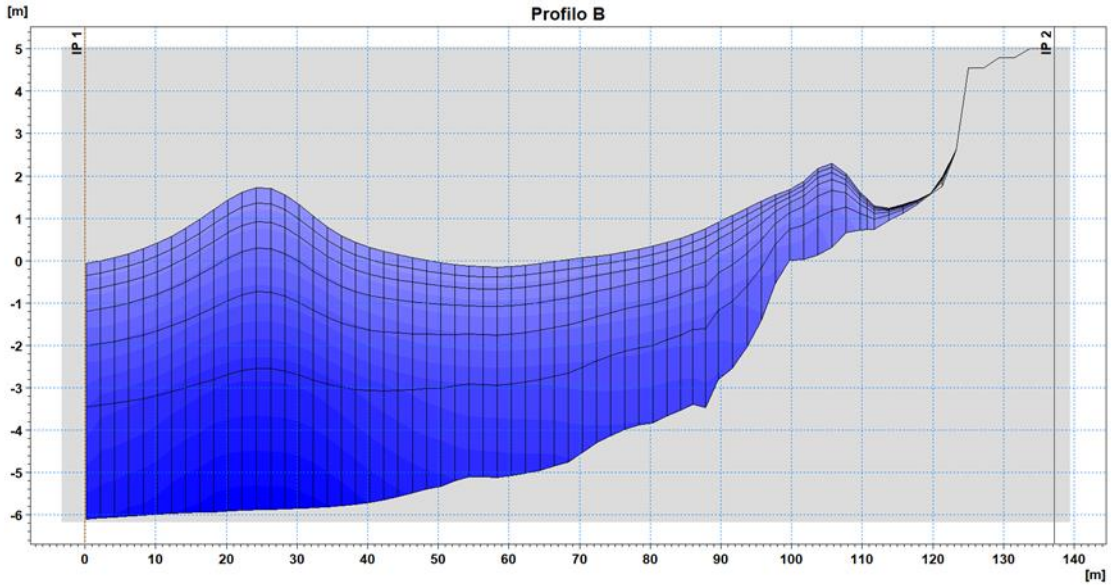


Figura 5-26 Configurazione di stato attuale: esempio di risalita dell'onda lungo il profilo B in un istante della mareggiata del 6 Marzo 2020 (Time Step 577)

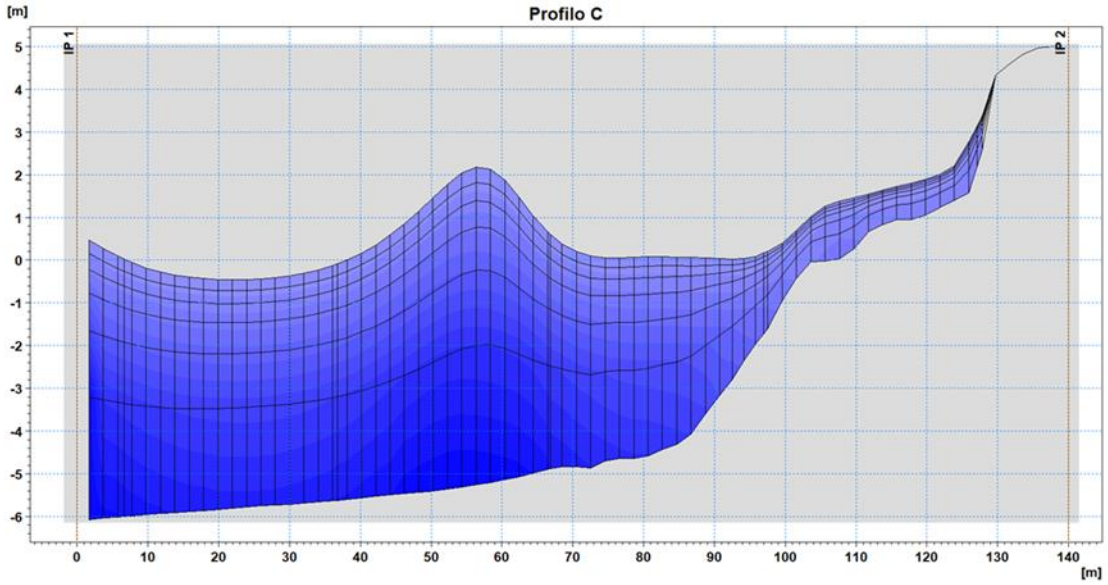


Figura 5-27 Configurazione di stato attuale: esempio di risalita dell'onda lungo il profilo C in un istante della mareggiata del 6 Marzo 2020 (Time Step 1210)

5.3.2 Configurazione di progetto A

A seguire si riportano i risultati relativi alla configurazione progettuale comprensiva del solo intervento di ripascimento.

Nella rappresentazione della risalita dell'onda lungo la spiaggia si è deciso di cambiare il colore (per la configurazione di progetto A in giallo) per agevolare il confronto dei risultati grafici.

Mareggiata 2018

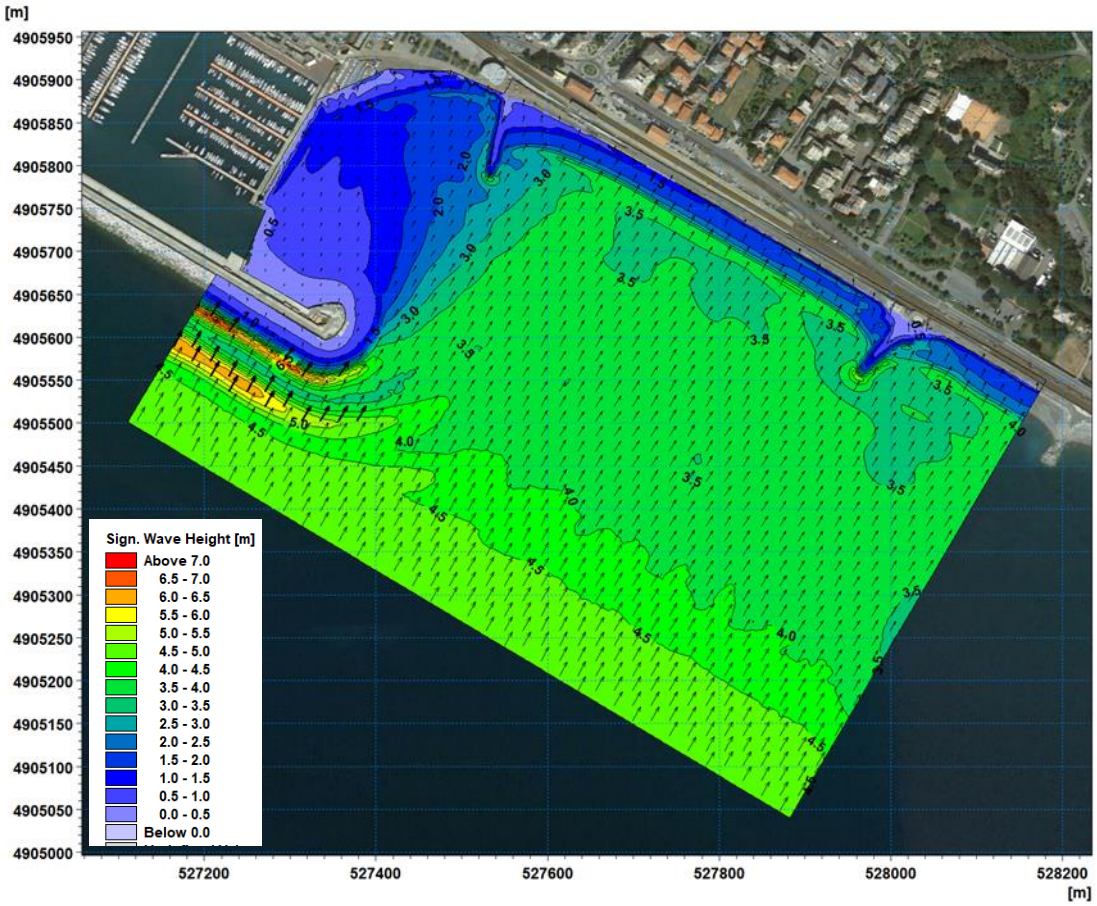


Figura 5-28 Configurazione di progetto A, comprensiva dell'intervento di ripascimento / picco di mareggiata 30 Ottobre 2018: mappa di distribuzione dell'altezza d'onda significativa Hs

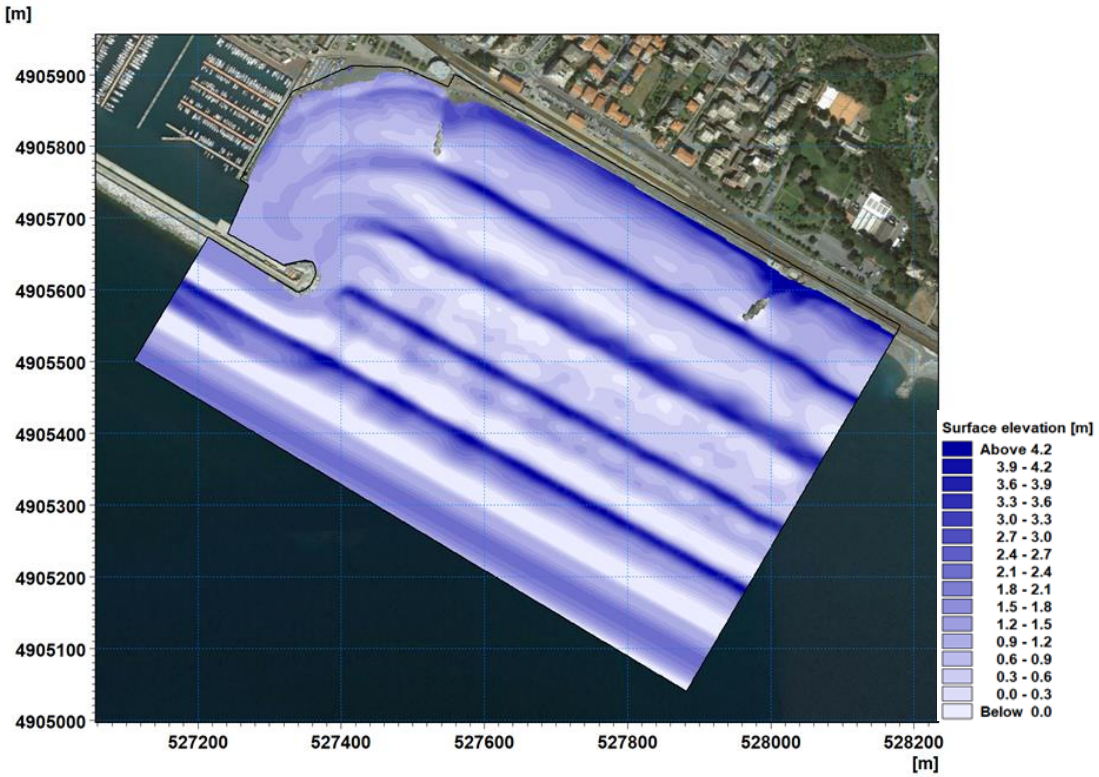


Figura 5-29 Configurazione di progetto A, comprensiva dell'intervento di ripascimento / picco di mareggiata del 30 Ottobre 2018: esempio di distribuzione dell'elevazione della superficie libera durante l'evento

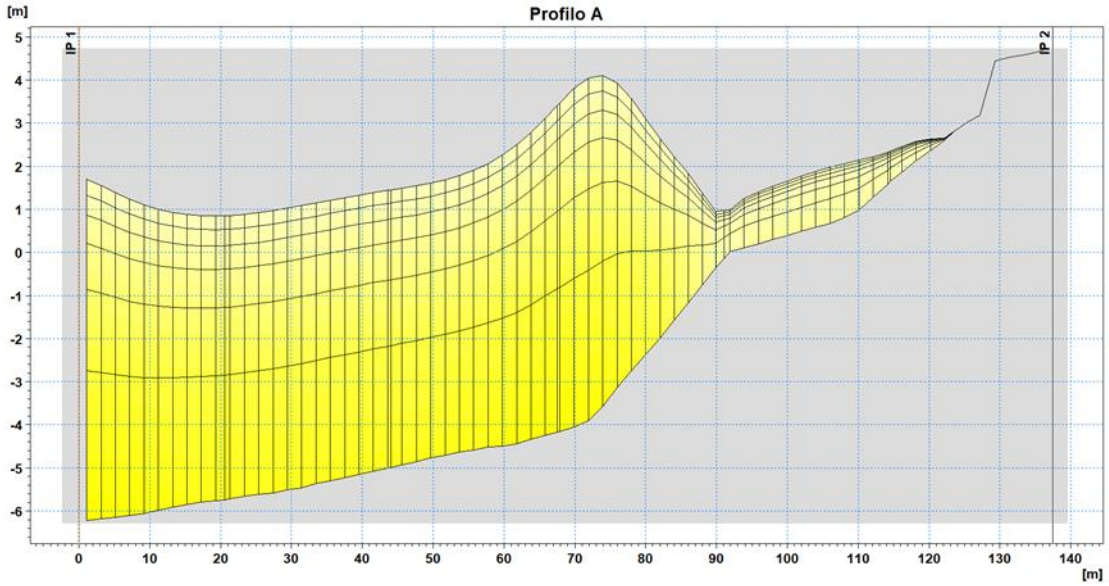


Figura 5-30 Configurazione di progetto A: esempio di risalita dell'onda lungo il profilo A in un istante della mareggiata del 30 Ottobre 2018 (Time Step 1827)

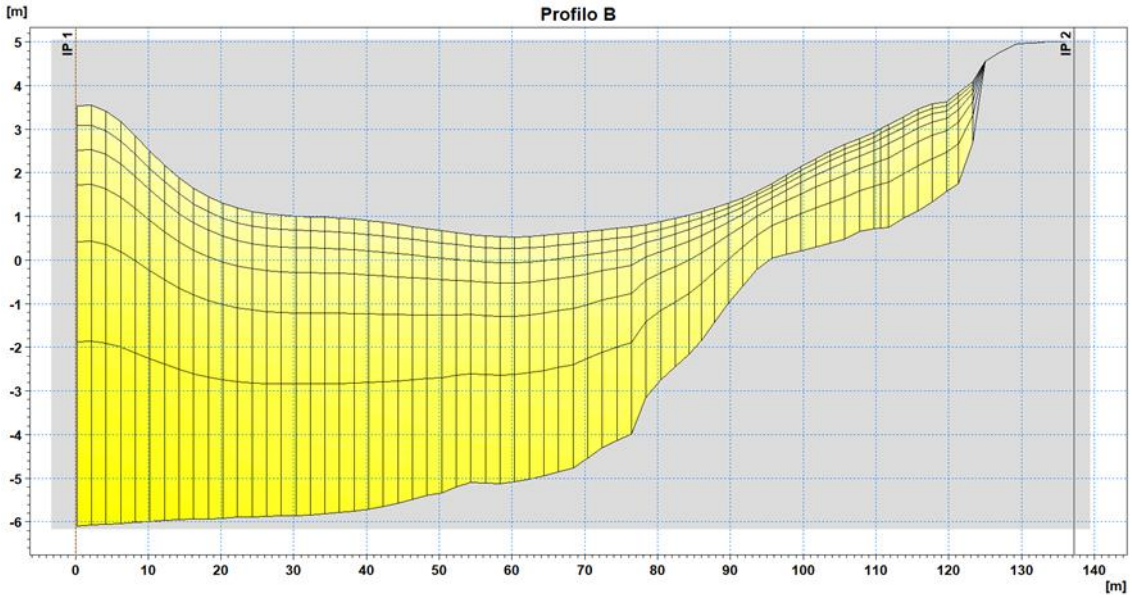


Figura 5-31 Configurazione di progetto A: esempio di risalita dell'onda lungo il profilo B in un istante della mareggiata del 30 Ottobre 2018 (Time Step 2753)

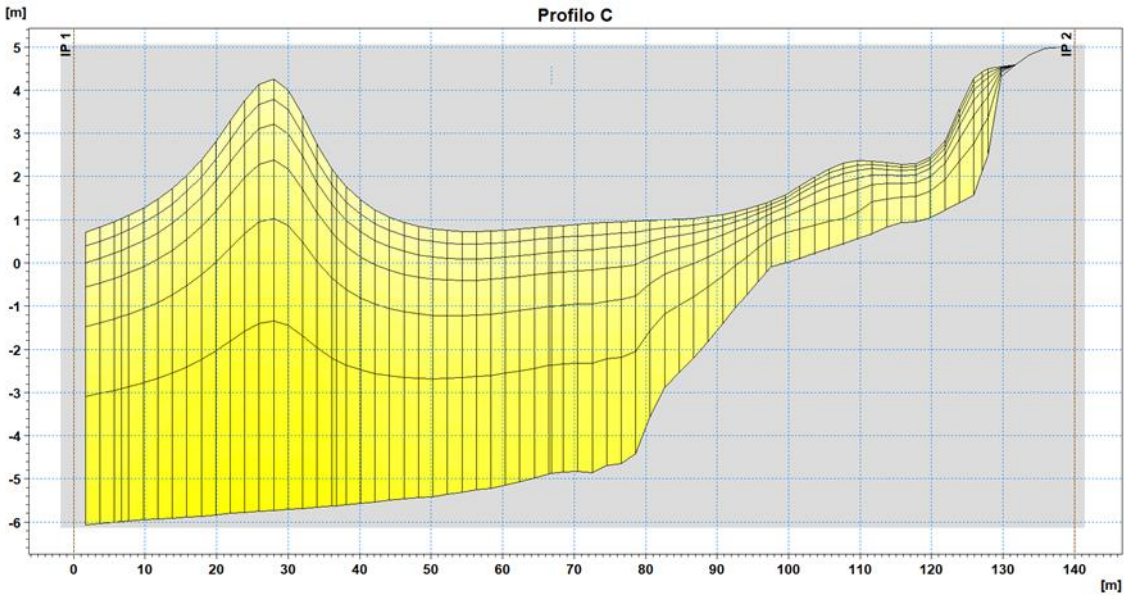


Figura 5-32 Configurazione di progetto A: esempio di risalita dell'onda lungo il profilo C in un istante della mareggiata del 30 Ottobre 2018 (Time Step 3105)

Mareggiata 2013

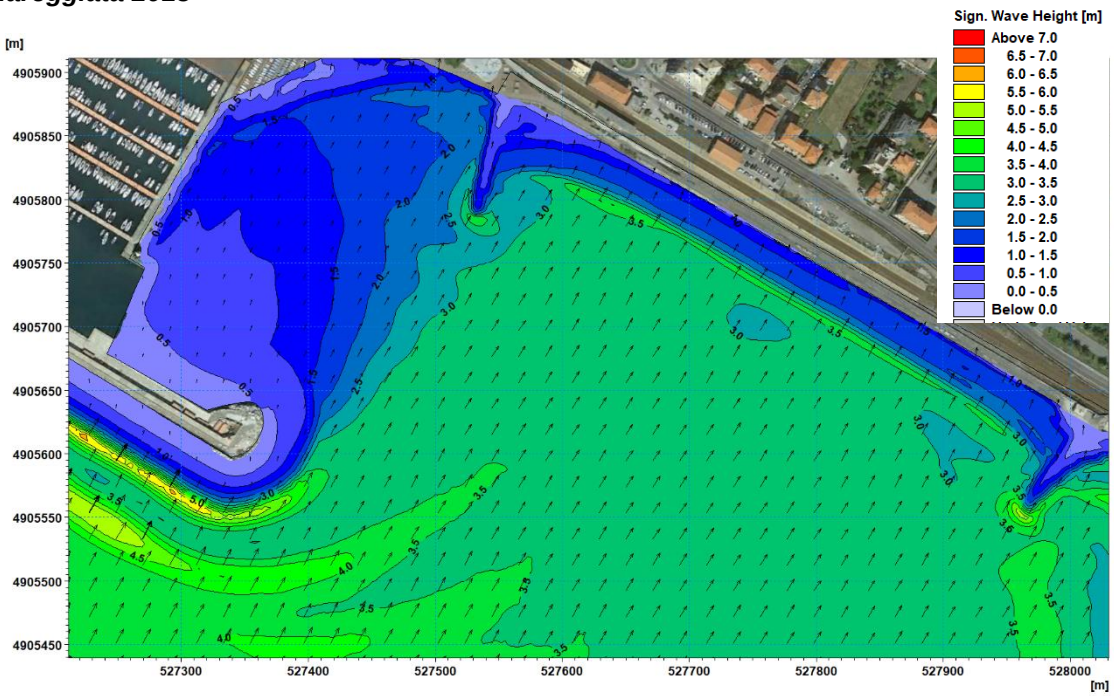


Figura 5-33 Configurazione di progetto A, comprensiva dell'intervento di ripascimento / picco di mareggiata del 26 Dicembre 2013: dettaglio della distribuzione dell'altezza d'onda significativa Hs

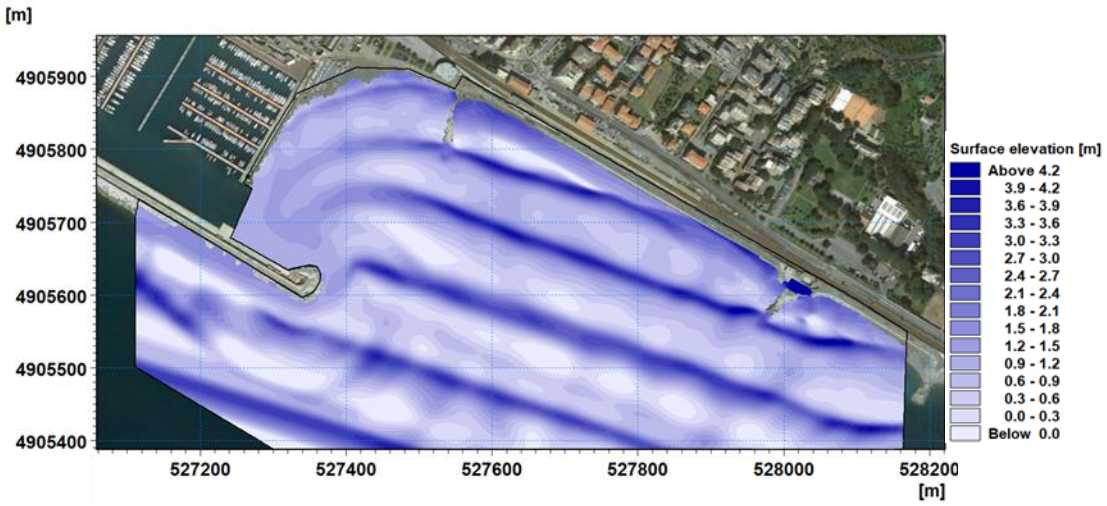


Figura 5-34 Configurazione di progetto A, comprensiva dell'intervento di ripascimento / picco di mareggiata del 26 Dicembre 2013: esempio di distribuzione dell'elevazione della superficie libera durante l'evento

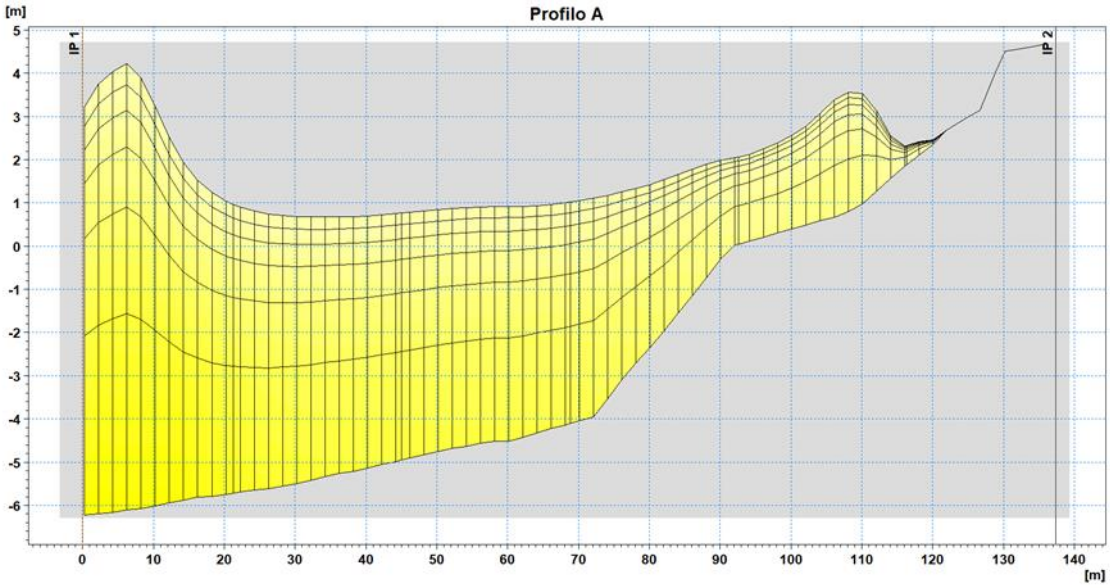


Figura 5-35 Configurazione di progetto A: esempio di risalita dell'onda lungo il profilo A in un istante della mareggiata del 26 Dicembre 2013 (Time Step 291)

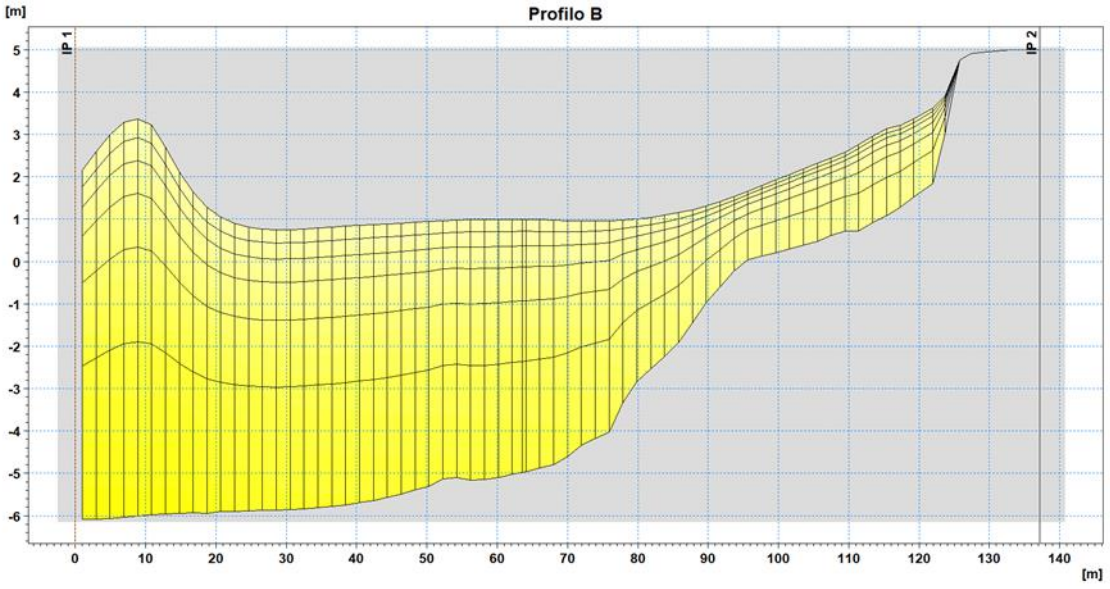


Figura 5-36 Configurazione di progetto A: esempio di risalita dell'onda lungo il profilo B in un istante della mareggiata del 26 Dicembre 2013 (Time Step 102)

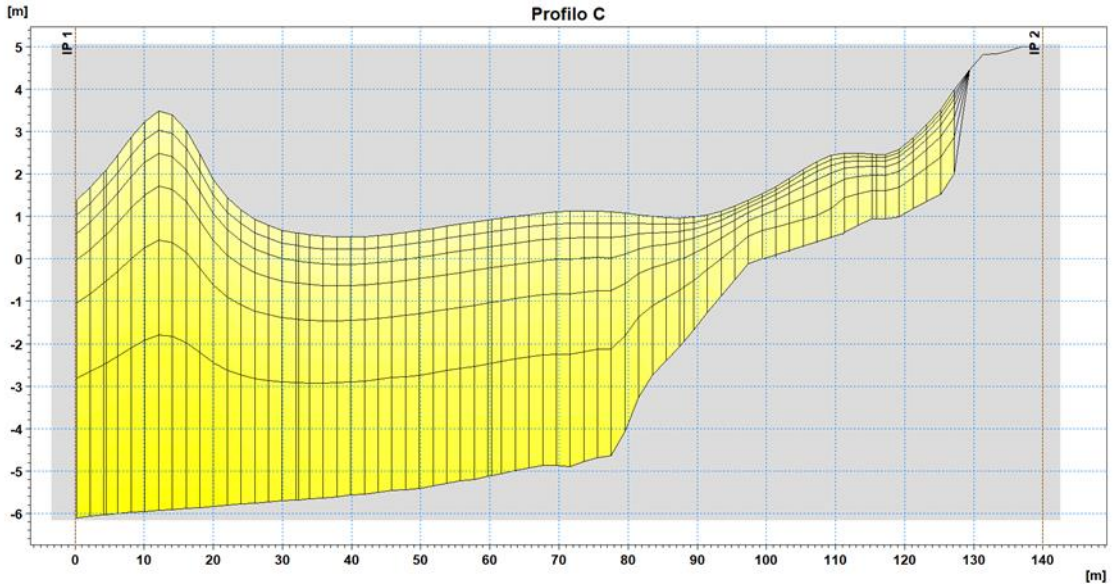


Figura 5-37 Configurazione di progetto A: esempio di risalita dell'onda lungo il profilo C in un istante della mareggiata del 26 Dicembre 2013 (Time Step 98)

Mareggiata 2020

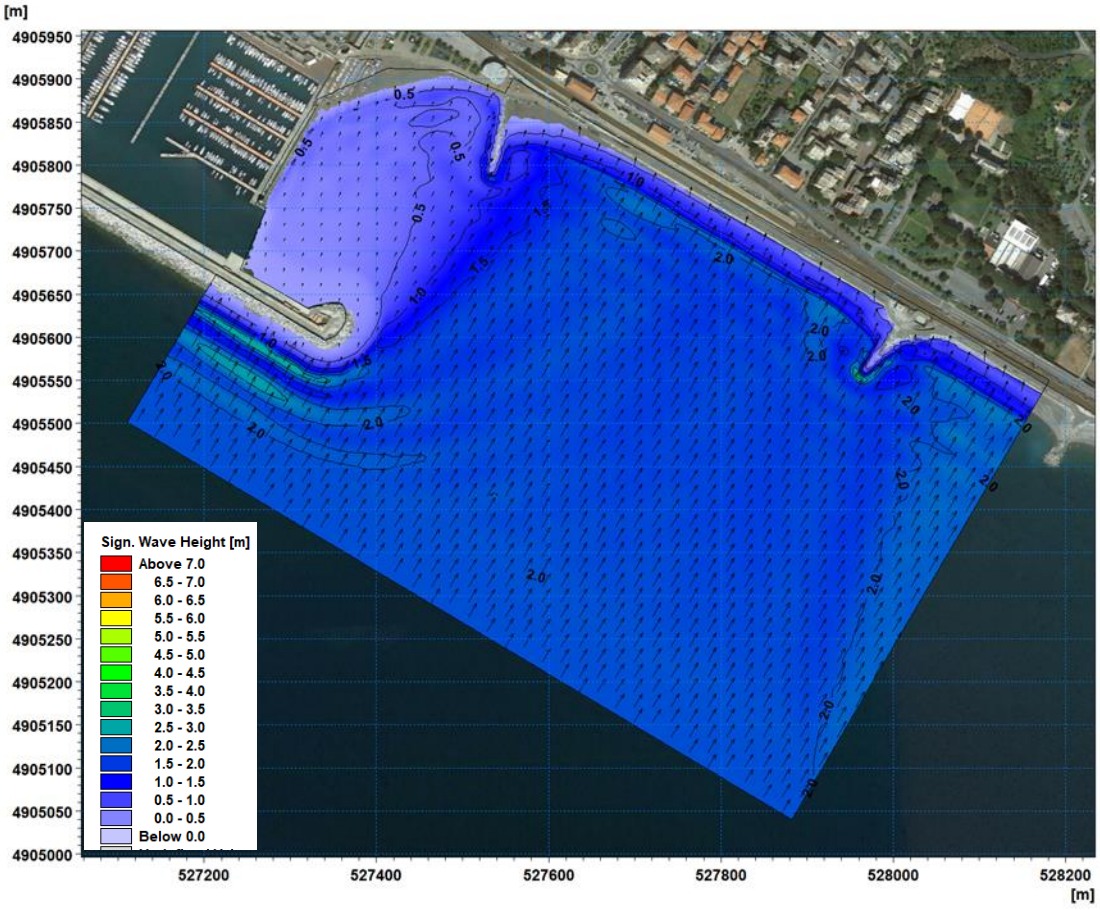


Figura 5-38 Configurazione di progetto A, comprensiva dell'intervento di ripascimento / picco di mareggiata del 6 Marzo 2020: mappa di distribuzione dell'altezza d'onda significativa Hs

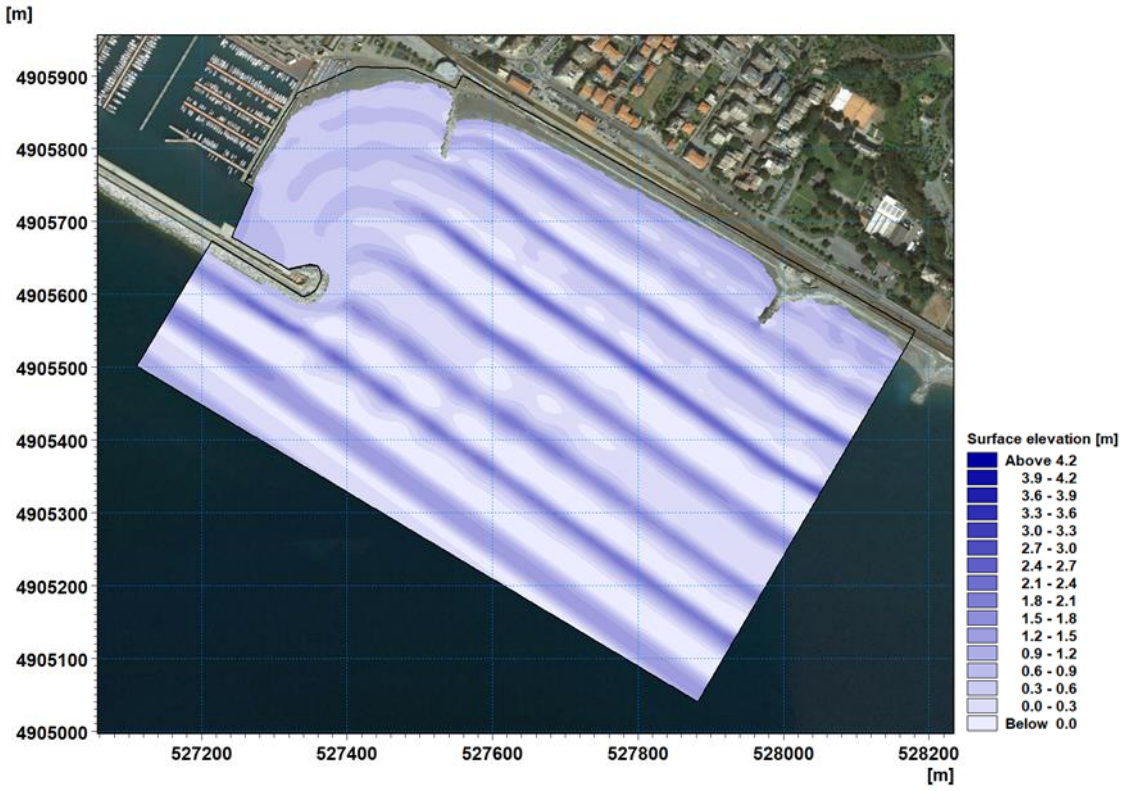


Figura 5-39 Configurazione di progetto A, comprensiva dell'intervento di ripascimento / picco di mareggiata del 6 Marzo 2020: esempio di distribuzione dell'elevazione della superficie libera durante l'evento

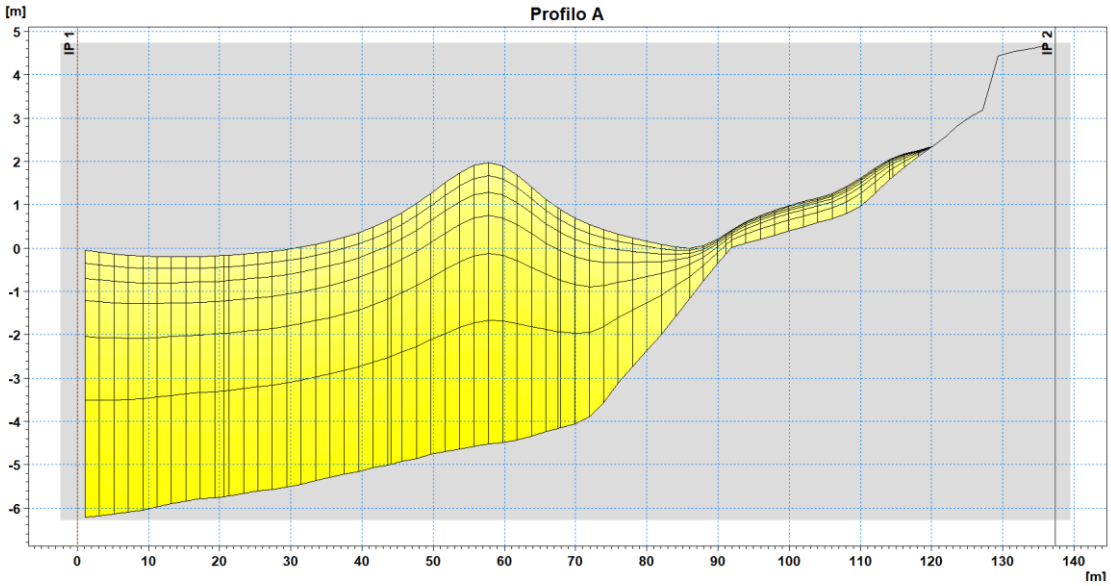


Figura 5-40 Configurazione di progetto A: esempio di risalita dell'onda lungo il profilo A in un istante della mareggiata del 6 Marzo 2020 (Time Step 1038)

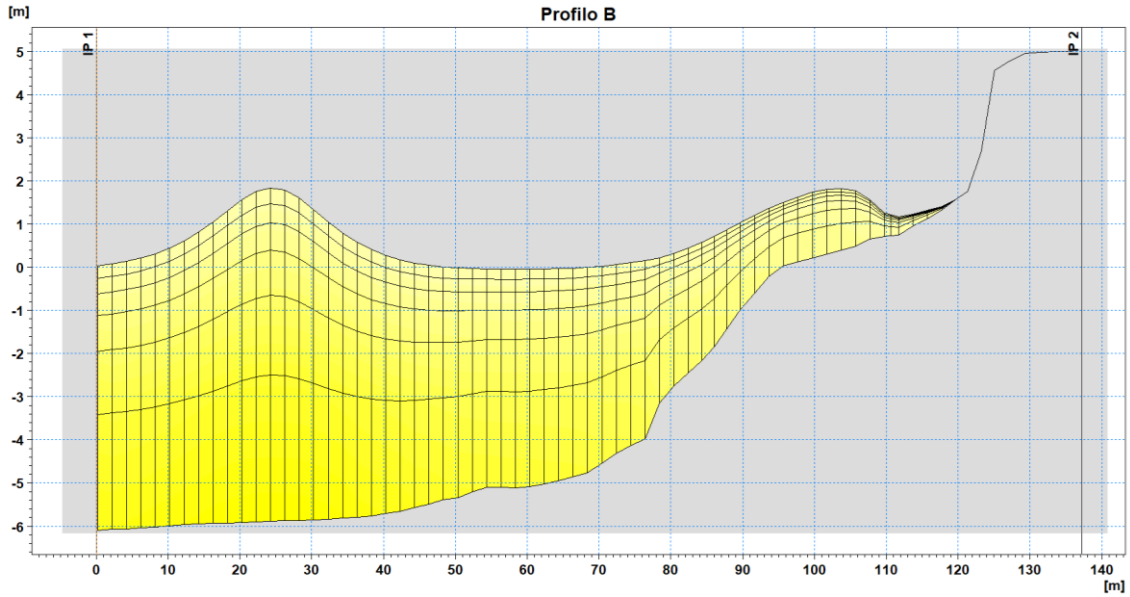


Figura 5-41 Configurazione di progetto A: esempio di risalita dell'onda lungo il profilo B in un istante della mareggiata del 6 Marzo 2020 (Time Step 577)

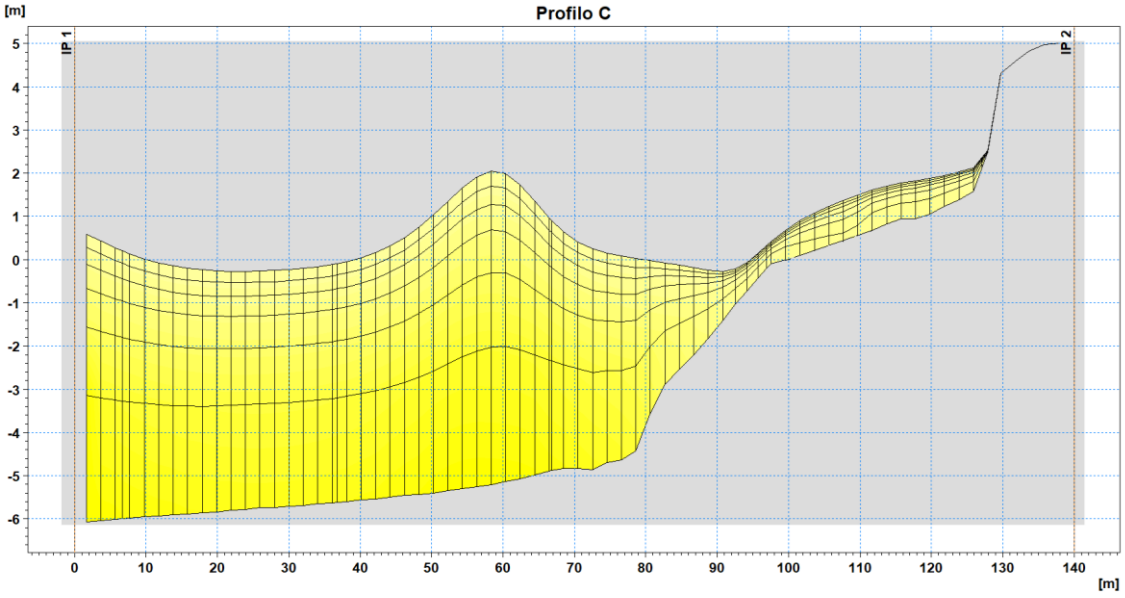


Figura 5-42 Configurazione di progetto A: esempio di risalita dell'onda lungo il profilo C in un istante della mareggiata del 6 Marzo 2020 (Time Step 1210)

5.3.3 Configurazione di progetto B

A seguire si riportano i risultati per la configurazione di progetto B che include, oltre al ripascimento strutturale previsto e già approvato, anche la realizzazione di un'opera in massi a delimitazione della cella, in analogia con quanto già realizzato per le altre celle del litorale di Lavagna-Cavi.

Nella rappresentazione della risalita dell'onda lungo la spiaggia si è deciso di cambiare il colore (per la configurazione di progetto B in colore) per agevolare il confronto dei risultati grafici.

Mareggiata 2018

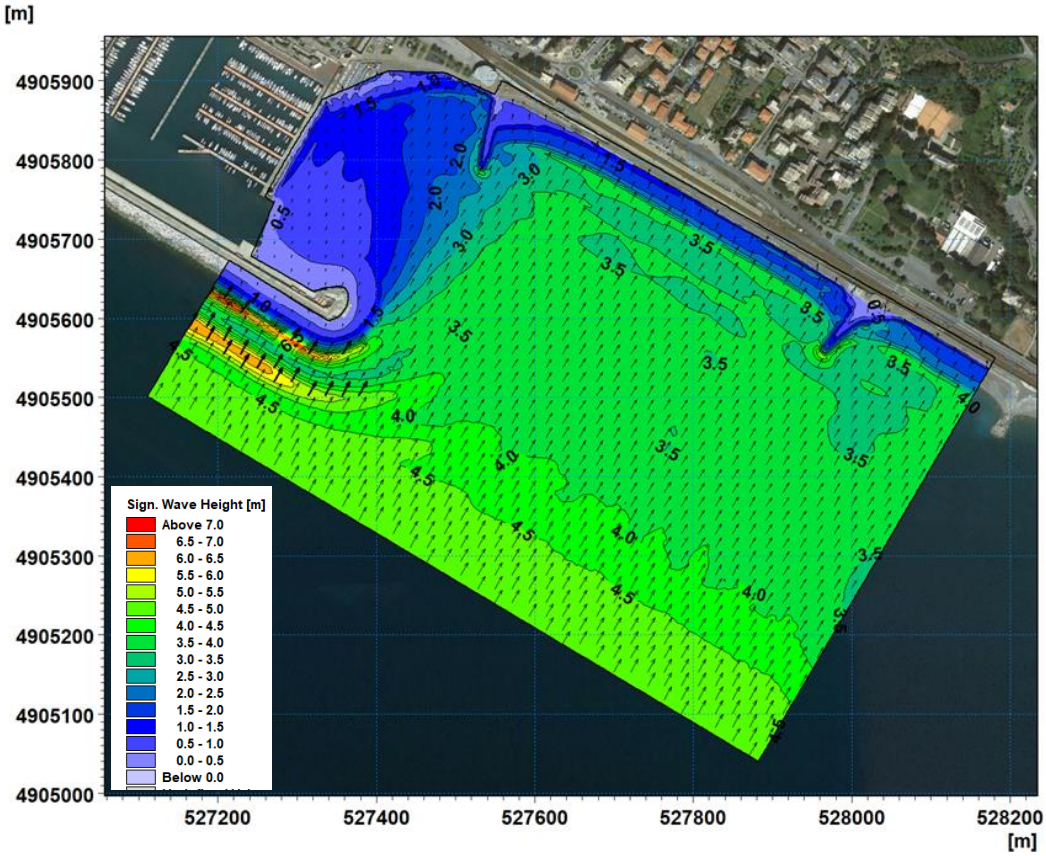


Figura 5-43 Configurazione di progetto B / picco di mareggiata del 30 Ottobre 2018: mappa di distribuzione dell'altezza d'onda significativa Hs

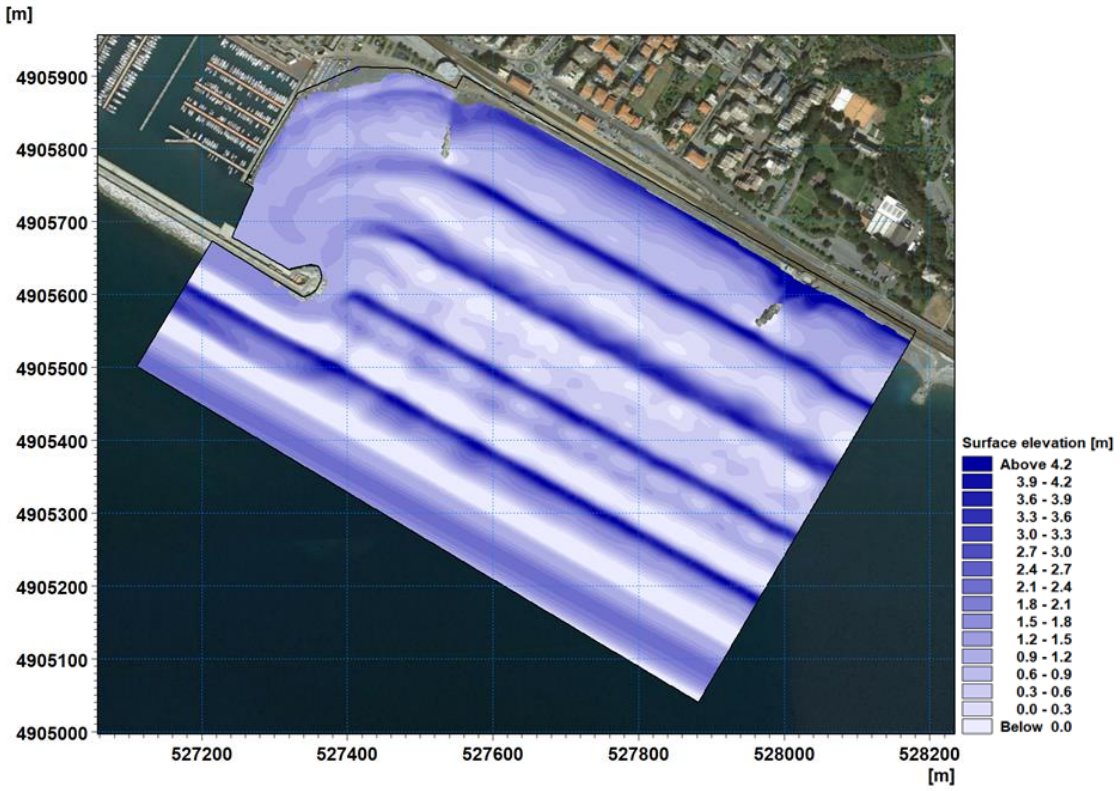


Figura 5-44 Configurazione di progetto B, comprensiva dell'intervento di ripascimento / picco di mareggiata del 30 Ottobre 2018: esempio di distribuzione dell'elevazione della superficie libera durante l'evento

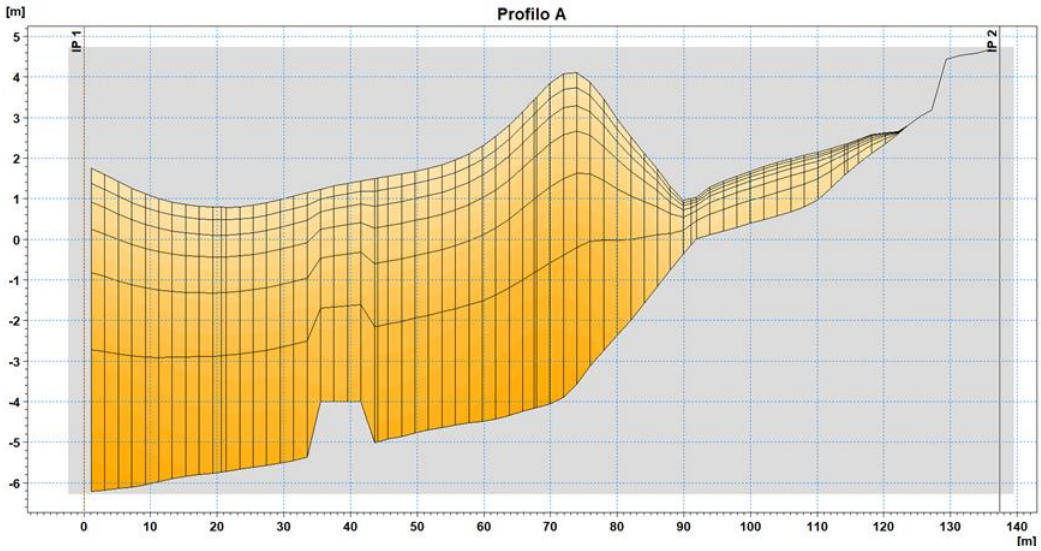


Figura 5-45 Configurazione di progetto B: esempio di risalita dell'onda lungo il profilo A in un istante della mareggiata del 30 Ottobre 2018 (Time Step 1827)

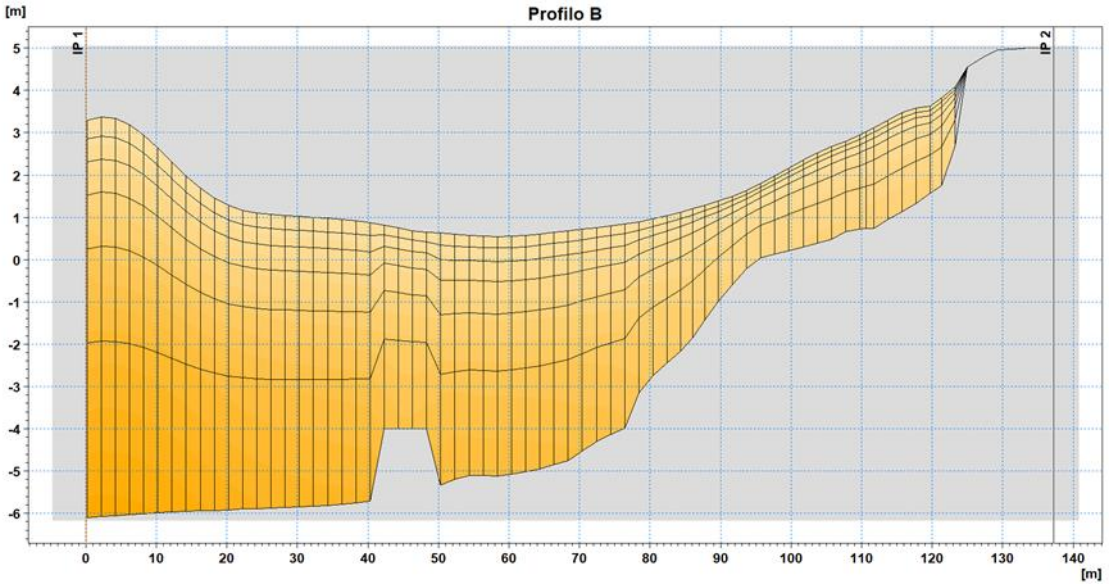


Figura 5-46 Configurazione di progetto B: esempio di risalita dell'onda lungo il profilo B in un istante della mareggiata del 30 Ottobre 2018 (Time Step 2753)

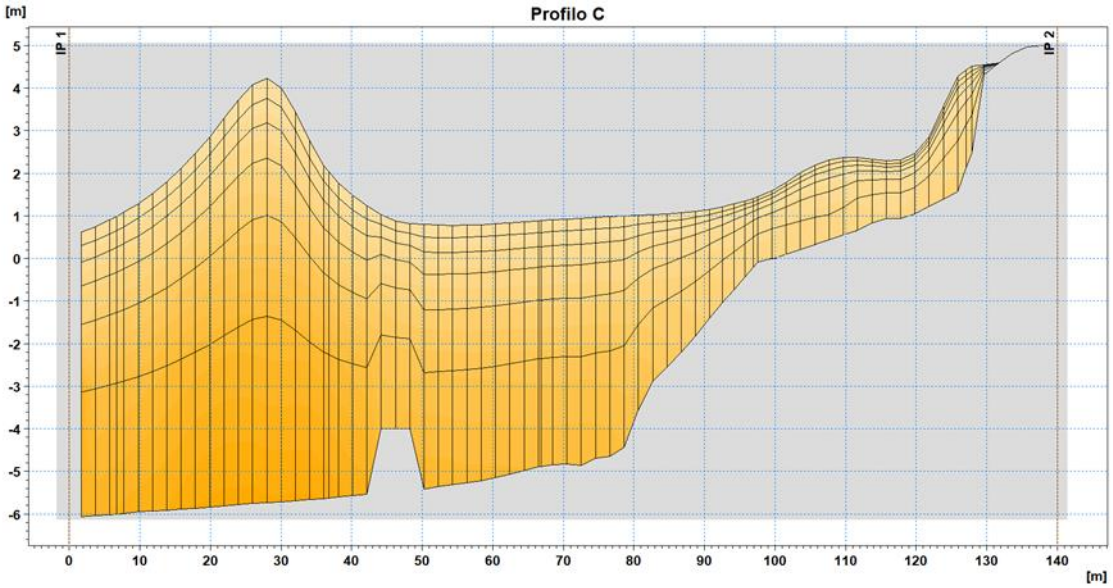


Figura 5-47 Configurazione di progetto B: esempio di risalita dell'onda lungo il profilo C in un istante della mareggiata del 30 Ottobre 2018 (Time Step 3105)

Mareggiata 2013

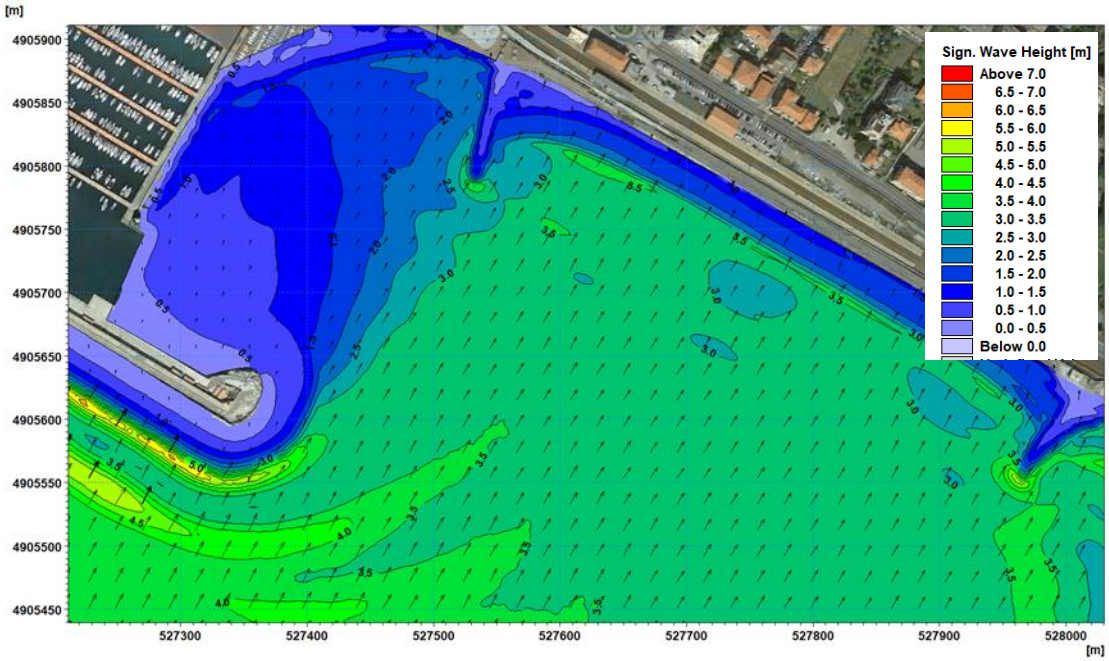


Figura 5-48 Configurazione di progetto B / picco di mareggiata del 26 Dicembre 2013: dettaglio della mappa di distribuzione dell'altezza d'onda significativa Hs

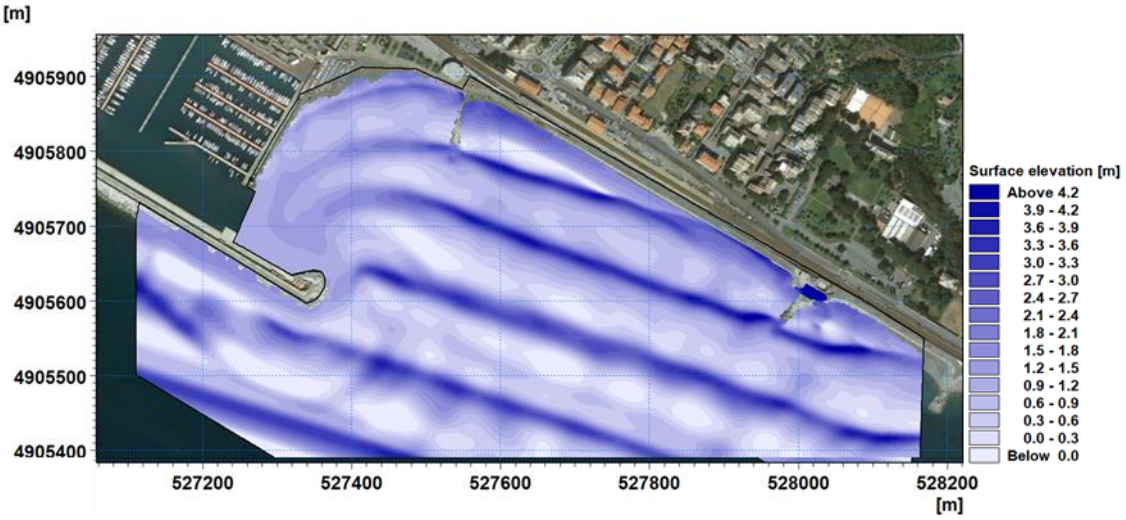


Figura 5-49 Configurazione di progetto B, comprensiva dell'intervento di ripascimento / picco di mareggiata del 26 Dicembre 2013: esempio di distribuzione dell'elevazione della superficie libera durante l'evento

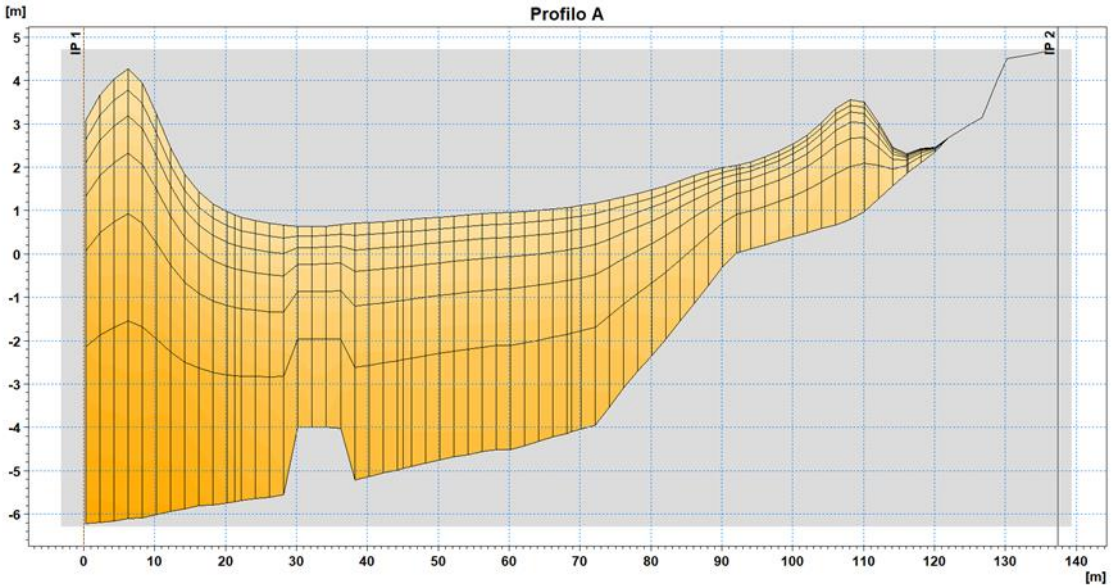


Figura 5-50 Configurazione di progetto B: esempio di risalita dell'onda lungo il profilo A in un istante della mareggiata del 26 Dicembre 2013 (Time Step 291)

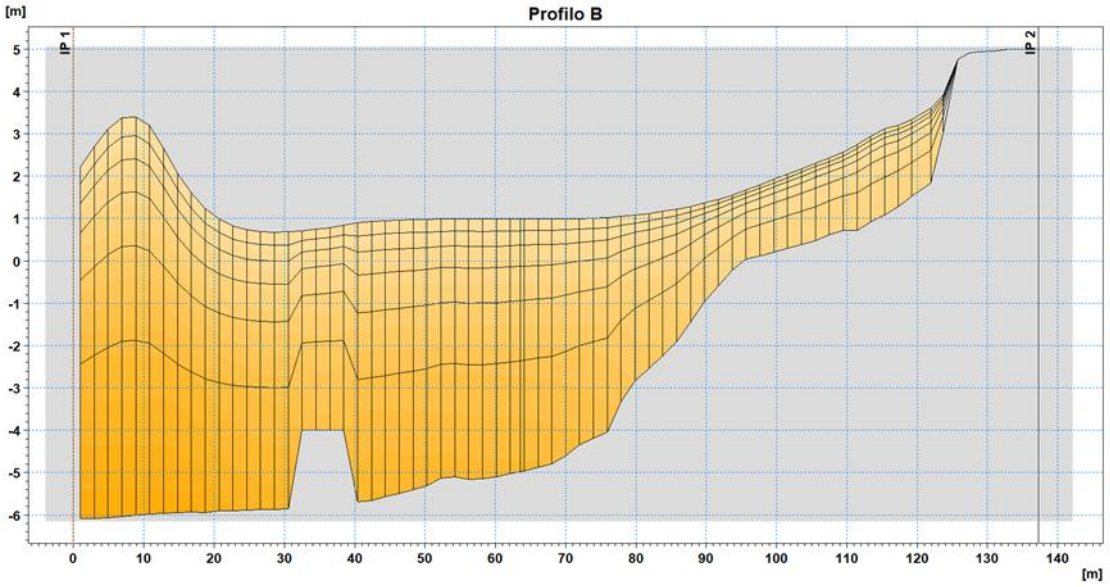


Figura 5-51 Configurazione di progetto B: esempio di risalita dell'onda lungo il profilo B in un istante della mareggiata del 26 Dicembre 2013 (Time Step 102)

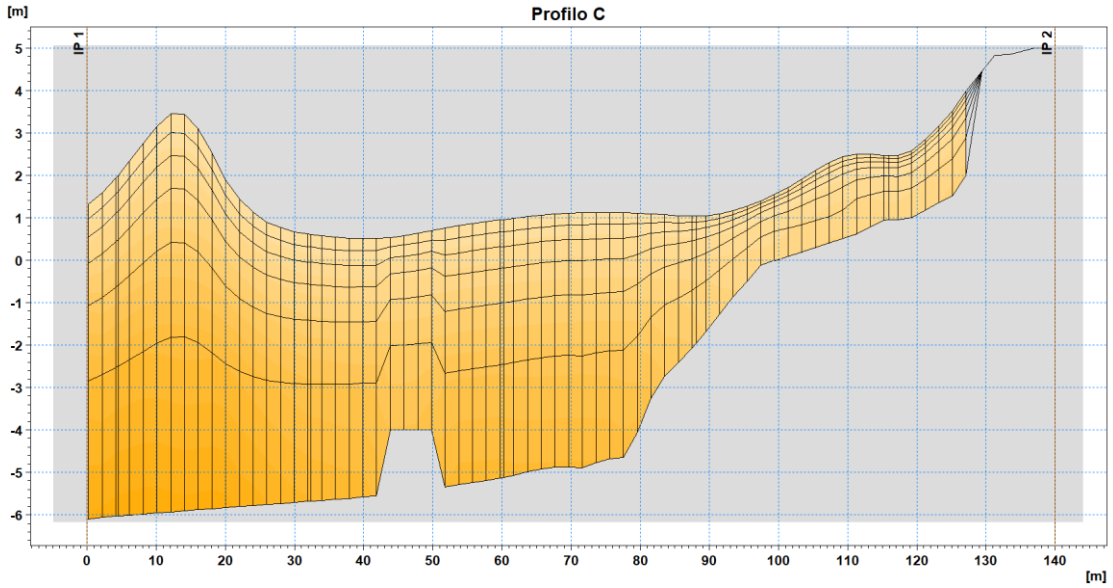


Figura 5-52 Configurazione di progetto B: esempio di risalita dell'onda lungo il profilo C in un istante della mareggiata del 26 Dicembre 2013 (Time Step 98)

Mareggiata 2020

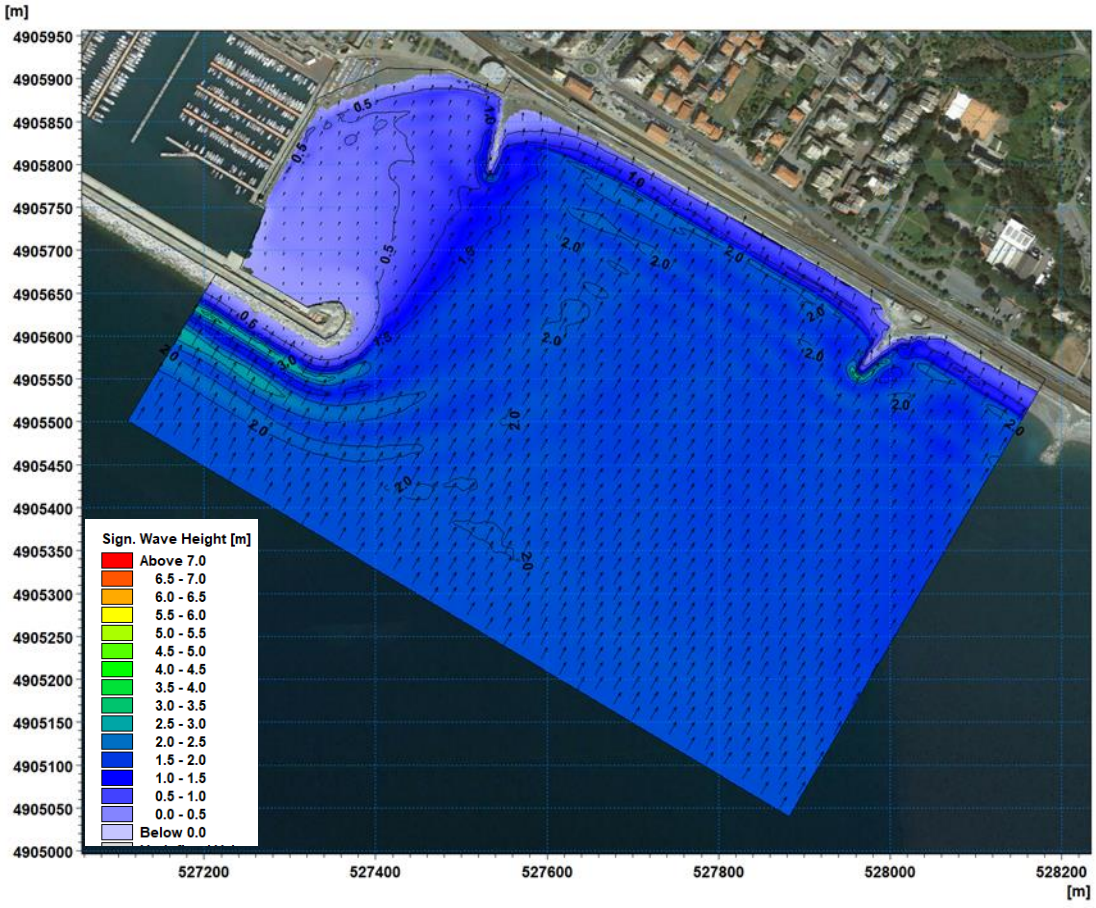


Figura 5-53 Configurazione di progetto B / picco di mareggiata del 6 Marzo 2020: mappa di distribuzione dell'altezza d'onda significativa Hs

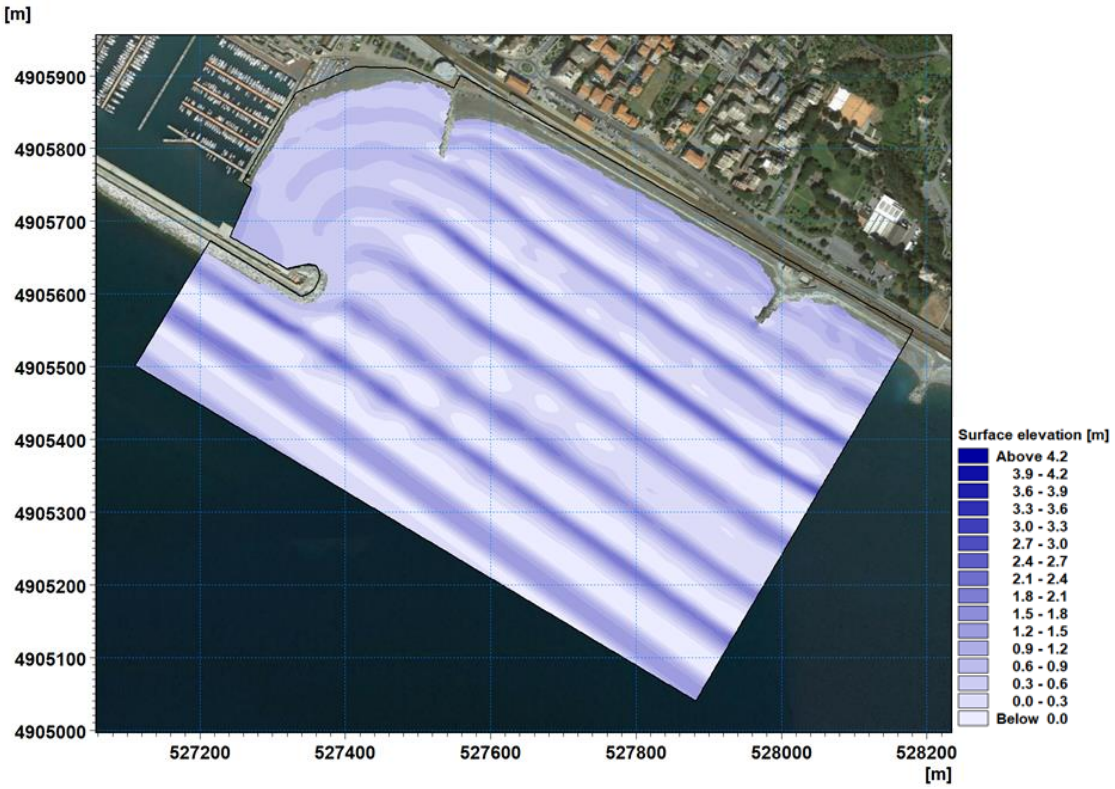


Figura 5-54 Configurazione di progetto B, comprensiva dell'intervento di ripascimento / picco di mareggiata del 6 Marzo 2020: esempio di distribuzione dell'elevazione della superficie libera durante l'evento

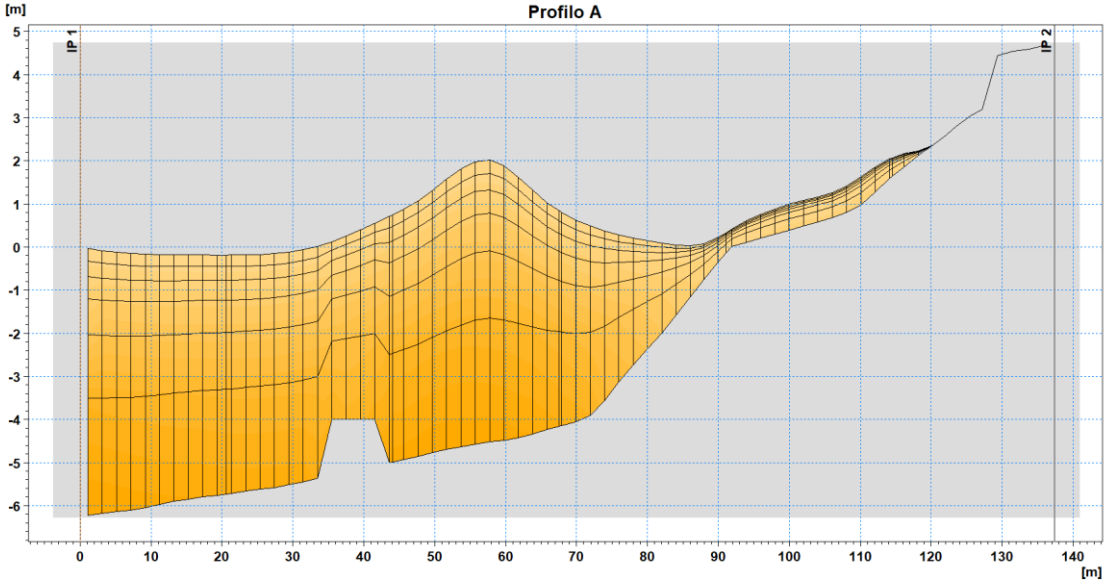


Figura 5-55 Configurazione di progetto B: esempio di risalita dell'onda lungo il profilo A in un istante della mareggiata del 6 Marzo 2020 (Time Step 1038)

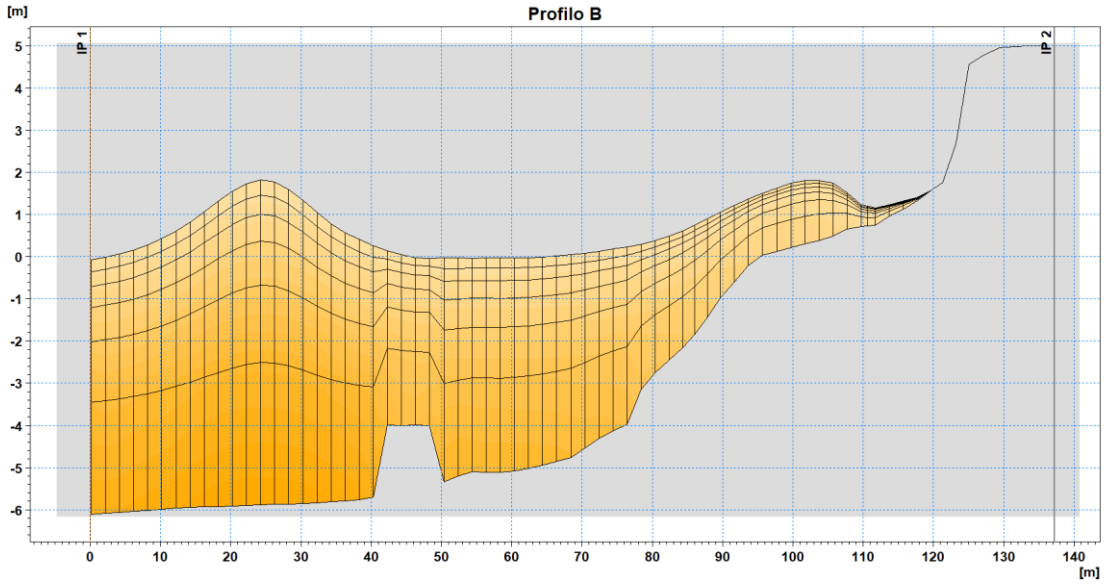


Figura 5-56 Configurazione di progetto B: esempio di risalita dell'onda lungo il profilo B in un istante della mareggiata del 6 Marzo 2020 (Time Step 577)

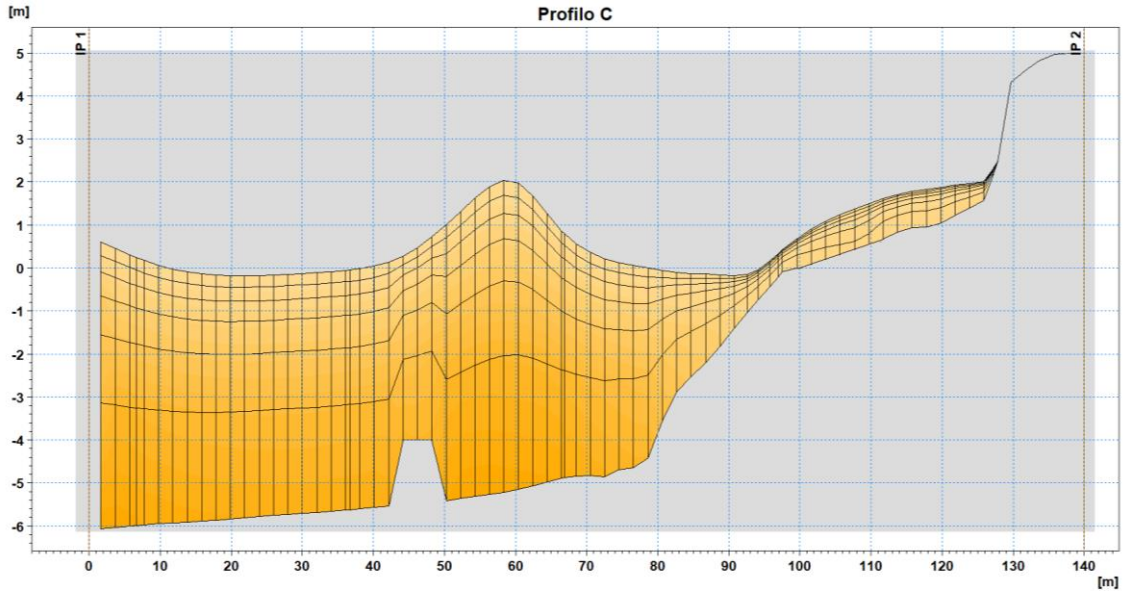


Figura 5-57 Configurazione di progetto B: esempio di risalita dell'onda lungo il profilo C in un istante della mareggiata del 6 Marzo 2020 (Time Step 1210)

5.3.4 Sintesi dei risultati del modello

Dal confronto tra le mappe di distribuzione dell'altezza d'onda significativa e dei profili di risalita delle singole onde sulla spiaggia di Lavagna nelle varie configurazioni, emerge che:

- la presenza della diga sopraflutto del porto di Lavagna protegge significativamente dalle onde da Libeccio una porzione di 80-100 m della spiaggia (lato ponente), con un significativo abbattimento dell'energia; per questa porzione di spiaggia, per le mareggiate provenienti dal settore 200°N-220°N, le differenze tra le varie configurazioni sono molto limitate;

- per la zona centrale della cella, nella configurazione di progetto A l'energia ondosa viene sensibilmente attenuata rispetto alla configurazione attuale, con una diminuzione del 10-15% nei valori di altezza d'onda significativa;
- per la zona di spiaggia più a levante, la riduzione dell'altezza d'onda significativa tra la configurazione di progetto A e lo stato attuale arriva fino a differenze del 20-23%;
- l'intervento di ripascimento riduce la risalita sull'arenile (run-up) mediamente di 6 - 8 m in planimetria e di 0.30 – 0.50 m in quota; queste stime derivano dal confronto del run-up nei vari profili durante la mareggiata del Marzo 2020 (in configurazione di stato attuale, da Figura 5-25, a Figura 5-27, in configurazione di progetto A, da Figura 5-35 a Figura 5-37) e durante la mareggiata del Dicembre 2013 (in configurazione di stato attuale, da Figura 5-20 a Figura 5-22, in configurazione di progetto A, da Figura 5-40, a Figura 5-42). Per l'intenso evento dell'Ottobre 2018, il picco riprodotto modellisticamente comporta il raggiungimento della passeggiata per tutti e tre i profili in esame con il layout di stato attuale, mentre per la configurazione progettuale si osserva il raggiungimento del limite della scogliera a protezione del lungomare solo per il profilo C;
- la riprofilatura della spiaggia proposta riduce sensibilmente la frequenza di raggiungimento del piano della passeggiata da parte delle onde;
- dal confronto tra le mappe di distribuzione dell'altezza d'onda significativa e della risalita del moto ondoso lungo la spiaggia si evince che per eventi intensi l'inserimento dell'opera in massi a delimitazione della cella, prevista nella configurazione di progetto B, non incide in modo apprezzabile sulla riduzione dell'energia e non influenza il run-up.

6 Modellazione del trasporto litoraneo

Il modulo LITDRIFT permette di simulare la distribuzione delle altezze d'onda, del *set-up* e del *set-down*, delle correnti *longshore* e del trasporto di sedimenti non coesivi lungo profili trasversali alla costa. LITDRIFT utilizza il modulo STP per calcolare la distribuzione trasversale del trasporto longitudinale di sedimenti (dato dalla somma del trasporto di sedimenti al fondo ed in sospensione) per un determinato profilo batimetrico, per onde regolari e irregolari. Il trasporto al fondo viene calcolato facendo riferimento allo *shear stress* istantaneo che si verifica durante il ciclo d'onda, mentre il trasporto dei sedimenti sospesi è dato dall'integrazione della velocità istantanea con le concentrazioni lungo i profili verticali.

STP descrive inoltre nel dettaglio le condizioni idrodinamiche, inclusi i processi di rifrazione, *shoaling* e frangimento delle onde, il calcolo delle forzanti derivanti dai gradienti di *radiation stress*, il bilancio dei momenti per le direzioni trasversali e longitudinali che forniscono il set-up dell'onda e le velocità di corrente longitudinali.

Pertanto, l'applicazione del modulo LITDRIFT permette di definire il budget sedimentario in determinate zone di interesse, sulla base del clima meteomarino e delle quote batimetriche lungo un profilo. In particolare, il trasporto viene calcolato lungo profili scelti come rappresentativi di tratti costieri che possano essere considerati uniformi e rettilinei. Tali profili devono coprire l'intera *surf-zone*, ossia la fascia costiera dove avvengono i frangimenti delle onde, in quanto rappresenta la zona dove si verifica la maggiore movimentazione di sedimenti.

Una descrizione di dettaglio del codice di calcolo è disponibile in Allegato D.

Nell'ambito del presente studio, il modulo LITDRIFT è stato applicato al fine di:

- individuare la profondità di chiusura del sistema, ossia la profondità oltre la quale il trasporto di sedimenti si può considerare trascurabile, lungo il litorale;
- individuare l'orientazione di equilibrio del litorale in esame.

A tale scopo è stato identificato un profilo trasversale a costa, centrale nella cella in esame, rappresentativo della spiaggia, denominato “profilo T” (Figura 6-1), che copre l’intera *surf-zone*, estendendosi fino alla profondità di circa 8 m.



Figura 6-1 Ubicazione del profilo T

6.1 Clima ondoso sottocosta

Le condizioni d’onda sono state estratte in corrispondenza delle estremità di largo del profilo dal modello di propagazione del moto ondoso largo-riva descritto nella sezione 4, per l’intera finestra temporale di 42 anni a disposizione (dal 1979 al 2020).

Dall’analisi del clima ondoso estratto a circa 330 m dalla linea di riva, si osserva che il settore di provenienza delle onde si riduce sostanzialmente al terzo quadrante (Figura 6-2).

Le massime altezze d’onda e le frequenze di provenienza delle onde più alte si registrano per le direzioni comprese tra i 205°N e i 225°N.

Le caratteristiche del sedimento in termini di diametro medio d_{50} e di *grading* (definito come la radice quadrata del rapporto tra d_{84} e d_{16}) utilizzati nelle simulazioni modellistiche sono stati impostati sulla base dei dati illustrati alla sezione 3.3.

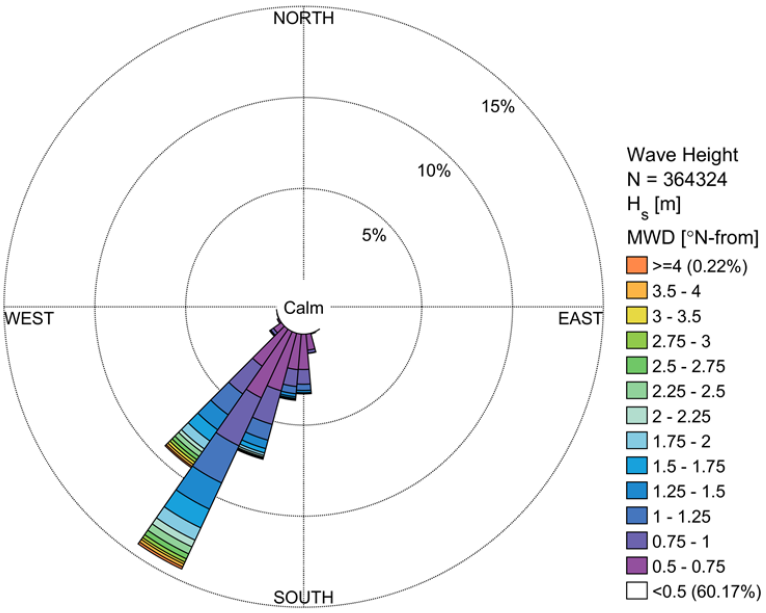


Figura 6-2 Rosa delle onde ottenuta sulla base della serie estratta nel punto posto al limite di largo del profilo T

6.2 Risultati del modello e calcolo della profondità di chiusura

I risultati ottenuti dalla simulazione del periodo di 42 anni sono rappresentati in termini di andamento del trasporto potenziale *longshore* medio annuo (lordo, netto e nelle due direzioni) lungo il profilo T (Figura 6-3).

Il trasporto sedimentario longitudinale avviene entro i primi 5.85 m di profondità, facendo riferimento al 95% del trasporto potenziale complessivo. La profondità interessata dal trasporto aumenta fino a 6.33 m con riferimento al 98 % del trasporto potenziale complessivo. La profondità di 5.85 metri può essere assunta come profondità di chiusura per il litorale in studio. Si precisa che tale trasporto è da intendersi potenziale, ovvero il trasporto che si avrebbe in caso di effettiva disponibilità di materiale da movimentare.

Un'ulteriore considerazione sui risultati modellistici ottenuti è relativa alla localizzazione del picco del trasporto lungo il profilo trasversale, che si colloca ad una profondità compresa tra 0.5 m e 1.0 m, a conferma che la maggior parte della movimentazione del materiale avviene in una stretta fascia costiera.

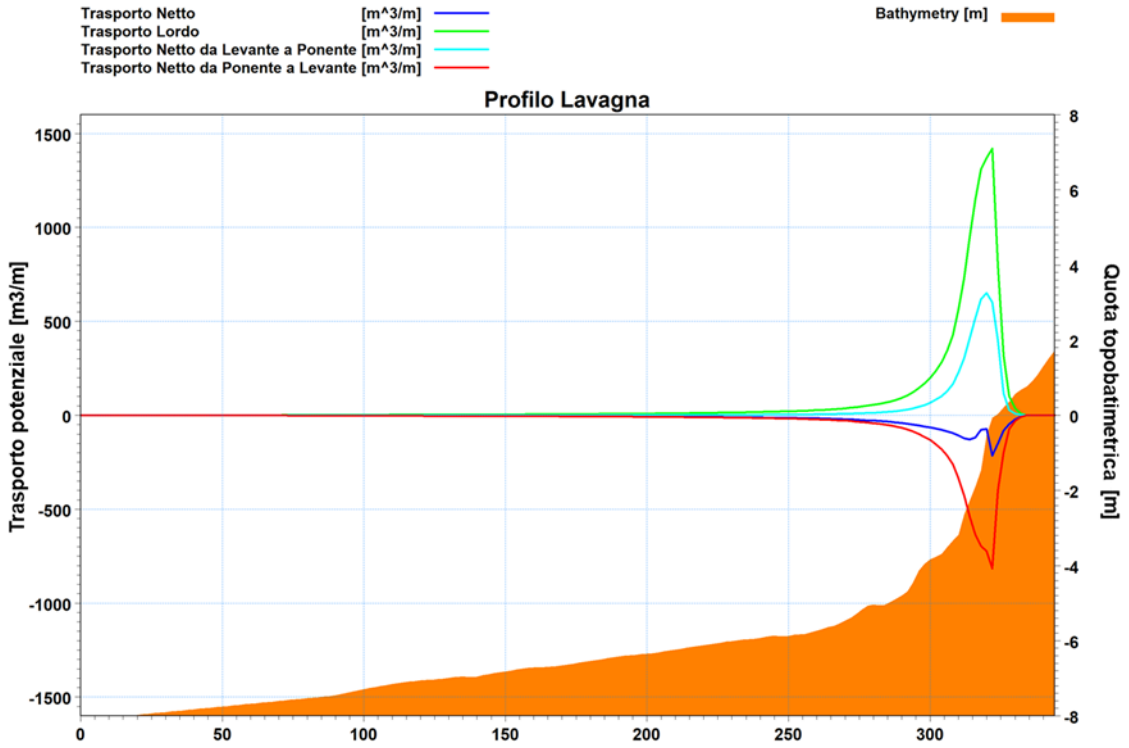


Figura 6-3 Distribuzione del trasporto potenziale medio annuale netto, lordo e nelle due direzioni lungo il profilo T

6.3 Orientazione di equilibrio

Il modello ha permesso inoltre di simulare svariati angoli di orientazione del profilo di riferimento per le simulazioni, in modo da stimare l'orientazione di equilibrio, che corrisponde all'orientazione per la quale il trasporto litoraneo medio netto annuo si riduce a valori prossimi a zero.

Il grafico a seguire riporta la curva Q-alpha, ovvero la quantificazione del trasporto litoraneo (Q) al variare dell'orientazione della linea di riva (alpha), per il transetto in esame. Tale informazione è di fondamentale importanza nella definizione preliminare delle tendenze evolutive del ripascimento all'interno della cella.

Come evidenziato dalla linea, l'attuale orientazione del litorale, pari a 210°N, è molto prossima a quella che minimizza il trasporto litoraneo longitudinale, pari a 210.5°N.

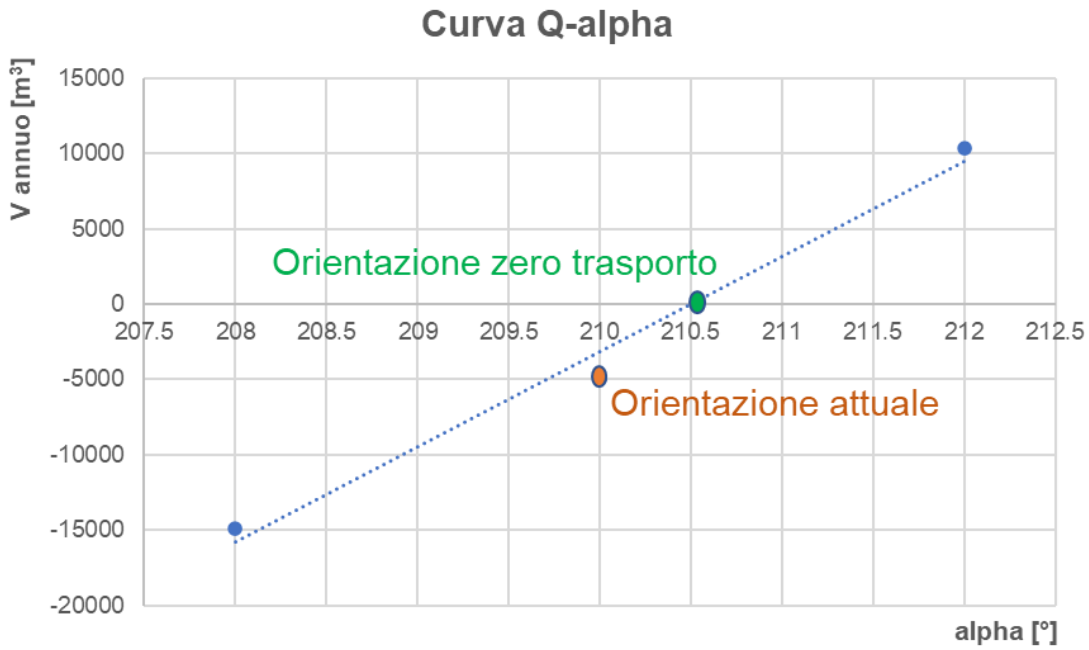


Figura 6-4 Curva Q-alpha per il profilo T della cella in esame

7 Simulazione delle dinamiche costiere con modellazione 2D

Al fine di identificare le principali dinamiche locali dell'area di studio, sia della cella in oggetto che della limitrofa zona dell'imboccatura del porto turistico di Lavagna, il modello d'onda MIKE 21 SW (Spectral Waves), già descritto in precedenza per la trasposizione da largo a riva, è stato integrato con il modulo idrodinamico MIKE 21 HD (Hydrodynamics).

Il modulo MIKE 21 HD (Hydrodynamics), cuore del codice bidimensionale MIKE 21, simula le variazioni di livello e di corrente in risposta alle differenti tipologie di forzanti considerate. Il sistema modellistico si basa sulla soluzione numerica delle equazioni dei Navier-Stokes mediate (Reynolds Averaged Navier-Stokes equations) sotto le ipotesi di Boussinesq e in condizioni di pressione idrostatica. La versione Flexible Mesh utilizza un metodo ai volumi finiti per la discretizzazione delle equazioni di flusso e trasporto con valori centrati sul singolo elemento. Il dominio spaziale, al pari del modello d'onda, è discretizzato attraverso una maglia non strutturata costituita da triangoli.

Il modulo necessita di una serie di dati di input, che si possono raggruppare in differenti categorie, ovvero:

- parametri di base (es. mesh di calcolo, durata della simulazione);
- fattori di calibrazione (es. scabrezza, viscosità turbolenta);
- condizioni iniziali (es. livelli e campi di corrente);
- condizioni al contorno (es. oscillazioni di marea, portate);
- altre forzanti (es. campi di vento, radiation stress, apporti puntuali di portata).

L'utilizzo di un approccio di tipo bidimensionale permette di indagare non solo l'intensità del fenomeno, ma anche la direzione e il verso del vettore velocità in ogni cella della matrice. Per ciascun elemento di calcolo, è possibile ottenere le variazioni temporali delle seguenti variabili:

- profondità e livelli idrici;
- velocità di corrente e direzione;

- densità, temperatura e salinità (se rilevanti).

Una descrizione di dettaglio del modulo idrodinamico HD del codice di calcolo MIKE 21 è disponibile in Allegato E.

La principale finalità dell'applicazione del modello di dettaglio bidimensionale è stata la ricostruzione dei pattern di circolazione dell'area di studio al variare della direzione di provenienza del moto ondoso. L'approfondimento svolto sulla circolazione ha permesso di interpretare le dinamiche evolutive e di confermare gli esiti dell'analisi del trasporto litoraneo descritto nella sezione precedente.

7.1 Dominio di calcolo, batimetria

Il modello integrato 2D onda-corrente è stato implementato su un dominio di calcolo più ridotto rispetto a quello utilizzato per la propagazione dal largo verso riva, ma ben più esteso rispetto al MIKE 3 Wave. Esso risulta esteso lungo costa per circa 7.5 km e verso il largo per circa 2.5 km.

Il risultato finale di interpolazione dei dati batimetrici a disposizione (par.3.3) è mostrato nell'immagine a seguire, in cui è rappresentata la batimetria.

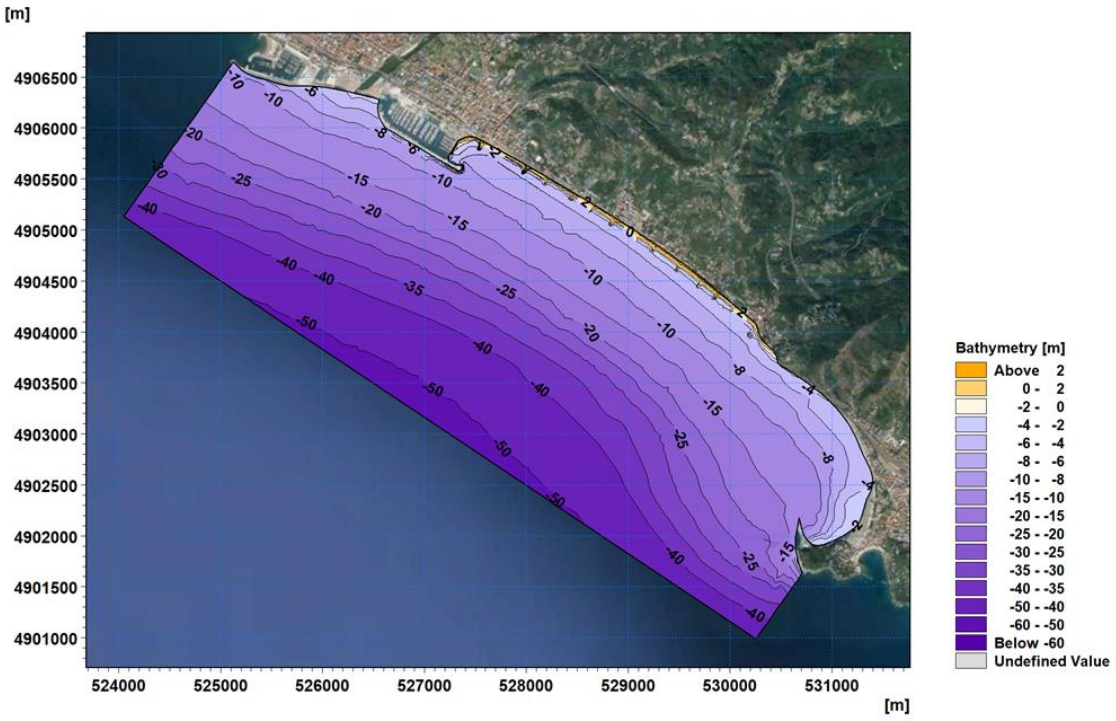


Figura 7-1 Batimetria del modello di dettaglio ottenuta dal processamento dei dati a disposizione

Al fine di rappresentare opportunamente la peculiare variabilità batimetrica del sito al dettaglio richiesto per una rappresentazione della propagazione del moto ondoso e delle principali dinamiche su profondità limitate, e garantire allo stesso tempo la sostenibilità dei tempi computazionali, l'area è stata suddivisa in differenti sottodomini, ognuno caratterizzato da una risoluzione (intesa come lato del triangolo della mesh) differente.

Nello specifico, si passa da una risoluzione di circa 60 m nella zona più al largo, a una zona intermedia a 18 m, sino a 6 m per l'area di interesse, infittita a 2 metri per la zona della cella compresa tra i pennelli P1 e P2 (Figura 7-2).



Figura 7-2 Risoluzione adottata nel modello di dettaglio: 60 m per le profondità maggiori; 18 m per la zona intermedia; 6 m e 2 m per la zona di studio

La scelta di aumento incrementale di risoluzione verso costa consente la rappresentazione dettagliata delle opere di difesa presenti e permette la riproduzione delle dinamiche prettamente costiere (frangimento, rifrazione, *shoaling*, attrito con il fondo) ad un grado di dettaglio adeguato agli obiettivi prefissati.

La mesh di calcolo del modello è complessivamente costituita da circa 99’000 elementi.

7.2 Selezione delle condizioni d’onda rappresentative

Il modello di dettaglio integrato onda-corrente, come anticipato, è stato utilizzato per l’identificazione e l’analisi delle principali dinamiche in corrispondenza della cella oggetto dell’intervento e della limitrofa imboccatura del porto turistico di Lavagna.

A tal fine è stato preliminarmente necessario selezionare una serie di condizioni d’onda rappresentative. Essendo l’approfondimento focalizzato all’identificazione dei vari pattern di circolazione si è assunto di riprodurre 4 eventi caratterizzati dalla stessa altezza d’onda significativa Hs, pari a 2 m, e periodo di picco Tp pari a 9 s, ma con differente direzione di provenienza del moto ondoso:

- onda 1: MWD=170°N (frequenza di occorrenza media annua pari a 5h/anno)
- onda 2: MWD=190°N (frequenza di occorrenza media annua pari a 6h/anno);
- onda 3: MWD=210°N (frequenza di occorrenza media annua pari a 2gg/anno);
- onda 4: MWD=220°N (frequenza di occorrenza media annua pari a 3gg/anno).

L’onda 1 e 2 hanno una bassissima frequenza di accadimento (qualche ora ogni anno), mentre la 3 e 4 sono eventi che di riscontrano 8-10 volte in più, ovvero rispettivamente per 2 e 3 giorni all’anno.

7.3 Simulazione della circolazione nella configurazione di stato attuale

A seguire si riportano le mappe di velocità e direzione di corrente per le 4 condizioni d’onda selezionate, che forniscono una buona rappresentazione dell’attuale circolazione locale.

Le correnti litoranee sono generate per effetto dei gradienti dei *radiation stress* indotti dalle onde sul fondo, massimi in corrispondenza del frangimento. Le condizioni di moto ondoso, a seconda della loro intensità e direzione (e quindi della localizzazione della fascia di frangenti, più o meno spostata verso largo), sono in grado di generare correnti in una fascia più o meno prossima alla costa. La direzione prevalente della corrente risulta invece influenzata dall’angolo formato tra il fronte d’onda e le isobate.

Le mappe di distribuzione dell’intensità di corrente evidenziano come per le onde provenienti da direzioni Sud-Est/Sud (onda 1 con MWD=170°N in Figura 7-3 onda 2 con MWD=190°N in Figura 7-4), la direzione del flusso principale si presenti da levante verso ponente. La corrente lambisce il litorale con massime intensità in corrispondenza della linea dei frangenti. La direzione del flusso è ben evidente anche lungo la protezione in massi della diga sopraflutto del porto di Lavagna. In corrispondenza della porzione di mare protetta dal molo di sopraflutto, limitrofa all’imboccatura portuale, si genera un ampio vortice, caratterizzato da una direzione della corrente antioriaria, che tende a separarsi in corrispondenza del pennello P1, generando una corrente di ritorno (rip), diretta verso Sud-Est. Si specifica che, come evidenziato nella caratterizzazione del clima ondoso sottocosta (Figura 4-7) le mareggiate provenienti da questo settore sono quelle meno frequenti ed intense.

Per gli eventi da Libeccio, (onda 3 con MWD=210°N in Figura 7-5 onda 4 con MWD=220°N in Figura 7-6), la corrente litoranea principale caratterizzata da una direzione da ponente verso levante. All’interno della cella si osserva un maggior idrodinamismo con:

- formazione di vortici localizzati, in corrispondenza del pennello P2;
- generazione di un flusso diretto da levante a ponente nella zona centrale della cella;
- generazione di un flusso diretto da ponente a levante nella zona limitrofa al pennello P1.

Anche per questi eventi si osserva la generazione di un vortice nell’area compresa tra l’imboccatura portuale, il pennello P1 e la testata del molo di sopraflutto. La dimensione di tale vortice è tanto minore quanto è maggiore l’angolo tra la direzione di provenienza del moto ondoso e la perpendicolare alla costa. Questi sono gli eventi caratterizzati da una maggior frequenza di accadimento.

In caso di attivazione di un non trascurabile trasporto litoraneo longshore, il pattern di circolazione evidenzia come le potenziali aree di accumulo si collochino in corrispondenza della radice del molo di sottoflutto e della zona centrale del vortice, a Sud-Ovest del pennello P1, entrambe caratterizzate dalle minori intensità della corrente.

A seguire si riportano le mappe di intensità di corrente di tutte le condizioni d’onda simulate.

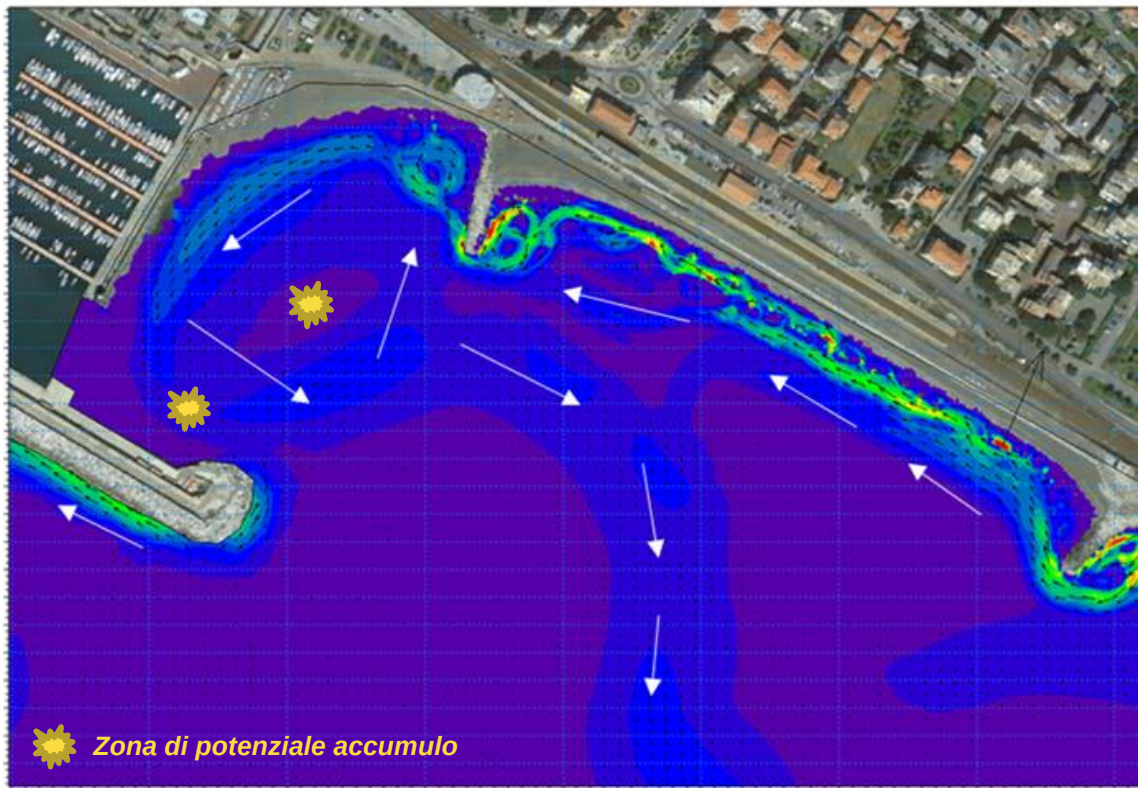


Figura 7-3 Mappa di distribuzione delle intensità di corrente per l'onda 1 (Hs=2m, Tp=9s, MWD=170°N)

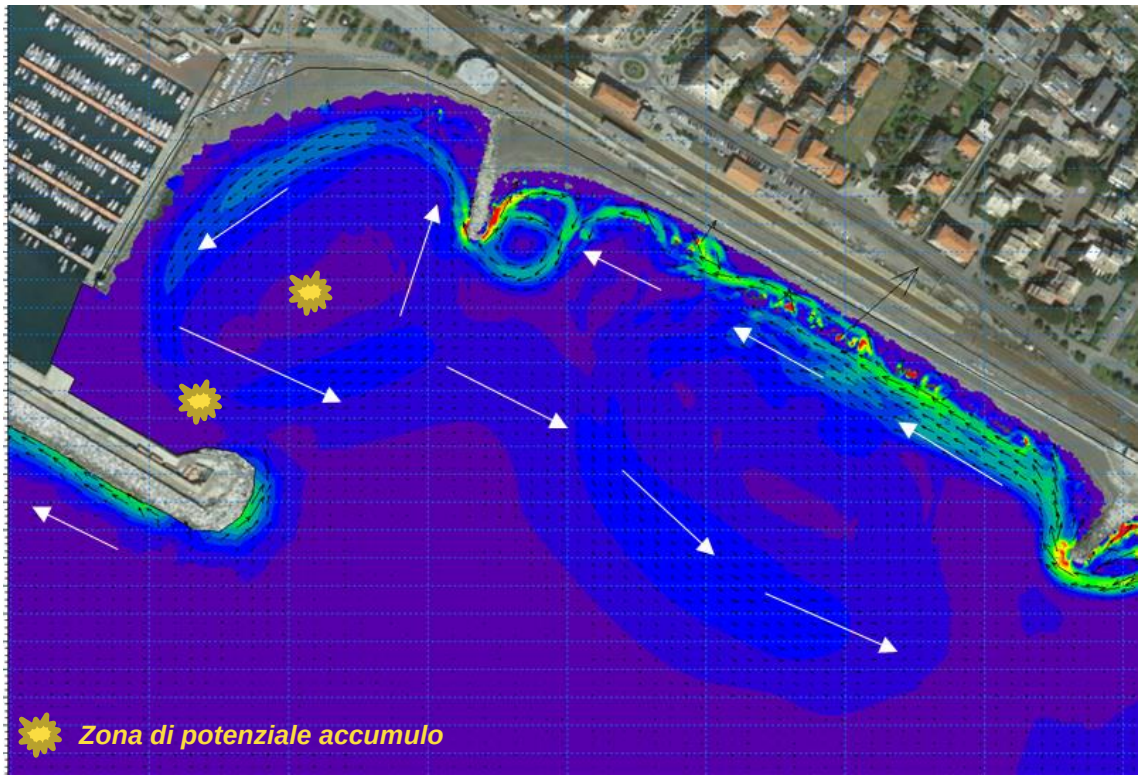


Figura 7-4 Mappa di distribuzione delle intensità di corrente per l'onda 2 (Hs=2m, Tp=9s, MWD=190°N)

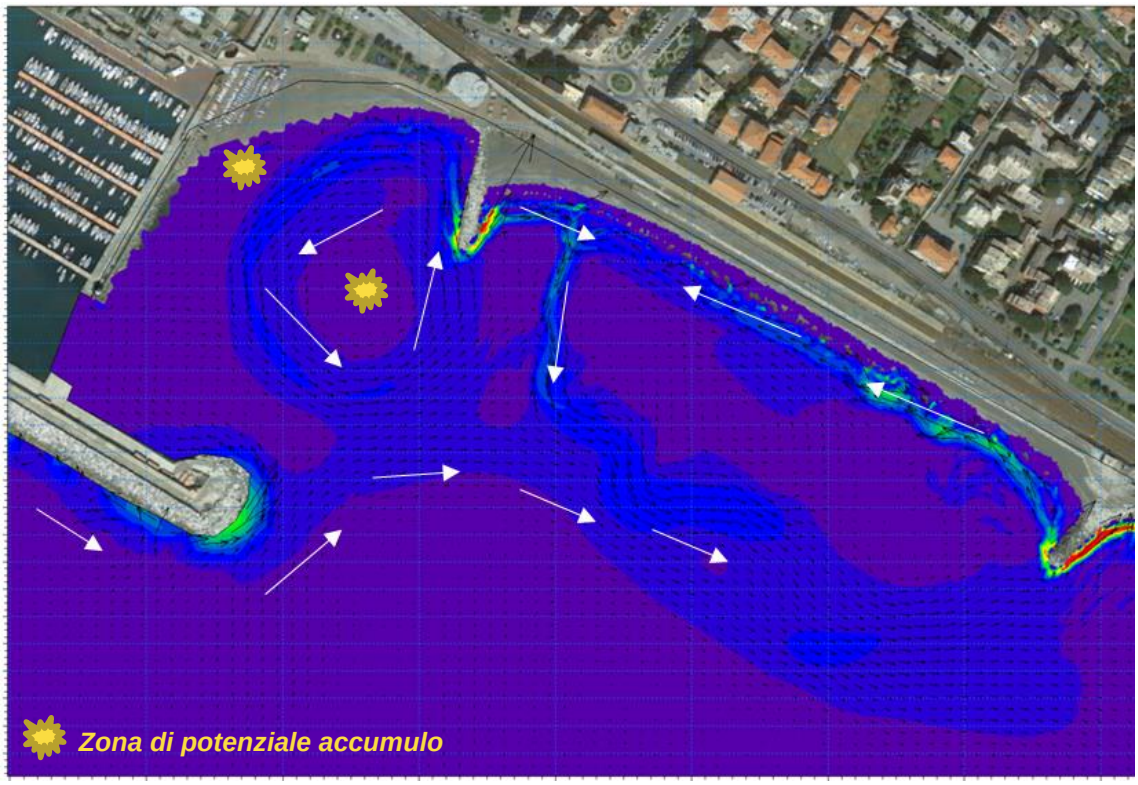


Figura 7-5 Mappa di distribuzione delle intensità di corrente per l'onda 3 (Hs=2m, Tp=9s, MWD=210°N)

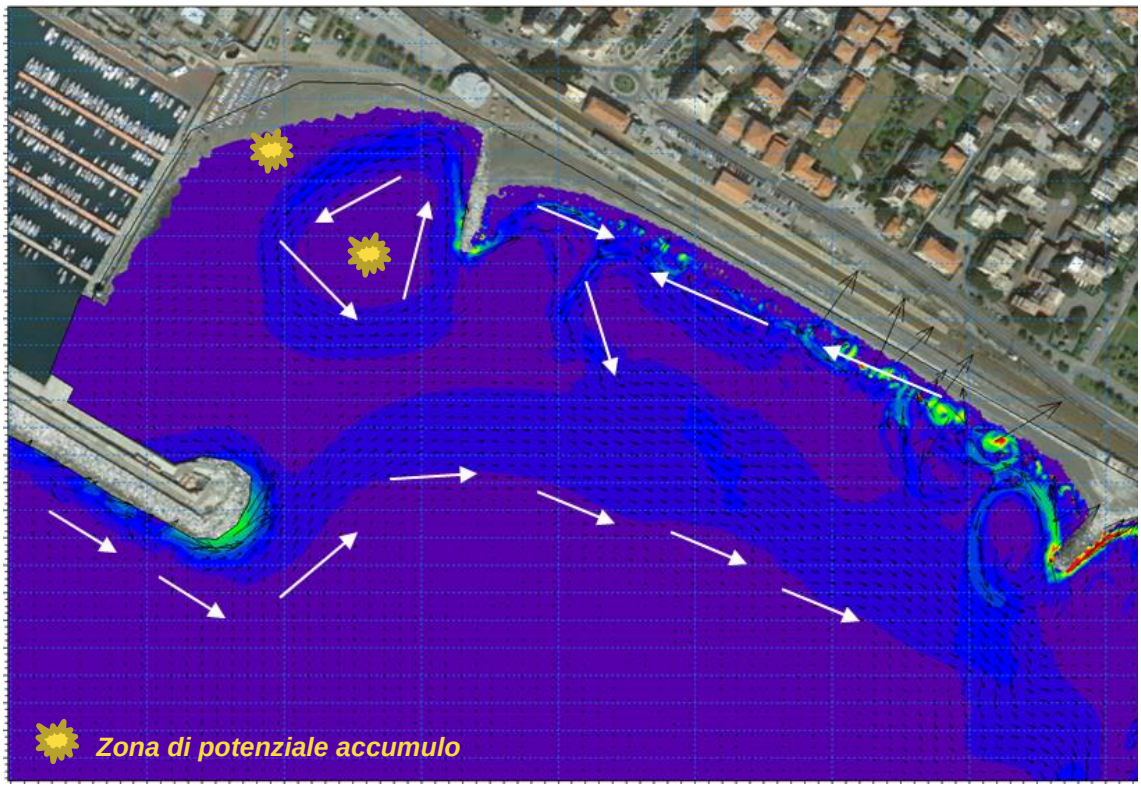


Figura 7-6 Mappa di distribuzione delle intensità di corrente per l'onda 4 (Hs=2m, Tp=9s, MWD=220°N)

8 Analisi della capacità di trasporto sedimentario

Per la quantificazione del sedimento potenzialmente movimentato in caso di mareggiata lungo il profilo di spiaggia, è fondamentale lo studio e la conoscenza delle intensità delle correnti litoranee che agiscono in direzione parallela e perpendicolare alla linea di riva, dette rispettivamente correnti longshore e cross-shore.

Nelle sezioni precedenti sono state illustrate le principali dinamiche della corrente litoranea, con la conseguente identificazione della direzione prevalente del trasporto *longshore* per direzione di provenienza del moto ondoso, nonché delle aree laddove l'andamento dei gradienti di velocità favorisce l'accumulo potenziale del sedimento. La presente trattazione si focalizza invece sulla movimentazione del sedimento trasversalmente alla costa.

Per poter identificare lo schema di difesa più efficace e valutare l'effettivo beneficio di una protezione in massi a chiusura della cella, in analogia con la soluzione già presente nelle celle contingue, si è proceduto con un'analisi del trasporto trasversale cross-shore.

Con riferimento alle simulazioni svolte con il modello tridimensionale MIKE 3 Wave (Sezione 5), si è proceduto con l'estrazione e il confronto delle velocità al fondo nelle tre configurazioni riprodotte, ovvero configurazione di stato attuale, di progetto A (con solo ripascimento strutturale) e di progetto B (comprensivo di ripascimento e opera al piede).

Il primo passo è un'analisi di tipo puntuale: sono stati identificati 24 punti di controllo, 12 a distanza di 5 m circa dall'impronta dell'opera in massi prevista a chiusura della cella e altri 12 a distanza di 10 m (anagrafica e ubicazione grafica in Figura 8-1).

I valori di velocità media al fondo sono stati estratti per la più severa tra le condizioni d'onda simulate con il MIKE 3 Wave (evento dell'Ottobre 2018), nelle tre differenti configurazioni (attuale, progetto A e progetto B) La Tabella 8-1 evidenzia come la riprofilatura del fondale a seguito del previsto ripascimento determini un benefico effetto di riduzione delle intensità di corrente trasversale a costa.

Nella fascia di spiaggia sommersa in esame, per la configurazione di progetto A si osserva una riduzione delle velocità medie al fondo del 6-8% rispetto ai valori dello stato attuale. L'inserimento di una struttura in massi (configurazione di progetto B) induce un ulteriore decremento delle intensità di corrente del 2-4%.

Si vuole altresì sottolineare come la presenza della struttura sommersa non sia solo funzionale ad un decremento locale delle velocità al fondo, ma costituisca una "trappola" per l'eventuale movimentazione del sedimento verso il largo, evitando una perdita definitiva del materiale.

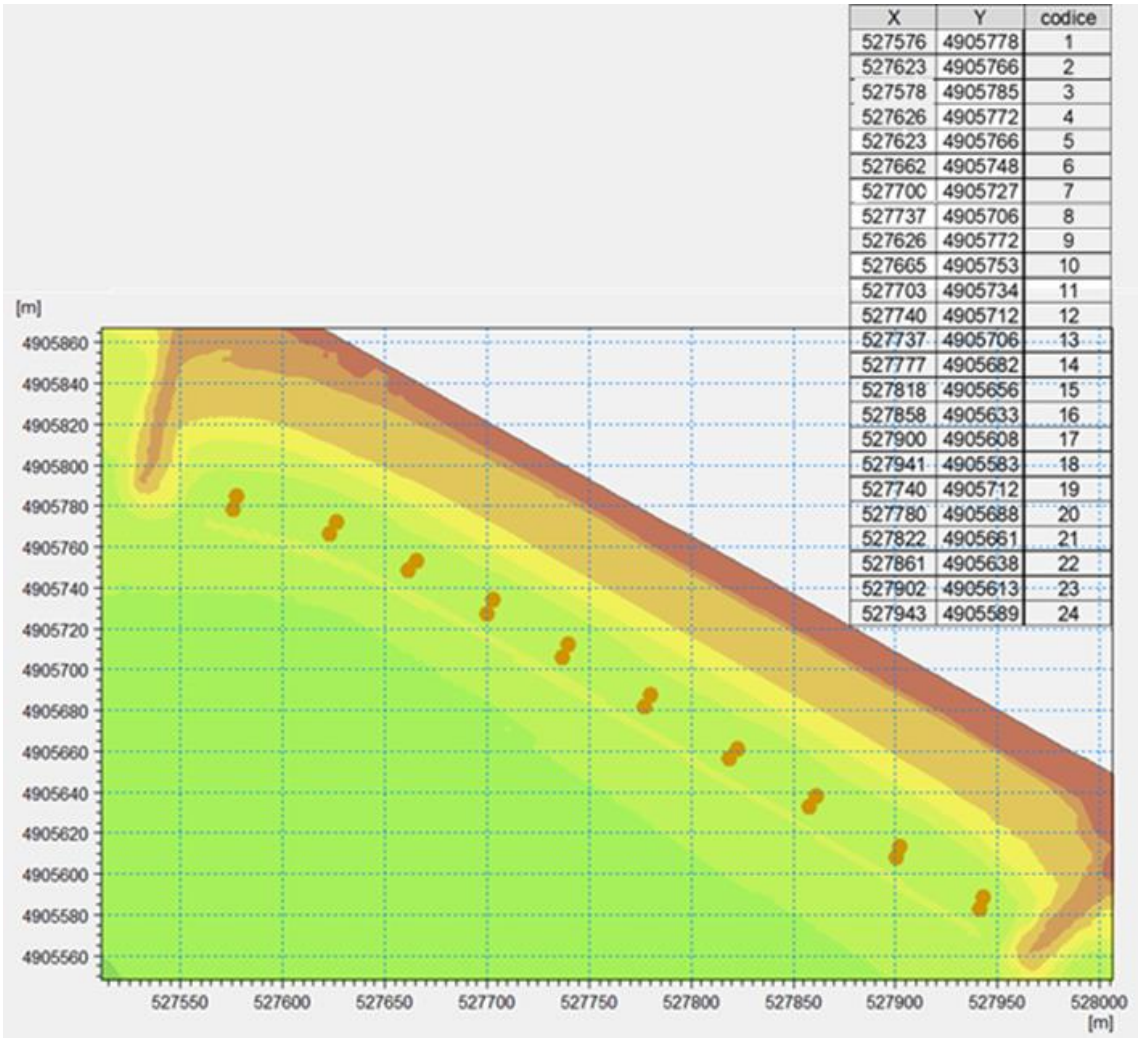


Figura 8-1 Ubicazione ed anagrafica punti di controllo

Tabella 8-1 Intensità di corrente al fondo trasversale a costa nei 24 punti di controllo, per le tre configurazioni in esame: stato attuale,configurazione di progetto A (comprensivo di ripascimento), configurazione di progetto B (comprensivo di ripascimento e opera in massi a chiusura della cella)

	V [m/s]																							
punto	1	2	3	4	5	6	7	8	9	10	11	12	13	14	15	16	17	18	19	20	21	22	23	24
Attuale	0.76	0.87	0.76	0.90	0.87	0.94	0.97	0.91	0.90	0.99	1.00	0.93	0.91	0.94	0.90	0.89	0.84	0.81	0.93	0.99	0.94	0.93	0.87	0.82
Progetto A	0.75	0.83	0.75	0.86	0.83	0.84	0.81	0.82	0.86	0.86	0.82	0.82	0.82	0.81	0.82	0.84	0.83	0.80	0.82	0.82	0.84	0.87	0.85	0.80
Progetto B	0.74	0.81	0.74	0.85	0.81	0.82	0.79	0.79	0.85	0.85	0.80	0.81	0.79	0.80	0.80	0.83	0.81	0.78	0.81	0.81	0.83	0.86	0.84	0.78

Successivamente, il confronto delle velocità di corrente trasversale nelle varie configurazioni è stato esteso a 2 profili rappresentativi della cella in esame, L1 e L2 (Figura 8-2).

A seguire si riportano a confronto la distribuzione della velocità lungo i due profili L1 e L2, per due istanti della simulazione. Dal confronto tra la configurazione di progetto A e di progetto B, si evidenzia una leggera accelerazione del flusso in corrispondenza della berma della struttura in massi, conseguente al restringimento della sezione idraulica, e un decremento delle intensità nella fascia adiacente l'opera, lato spiaggia, che tende a favorire l'accumulo di materiale.



Figura 8-2 Ubicazione profili di controllo della cella oggetto del presente studio (L1 a ponente e L2 a levante)

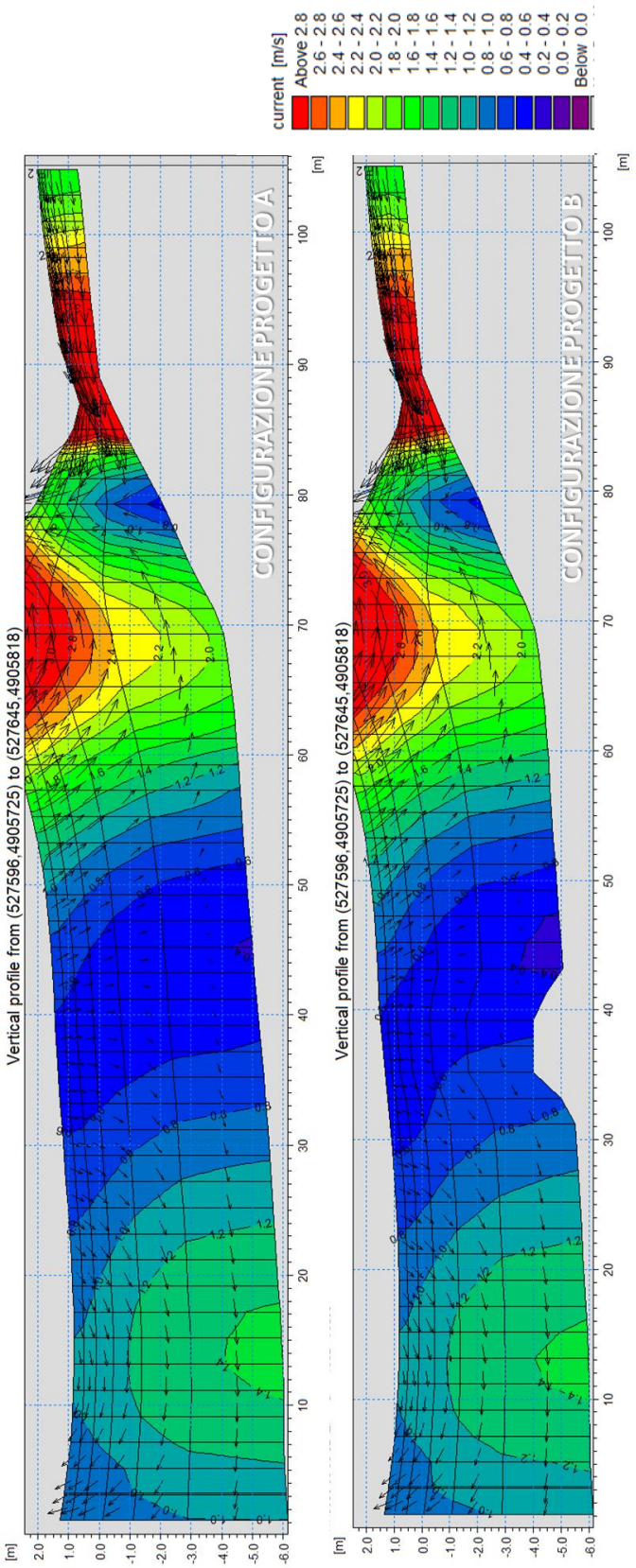


Figura 8-3 Distribuzione della velocità lungo il profilo L1 durante il picco di mareggiata dell'Ottobre 2018, (Time step 1827) per la configurazione di progetto A a confronto con la configurazione di progetto B

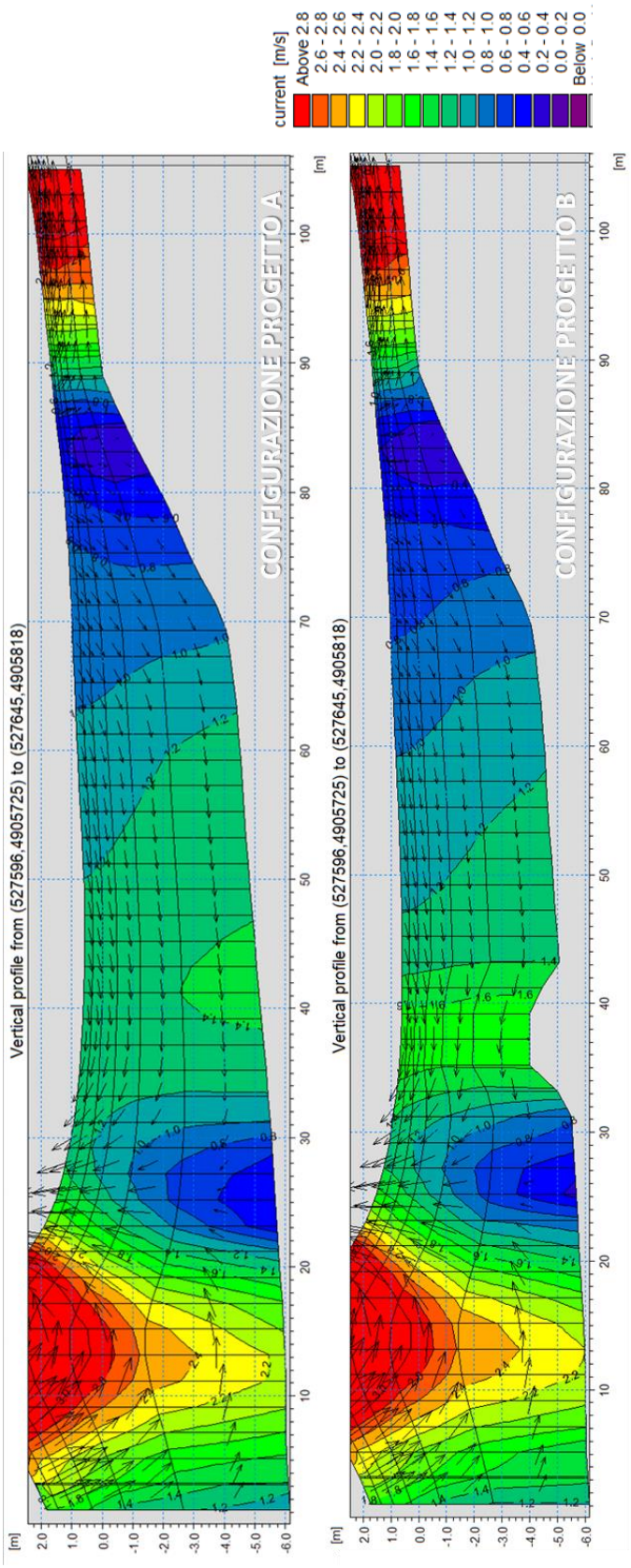


Figura 8-4 Distribuzione della velocità lungo il profilo L1 durante il picco di mareggiata dell'Ottobre 2018 (Time step 3105) , per la configurazione di progetto A a confronto con la configurazione di progetto B

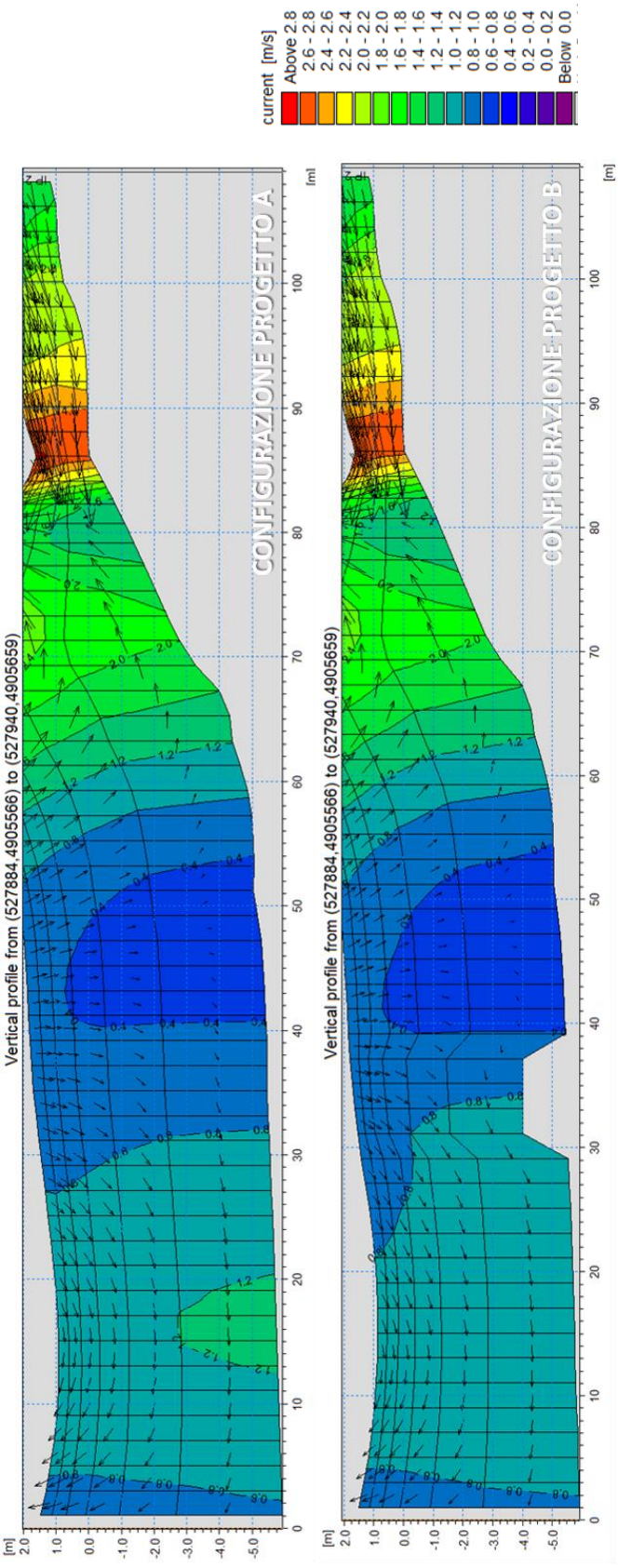


Figura 8-5 Distribuzione della velocità lungo il profilo L2 durante il picco di mareggiata dell'Ottobre 2018 (Time Step 1827), per la configurazione di progetto A a confronto con la configurazione di progetto B

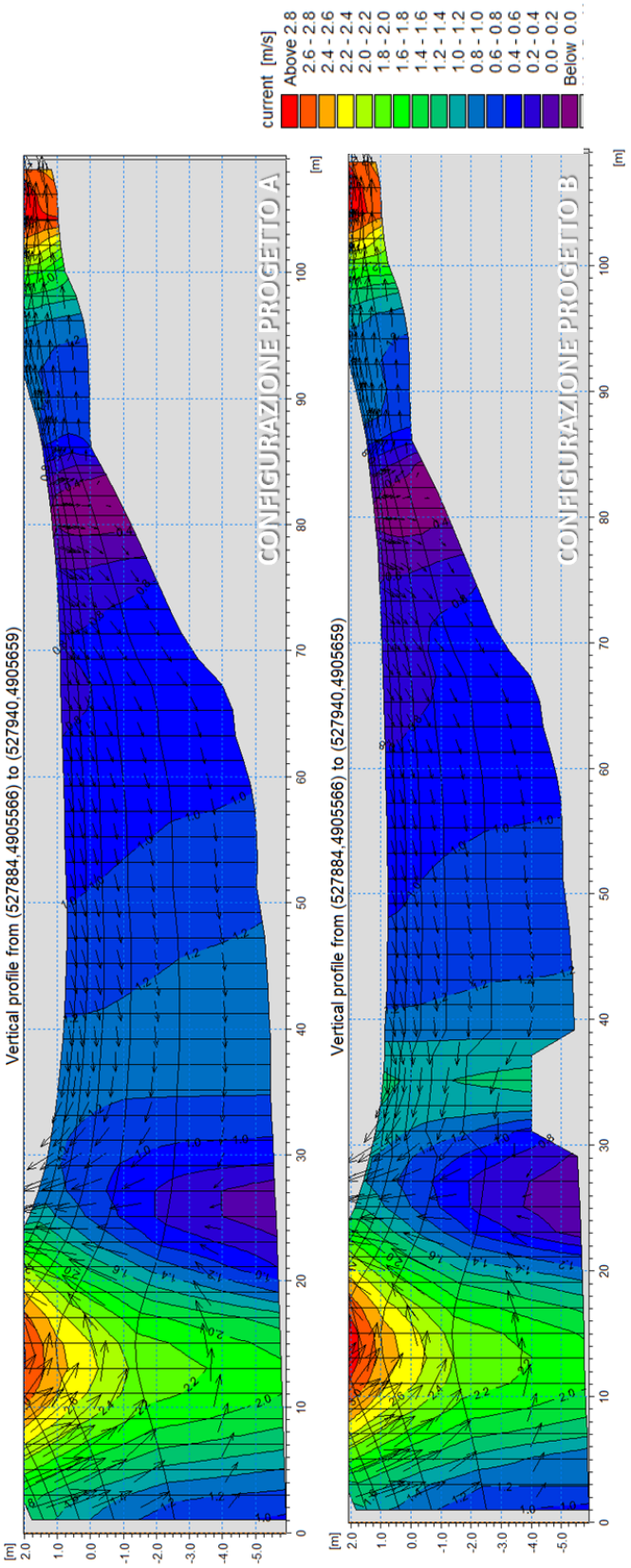


Figura 8-6 Distribuzione della velocità lungo il profilo L2 durante il picco di mareggiata dell'Ottobre 2018 (Time Step 3105), per la configurazione di progetto A a confronto con la configurazione di progetto B

A completamento dell'analisi è stata effettuata un'analisi sulla capacità di trasporto al variare della profondità, con la finalità di definire, per la configurazione proposta, una stima di massima dei potenziali volumi di materiale movimentabili durante un evento di mareggiata.

Per questa valutazione si è assunto di fare riferimento all'evento del Marzo 2020, intenso ma non eccezionale.

Con riferimento ai quattro punti riportati in Figura 8-7, la cui anagrafica è riportata in Tabella 8-2, si è proceduto con l'estrazione dei risultati delle condizioni di onda e all'applicazione del modulo STP. Tale strumento, già descritto nell'ambito della trattazione del modello LitDrift per il trasporto litoraneo, è utile alla stima del trasporto sedimentario (dato dalla somma del trasporto di sedimenti al fondo ed in sospensione) in modalità puntuale.

In Tabella 8-3 sono riportati i volumi movimentabili mantenendo per tre ore le condizioni d'onda al picco della mareggiata del Marzo 2020 lungo tutta l'estensione del litorale compreso tra il pennello P1 e il pennello P2.

I risultati ottenuti evidenziano come all'aumentare della profondità il volume di sedimento movimentato diminuisca, fino quasi ad annullarsi in prossimità della batimetrica -5 m.

Questa ulteriore analisi conferma un trasporto sedimentario limitato ad una fascia di spiaggia conterminata dalle opere trasversali lateralmente e dalla scogliera soffolta lato mare.

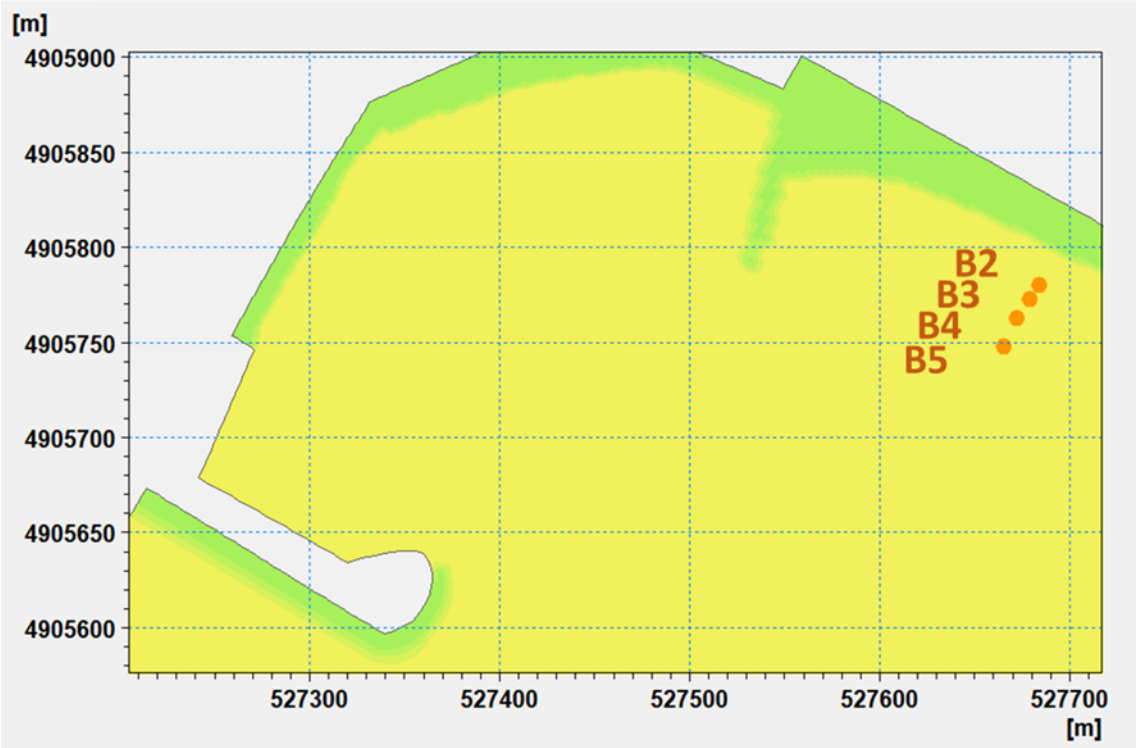


Figura 8-7 Indicazione dei punti di controllo per la stima della capacità di trasporto

Tabella 8-2 Anagrafica punti di controllo per la stima della capacità di trasporto

Codice	X[m]	Y[m]	z[m]
B2	527684	4905780	-2
B3	527679	4905773	-3
B4	527672	4905763	-4
B5	527665	4905748	-5

Tabella 8-3 Stima della capacità di trasporto nella configurazione di progetto A

Codice	Qtot [m^3]
	progetto
B2	776
B3	105
B4	35
B5	11

9 Valutazioni su un'ulteriore configurazione di ripascimento

Oltre all'intervento di ripascimento oggetto delle attività di modellazione fin qui illustrate (sia nella configurazione in assenza, sia in presenza dell'opera in massi a chiusura della cella, rispettivamente configurazione A e B), l'Amministrazione Comunale ha richiesto la valutazione e verifica di un intervento che preveda la ricostruzione ed il riequilibrio del litorale con un ulteriore ripascimento strutturale dell'arenile con realizzazione della spiaggia emersa e sommersa in ghiaia di cava.

La variante proposta, qui definita *configurazione di progetto C*, prevede uno sversamento di 44'450 m^3 di materiale a riempimento della fascia di spiaggia sommersa compresa tra l'opera in massi a chiusura della cella e la linea di riva (Figura 9-1).

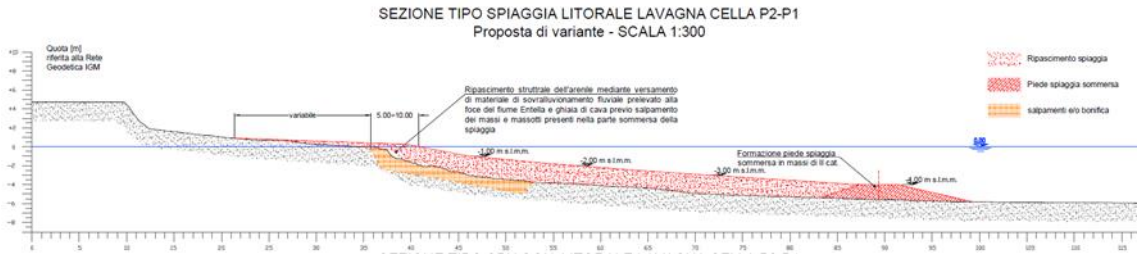


Figura 9-1 Sezione tipologica della variante progettuale proposta

Come per le altre configurazioni progettuali studiate, si è proceduto all'analisi dell'efficacia dello schema proposto con la simulazione con modello 2D e 3D delle tre mareggiate selezionate (capitolo 5).

A seguire si riportano alcuni risultati grafici, dalla distribuzione dell'altezza d'onda risultante per le condizioni di mareggiata del Marzo del 2020 (Figura 9-2), alla risalita lungo la spiaggia sommersa ed emersa per specifici istanti significativi sia dell'evento di Marzo 2020 sia di quello dell'Ottobre 2018 (da Figura 9-3 a Figura 9-6).

Osservando la mappa della propagazione dell'onda sottocosta emerge come la riduzione della profondità del fondale, conseguente all'ingente apporto di materiale, comporti un abbattimento dell'energia dell'onda più regolare rispetto allo stato attuale. Risulta ben evidente l'ubicazione della struttura in massi che rappresenta una discontinuità nell'andamento delle batimetriche.

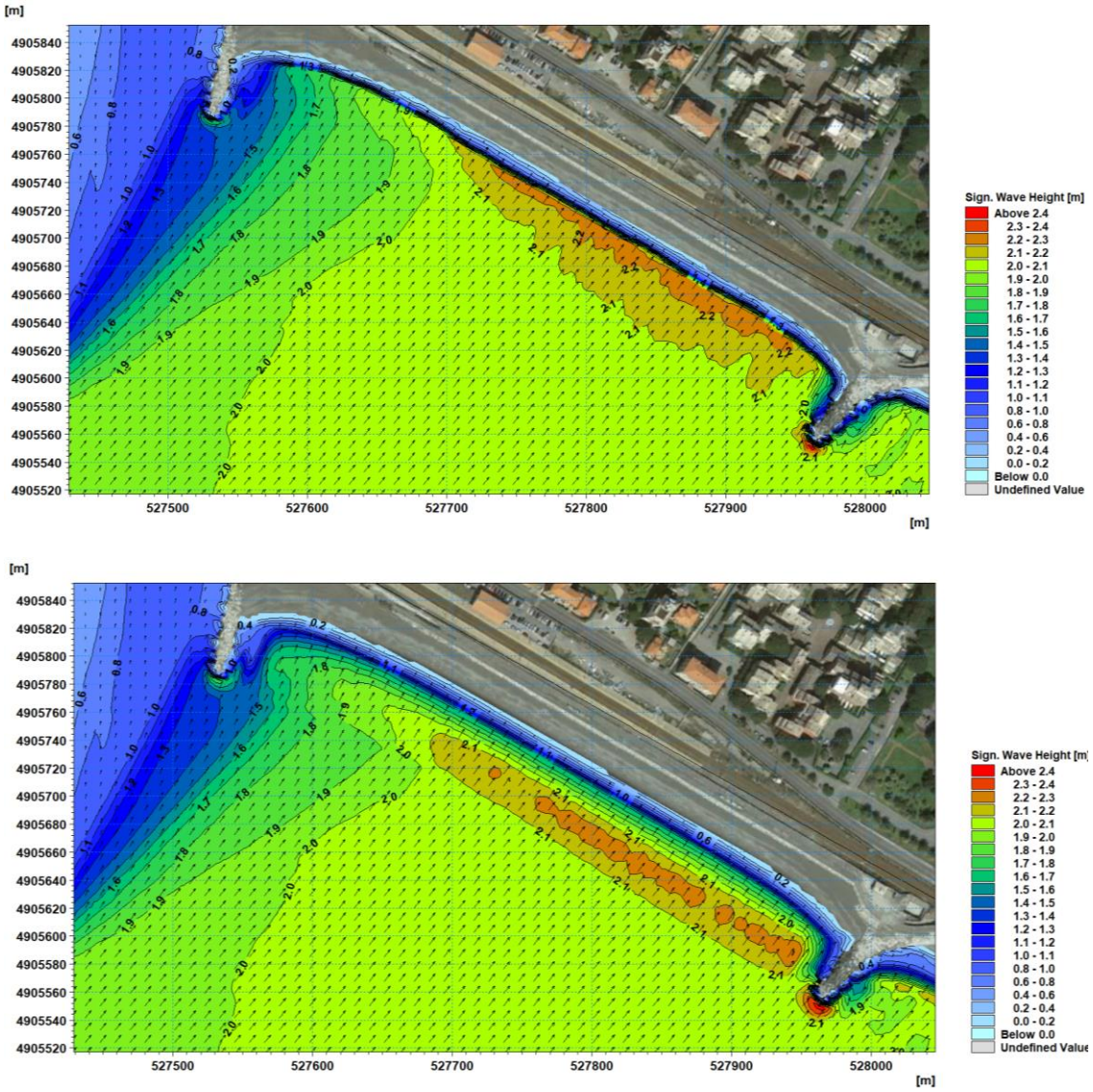


Figura 9-2 Confronto della distribuzione della altezza d'onda significativa al picco di mareggiata del Marzo 2020 per la configurazione progettuale C (in basso) e la configurazione attuale (in alto)

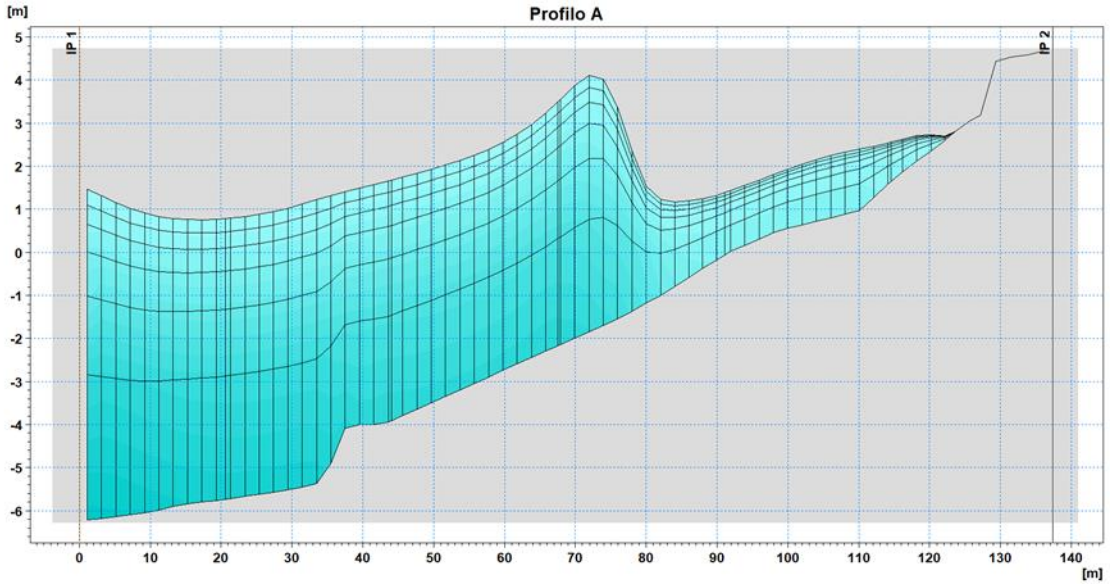


Figura 9-3 Configurazione di progetto C: esempio di risalita dell'onda lungo il profilo A, in un istante della mareggiata dell'Ottobre 2018 (Time Step 1827)

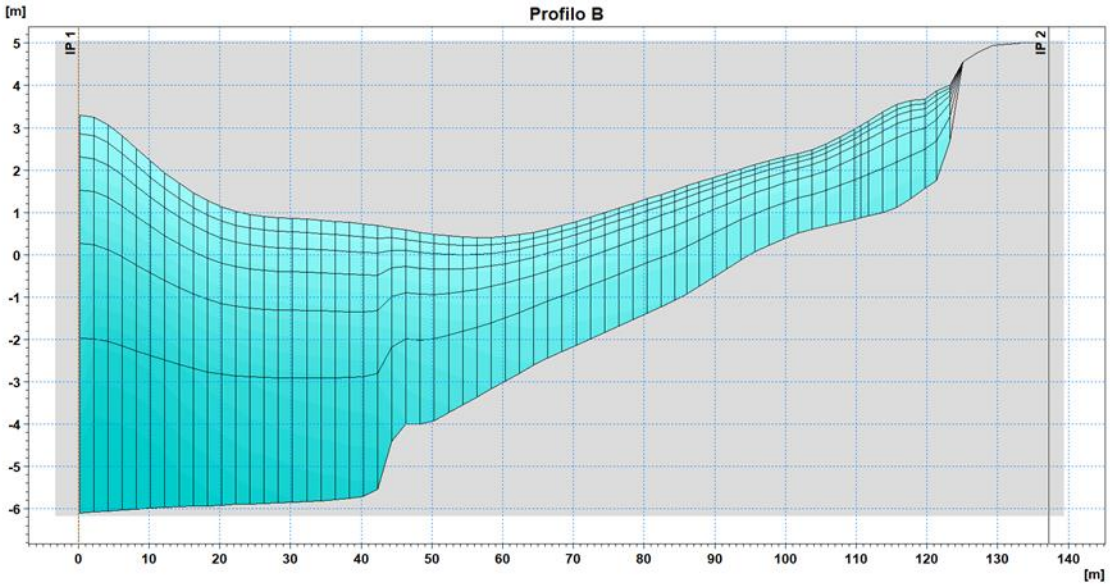


Figura 9-4 Configurazione di progetto C: esempio di risalita dell'onda lungo il profilo B, in un istante della mareggiata dell'Ottobre 2018 (Time Step 2753)

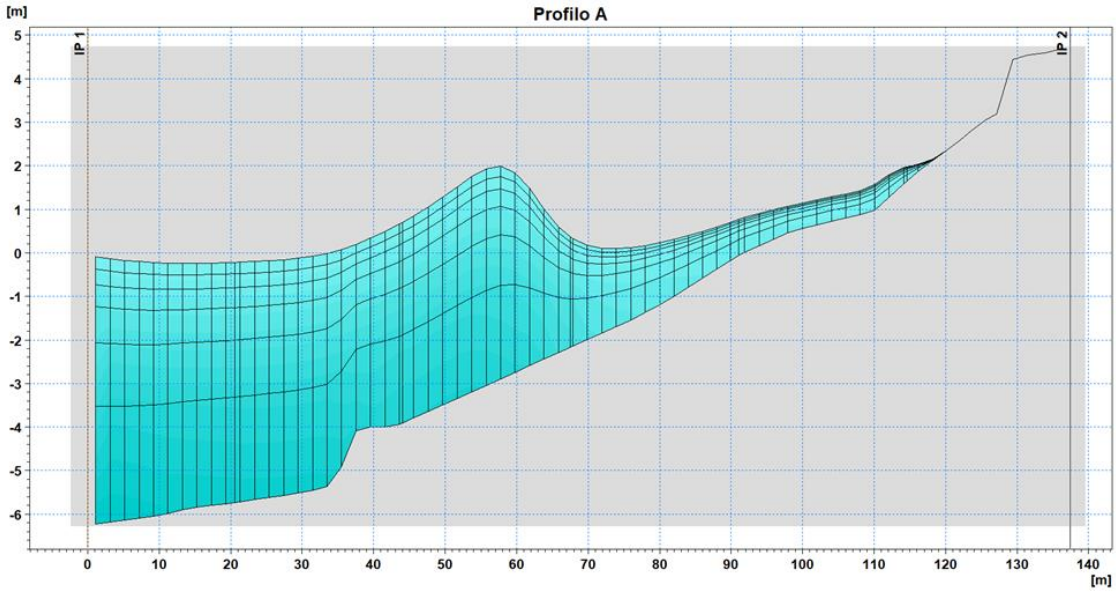


Figura 9-5 Configurazione di Progetto C: esempio di risalita dell'onda lungo il profilo A, in un istante della mareggiata del Marzo 2020 (Time Step 1038)

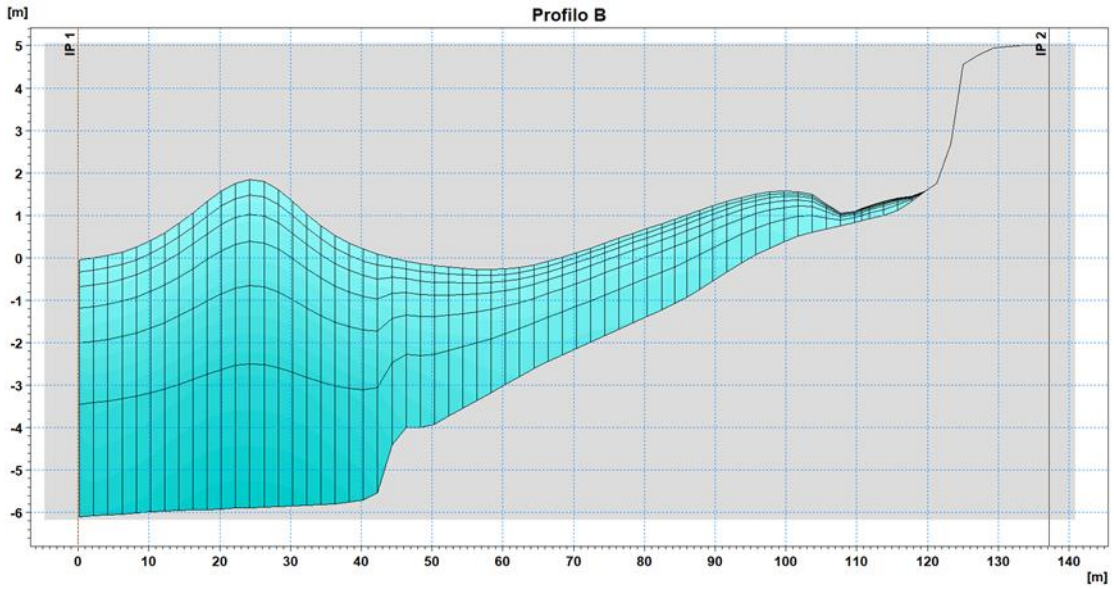


Figura 9-6 Configurazione di Progetto C: esempio di risalita dell'onda lungo il profilo B, in un istante della mareggiata del Marzo 2020 (Time Step 577)

In termini di risalita del moto ondoso sulla spiaggia emersa, la nuova configurazione comporta un ulteriore decremento di circa 2 m in planimetria rispetto alla configurazione di progetto B.

Infine, è stata svolta un'analisi sulla capacità di trasporto al variare della profondità, con la finalità di definire, per la configurazione proposta, una stima dei potenziali volumi di materiale movimentabili durante un evento di mareggiata.

Per questa valutazione, analogamente a quanto predisposto per la configurazione di progetto A, si è assunto di fare riferimento all'evento del Marzo del 2020, intenso ma non eccezionale.

Dai risultati ottenuti, riportati in Tabella 9-1, si evince una maggior movimentazione alla profondità dei 3 m, con una fascia attiva caratterizzata da maggior larghezza rispetto alle configurazioni

precedentemente analizzate, ma con una tendenza ad una significativa diminuzione del trasporto per le batimetriche dei 4 e 5 m.

Tabella 9-1 Stima della capacità di trasporto nella configurazione di progetto C

Codice	Qtot [m^3] variante
B2	273
B3	368
B4	43
B5	40

10 Conclusioni

Le attività di studio e di modellazione numerica del presente studio sono state svolte a supporto della progettazione degli interventi di ripascimento strutturale del litorale di Lavagna (GE). In particolare gli approfondimenti hanno fatto riferimento alla prima cella di ponente, limitrofa al porto turistico, compresa tra i pennelli “P1” e “P2” del lungo litorale di Lavagna-Cavi.

I principali obiettivi dello studio sono:

- la verifica dell’adeguatezza del ripascimento previsto ai fini di un’efficace difesa della risalita del moto ondoso sulla battigia;
- la quantificazione dei benefici della possibile realizzazione di una protezione in massi a chiusura della cella, a collegamento delle testate dei pennelli che delimitano la cella;
- la stima della capacità di trasporto sedimenatario nella nuova configurazione progettuale.

Nel corso dell’analisi sono stati utilizzati diversi codici di calcolo, tutti appartenenti alla suite MIKE by DHI, monodimensionali, bidimensionali e tridimensionali.

Per le condizioni di onda si è fatto riferimento al database del Mar Mediterraneo (MWM - Mediterranean Wind Wave Model) che ha permesso:

- la caratterizzazione del clima meteomarino al largo;
- la propagazione dell’intera serie ultra-quarantennale di moto ondoso da largo verso costa;
- la definizione delle condizioni di onda di tre eventi da riprodurre con un modello tridimensionale di dettaglio, focalizzato sulla zona in esame;
- l’identificazione delle condizioni di onda sottocosta da utilizzarsi per la modellazione del trasporto litoraneo.

Al fine di raggiungere gli obiettivi dello studio è stato utilizzato il nuovo modulo MIKE 3 Wave FM, pienamente non lineare, che permette la **simulazione delle dinamiche di frangimento, run-up e overtopping**. Sulla base di tre eventi selezionati, le mareggiate di Ottobre 2018, Dicembre 2013 e Marzo 2020, differenti per direzione di provenienza e/o intensità di evento, è stato possibile verificare l’adeguatezza della nuova configurazione progettuale, definita nello studio “configurazione di progetto A”, con la conferma di una sensibile riduzione nella risalita del moto ondoso rispetto alla configurazione attuale, quantificabile in 6-8 m in planimetria (avanzamento del fronte d’onda sulla battigia) e 0.3-0.5 m in quota.

I test svolti hanno anche permesso di affermare che la riprofilatura della spiaggia con il ripascimento previsto comporta una significativa riduzione della frequenza di raggiungimento del piano della passeggiata da parte del moto ondoso.

Successivamente, sono state predisposte simulazioni numeriche del **trasporto sedimentario longitudinale (*long-shore*) e trasversale (*cross-shore*)**, impiegando i modelli numerici monodimensionali “LITDRIFT” (per la quantificazione del trasporto *long-shore* medio annuo netto e lordo, della profondità di chiusura e dell’orientazione di equilibrio), il modello bidimensionale MIKE 21 SW-HD (per la definizione dei pattern di circolazione locale e la direzione del trasporto) e il modulo monodimensionale “STP” (per la stima della capacità di trasporto della configurazione di progetto all’aumentare della profondità).

La stima della profondità di chiusura, che delimita la fascia attiva della spiaggia sommersa ove avviene la movimentazione del materiale ha confermato l’adeguato posizionamento dell’opera in massi a chiusura della cella. La lieve diminuzione delle velocità di corrente al fondo riscontrate comparando i risultati della modellazione della configurazione di progetto A con la configurazione di progetto B confermano un locale effetto dell’opera nell’indurre la sedimentazione del materiale, oltre alla funzione di barriera fisica che tende a ridurre la perdita definitiva di materiale verso il largo.

L’analisi della capacità di trasporto ha inoltre evidenziato che all’aumentare della profondità vi è una significativa riduzione dei volumi movimentabili, che raggiungono valori minimi alla profondità di 5 m.

E’ infine stata verificata una ulteriore configurazione progettuale “C”, che prevede un incremento dei volumi di ripascimento rispetto alle configurazioni A e B, variante progettuale finalizzata ad aumentare ulteriormente la resilienza della spiaggia, con una significativa integrazione al ripascimento già previsto con materiale di cava, la cui stesura avverrebbe tra la linea di riva e l’opera in massi, alla quale verrebbe pertanto “appoggiato” il ripascimento.

Le verifiche svolte su quest’ultima configurazione hanno confermato una riduzione in termini di altezza d’onda significativa oltre che della capacità di trasporto rispetto alla configurazione progettuale B; per tale integrazione è in corso una specifica richiesta di variante progettuale.

11 Riferimenti

[1] G. Contento, L. Donatini, G. Lupieri, A. Pedroncini e L. Cusati, «MWM: A 35 years wind & wave high resolution hindcast dataset and an operational forecast service for the Mediterranean Sea,» in *18th International Conference on Ships and Shipping Research, pp. 116-125, ISBN 978-88-940557-1-9*, 2015.

[2] DHI, «MIKE 3 Flow Model HD FM, Hydrodynamics Flexible Mesh, Scientific Documentation,» MIKE by DHI, Hørsholm, 2021.

[3] DHI, «LITPACK Littoral Processes FM, Scientific Documentation,» 2021, Hørsholm

[4] Jeppesen Marine, «CM-93, Global Electronic Chart Database Professional+,» Jeppesen Marine, Norway, 2021DHI,

[5] «MIKE C-MAP, Extraction of World Wide Bathymetry Data and Tidal Information, Scietific Documentation,» MIKE by DHI, Hørsholm, 2021.

[6] DHI, «MIKE 21 SW - Spectral Wave Module, Scientific Documentation,» MIKE by DHI, Hørsholm, 202

ALLEGATI

ALLEGATO A

Mediterranean Wind Wave Model

General description of the models' chain

The models and datasets used for the development of the MWM database are:

- the *CFSR* (*Climate Forecast System Reanalysis*) global re-analysis dataset, produced and freely published by NCEP (*National Centers for Environmental Prediction*) (Saha et al, 2010; http://rda.ucar.edu/datasets/ds093.0/index.html#description), hourly (re-forecast) data with a space resolution of 0.5°; these data are used as initial (IC) and boundary conditions (BC) of the *WRF-ARW model* (below);

- the atmospheric model *WRF-ARW – version 3.4.1* (*Weather Research and Forecast - Advanced Research WRF*), model developed by NCAR (*National Center for Atmospheric Research*) (Skamarock and Klemp, 2007; Michalakes et al, 2001; Michalakes et al, 2005); *WRF-ARW* is presently considered among the best state-of-the-art non-hydrostatic meteorological models; it is supported by a massive worldwide community that contributes to its local use and development (http://www.mmm.ucar.edu/wrf/OnLineTutorial/index.htm; http://www.wrf-model.org/index.php);

- the wave model MIKE 21 Spectral Waves (SW) developed by DHI (former Danish Hydraulic Institute) (Sorensen, O.R., Kofoed-Hansen, H., Rugbjerg, M. and Sorensen, L.S., 2004). MIKE 21 SW is among the state of the art wave models, widely used in thousands of offshore and coastal applications worldwide.

In the following a description of the CFSR dataset, the WRF-ARW and the MIKE 21 SW model is given, with specific interest to the implementation adopted in MWM.

CFSR Dataset

The CFSR dataset (Fig. A.1) is the result of a long and complex process performed by NCEP, an ensemble of nine weather prediction centers in the United States belonging to the NWS (*National Weather Service*) of the NOAA (*National Oceanic and Atmospheric Administration*). The simulation, completed in 2011, is based on a global atmospheric numerical model including atmosphere-ocean and sea-ice couplings, with a systematic ingestion of both conventional (point) and satellite observations with data assimilation procedures.

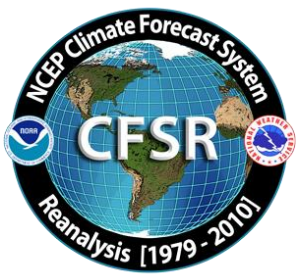


Figure A.1

The CFSR now covers a 35-year period from 1979 to 2013 (included) and is continuously updated with new recent data. The simulations were performed as 9 hours forecast simulations, initialized 4 times a day (at 00:00, 06:00, 12:00 and 18:00) between the 6-hourly re-analysis frames. The

results of these simulations, gathered in the CFSR dataset, consist in complete atmospheric data over ocean and lands with a one hour time resolution and a 0.5° horizontal resolution, while the vertical resolution changes greatly amongst the atmospheric variables, spanning from the single surface value up to values at 64 different isobaric levels.

MWM dataset ingest the 6-hourly CFSR data, specifically the *ds093.0* dataset.

Chawla et al (2013) presented a thorough analysis of the *CFSR* dataset against satellite and oceanic buoys data. The final goal of that study is the use of the U_{10} wind data from the *CFSR* dataset as the forcing term of *WWIII* to generate wave fields at global scale, without any assimilation of wave data. The analysis of the *CFSR* dataset shown in that paper includes the intrinsic performance of the model in terms of the seasonal and annual variability of the percentiles. A moving average is applied to smooth the altimeter data from the satellites and from the buoys. The normalized percentiles ("...normalized with the wind speeds at corresponding percentiles from the altimeters") computed over the satellite tracks exhibit an oscillatory behavior, never below 0.93 or 0.90 in the Northern and Southern hemisphere respectively. From that analysis, the wind and wave *CFSR* and *WWIII* data compare very well with satellite data in terms of normalized percentiles. The Q-Q plots at selected offshore buoys are generally good or very good, with some unexpected variations from case to case for some buoys close to the coast, with even a contradictory behavior between U_{10} and H_s in some locations.

The analysis of the wind field of the *CFSR* dataset is far beyond the scope of the present work but still some checks have been done in specific cases, like the event of November 1999 in Trieste (Italy). The performance of a local area model is directly related to the information contained in the global model used as boundary and initial conditions; Fig. A.2 after Contento et al (2014) shows the wind speed for the case of November 1999 in Trieste (Northern Adriatic Sea - Italy); the red dots are experimental data by NOAA (http://gis.ncdc.noaa.gov/map/viewer/#app=cdo&cfg=cdo&theme=hourly&layers=1&node=gis); the yellow line corresponds to the re-analysis data *CFSR d093.0* (Saha et al, 2010; http://rda.ucar.edu/datasets/ds093.0/index.html#description) interpolated at the same position of the station; the blue dots are related to a fully certified and verified measurement station of the Regional Agency for the Environment Protection (ARPA FVG-OSMER, http://www.osmer.fvg.it/home.php) located few meters far from the station used by NOAA (http://gis.ncdc.noaa.gov/map/viewer/#app=cdo&cfg=cdo&theme=hourly&layers=1&node=gis); the cyan line corresponds to the present hindcast dataset (model *WRF-ARW*). It is rather evident that the CFSR dataset ingests the experimental data from NOAA but there are some non-negligible discrepancies between the two experimental datasets (private communication with ARPA FVG-OSMER - Regional Agency for the Environment Protection – Friuli Venezia Giulia Region, Italy). In this case the local model *WRF-ARW* is able to develop the local wind field and matches correctly the measurement by ARPA, irrespective of the wrong assimilated data as BC and IC; this, however, cannot be always guaranteed.

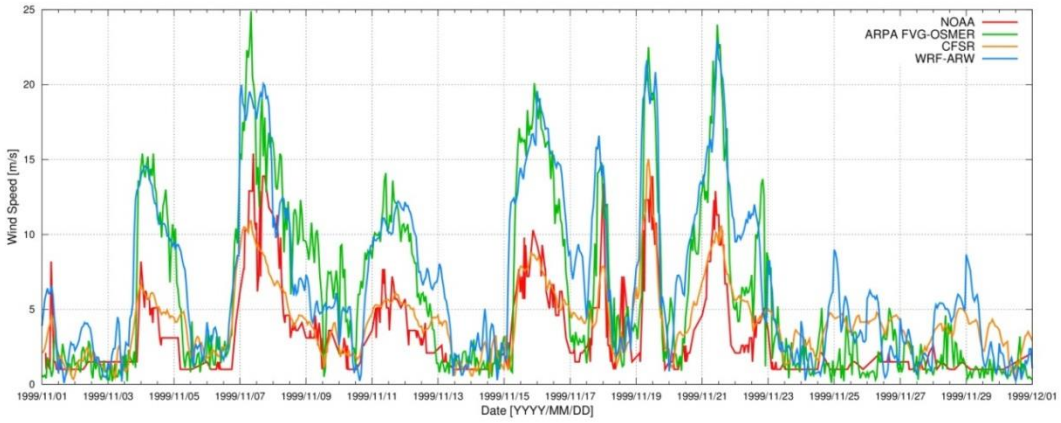


Figure A.2 Comparison between measured wind speed at two ground neighbor (few meters from each other) stations in Trieste (Italy - Northern Adriatic Sea) from the database of NOAA

(http://gis.ncdc.noaa.gov/map/viewer/#app=cdo&cfg=cdo&theme=hourly&layers=1&node=gis) (red line) and from ARPA-FVG OSMER (http://www.osmer.fvg.it/home.php) (blue line). Model data from *CFSR* (Saha et al, 2010) (yellow line) and the present simulations with *WRF-ARW* (cyan line) are overlapped.

The scope of these checks was solely to verify the sensitivity of the *CFSR* wind pattern to a complex steep geographic area facing the sea. The eastern coast of the Adriatic Sea is just an example among many others. The availability of certified wind data from the local Regional Agency for the Environment Protection – Friuli Venezia Giulia (ARPA FVG-OSMER, http://www.osmer.fvg.it/home.php) related to ground stations and to a fixed station in the middle of the Gulf of Trieste (Northern Adriatic Sea *http://www.ts.ismar.cnr.it/node/84*]), helped a lot in defining the set-up of the local area meteorological model. The aim of the set-up process was to let the model *WRF-ARW* develop mesoscale and local weather structures, thus using a domain large enough to develop these structures, but at the same time avoiding the use of too large a domain that may lead to a model drift from the experimental data. These undesired effects were observed along the entire Adriatic Sea, specifically on the eastern side (Contento et al, 2011; Contento et al, 2014).

WRF-ARW meteorological model

The WRF model is an open source mesoscale to microscale atmospheric model developed by the American atmospheric research center NCAR in cooperation with many other meteorological institutions. It is largely used worldwide for both atmospheric research and forecast or hindcast purposes due to its ability to perform atmospheric simulations over a wide range of length scales spanning from less then 1 kilometer to thousands of kilometers. This flexibility is further increased by its capability of performing two way coupled nested runs.

The WRF modelling system includes a pre-processor system (WPS), a data assimilation system (WRF-DA) and the dynamic solver. During this work the ARW dynamic solver, developed and maintained by the Mesoscale and Microscale Meteorology Division of NCAR, has been used. The ARW dynamic core is a fully compressible and non-hydrostatic model, based on a terrain-following hydrostatic pressure vertical coordinate system and on an Arakawa C-grid staggered evaluation of the vector quantities. The solver uses high order time integration and 3-D advection schemes.

The WRF model works internally with NetCDF files, a self-describing and machine-independent data format particularly suitable for the manipulation of long arrays of scientific data.

A WRF-ARW model run is a quite complex process, since it involves several different steps to be run in a precise order. First of all, WRF requires boundary and initial conditions; these conditions can be supplied by the GRIB files obtained from the CFSR dataset files described in CISL RDA: NCEP Climate Forecast System Re-analysis (CFSR) 6-hourly Products, January 1979 to December 2010." [Online] Available at http://rda.ucar.edu/datasets/ds093.0/index.html#description

GRIB files needed to cover completely the whole simulated period must be fed to the model to complete the simulation process successfully.

Moreover, since the atmosphere behaviour is strongly dependent on the soil characteristics, detailed data about these characteristics must be fed to the model too in order to let it develop the local weather phenomena correctly. However, there is no need to produce this type of data since suitable 30" resolved geographic data are included in the default WRF pre-processing (WPS). Since these data are time-independent they need to be downloaded only once, and they remain valid for every simulation unlike the GRIB files. Actually, some of the parameters contained in the geographic data cannot be considered as completely time-independent; in fact, some of the parameters show a time dependence which, however, is limited to seasonal changes, e.g. the

reduced vegetation cover in winter. The possible seasonal variability of the geographical parameters is included in the geographical data archive of WPS.

A complete WRF-ARW simulation needs the WPS (*WRF Pre-processor System*) to be run before the numerical solver (*wrf.exe*). The WPS pre-processor system deals with both the domain set-up and the preliminary input manipulations; it is composed by three main executables carrying out different tasks:

- *geogrid.exe* is responsible for the definition of the horizontal grid as well as for the interpolation of the geographic data on the user-defined grid. When performing nested runs, the *geogrid.exe* run produces a NetCDF file *geo_em.dxx.nc* containing the grid and geographic data for each domain, where xx stands for the code of the domain (01, 02, …).

- *ungrib.exe* is responsible for the decoding of the input GRIB files used as initial and boundary conditions. The GRIB files, which need to be linked to the work directory of WPS by means of the script *link_grib.csh*, are "ungribbed" and rewritten in an intermediate format suitable for further manipulations, excluding all the fields not needed for the following model run.

- *metgrid.exe* is responsible for the horizontal interpolation of the intermediate input files produced by ungrib.exe on the grid defined by geogrid.exe. Moreover, the geographic data contained in the *geo_em* files are ingested by metgrid and written on its output files. The output of metgrid.exe is in fact composed by the NetCDF files *met_em.dxx.YYYY-MM-DD_HH:00:00.nc*, each containing the interpolated boundary conditions and geographic data for the xx domain and for every timestep of the supplied GRIB files. In the case considered, as the CFSR dataset is composed of hourly data, the produced *met_em* files are hourly spaced too.

The whole WPS process is controlled by a single external configuration file: *namelist.wps*, which contains the user specified parameters defining the time length and the domain of the simulation as well as the time and space resolutions.

An additional manipulation is needed before launching the actual solver: the NetCDF data produced by metgrid.exe must be vertically interpolated onto the user- defined vertical levels of the WRF simulation. This task is performed by the *real.exe* executable, which, despite actually being a pre-processing routine, is not included in the WPS system. The real.exe run finally produces the NetCDF files needed by the bare solver: *wrfinput_dxx* and *wrfbdy_dxx*, containing respectively, for each of the nested domains under simulation, the initial condition inclusive of the domain geographic data and the boundary conditions forcing the domain over time.

The last step of a WRF-ARW model simulation is the *wrf.exe* solver run which performs the numerical integration and produces the final output files *wrfout_dxx_YYYY-MM-DD_HH:MN:SS,* one for each simulated domain and for every temporal frame in the total simulated period. Each wrfout file contains therefore the complete atmospheric variables set calculated by the ARW solver for every point of the user defined simulation 3-D grid at a single temporal frame.

Both real.exe and wrf.exe are controlled by *namelist.input*, an external configuration file gathering the user defined parameters regarding the vertical resolution of the simulation, the atmosphere microphysical parameters and, again, the time / length scales and resolutions of the simulation.

A script that makes all steps involved automatic in a WRF-ARW simulation procedure, from the set-up of the configuration files to the archiving of output files, was developed and tested extensively.

The above depicted working scheme is summarized in Figure A.3:

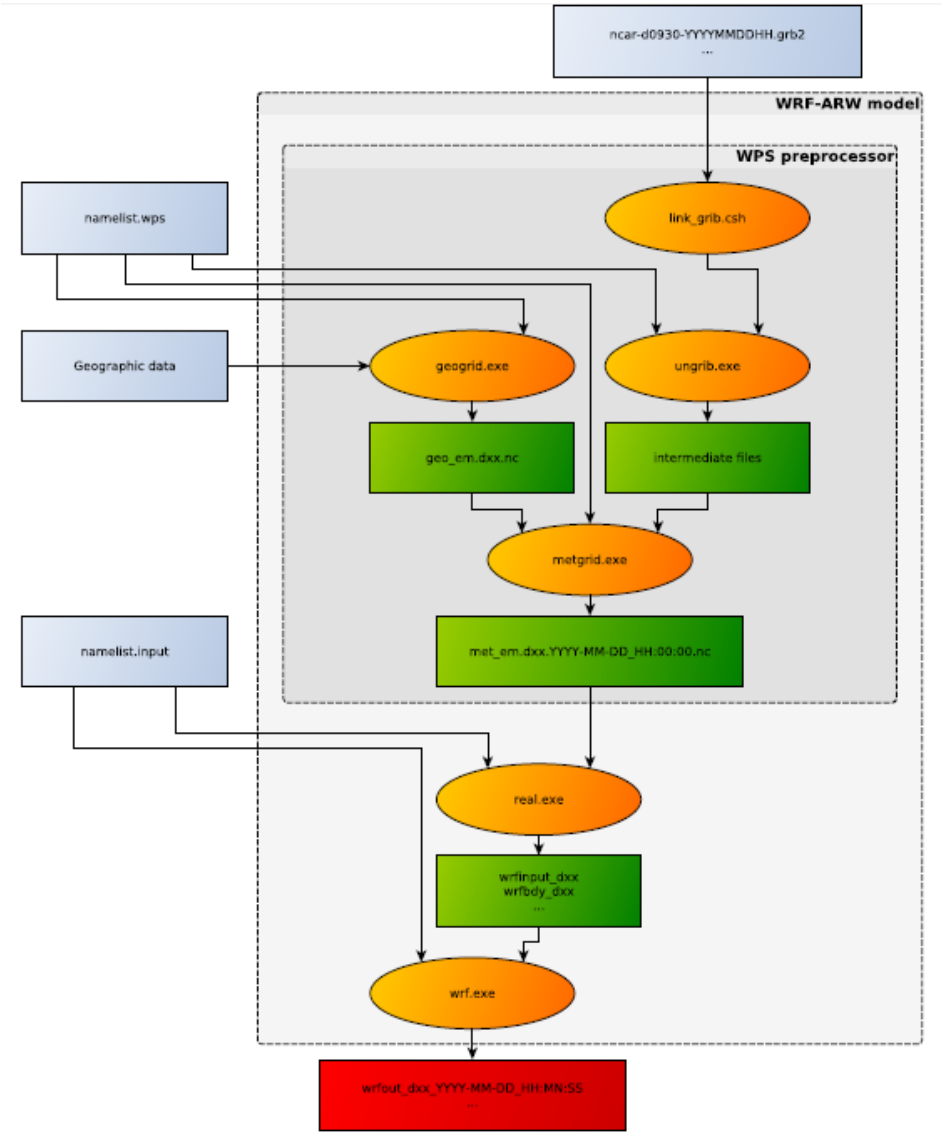


Figure A.3 Working scheme of the WRF-ARW model.

WRF-ARW domains, resolution, set-up in MWM

The preliminary set-up and tuning of the met-ocean models chain was performed simulating the month of November 1999, chosen for the remarkable number of very intense storms occurred over the Mediterranean Sea. The second step, before running the entire period 1979-2013, was done simulating one complete year, from November 1999 to October 2000, relying on 41 ground stations along the Mediterranean coast and 25 wave buoys for comparison. The results obtained in these steps are summarized in Contento et al. (2014), Contento et al. (2012-2014) and Donatini (2013).

The two-steps set-up started with the meteorological model *WRF-ARW*, adopting different configurations (domain size, resolution, run length, spin-up time) and comparing the wind speed and direction with observational data from ground stations. Since the *CFSR* (Saha et al, 2010) re-analysis dataset reproduces large scale events correctly, after several tests the final decision was to adopt three relatively small, overlapping domains, which cover respectively the Western, Eastern and Central Mediterranean Sea (Fig. A.4). Hereafter these domains will be referred as MEW, MEE and MEC respectively. The wind field obtained from the 3 domains was merged in a

single dataset by a bi-linear interpolation on a Lat-Lon grid and by a linear blending of the results inside the two overlapping zones (Fig. A.4).

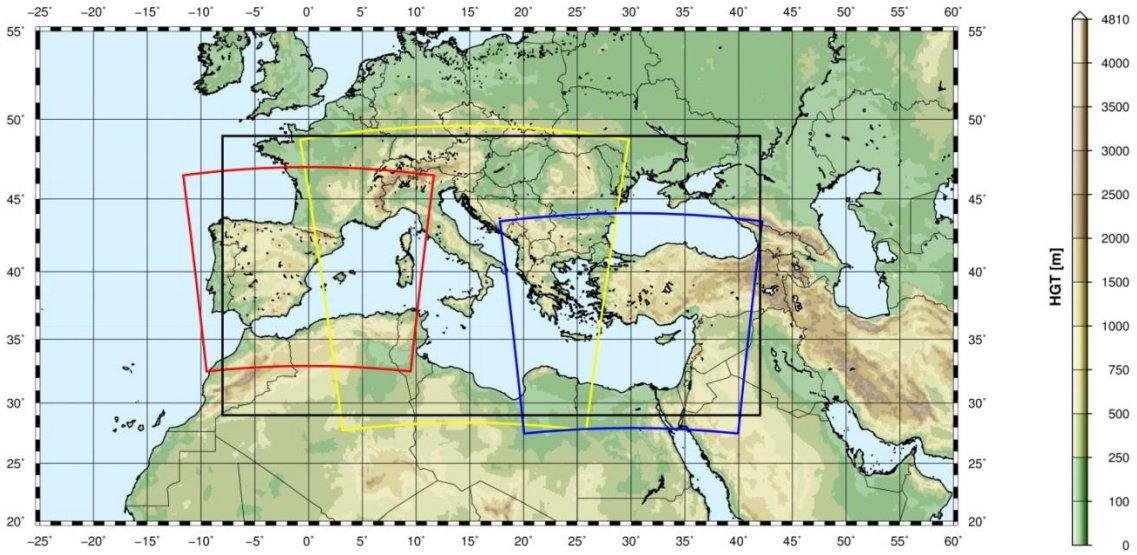


Figure A.4 WRF-ARW domains (red=domain MEW, yellow=domain MEC, blue=domain MEE) and interpolation/blending domain (black line).

The horizontal resolution of *WRF-ARW* was set to 10.53 km, with a grid ratio to the *CFSR* re-analysis data of 1:5 approximately. An additional domain (ITN) with a resolution of 3.51 km was run over Northern Italy as a nested domain of MEC.

The time length of the model run, in terms of hours simulated continuously between two consecutive model initializations with *CFSR* frames,proved to be among the most important parameters that influence the quality of the results. Keeping a small run length reduces the risk of model drift. On the other hand, shortening it excessively may lead to a too constrained behavior of the model, which prevents the correct development of the mesoscale weather structures. The problem of the model drift proved to be particularly tough over the Adriatic Sea where the orography is rather complex and the North-Eastern wind (Bora) can occasionally reach the speed of 150 km/h or more in very narrow zones.

A spin-up time window was used in order to let the model *WRF-ARW* ingest and process the coarser initial conditions from *CFSR*, thus letting it evolve and develop local weather structures. This spin-up window was overlapped with the tail of the previous run so that the data of the simulation during the spin-up window were discarded. The time length of this overlapping window is typically of few hours.

The Mediterranean Sea is a very complex basin from the meteorological point of view, with violent storms usually characterized by a short duration. The two examples given below show the importance of resolving the large space and time gradients of the variables.

Fig. A.5 shows a typical winter wind pattern (from the present simulations, 5 December 2009). The well-known 3 major narrow gates of the “Bora” wind over the Adriatic Sea are well captured by the model, i.e. Trieste (Italy), Rijeka and Sibenik (Croatia). The reference distance of these large variations is of 1° at most.

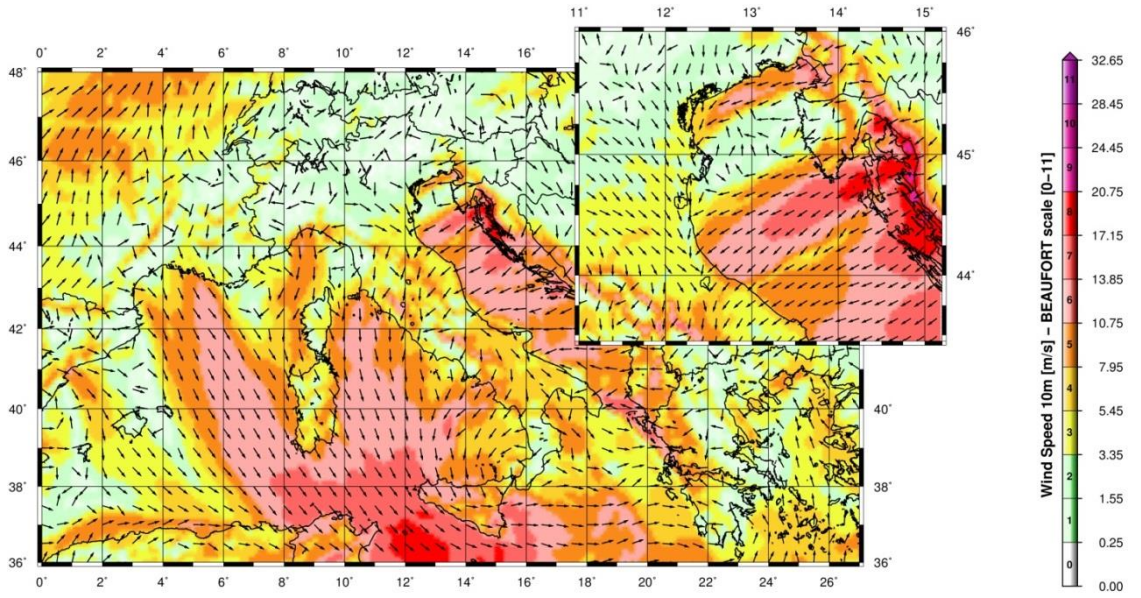


Figure A.5 A typical winter wind pattern over the Mediterranean Sea (from the present simulations, 5 December 2009). The well-known 3 major narrow gates of the "Bora" wind over the Adriatic Sea are well captured by the model, i.e. Trieste (Italy), Rijeka and Sibenik (Croatia). The upper-right figure shows a zoom over the Northern part of the Adriatic Sea (Istria peninsula).

Fig. A.6 (Contento et al., 2011) shows the time series of the wind speed during a squall event occurred on August 2008 in the Gulf of Trieste that caused the loss of two human lives and damages in the main harbor. The squall lasted about 10 min reaching more than 20 m/s from an almost calm situation. The red line corresponds to the results of the operational forecast meteorological model *WRF-ARW* run at that time by some of the authors of this work for ARPA FVG-OSMER, http://www.osmer.fvg.it/home.php. The black line corresponds to the measurement at the station PALOMA (45° 37' 06" N, 13° 33' 55" E) [*http://www.ts.ismar.cnr.it/node/84*]. The station is a fixed pole in the middle of the Gulf of Trieste. The measured wind speed is 5 min averaged with 5 min samples. The time step of the model is approximately 13 s. This situation is not uncommon in the Adriatic zone, mostly during the summer, with violent fronts from North and North-West then rotating to North-East.

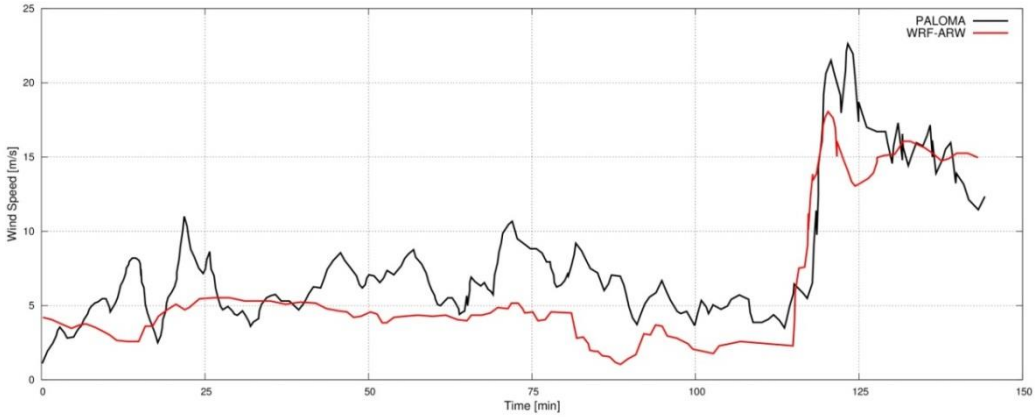


Figure A.6 Time series of the wind speed during a squall event occurred on August 2008 in the Gulf of Trieste. The squall lasts about 10 min reaching over 20 m/s from an almost calm situation. The red line corresponds to the results of the operational forecast meteorological model *WRF-ARW*. The black line corresponds to the measurement at the measurements station PALOMA (45° 37' 06" N, 13° 33' 55" E) [*http://www.ts.ismar.cnr.it/node/84*]. The measured wind speed is 5 min averaged with 5 min samples. The time step of the model is approximately 13 s.

MIKE 21 SW wave model

The wave modeling system includes the state of the art third generation spectral wind-wave model MIKE 21 SW, developed by DHI. MIKE 21 SW simulates the growth, decay and transformation of wind-generated waves and swell in offshore and coastal areas.

MIKE 21 SW includes two different formulations:

- Directional decoupled parametric formulation
- Fully spectral formulation

and includes the following physical phenomena:

- Wave growth by action of wind
- Non-linear wave-wave interaction
- Dissipation due to white-capping
- Dissipation due to bottom friction
- Dissipation due to depth-induced wave breaking
- Refraction and shoaling due to depth variations
- Wave-current interaction
- Effect of time-varying water depth

The discretization of the governing equation in geographical and spectral space is performed using cell-centered finite volume method. In the geographical domain, an unstructured mesh technique is used. The time integration is performed using a fractional step approach where a multisequence explicit method is applied for the propagation of wave action.

For the production of the MWM database, the fully spectral formulation has been adopted, based on the wave action conservation equation, as described in e.g. Komen et al. and Young where the directional-frequency wave action spectrum is the dependent variable.

The time integration of the governing equations is done by using a dynamically determined time step. The time step is determined in order to verify the stability criteria (CFL number).

The only driving force is represented by the two components of wind fields U10 and V10, (x and y component of wind at the elevation of 10m). The process by which the wind transfers energy into the water body for generating waves is controlled by a uncoupled air-sea interaction.

The spectral discretization adopted in the wave model has been deeply investigated and the final configuration is able to guarantee at the same time a high level of accuracy of the results and a reasonable computational effort.

The model domain covers the whole Mediterranean Sea but the spatial resolution is not the same everywhere: while in the offshore areas the spatial resolution is around 0.1°, when approaching the coast the spatial resolution increases up to around 0.03°.

The wave model is forced by the wind fields coming from the WRF Atmospheric models, illustrated above. The wave model generated results in terms of wave parameters (Significant Wave Height, Wave Periods, Wave Directions, etc.) over the whole domain and, in addition, spectral parameters in predefined output locations have been stored, too.

MIKE 21 SW domain, resolution, set-up in MWM

The model domain, covering the entire Mediterranean Sea, is illustrated in Figure A.7.

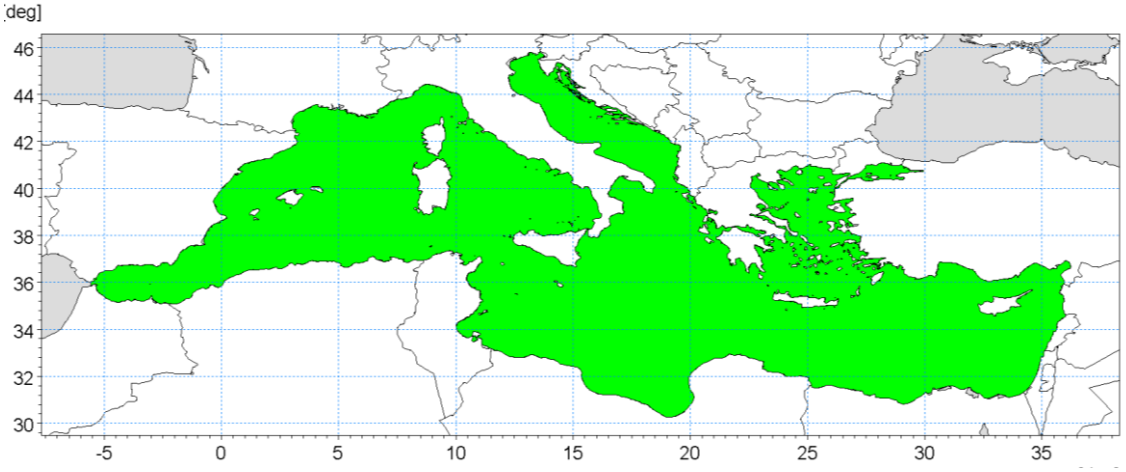


Figure A.7 Wave model domain filled in green

The unstructured mesh, generated over the entire domain by means of a specific tool included in MIKE 21 package, is characterized by different resolutions (in terms of mean length of triangle sides) over the domain. In particular the following criteria have been adopted:

- a coarser resolution of 0.1° (about 10 Km) is used for offshore areas;
- a finer resolution of 0.03° (about 3 Km) has been adopted in shallow water areas, where bathymetry is less than 100m depth or, in coastal areas characterized by very steep profiles, where the distance from the coastline is less than 5÷10 Km.

Figure A.8 illustrates the computational mesh of the Mediterranean wave model.

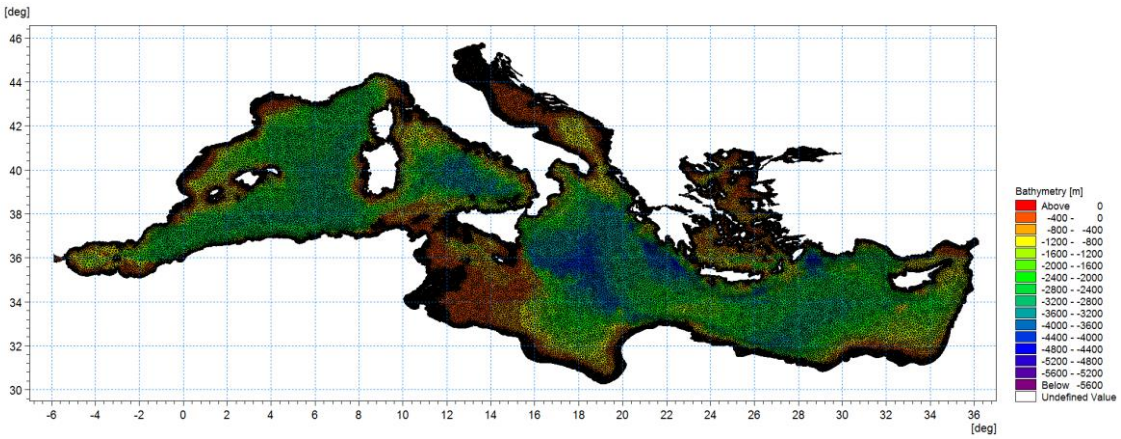


Figure A.8 - Mediterranean wave model computational mesh

Figure A.9 illustrates a detail of the above computational mesh, with special focus on the Adriatic Sea.

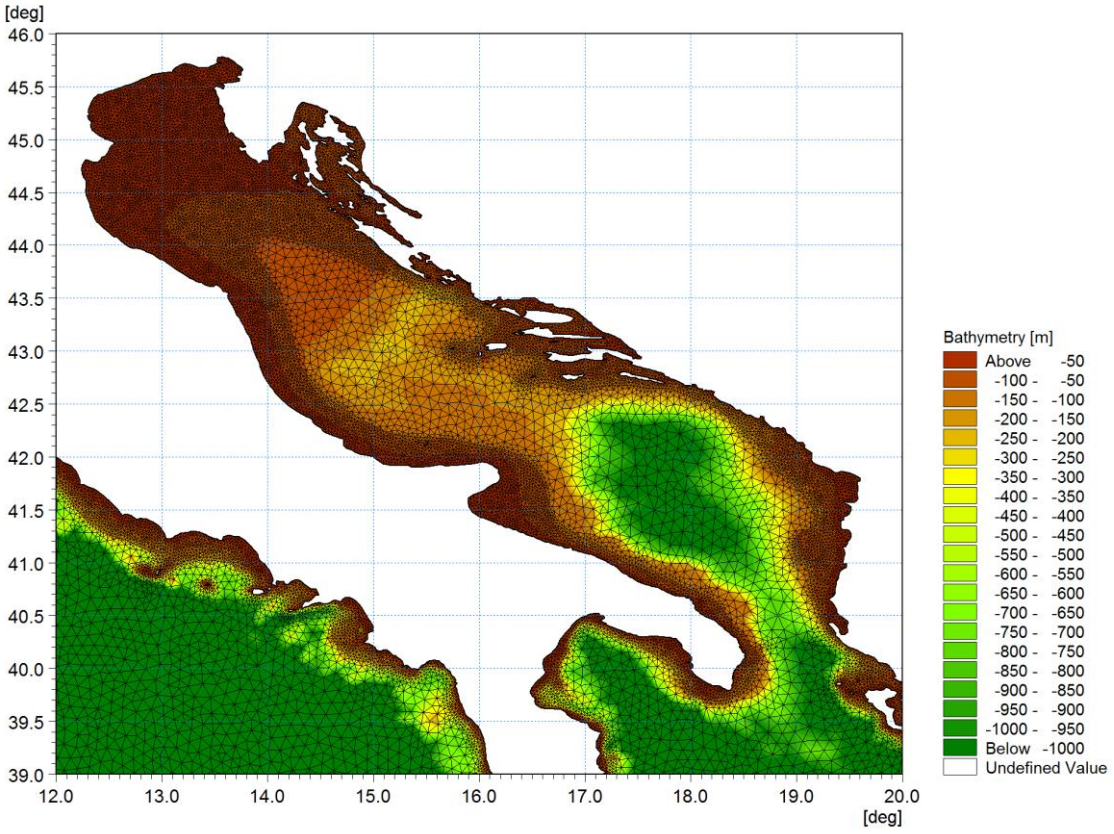


Figure A.9 - Detail of the mesh – Adriatic Sea

Scatter bathymetry data have been derived from GEBCO_08 database. The GEBCO_08 Grid is a 30 arc-second grid of global elevations and it is a continuous terrain model for ocean and land. The grid was generated by combining quality-controlled ship depth soundings with interpolation between sounding points guided by satellite-derived gravity data.

The gridded data are stored in a netCDF data file. Grids are stored as one dimensional arrays of 2-byte signed integer values. The complete data sets provide global coverage. Each data set consists of 21,600 rows x 43,200 columns, resulting in a total of 933,120,000 data points. The data start at the Northwest corner of the file, i.e. for the global file, position 89°59'45"N, 179°59'45"W, and are arranged in latitudinal bands of 360 degrees x 120 points/degree = 43,200 values. The data range eastward from 179°59'45"W to 179°59'45"E. Thus, the first band contains 43,200 values for 89°59'45"N, then followed by a band of 43,200 values at 89°59'15"N and so on at 30 arc-second latitude intervals down to 89°59'45"S. Data values are pixel centred registered, they refer to elevations at the centre of grid cells.

Figure A.10 illustrates GEBCO_08 scatter data for the entire area of the Mediterranean Sea.

GEBCO scatter data have not been used in the whole domain of the Mediterranean Sea. Following a detailed check of agreement and discrepancies between GEBCO database and nautical charts, it has been assumed to limit the use of GEBCO database for offshore areas (up to 500 m water depth) and to use nautical charts for shallower water areas (mainly coastal areas).

The nautical charts database which has been used is the CM93/3 database from CMAP.

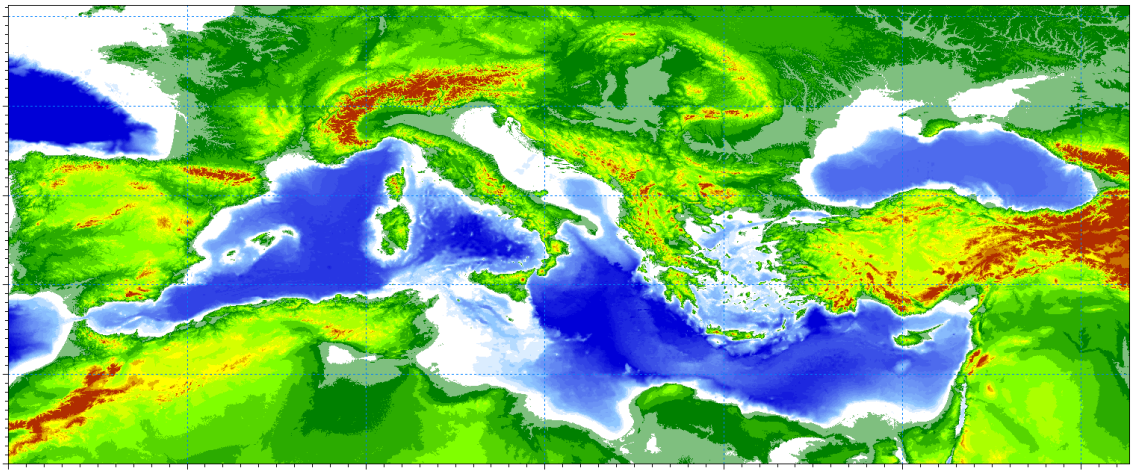


Figure A.10 - Scatter bathymetry data derived from GEBCO_08 database

The number of discrete frequencies and directions form the so called “spectral resolution”, which is a key parameter for wave models in general. The number of discrete frequencies and directions should in fact be high enough to properly represent the “real shape” of the wave spectrum and, on the other hand, it can’t be too high, since it would lead to unacceptable computational times and memory consumption.

In terms of frequency range, the minimum frequency f_{min} (which corresponds to the maximum wave period T_{max}, according to the common relation $= \frac{1}{T}$) should be able to capture the longest wave periods that can occur in the Mediterranean Sea.

The analysis of ordinary and extreme waves in the Mediterranean Sea (from available data of wave buoys) has highlighted that almost all the wave energy associated to waves in the Mediterranean Sea are associated to wave periods between 1.5 seconds and 20 seconds.

In addition, a logarithmic distribution for the discrete frequencies acts better than a simple linear distribution, since most of the wave periods are concentrated below 8-10 seconds. A number of frequencies around 30 is widely considered as adequate for a proper discretization of wave energy spectra in the Mediterranean Sea. The following formulation has therefore been adopted:

$$f_{n=}0.04 \cdot \ 1.1^{n},$$

where n goes from 0 to 29 (30 frequencies in total). The discrete frequencies range from 0.04 Hz to 0.63 Hz (from 1.6s to 25.0s of Mean Wave Period T_m).

Also the choice of the number of discrete directions (directional discretization) is the result of detailed investigations and tests. In particular, a high number of wave model tests, each one characterized by a different spectral resolution (directional), i.e. by a different number of discrete directions have been setup and run.

Few examples of the results of the above model tests are illustrated from Figure A.11 to Figure A.13 in terms of short time series of wave heights extracted at 3 different locations where also measurements were available (La Spezia wave buoy, Ponza wave buoy, Cetraro wave buoy).

In all the below test cases, it appears that the two time series of wave height characterized by 24 and 36 discrete directions are almost coincident. Higher discrepancies can be found for a much limited number of discrete directions (12). After a high number of tests, the 24 directions solution has been assumed as a very good compromise between accuracy of results and computational time (the computational time of the wave model is linearly dependent on the number of discrete directions).

Provided that wave directions can vary within the 360° rose, the directional resolution of the wave model is 360°/24 = 15°

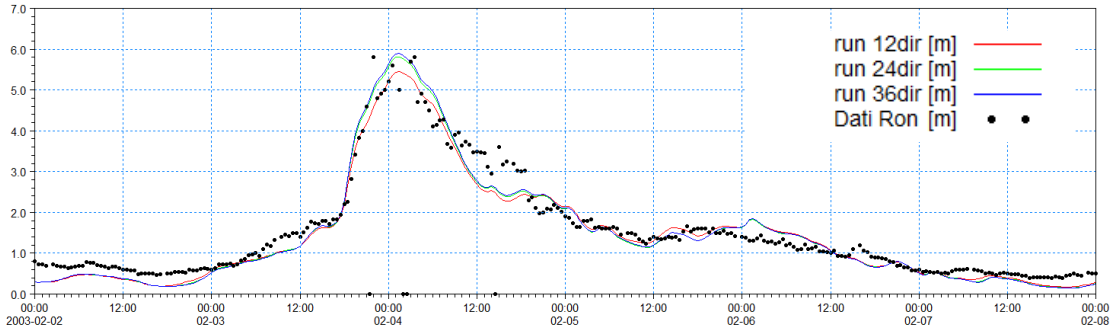


Figure A.11 - Time series of wave height at La Spezia buoy location for 3 different numbers of discrete directions

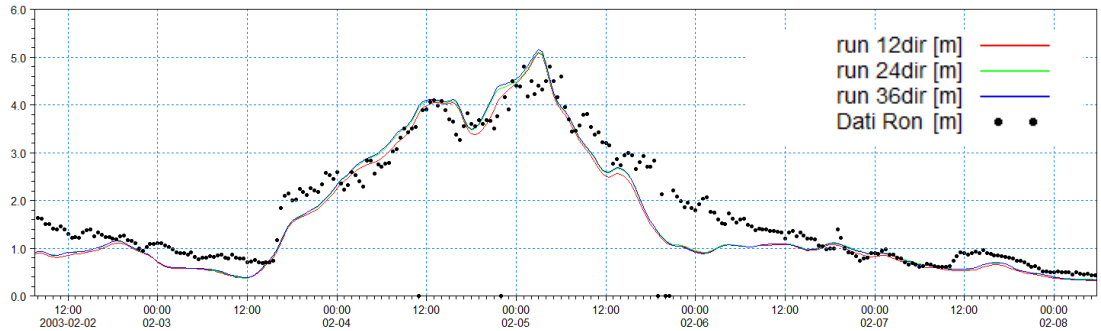


Figure A.12 - Time series of wave height at Ponza buoy location for 3 different numbers of discrete directions

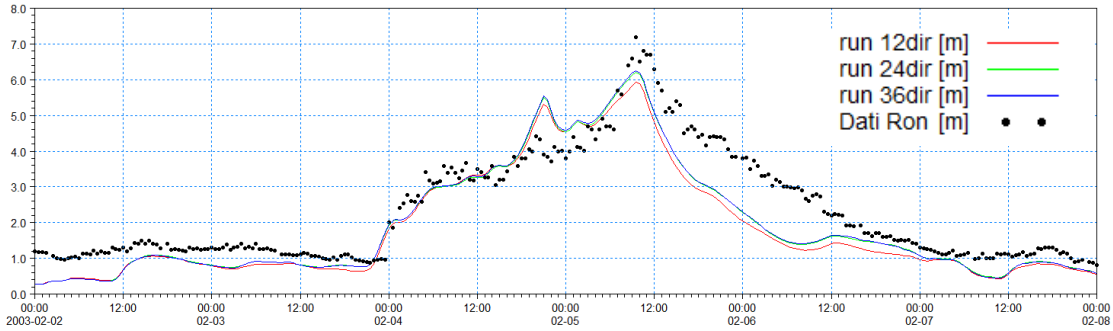


Figure A.13 - Time series of wave height at Cetraro buoy location for 3 different numbers of discrete directions

Available products of the MWM database

The results of the wind and wave model are stored, in the whole domain, in terms of wind parameters and wave parameters averaged over the wave period ("phase averaged results"). In particular, the following hourly time series are available:

- Wind speed, WS [m/s]
- Wind direction, WD [deg]
- Significant Wave height, Hs [m]
- Mean wave period, Tm [s]
- Peak wave period, Tp [s]
- Zero crossing period, Tz [s]
- Mean wave direction, MWD [deg]
- Peak wave direction, PWD [deg]
- Directional standard deviation, DSD [deg]

In addition, hourly spectral results (in terms of wave energy associated to the frequency-direction bins) are saved on a regular grid with an equidistant spatial resolution of 0.1°.

Figure A.14 and Figure A-15 illustrate respectively an example of phase averaged results over a portion of Mediterranean Sea (Hs) and an local example of spectral results.

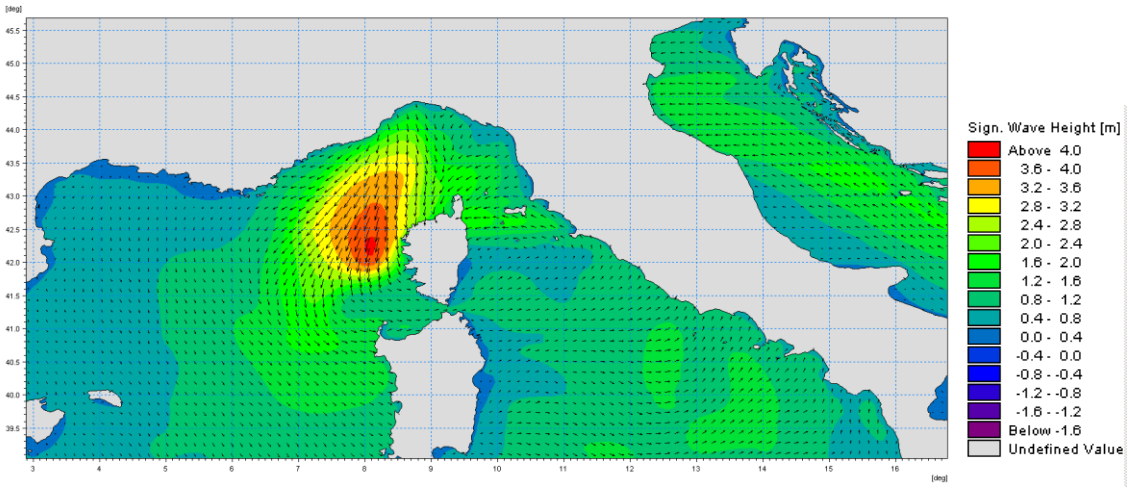


Figure A.14 Phase averaged results: Field of significant wave height and direction

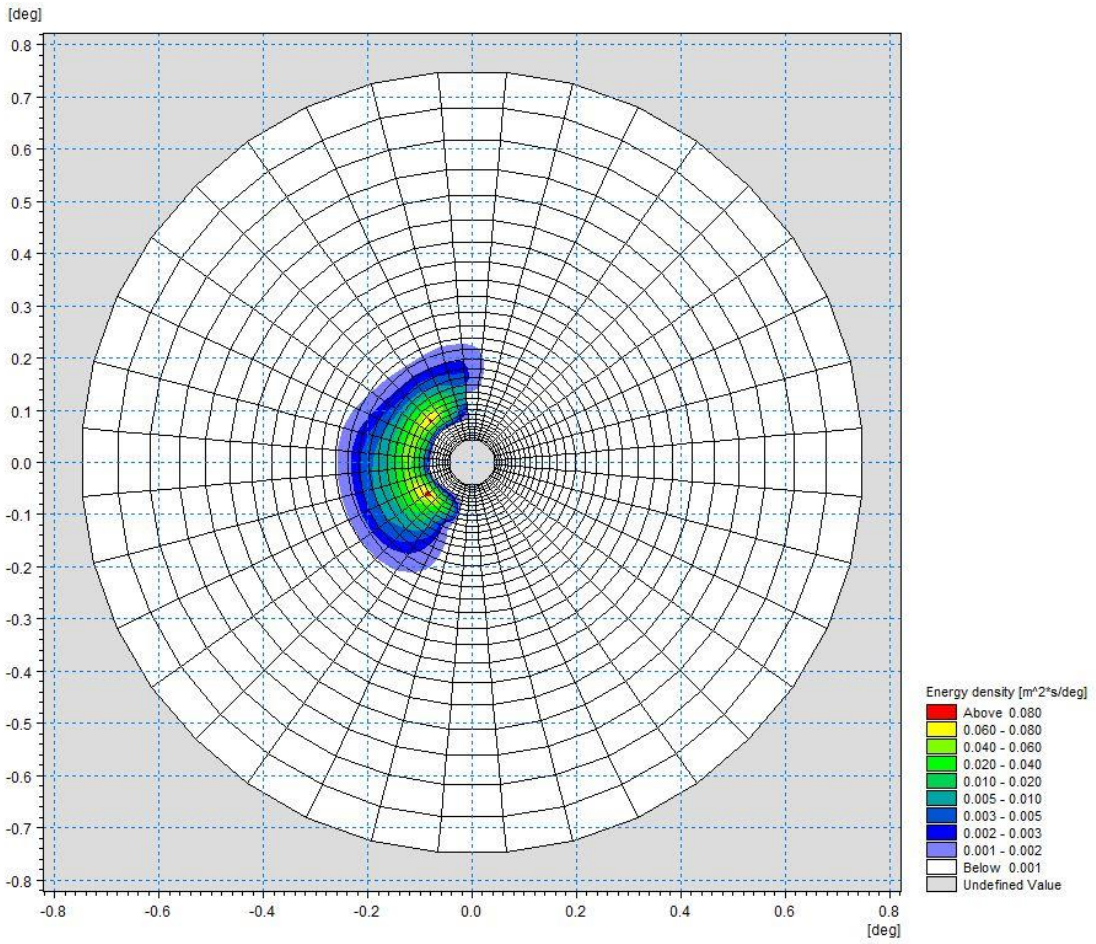


Figure A.15 Polar plot of spectral results. Wave energy density (coloured contours) as a function of directions (angular coordinate) and frequencies (radial coordinate)

References

Ardhuin, F., Bertotti, L., Bidlot, J.R., Cavaleri, L., Filipetto, V., Lefevre, J.M,, Wittmann, P., 2007, Comparison of wind and wave measurements and models in the Western Mediterranean Sea. *Ocean Engineering*, Vol. 34, pp. 526-541.

Athanassoulis, G., Stefanakos, Ch., Cavaleri, L., Ramieri, E., NoEL, C., Lefevre, J.M., Gaillard, P., 2004, RTP 10.10 / WW_MEDATLAS Scientific Report.

Battjes, J.A., Janssen, J.P.F.M., 1978, Energy loss and set-up due to breaking of random waves, Proceedings, 16th Int. Conf. Coastal Eng., ASCE, pp.569-587.

Bolaños-Sanchez, R., Sanchez-Arcilla, A., Cateura, J., 2007, Evaluation of two atmospheric models for wind-.wave modeling in the NW Mediterranean. *Journal of Marine Systems* 65:336-353.

Cavaleri, L., Bertotti, L., 2004, Accuracy of the modelled wind and wave fields in enclosed seas. Tellus, Vol. 56, pp. 167-175.

Cavaleri, L., 2005, The wind and wave atlas of the Mediterranean Sea – the calibration phase. *Advances in Geosciences*, Vol. 2, pp. 255-257.

Cavaleri, L., Sclavo., M., 2006, The calibration of wind and wave model data in the Mediterranean Sea. Coastal Engineering, Vol.53, pp. 613-627.

Chawla, A., Spindler, D.M., Tolman, H.L., 2013, Validation of a thirty year wave hindcast using the Climate Forecast System Reanalysis winds, Ocean Modelling, Vol. 70, pp. 189-206.

Contento, G., Lupieri, G., Venturi, M. Ciuffardi, T., 2011, A medium-resolution wave hindcast study over the Central and Western Mediterranean Sea, *Journal of Marine Science and Technology*, Vol. 16(2), pp. 181–201.

Contento, G., Lupieri, G., Donatini, L, Feudale, L, Pedroncini, A., Cusati, L.A., 2014, A state-of-the-art met-ocean model chain for wind&wave hindcast over the Mediterranean and Black Seas: implementation, tuning and validation against field data, accepted for presentation at the 21th Symposium Theory and Practice of Shipbuilding SORTA 2014, Oct. 2-4, 2014, Baška, Island of Krk, Croatia.

Contento, G., Lupieri, G., Donatini, L, 2012-2014, Project SEAPOL - Sistema modellistico ad Elevata risoluzione per l'Analisi storica e la Previsione del moto Ondoso nel mar Ligure, Department of Engineering and Architecture, University of Trieste, Technical Reports codes SEAPOL_UT_1.1.0 to SEAPOL_UT_5.1.0.

Donatini, L., 2013, Implementation of a state-of-art met-ocean model chain for hindcast wave simulations over the Mediterranean Sea and comparison of results with field data, Master Degree Thesis, Department of Engineering and Architecture, University of Trieste, Italy.

Donatini, L., Lupieri, G., Contento, G., 2014, A medium resolution wind&wave hindcast study for the Mediterranean Sea, Journal Paper, under review.

Hasselmann, K., Barnett, T.P., Bouws, E., Carlson, H., Cartwright, D.E., Enke, K., Ewing, J.A., Gienapp, H., Hasselmann, D.E., Krusemann, P., Meerburg, A., Mueller, P., Olbers, D.J., Richter, K., Sell, W., Walden, H., 1973, Measurements of wind-wave growth and swell decay during the Joint North Sea Wave Project (JONSWAP). Ergaenzungsheft zur Deutschen Hydrographischen Zeitschrift, Reihe, A(8), 12, 95 pp.

Hasselmann, S., Hasselmann, K., Allender, J.H., Barnett, T.P., 1985. Computations and parametrizations of the nonlinear energy transfer in a gravity-wave spectrum, Part II: Parametrizations of the nonlinear energy transfer for applications in wave models. J. Phys. Oceanogr. Vol. 15, pp. 1378–1391.

ISPRA (formerly APAT), 2004, Agenzia per la Protezione dell'Ambiente e per i servizi Tecnici, Dipartimento Tutela Acque Marine ed Interne, Servizio difesa delle coste, Analisi preliminare dei dati marini lungo le coste italiane – Atlante delle coste – Il moto ondoso al largo delle coste italiane, Technical Report (in Italian). http://www.apat.gov.it/site/_files/Atlante_coste/Introduzione.pdf.

Janssen, P.A.E.M., Abdalla, S., Hersbach, H., Bidlot, J.R., 2007: Error Estimation of Buoy, Satellite, and Model Wave Height Data. *J. Atmos. Oceanic Technol.*, Vol. **24**, pp. 1665–1677. doi: http://dx.doi.org/10.1175/JTECH2069.1

Michalakes, J., Chen, S., Dudhia, J., Hart, L., Klemp, J., Middlecoff, J., Skamarock, W., 2001, Development of a Next Generation Regional Weather Research and Forecast Model. *Developments in Teracomputing. In Proceedings of the 9th ECMWF Workshop on the Use of High Performance Computing in Meteorology.* Eds. Walter Zwieflhofer and Norbert Kreitz. World Scientific, 269-276.

Michalakes, J., Dudhia, J., Gill, D., Henderson, T., Klemp, J., Skamarock, W., Wang, W., 2005, The Weather Research and Forecast Model: Software Architecture and Performance. In *Proceedings of the 11th ECMWF Workshop on the Use of High Performance Computing in Meteorology.* Eds. Walter Zwieflhofer and George Mozdzynski. World Scientific, 56 - 168.

Ponce del León, S., Guedes Soares, C., 2008, Sensitivity of wave model predictions to wind fields in the Western Mediterranean Sea. *Coastal Engineering*, Vol. 55, pp. 920-929.

Puertos del Estado, Spain, 2009, – (http://www.puertos.es/oceanografia_y_meteorologia/), private communication.

Queffeulou, P., 2004, Long term validation of wave height measurements from altimeters. Marine Geodesy, Vol. 27, 495-510.

Queffeulou, P., Croizé-Fillon, D., 2010, Global altimeter SWH data set, version 7, Technical Report, Ifremer, ftp://ftp.ifremer.fr/cersat/products/swath/altimeters/waves/documentation/altimeter_wave_merge__7.0.pdf

Queffeulou, P., 2009, Altimeter Wave Height Measurements - Validation of Long Time Series.Poster: Ocean Surface Topography Science Team meeting, Seattle, Washington,USA.(http://www.aviso.oceanobs.com/en/courses/oststt/oststt-2009-seattle/posters/).

Saha, S., Moorthi, S., Pan, H., Wu, X., Wang, J., Nadiga, S., Tripp, P., Kistler, R., Wollen, J., Behringer, D., Liu, H., Stokes, D., Grumbine, R., Gayno, G., Wang, J., Hou, Y., Chuang, H., Juang, H., Sela, J., Iredell, M., Treadon, R., Kleist, D., VanDelst, P., Keyser, D., Derber, J., Ek, M., Meng, J., Wei, H., Yang, R., Lord, S., van den Dool, H., Kumar, A., Wang, W., Long, C., Chelliah, M., Xue, Y., Huang, B., Schemm, J., Ebisuzaki, W., Lin, R., Xie, P., Chen, M., Zhou, S., Higgins, W., Zou, C., Liu, Q., Chen,Y., Han, Y., Cucurull, L., Reynolds, R., Rutledge, G., Goldberg, M., 2010, The NCEP Climate Forecast System Reanalysis. *Bull. Amer. Meteor. Soc.*, Vol. 91, 1015–1057.

Skamarock WC, Klemp JB, 2007, A time-split nonhydrostatic atmospheric model for research and NWP applications. *J. Comp. Phys.* Special issue on environmental modeling.

Sorensen, O.R., Kofoed-Hansen, H., Rugbjerg, M. and Sorensen, L.S., 2004: A Third Generation Spectral Wave Model Using an Unstructured Finite Volume Technique. In Proceedings of the 29th International Conference of Coastal Engineering, 19-24 September 2004, Lisbon, Portugal.

Tolman, H.L., 2002a. Alleviating the garden sprinkler effect in wind wave models. Ocean Modelling, Vol. 4, pp. 269–289.

Tolman, H.L., 2002f, Validation of WAVEWATCH III, version 1.15 for a global domain. Tech. Note 213, NOAA/NWS/NCEP/OMB, 33p.

Tolman, H.L., 2008, http://cioss.coas.oregonstate.edu/CIOSS/workshops/Altimeter_workshop_08/Coastal_Alt_Presentations/18_Tolman_Sig_Wave_Ht.pdf

Sorensen, O.R., Kofoed-Hansen, H., Rugbjerg, M. and Sorensen, L.S., 2004: A Third Generation Spectral Wave Model Using an Unstructured Finite Volume Technique. In Proceedings of the 29th International Conference of Coastal Engineering, 19-24 September 2004, Lisbon, Portugal.

Komen,G.J., Cavaleri,L., Doneland,M., Hasselmann,K., Hasselmann,S. and Janssen,P.A.E.M., (1984). Dynamics and modelling of ocean waves. Cambridge University Press, UK, 560 pp.

Young,I.R., (1999). Wind generated ocean waves, in Elsevier Ocean Engineering Book Series, Volume 2, Eds. R. Bhattacharyya and M.E. McCormick, Elsevier.

WAMDI-group: S. Hasselmann, K. Hasselman, E. Bauer, P.A.E.M. Janssen, G.J. Komen, L. Bertotti, P. Lionello, A. Guillaume, V.C. Cardone, J.A. Greenwood, M. Reistad, L. Zambresky and J.A. Ewing, (1988) “The WAM model – a third generation ocean wave prediction model”, J. Phys. Oceanogr., 18, 1775-1810

General Bathymetric Chart of the Oceans (GEBCO) – www.gebco.net

CM-93 Edition 3.0, CM-93/3 - www.jeppesen.com/marine/commercial/professional/

Ole Baltazar Andersen (1995), Global ocean tides from ERS 1 and TOPEX/POSEIDON altimetry, J. of Geophys. Res., 100, C12, p. 25249-25260

Doodson, A. T., Warburg, H. D., 1941 “Admiralty manual of tides”

Web references

ARPA-FVG OSMER, [Online] http://www.osmer.fvg.it/home.php

ARW Online Tutorial.” [Online] Available at http://www.mmm.ucar.edu/wrf/OnLineTutorial/index.htm

CISL RDA: NCEP Climate Forecast System Re-analysis (CFSR) 6-hourly Products, January 1979 to December 2010.” [Online] Available at http://rda.ucar.edu/datasets/ds093.0/index.html#description

NOAA, Hourly/Sub-Hourly Observational Data.” [Online] Available at http://gis.ncdc.noaa.gov/map/viewer/#app=cdo&cfg=cdo&theme=hourly&layers=1&node=gis

The Weather Research&Forecasting Model Website.” [Online] Available at http://www.wrf-model.org/index.php

ALLEGATO B

MIKE 21 Spectral Waves (SW)



MIKE 21 Wave Modelling

MIKE 21 Spectral Waves FM

Short Description



DHI headquarters
Agern Allé 5
DK-2970 Hørsholm
Denmark

+45 4516 9200 Telephone
+45 4516 9333 Support
+45 4516 9292 Telefax

mike@dhigroup.com
www.mikepoweredbydhi.com

MIKE21_SW_FM_Short_Description.docx / HKH/AJS / 2017-10-03

© DHI

MIKE 21 SW - SPECTRAL WAVE MODEL FM

MIKE 21 SW is a state-of-the-art third generation spectral wind-wave model developed by DHI. The model simulates the growth, decay and transformation of wind-generated waves and swells in offshore and coastal areas.

MIKE 21 SW includes two different formulations:

- Fully spectral formulation
- Directional decoupled parametric formulation

The fully spectral formulation is based on the wave action conservation equation, as described in e.g. Komen et al (1994) and Young (1999). The directional decoupled parametric formulation is based on a parameterisation of the wave action conservation equation. The parameterisation is made in the frequency domain by introducing the zeroth and first moment of the wave action spectrum. The basic conservation equations are formulated in either Cartesian co-ordinates for small-scale applications and polar spherical co-ordinates for large-scale applications.

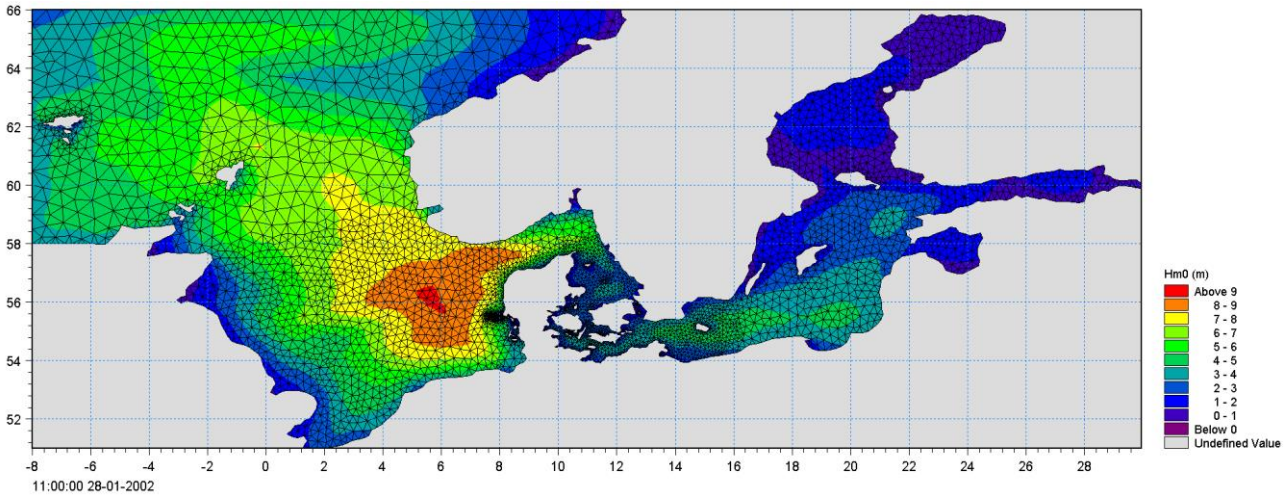
The fully spectral model includes the following physical phenomena:

- Wave growth by action of wind
- Non-linear wave-wave interaction
- Dissipation due to white-capping
- Dissipation due to bottom friction
- Dissipation due to depth-induced wave breaking
- Refraction and shoaling due to depth variations
- Wave-current interaction
- Effect of time-varying water depth
- Effect of ice coverage on the wave field

The discretisation of the governing equation in geographical and spectral space is performed using cell-centred finite volume method. In the geographical domain, an unstructured mesh technique is used. The time integration is performed using a fractional step approach where a multi-sequence explicit method is applied for the propagation of wave action.



MIKE 21 SW is a state-of-the-art numerical modelling tool for prediction and analysis of wave climates in offshore and coastal areas. © BIOFOTO/Klaus K. Bentzen



A MIKE 21 SW forecast application in the North Sea and Baltic Sea. The chart shows a wave field (from the NSBS model) illustrated by the significant wave height in top of the computational mesh. See also www.waterforecast.com

Computational Features

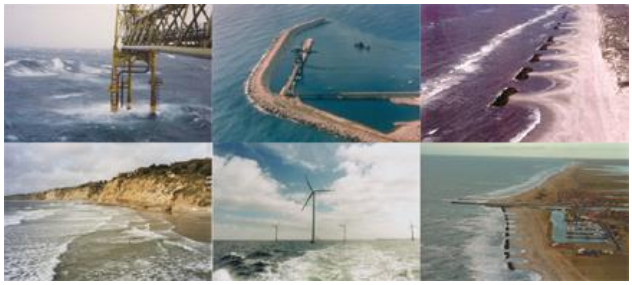
The main computational features of MIKE 21 SW - Spectral Wave Model FM are as follows:

- Fully spectral and directionally decoupled parametric formulations
- Source functions based on state-of-the-art 3rd generation formulations
- Instationary and quasi-stationary solutions
- Optimal degree of flexibility in describing bathymetry and ambient flow conditions using depth-adaptive and boundary-fitted unstructured mesh
- Coupling with hydrodynamic flow model for modelling of wave-current interaction and time-varying water depth
- Flooding and drying in connection with time-varying water depths
- Cell-centred finite volume technique
- Fractional step time-integration with an multi-sequence explicit method for the propagation
- Extensive range of model output parameters (wave, swell, air-sea interaction parameters, radiation stress tensor, spectra, etc.)

Application Areas

MIKE 21 SW is used for the assessment of wave climates in offshore and coastal areas - in hindcast and forecast mode.

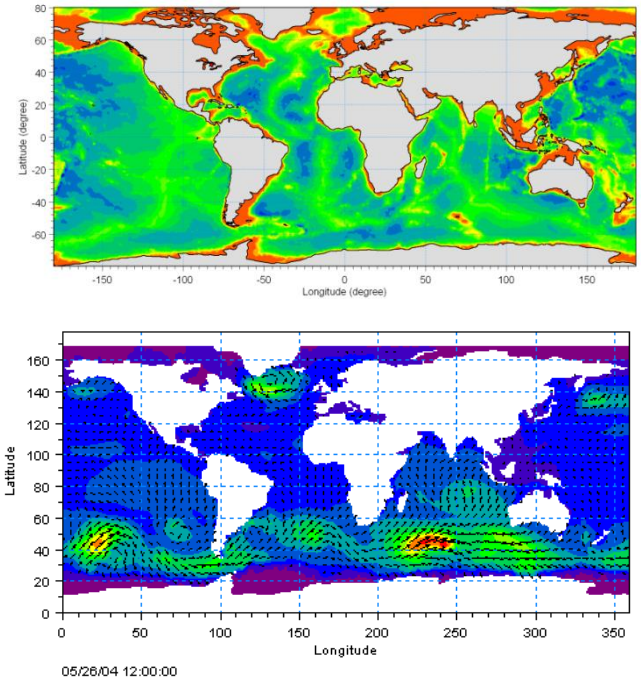
A major application area is the design of offshore, coastal and port structures where accurate assessment of wave loads is of utmost importance to the safe and economic design of these structures.



Illustrations of typical application areas of DHI's MIKE 21 SW – Spectral Wave Model FM

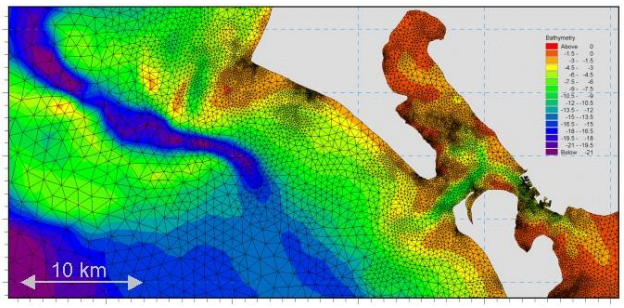
Measured data are often not available during periods long enough to allow for the establishment of sufficiently accurate estimates of extreme sea states.

In this case, the measured data can then be supplemented with hindcast data through the simulation of wave conditions during historical storms using MIKE 21 SW.



Example of a global application of MIKE 21 SW. The upper panel shows the bathymetry. Results from such a model (cf. lower panel) can be used as boundary conditions for regional scale forecast or hindcast models. See http://www.waterforecast.com for more details on regional and global modelling

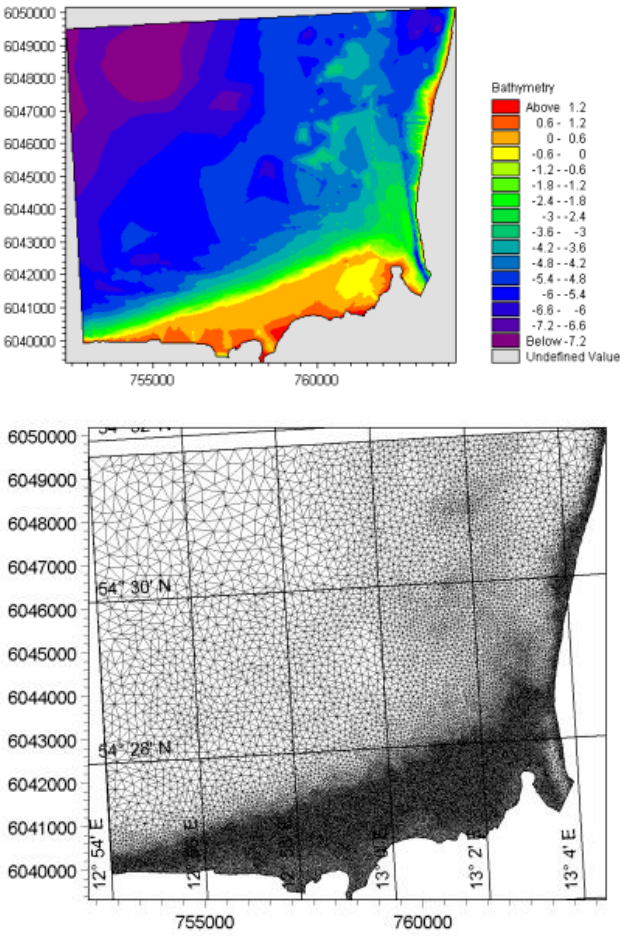
MIKE 21 SW is particularly applicable for simultaneous wave prediction and analysis on regional scale and local scale. Coarse spatial and temporal resolution is used for the regional part of the mesh and a high-resolution boundary and depth-adaptive mesh is describing the shallow water environment at the coastline.



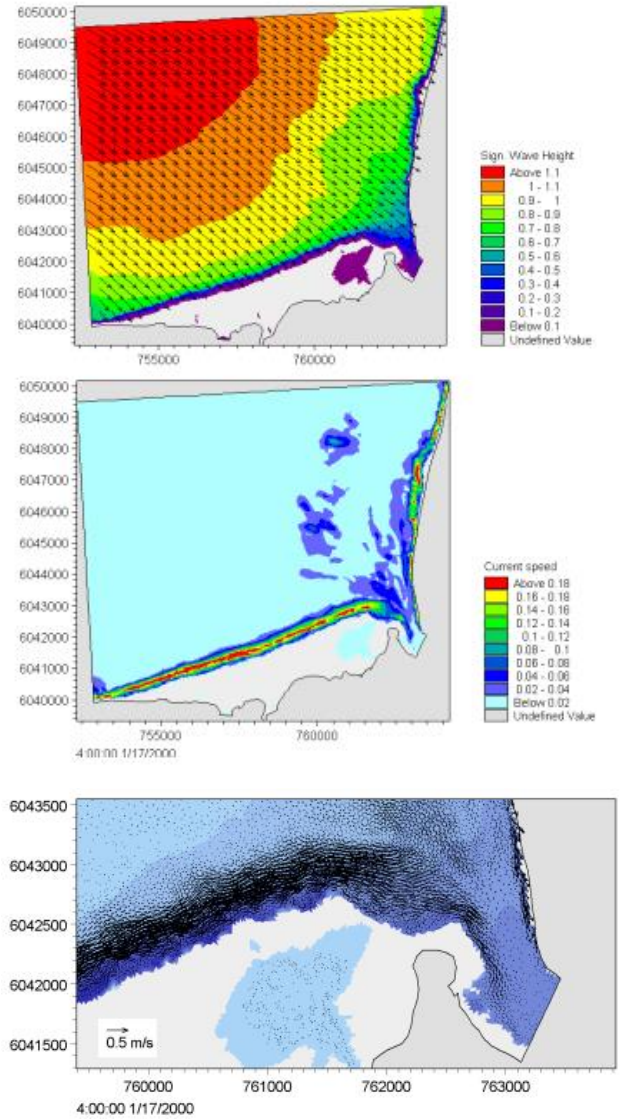
Example of a computational mesh used for transformation of offshore wave statistics using the directionally decoupled parametric formulation

MIKE 21 SW is also used for the calculation of the sediment transport, which for a large part is determined by wave conditions and associated wave-induced currents. The wave-induced current is generated by the gradients in radiation stresses that occur in the surf zone.

MIKE 21 SW can be used to calculate the wave conditions and associated radiation stresses. The long-shore currents and sediment transport are then calculated using the flow and sediment transport models available in the MIKE 21 package. For such type of applications, the directional decoupled parametric formulation of MIKE 21 SW is an excellent compromise between the computational effort and accuracy.



Bathymetry (upper) and computational mesh (lower) used in a MIKE 21 SW application on wave induced currents in Gellen Bay, Germany



Map of significant wave height (upper), current field (middle) and vector field (lower). The flow field is simulated by DHI's MIKE 21 Flow Model FM, which is dynamically coupled to MIKE 21 SW

Model Equations

In MIKE 21 SW, the wind waves are represented by the wave action density spectrum $N(\sigma,\theta)$. The independent phase parameters have been chosen as the relative (intrinsic) angular frequency, $\sigma = 2\pi f$ and the direction of wave propagation, θ. The relation between the relative angular frequency and the absolute angular frequency, ω, is given by the linear dispersion relationship

$$\sigma = \sqrt{gk\tanh(kd)} = \omega - \bar{k}\cdot\bar{U}$$

where *g* is the acceleration of gravity, *d* is the water depth and $\bar{U}$ is the current velocity vector and $\bar{k}$ is the wave number vector with magnitude *k* and direction θ. The action density, $N(\sigma,\theta)$, is related to the energy density $E(\sigma,\theta)$ by

$$N = \frac{E}{\sigma}$$

Fully Spectral Formulation

The governing equation in MIKE 21 SW is the wave action balance equation formulated in either Cartesian or spherical co-ordinates. In horizontal Cartesian co-ordinates, the conservation equation for wave action reads

$$\frac{\partial N}{\partial t} + \nabla\cdot(\bar{v}N) = \frac{S}{\sigma}$$

where $N(\bar{x},\sigma,\theta,t)$ is the action density, *t* is the time, $\bar{x} = (x,y)$ is the Cartesian co-ordinates, $\bar{v} = (c_x, c_y, c_\sigma, c_\theta)$ is the propagation velocity of a wave group in the four-dimensional phase space $\bar{x}$, σ and θ. *S* is the source term for energy balance equation. ∇ is the four-dimensional differential operator in the $\bar{x}$, σ, θ-space. The characteristic propagation speeds are given by the linear kinematic relationships

$$(c_x, c_y) = \frac{d\bar{x}}{dt} = \bar{c}_g + \bar{U} = \frac{1}{2}\left(1 + \frac{2kd}{\sinh(2kd)}\right)\frac{\sigma}{k} + \bar{U}$$

$$c_\sigma = \frac{d\sigma}{dt} = \frac{\partial\sigma}{\partial d}\left[\frac{\partial d}{\partial t} + \bar{U}\cdot\nabla_{\bar{x}} d\right] - c_g\bar{k}\cdot\frac{\partial\bar{U}}{\partial s}$$

$$c_\theta = \frac{d\theta}{dt} = -\frac{1}{k}\left[\frac{\partial\sigma}{\partial d}\frac{\partial d}{\partial m} + \bar{k}\cdot\frac{\partial\bar{U}}{\partial m}\right]$$

Here, *s* is the space co-ordinate in wave direction θ and *m* is a co-ordinate perpendicular to *s*. $\nabla_{\bar{x}}$ is the two-dimensional differential operator in the $\bar{x}$-space.

Source Functions

The source function term, *S*, on the right hand side of the wave action conservation equation is given by

$$S = S_{in} + S_{nl} + S_{ds} + S_{bot} + S_{surf}$$

Here S_{in} represents the momentum transfer of wind energy to wave generation, S_{nl} the energy transfer due non-linear wave-wave interaction, S_{ds} the dissipation of wave energy due to white-capping (deep water wave breaking), S_{bot} the dissipation due to bottom friction and S_{surf} the dissipation of wave energy due to depth-induced breaking.

The default source functions S_{in}, S_{nl} and S_{ds} in MIKE 21 SW are similar to the source functions implemented in the WAM Cycle 4 model, see Komen et al (1994).

The wind input is based on Janssen's (1989, 1991) quasi-linear theory of wind-wave generation, where the momentum transfer from the wind to the sea not only depends on the wind stress, but also the sea state itself. The non-linear energy transfer (through the resonant four-wave interaction) is approximated by the DIA approach, Hasselmann et al (1985). The source function describing the dissipation due to white-capping is based on the theory of Hasselmann (1974) and Janssen (1989). The bottom friction dissipation is modelled using the approach by Johnson and Kofoed-Hansen (2000), which depends on the wave and sediment properties. The source function describing the bottom-induced wave breaking is based on the well-proven approach of Battjes and Janssen (1978) and Eldeberky and Battjes (1996).

A detailed description of the various source functions is available in Komen et al (1994) and Sørensen et al (2003), which also includes the references listed above.

Directional Decoupled Parametric Formulation

The directionally decoupled parametric formulation is based on a parameterisation of the wave action conservation equation. Following Holthuijsen et al (1989), the parameterisation is made in the frequency domain by introducing the zeroth and first moment of the wave action spectrum as dependent variables.

A similar formulation is used in the MIKE 21 NSW Near-shore Spectral Wind-Wave Model, which is one of the most popular models for wave transformation in coastal and shallow water environment. However, with MIKE 21 SW it is not necessary to set up a number of different orientated bathymetries to cover varying wind and wave directions.

The parameterisation leads to the following coupled equations

$$\frac{\partial(m_0)}{\partial t}+\frac{\partial(c_x m_0)}{\partial x}+\frac{\partial(c_y m_0)}{\partial y}+\frac{\partial(c_\theta m_0)}{\partial \theta}=T_0$$

$$\frac{\partial(m_1)}{\partial t}+\frac{\partial(c_x m_1)}{\partial x}+\frac{\partial(c_y m_1)}{\partial y}+\frac{\partial(c_\theta m_1)}{\partial \theta}=T_1$$

where $m_0(x, y, \theta)$ and $m_1(x, y, \theta)$ are the zeroth and first moment of the action spectrum $N(x, y, \sigma, \theta)$, respectively. $T_0(x, y, \theta)$ and $T_1(x, y, \theta)$ are source functions based on the action spectrum. The moments $m_n(x, y, \theta)$ are defined as

$$m_n(x,y,\theta)=\int_0^\infty \omega^n N(x,y,\omega,\theta)d\omega$$

The source functions T_0 and T_1 take into account the effect of local wind generation (stationary solution mode only) and energy dissipation due to bottom friction and wave breaking. The effects of wave-current interaction are also included. The source functions for the local wind generation are derived from empirical growth relations, see Johnson (1998) for details.

Numerical Methods

The frequency spectrum (fully spectral model only) is split into a prognostic part for frequencies lower than a cut-off frequency σ_{max} and an analytical diagnostic tail for the high-frequency part of the spectrum

$$E(\sigma,\theta)=E(\sigma_{\max},\theta)\left(\frac{\sigma}{\sigma_{\max}}\right)^{-m}$$

where m is a constant (= 5) as proposed by Komen et al (1994).





The directional decoupled parametric formulation in MIKE 21 SW is used extensively for calculation of the wave transformation from deep-water to the shoreline and for wind-wave generation in local areas

Space Discretisation

The discretisation in geographical and spectral space is performed using cell-centred finite volume method. In the geographical domain an unstructured mesh is used. The spatial domain is discretised by subdivision of the continuum into non-overlapping elements. Triangle and quadrilateral shaped polygons are presently supported in MIKE 21 SW. The action density, $N(\sigma,\theta)$ is represented as a piecewise constant over the elements and stored at the geometric centres.

In frequency space either an equidistant or a log-arithmic discretisation is used. In the directional space, an equidistant discretisation is used for both types of models. The action density is represented as piecewise constant over the discrete intervals, $\Delta\sigma$ and $\Delta\theta$, in the frequency and directional space.

Integrating the wave action conservation over an area A_i, the frequency interval $\Delta\sigma_l$ and the directional interval $\Delta\theta_m$ gives

$$\frac{\partial}{\partial t}\int_{\Delta\theta_m}\int_{\Delta\sigma_l}\int_{A_i} N d\Omega d\sigma d\theta - \int_{\Delta\theta_m}\int_{\Delta\sigma_l}\int_{A_i}\frac{S}{\sigma} d\Omega d\sigma d\theta$$
$$= \int_{\Delta\theta_m}\int_{\Delta\sigma_l}\int_{A_i} \nabla\cdot(\bar{v}N) d\Omega d\sigma d\theta$$

where Ω is the integration variable defined on A_i. Using the divergence theorem and introducing the convective flux $\bar{F} = \bar{v}N$, we obtain

$$\frac{\partial N_{i,l,m}}{\partial t} = -\frac{1}{A_i}\left[\sum_{p=1}^{NE}(F_n)_{p,l,m}\Delta l_p\right]$$
$$-\frac{1}{\Delta\sigma_l}\left[(F_\sigma)_{i,l+1/2,m} - (F_\sigma)_{i,l-1/2,m}\right]$$
$$-\frac{1}{\Delta\theta_m}\left[(F_\theta)_{i,l,m+1/2} - (F_\theta)_{i,l,m-1/2}\right] + \frac{S_{i,l,m}}{\sigma_l}$$

where NE is the total number of edges in the cell, $(F_n)_{p,l,m} = (F_x n_x + F_y n_y)_{p,l,m}$ is the normal flux trough the edge p in geographical space with length Δl_p. $(F_\sigma)_{i,l+1/2,m}$ and $(F_\theta)_{i,l,m+1/2}$ is the flux through the face in the frequency and directional space, respectively.

The convective flux is derived using a first-order upwinding scheme. In that

$$F_n = c_n\left(\frac{1}{2}(N_i + N_j) - \frac{1}{2}\frac{c}{|c|}(N_i - N_j)\right)$$

where c_n is the propagation speed normal to the element cell face.

Time Integration

The integration in time is based on a fractional step approach. Firstly, a propagation step is performed calculating an approximate solution N^* at the new time level (n+1) by solving the homogenous wave action conservation equation, i.e. without the source terms. Secondly, a source terms step is performed calculating the new solution N^{n+1} from the estimated solution taking into account only the effect of the source terms.

The propagation step is carried out by an explicit Euler scheme

$$N^*_{i,l,m} = N^n_{i,l,m} + \Delta t\left(\frac{\partial N_{i,l,m}}{\partial t}\right)^n$$

To overcome the severe stability restriction, a multi-sequence integration scheme is employed. The maximum allowed time step is increased by employing a sequence of integration steps locally, where the number of steps may vary from point to point.

A source term step is performed using an implicit method (see Komen et al, 1994)

$$N^{n+1}_{i,l,m} = N^*_{i,l,m} + \Delta t\left[\frac{(1-\alpha)S^*_{i,l,m} + \alpha S^{n+1}_{i,l,m}}{\sigma_l}\right]$$

where α is a weighting coefficient that determines the type of finite difference method. Using a Taylor series to approximate S^{n+1} and assuming the off-diagonal terms in $\partial S/\partial E = \gamma$ are negligible, this equation can be simplified as

$$N^{n+1}_{i,l,m} = N^n_{i,l,m} + \frac{(S^*_{i,l,m}/\sigma_l)\Delta t}{(1-\alpha\gamma\Delta t)}$$

For growing waves ($\gamma > 0$) an explicit forward difference is used ($\alpha = 0$), while for decaying waves ($\gamma < 0$) an implicit backward difference ($\alpha = 1$) is applied.



MIKE 21 SW is also applied for wave forecasts in ship route planning and improved service for conventional and fast ferry operators

Model Input

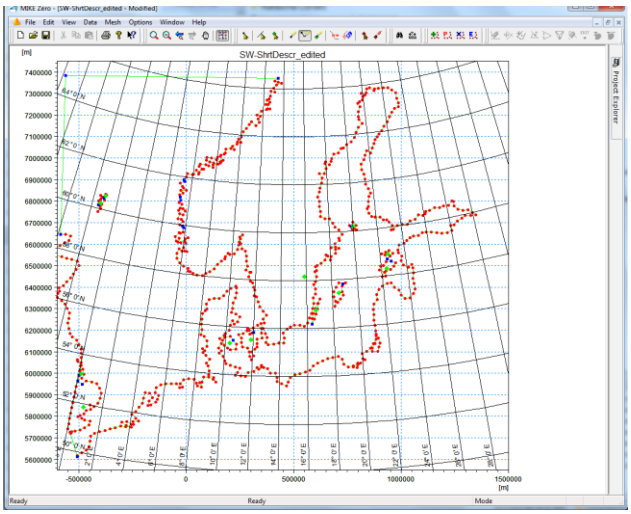
The necessary input data can be divided into following groups:

- Domain and time parameters:
  - computational mesh
  - co-ordinate type (Cartesian or spherical)
  - simulation length and overall time step
- Equations, discretisation and solution technique
  - formulation type
  - frequency and directional discretisation
  - number of time step groups
  - number of source time steps
- Forcing parameters
  - water level data
  - current data
  - wind data
  - ice data
- Source function parameters
  - non-linear energy transfer
  - wave breaking (shallow water)
  - bottom friction
  - white capping
- Structures
  - location and geometry
  - approach
  - structures coefficients
- Initial conditions
  - zero-spectrum (cold-start)
  - empirical data
  - data file
- Boundary conditions
  - closed boundaries
  - open boundaries (data format and type)

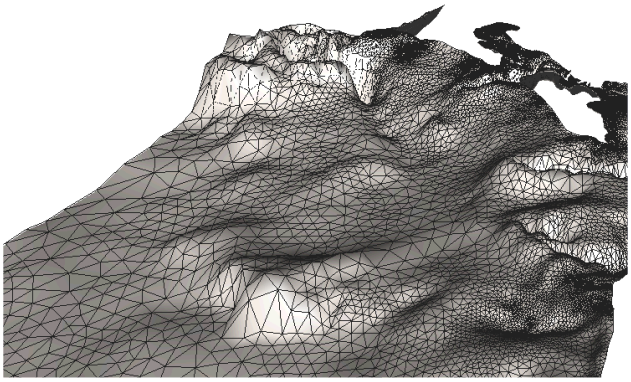
Providing MIKE 21 SW with a suitable mesh is essential for obtaining reliable results from the model. Setting up the mesh includes the appropriate selection of the area to be modelled, adequate resolution of the bathymetry, flow, wind and wave fields under consideration and definition of codes for essential and land boundaries.

Furthermore, the resolution in the geographical space must also be selected with respect to stability considerations.

As the wind is the main driving force in MIKE 21 SW, accurate hindcast or forecast wind fields are of utmost importance for the wave prediction.

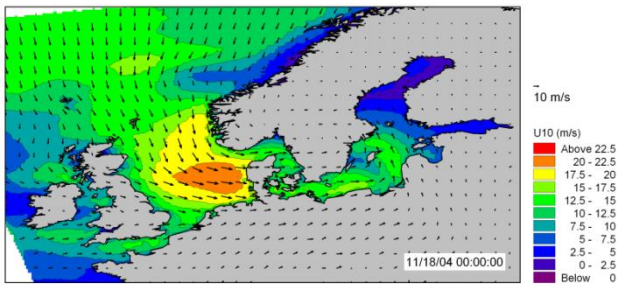


The Mesh Generator is an efficient MIKE Zero tool for the generation and handling of unstructured meshes, including the definition and editing of boundaries



3D visualisation of a computational mesh

If wind data is not available from an atmospheric meteorological model, the wind fields (e.g. cyclones) can be determined by using the wind-generating programs available in MIKE 21 Toolbox.

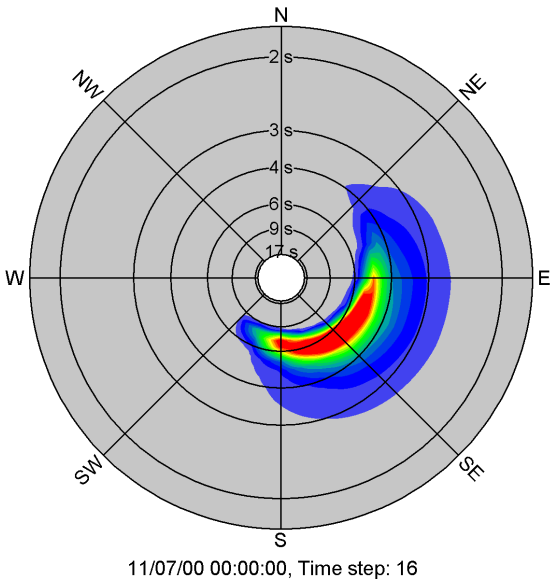


The chart shows an example of a wind field covering the North Sea and Baltic Sea as wind speed and wind direction. This is used as input to MIKE 21 SW in forecast and hindcast mode

Model Output

At each mesh point and for each time step four types of output can be obtained from MIKE 21 SW:

- Integral wave parameters divided into wind sea and swell such as
  - significant wave height, H_{m0}
  - peak wave period, T_p
  - averaged wave period, T_{01}
  - zero-crossing wave period, T_{02}
  - wave energy period, T_{-10}
  - peak wave direction, θ_p
  - mean wave direction, θ_m
  - directional standard deviation, σ
  - wave height with dir., $H_{m0} \cos\theta_m$, $H_{m0} \sin\theta_m$
  - radiation stress tensor, S_{xx}, S_{xy} and S_{yy}
  - particle velocities, *horizontal/vertical*
  - wave power, P, P_x *and* P_y



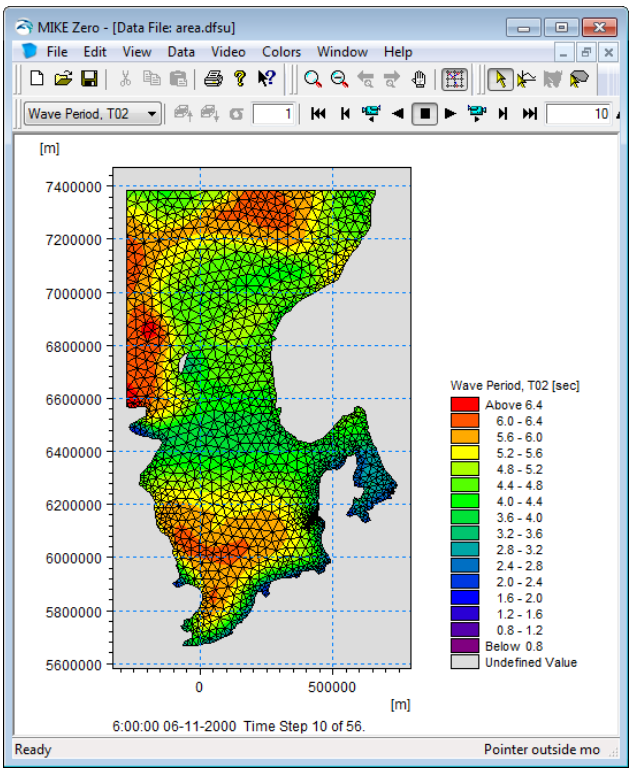
Example of model output (directional-frequency wave spectrum) processed using the Polar Plot control in the MIKE Zero Plot Composer

The distinction between wind-sea and swell can be calculated using either a constant threshold frequency or a dynamic threshold frequency with an upper frequency limit.

- Input parameters
  - water level, *WL*
  - water depth, *h*
  - current velocity, $\overline{U}$
  - wind speed, U_{10}
  - wind direction, θ_w
  - Ice concentration
- Model parameters
  - bottom friction coefficient, C_f
  - breaking parameter, γ
  - Courant number, *Cr*
  - time step factor, α
  - characteristic edge length, Δl
  - area of element, *a*
  - wind friction speed, u_*
  - roughness length, z_0
  - drag coefficient, C_D
  - Charnock parameter, z_{ch}
- Directional-frequency wave spectra at selected grid points and or areas as well as direction spectra and frequency spectra

Output from MIKE 21 SW is typically post-processed using the Data Viewer available in the common MIKE Zero shell. The Data Viewer is a tool for analysis and visualisation of unstructured data, e.g. to view meshes, spectra, bathymetries, results files of different format with graphical extraction of time series and line series from plan view and import of graphical overlays.

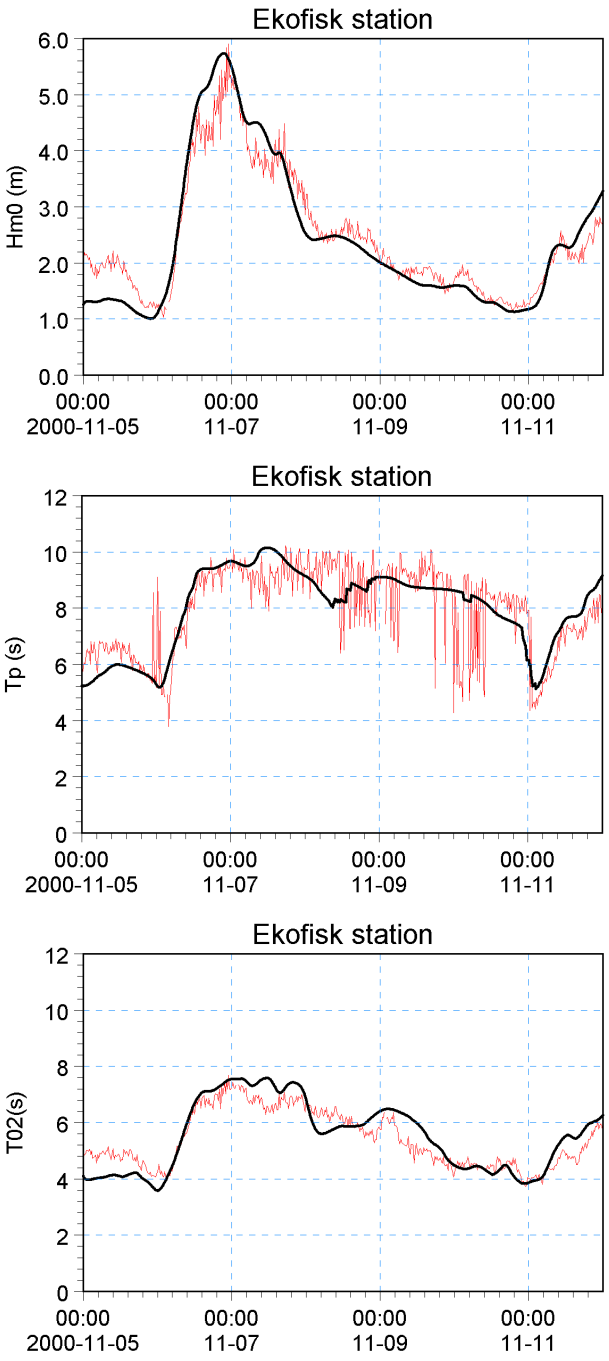
Various other editors and plot controls in the MIKE Zero Composer (e.g. Time Series Plot, Polar Plot, etc.) can be used for analysis and visualisation.



The Data Viewer in MIKE Zero – an efficient tool for analysis and visualisation of unstructured data including processing of animations

Validation

The model has successfully been applied to a number of rather basic idealised situations for which the results can be compared with analytical solutions or information from the literature. The basic tests covered fundamental processes such as wave propagation, depth-induced and current-induced shoaling and refraction, wind-wave generation and dissipation.

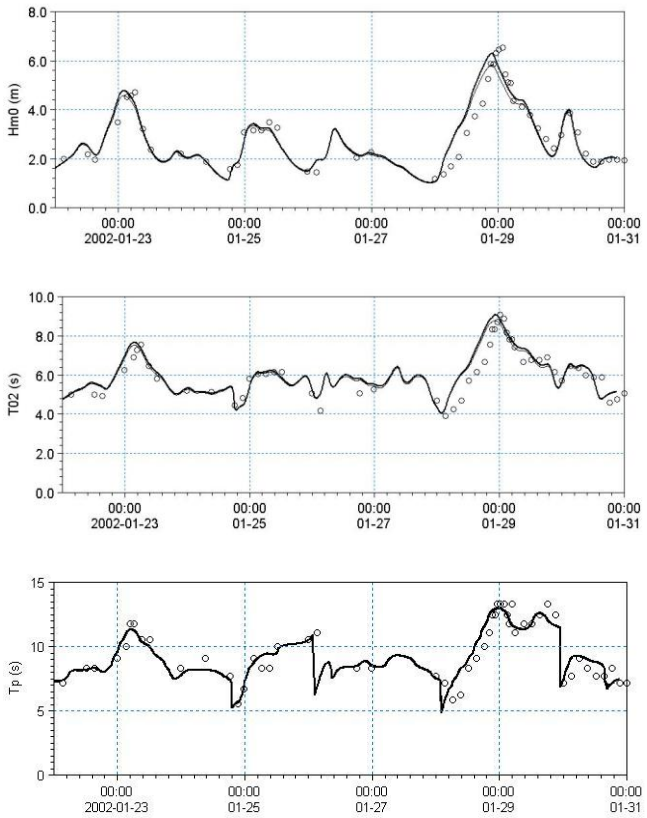


Comparison between measured and simulated significant wave height, peak wave period and mean wave period at the Ekofisk offshore platform (water depth 70 m) in the North Sea). (——) calculations and (——) measurements



A major application area of MIKE 21 SW is in connection with design and maintenance of offshore structures

The model has also been tested in natural geophysical conditions (e.g. in the North Sea, the Danish West Coast and the Baltic Sea), which are more realistic and complicated than the academic test and laboratory tests mentioned above.

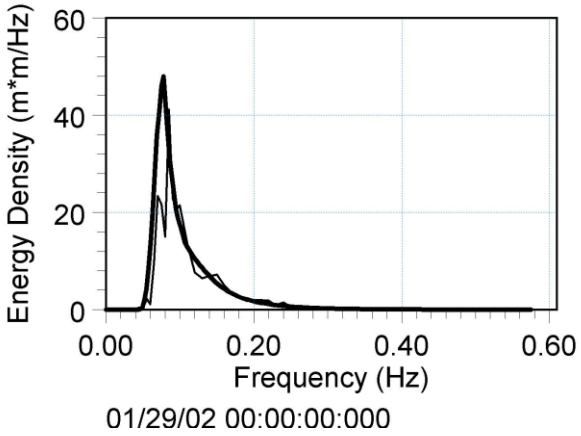


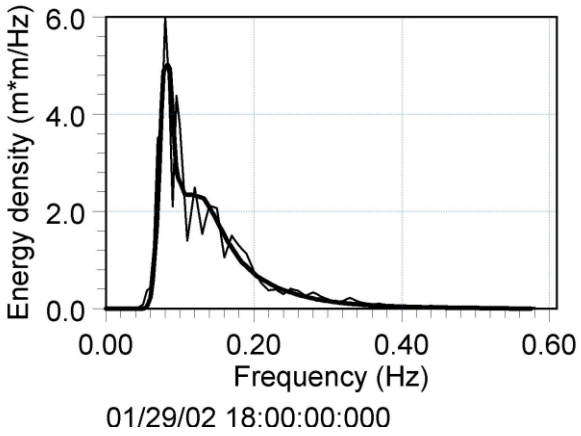
Comparison between measured and simulated significant wave height, peak wave period and mean wave period at Fjaltring located at the Danish west coast (water depth 17.5 m).(——) calculations and (o) measurements



The Fjaltring directional wave rider buoy is located offshore relative to the depicted arrow

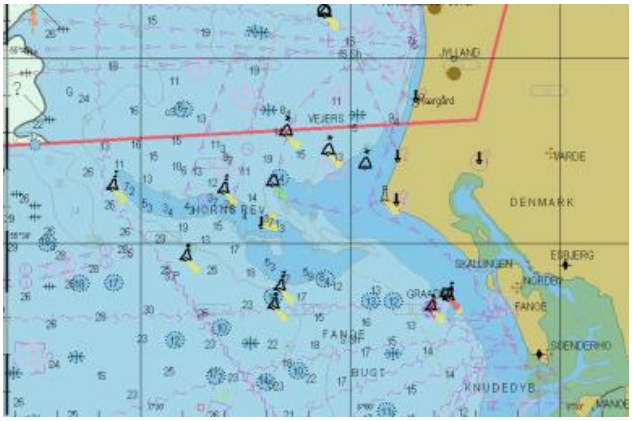
MIKE 21 SW is used for prediction of the wave conditions at the complex Horns Rev (reef) in the southeastern part of the North Sea. At this site, a 168 MW offshore wind farm with 80 turbines has been established in water depths between 6.5 and 13.5 m.

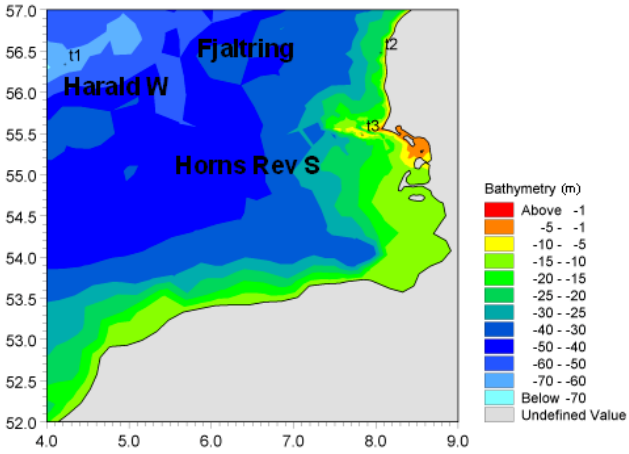


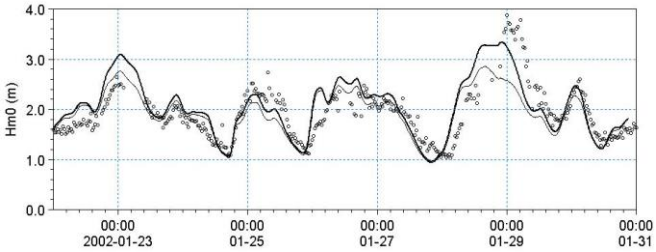


Comparison of frequency spectra at Fjaltring. (——) calculations and (——)measurements



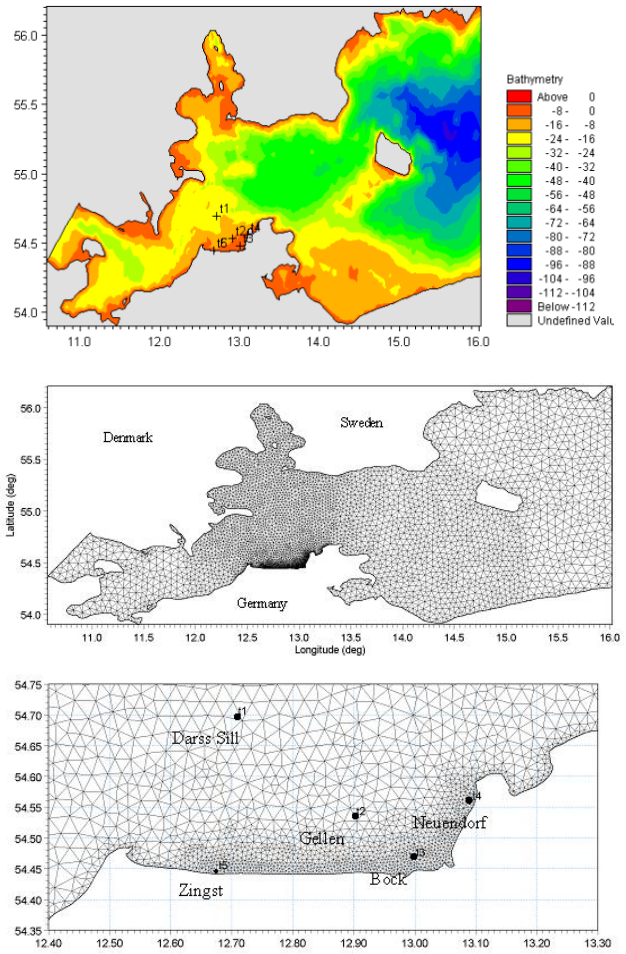




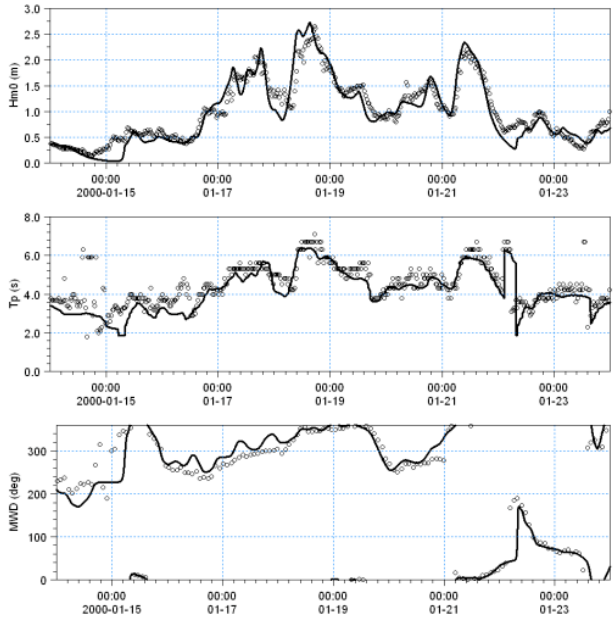


The upper panels show the Horns Rev offshore wind farm and MIKE C-map chart. 'The middle panel shows a close-up of the mesh near the Horns Rev S wave rider buoy (t3, 10 m water depth. The lower panel shows a comparison between measured and simulated significant wave height at Horns Rev S, (——) calculations including tide and surge and (—-) calculations excluding including tide and surge, (o) measurements

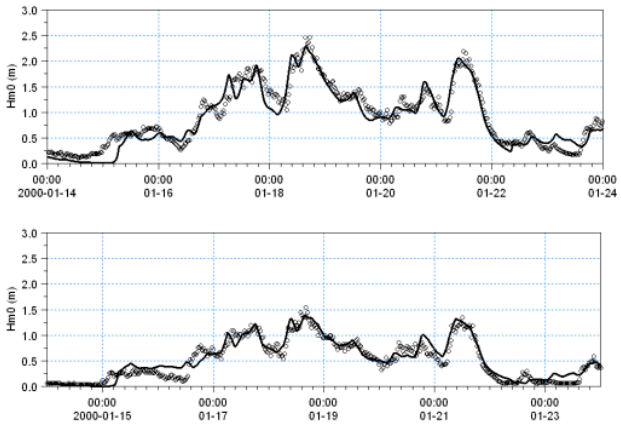
The predicted nearshore wave climate along the island of Hiddensee and the coastline of Zingst located in the micro-tidal Gellen Bay, Germany have been compared to field measurements (Sørensen et al, 2004) provided by the MORWIN project. From the illustrations it can be seen that the wave conditions are well reproduced both offshore and in more shallow water near the shore. The RMS values (on significant wave height) are less than 0.25m at all five stations.



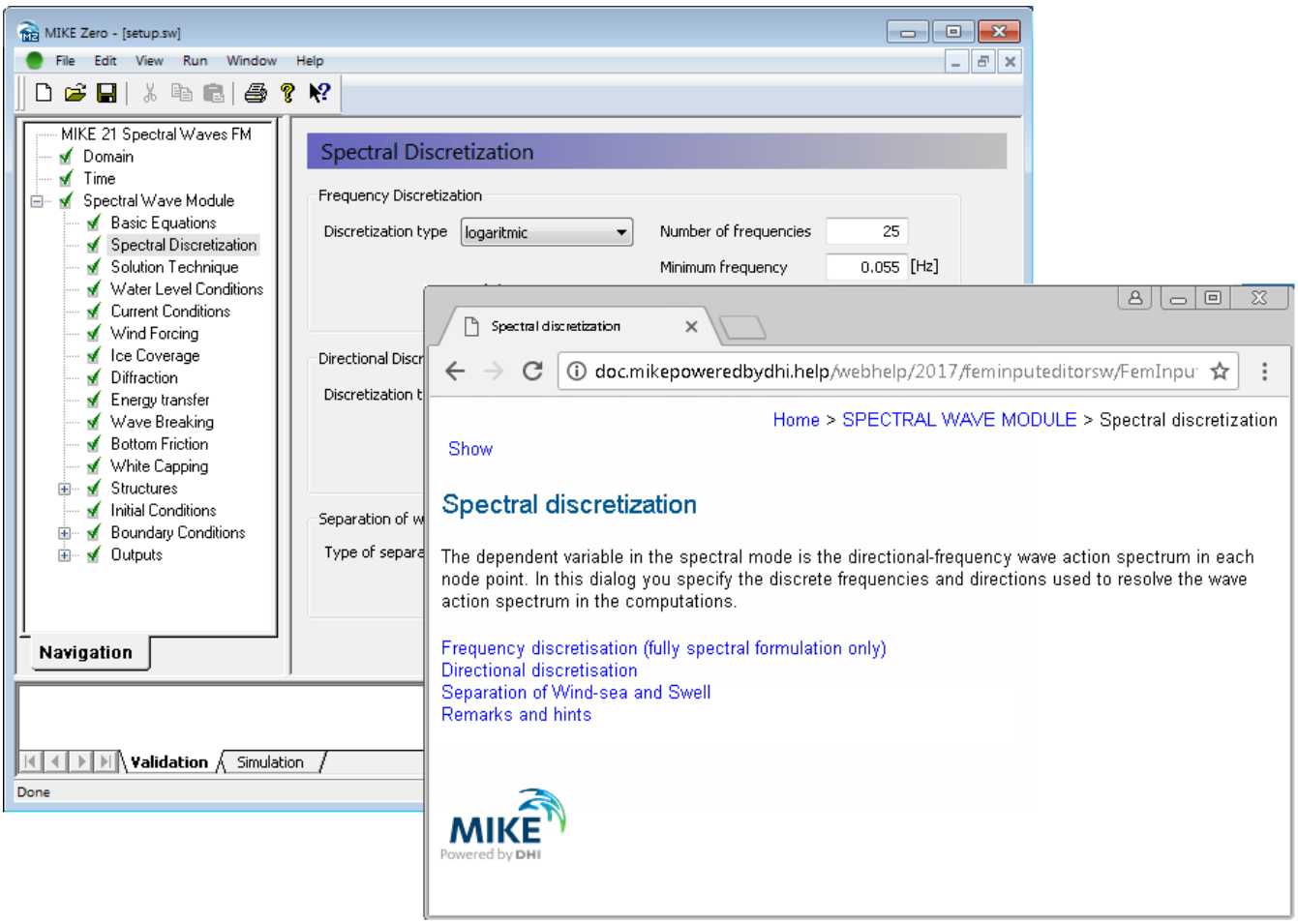
A MIKE 21 SW hindcast application in the Baltic Sea. The upper chart shows the bathymetry and the middle and lower charts show the computational mesh. The lower chart indicates the location of the measurement stations



Time series of significant wave height, H_{m0}, peak wave period, T_p , and mean wave direction, MWD, at Darss sill (Offshore, depth 20.5 m). (——) Calculation and (o) measurements. The RMS value on H_{m0} is approximately 0.2 m



Time series of significant wave height, H_{m0}, at Gellen (upper, depth 8.3m) and Bock (lower, depth 5.5 m). (——) Calculation and (o) measurements. The RMS value on H_{m0} is approximately 0.15 m



Graphical user interface of MIKE 21 SW, including an example of the Online Help System

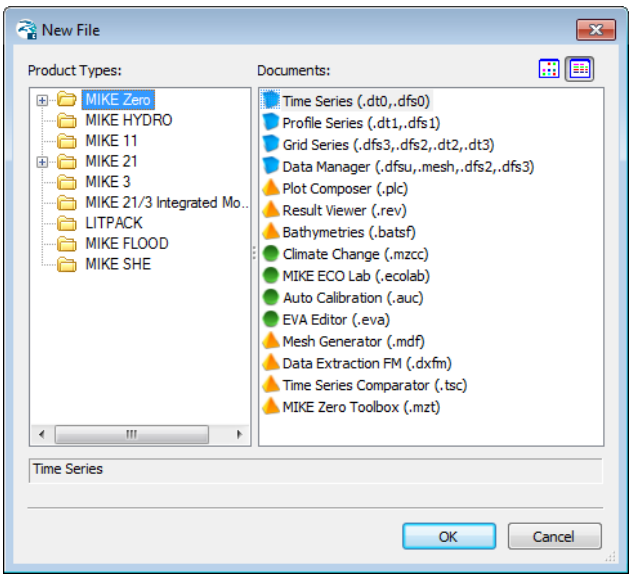
Graphical User Interface

MIKE 21 SW is operated through a fully Windows integrated Graphical User Interface (GUI). Support is provided at each stage by an Online Help System.

The common MIKE Zero shell provides entries for common data file editors, plotting facilities and a toolbox for/utilities as the Mesh Generator and Data Viewer.



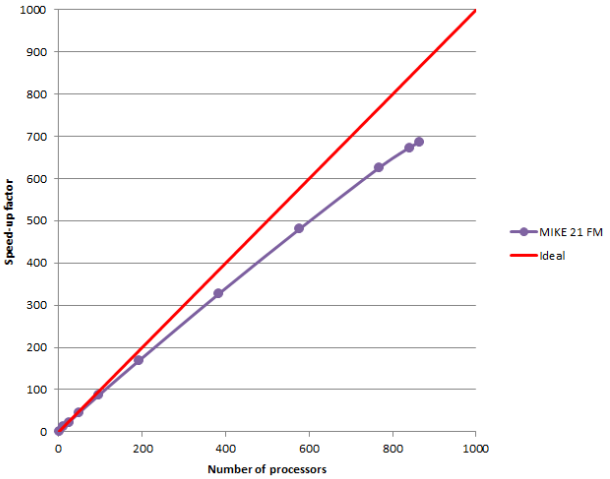
FEMA approval of the MIKE 21 package



Overview of the common MIKE Zero utilities

Parallelisation

The computational engines of the MIKE 21/3 FM series are available in versions that have been parallelised using both shared memory as well as distributed memory architecture. The latter approach allows for domain decomposition. The result is much faster simulations on systems with many cores.



Example of MIKE 21 HD FM speed-up using a HPC Cluster with distributed memory architecture (purple)

Hardware and Operating System Requirements

The MIKE Zero Modules support Microsoft Windows 7 Professional Service Pack 1 (64 bit), Windows 10 Pro (64 bit), Windows Server 2012 R2 Standard (64 bit) and Windows Server 2016 Standard (64 bit).

Microsoft Internet Explorer 9.0 (or higher) is required for network license management. An internet browser is also required for accessing the web-based documentation and online help.

The recommended minimum hardware requirements for executing the MIKE Zero modules are:

Processor:	3 GHz PC (or higher)
Memory (RAM):	2 GB (or higher)
Hard disk:	40 GB (or higher)
Monitor:	SVGA, resolution 1024x768
Graphics card: (GUI and visualisation)	64 MB RAM (256 MB RAM or higher is recommended)

Support

News about new features, applications, papers, updates, patches, etc. are available here:

www.mikepoweredbydhi.com/Download/DocumentsAndTools.aspx

For further information on MIKE 21 SW, please contact your local DHI office or the support centre:

MIKE Powered by DHI Client Care
Agern Allé 5
DK-2970 Hørsholm
Denmark

Tel: +45 4516 9333
Fax: +45 4516 9292

mike@dhigroup.com
www.mikepoweredbydhi.com

Documentation

The MIKE 21 & MIKE 3 FM models are provided with comprehensive user guides, online help, scientific documentation, application examples and step-by-step training examples.



References

Sørensen, O. R., Kofoed-Hansen, H., Rugbjerg, M. and Sørensen, L.S., (2004): A Third Generation Spectral Wave Model Using an Unstructured Finite Volume Technique. In Proceedings of the 29th International Conference of Coastal Engineering, 19-24 September 2004, Lisbon, Portugal.

Johnson, H.K., and Kofoed-Hansen, H., (2000). Influence of bottom friction on sea surface roughness and its impact on shallow water wind wave modelling. *J. Phys. Oceanog.,* **30,** 1743-1756.

Johnson, H.K., Vested, H.J., Hersbach, H. Højstrup, J. and Larsen, S.E., (1999). On the coupling between wind and waves in the WAM model. *J. Atmos. Oceanic Technol.,* **16,** 1780-1790.

Johnson, H.K. (1998). On modeling wind-waves in shallow and fetch limited areas using the method of Holthuijsen, Booij and Herbers. *J. Coastal Research,* **14**, 3, 917-932.

Young, I.R., (1999). Wind generated ocean waves, in Elsevier Ocean Engineering Book Series, Volume 2, Eds. R. Bhattacharyya and M.E. McCormick, Elsevier.

Komen, G.J., Cavaleri, L., Doneland, M., Hasselmann, K., Hasselmann S. and Janssen, P.A.E.M., (1994). Dynamics and modelling of ocean waves. Cambridge University Press, UK, 560 pp.

Holthuijsen, L.H, Booij, N. and Herbers, T.H.C. (1989). A prediction model for stationary, short-crested waves in shallow water with ambient currents, *Coastal Engr*., **13**, 23-54.

References on Applications

Kofoed-Hansen, H., Johnson, H.K., Højstrup, J. and Lange, B., (1998). Wind-wave modelling in waters with restricted fetches. In: Proc of 5th International Workshop on Wave Hindcasting and Forecasting, 27-30 January 1998, Melbourne, FL, USA, pp. 113-127.

Kofoed-Hansen, H, Johnson, H.K., Astrup, P. and Larsen, J., (2001). Prediction of waves and sea surface roughness in restricted coastal waters. In: Proc of 27th International Conference of Coastal Engineering, pp.1169-1182.

Al-Mashouk, M.A., Kerper, D.R. and Jacobsen, V., (1998). Red Sea Hindcast study: Development of a sea state design database for the Red Sea.. *J Saudi Aramco Technology*, **1**, 10 pp.

Rugbjerg, M., Nielsen, K., Christensen, J.H. and Jacobsen, V., (2001). Wave energy in the Danish part of the North Sea. In: Proc of 4th European Wave Energy Conference, 8 pp.

ALLEGATO C

MIKE 3 Wave FM

MIKE 3 Wave Model FM

Hydrodynamic module

Scientific Documentation



DHI A/S headquarters
Agern Allé 5
DK-2970 Hørsholm
Denmark

+45 4516 9200 Telephone
+45 4516 9333 Support
+45 4516 9292 Telefax

mike@dhigroup.com
www.mikepoweredbydhi.com

PLEASE NOTE

COPYRIGHT

This document refers to proprietary computer software, which is protected by copyright. All rights are reserved. Copying or other reproduction of this manual or the related programmes is prohibited without prior written consent of DHI A/S (hereinafter referred to as “DHI”). For details please refer to your ‘DHI Software License Agreement’.

LIMITED LIABILITY

The liability of DHI is limited as specified in your DHI Software License Agreement:

In no event shall DHI or its representatives (agents and suppliers) be liable for any damages whatsoever including, without limitation, special, indirect, incidental or consequential damages or damages for loss of business profits or savings, business interruption, loss of business information or other pecuniary loss arising in connection with the Agreement, e.g. out of Licensee's use of or the inability to use the Software, even if DHI has been advised of the possibility of such damages.

This limitation shall apply to claims of personal injury to the extent permitted by law. Some jurisdictions do not allow the exclusion or limitation of liability for consequential, special, indirect, incidental damages and, accordingly, some portions of these limitations may not apply.

Notwithstanding the above, DHI's total liability (whether in contract, tort, including negligence, or otherwise) under or in connection with the Agreement shall in aggregate during the term not exceed the lesser of EUR 10.000 or the fees paid by Licensee under the Agreement during the 12 months' period previous to the event giving rise to a claim.

Licensee acknowledge that the liability limitations and exclusions set out in the Agreement reflect the allocation of risk negotiated and agreed by the parties and that DHI would not enter into the Agreement without these limitations and exclusions on its liability. These limitations and exclusions will apply notwithstanding any failure of essential purpose of any limited remedy.

CONTENTS

MIKE 3 Wave Model FM
Hydrodynamic Module
Scientific Documentation

1 Introduction 1

2 Governing equations 3
2.1 Governing equations in a Cartesian coordinate system 3
2.1.1 Navier-Stokes equations 3
2.1.2 Turbulence model 5
2.2 Governing equations in a sigma coordinate system 10
2.2.1 Navier-Stokes equations 11
2.2.2 Turbulence model 13

3 Numerical method 15
3.1 Mesh and discretization scheme 15
3.1.1 Mesh 15
3.1.2 Discretization scheme 19
3.2 Finite volume method 20
3.3 Numerical solution of the Navier-Stokes equations 21
3.3.1 Time integration 21
3.3.2 Poisson equation 22
3.3.3 Space discretization 23
3.3.4 Flooding and drying 24
3.3.5 Sponge layer 25
3.3.6 Internal wave generation 26
3.3.7 Boundary conditions 27
3.4 Numerical solution of the Transport equations 27
3.4.1 Time integration 27
3.4.2 Spatial discretization 28
3.4.3 Boundary conditions 28
3.5 Time stepping procedure 28

4 Physics 31
4.1 Eddy viscosity 31
4.2 Bed resistance 31
4.3 Wall friction 32
4.4 Porosity 33

5 Parallelization 35
5.1 The domain decomposition 35
5.2 Data exchange 35
5.3 Input and output 36

6 References 37

APPENDICES

APPENDIX A – Governing equations in spherical coordinates

1 Introduction

This document presents the scientific background for the MIKE 3 Wave Model FM. The objective is to provide the user with a detailed description of the governing equations, numerical discretization and solution methods.

MIKE 3 Wave Model FM can be applied in the following areas:

- Ports and terminals
  - Wave agitation caused by short and long waves
  - Input to dynamic ship mooring analysis (MIKE 21 MA)
- Coastal areas
  - Non-linear wave transformation
  - Surf and swash zone hydrodynamics
  - Wave breaking and run-up
  - Coastal flooding
  - Tsunamis (transient) modelling
- Coastal structures
  - Wave overtopping
  - Wave transmission (and reflection) through porous structures
  - Input to wave load calculation
- Offshore environments
  - Transformation of steep nonlinear waves
  - 3D wave kinematics for structural load calculations

The model is based on the numerical solution of the three-dimensional incompressible Reynolds-averaged Navier-Stokes equations. Thus, the model consists of continuity and momentum equations, and it is closed by a turbulent closure scheme. The free surface is taken into account using a sigma coordinate transformation approach. The spatial discretization of the governing equations in conserved form is performed using a cell-centered finite volume method. The time integration is performed using a semi-implicit scheme. The vertical convective and diffusion terms are discretized using an implicit scheme to remove the stability limitations associated with the vertical resolution. The remaining terms are discretized using a second-order explicit Runge-Kutta scheme. The projection method is employed for the non-hydrostatic pressure. The interface convective fluxes are calculated using a HLLC approximate Riemann solver. This shock-capturing scheme enables robust and stable simulation of flows involving shocks or discontinuities such as bores and hydraulic jumps. This is essential for modelling of waves in the breaking zone or porous structures. The numerical dissipation accounts for the dissipation in the breaking waves.

2 Governing equations

The governing equations are solved in a sigma coordinate system or a combination of sigma coordinate system and a Cartesian coordinate system. For the hybrid system sigma coordinate is used from the free surface to a specified depth, and z-coordinate is used below. The most important advantage using sigma coordinate is the ability to accurately represent the bathymetry and provide consistent resolution near the bed. However, sigma coordinates can suffer from significant errors in the horizontal pressure gradients, advection and mixing terms in areas with sharp topographic changes (steep slopes). These errors can give rise to unrealistic flows. The use of z-level coordinate allows a simple calculation of the horizontal pressure gradients, advection and mixing terms, but the disadvantages are their inaccuracy in representing the bathymetry and that the stair-step representation of the bathymetry can result in unrealistic flow velocities near the bottom.

The governing equations can also be formulated in a spherical coordinate system. For more details, see Appendix A1.

2.1 Governing equations in a Cartesian coordinate system

2.1.1 Navier-Stokes equations

The non-hydrostatic model is based on the incompressible Navier-Stokes equations subject to the assumptions of Boussinesq and with the free surface described by a height function. In a Cartesian coordinate system the local continuity equation is written as

$$\frac{\partial u}{\partial x}+\frac{\partial v}{\partial y}+\frac{\partial w}{\partial z}=0 \tag{2.1}$$

and the conservative form of the momentum equation can be written

$$\frac{\partial u}{\partial t}+\frac{\partial u^2}{\partial x}+\frac{\partial vu}{\partial y}+\frac{\partial wu}{\partial z}=fv-\frac{1}{\rho_0}\frac{\partial q}{\partial x}-g\frac{\partial \eta}{\partial x}+F_u+\frac{\partial}{\partial z}\left(\nu_t^v\frac{\partial u}{\partial z}\right) \tag{2.2}$$

$$\frac{\partial v}{\partial t}+\frac{\partial uv}{\partial x}+\frac{\partial v^2}{\partial y}+\frac{\partial wv}{\partial z}=-fu-\frac{1}{\rho_0}\frac{\partial q}{\partial y}-g\frac{\partial \eta}{\partial y}+F_v+\frac{\partial}{\partial z}\left(\nu_t^v\frac{\partial v}{\partial z}\right) \tag{2.3}$$

$$\frac{\partial w}{\partial t}+\frac{\partial uw}{\partial x}+\frac{\partial vw}{\partial y}+\frac{\partial w^2}{\partial z}=-\frac{1}{\rho_0}\frac{\partial q}{\partial z}+F_w+\frac{\partial}{\partial z}\left(\nu_t^v\frac{\partial w}{\partial z}\right) \tag{2.4}$$

Here t is the time; x, y and z are the Cartesian coordinates; η is the surface elevation; u, v and w are the velocity components in the x, y and z direction; q is the non-hydrostatic pressure; $f=2\Omega sin\phi$ is the Coriolis parameter (Ω is the angular rate of revolution and ϕ the geographic latitude); ν_t^v is the vertical eddy viscosity; g is the gravitational acceleration; ρ_0, is the reference density of water. Eqs. (2.2)-(2.4) are obtained by splitting the total pressure, p, into a non-hydrostatic and a hydrostatic component, p_H, where

$$p_H=p_A+\rho_0 g(\eta-z)+g\int_z^\eta(\rho-\rho_0)dz \tag{2.5}$$

The atmospheric pressure, p_A, at the free surface is assumed to be constant over the domain, and the density of water, ρ, is assumed to be constant.

The horizontal diffusion terms are described using a gradient-stress relation, which is simplified to

$$F_u = \frac{\partial}{\partial x}\left(2\nu_t^h \frac{\partial u}{\partial x}\right) + \frac{\partial}{\partial y}\left(\nu_t^h\left(\frac{\partial u}{\partial y} + \frac{\partial v}{\partial x}\right)\right) \tag{2.6}$$

$$F_v = \frac{\partial}{\partial x}\left(\nu_t^h\left(\frac{\partial u}{\partial y} + \frac{\partial v}{\partial x}\right)\right) + \frac{\partial}{\partial y}\left(2\nu_t^h \frac{\partial v}{\partial y}\right) \tag{2.7}$$

$$F_w = \frac{\partial}{\partial x}\left(\nu_t^h \frac{\partial w}{\partial x}\right) + \frac{\partial}{\partial y}\left(\nu_t^h \frac{\partial w}{\partial y}\right) \tag{2.8}$$

where ν_t^h is the horizontal eddy viscosity.

The surface and bottom boundary conditions for u, v and w are

at $z = \eta$

$$\frac{\partial \eta}{\partial t} + u\frac{\partial \eta}{\partial x} + v\frac{\partial \eta}{\partial y} - w = 0, \qquad \left(\frac{\partial u}{\partial z}, \frac{\partial v}{\partial z}\right) = (0,0) \tag{2.9}$$

at $z = -d$

$$u\frac{\partial d}{\partial x} + v\frac{\partial d}{\partial y} + w = 0, \qquad \left(\frac{\partial u}{\partial z}, \frac{\partial v}{\partial z}\right) = \frac{1}{\rho_0 \nu_t^v}\left(\tau_{bx}, \tau_{by}\right) \tag{2.10}$$

Here d is the still water depth, and $\left(\tau_{bx}, \tau_{by}\right)$ are the x- and y-components of the bottom stresses.

The total water depth, $h = \eta + d$, is obtained by vertical integration of the local continuity equation and taking into account the boundary condition at the surface and the bottom

$$\frac{\partial h}{\partial t} + \frac{\partial h\bar{u}}{\partial x} + \frac{\partial h\bar{v}}{\partial y} = 0 \tag{2.11}$$

Where $\bar{u}$ and $\bar{v}$ are the depth–averaged velocities

$$h\bar{u} = \int_{-d}^{\eta} u dz, \quad h\bar{v} = \int_{-d}^{\eta} v dz \tag{2.12}$$

In matrix form the continuity equation and the momentum equations may be written

$$\frac{\partial h}{\partial t} + \nabla \cdot \boldsymbol{F}^c = 0 \tag{2.13}$$

$$\frac{\partial \boldsymbol{U}}{\partial t} + \nabla \cdot \boldsymbol{F}^m = \boldsymbol{S}_h + \boldsymbol{S}_q \tag{2.14}$$

Here $\boldsymbol{F}^c = \left(F_x^c,\ F_y^c\right)^T = (\mathrm{h}\bar{u}, \mathrm{h}\bar{v})^T$, $\boldsymbol{U} = (u, v, w)^T$ and $\boldsymbol{F}^m = \boldsymbol{F}^{mc} - \boldsymbol{F}^{md} = (\boldsymbol{F}_x^m, \boldsymbol{F}_y^m,\ \boldsymbol{F}_z^m)^T$. The flux components and the source terms can be written

$$\boldsymbol{F}_x^{mc} = \begin{pmatrix} uu + g\eta \\ uv \\ uw \end{pmatrix} \quad \boldsymbol{F}_y^{mc} = \begin{pmatrix} uv \\ vv + g\eta \\ vw \end{pmatrix} \quad \boldsymbol{F}_z^{mc} = \begin{pmatrix} uw \\ vw \\ ww \end{pmatrix} \tag{2.15}$$

$$\boldsymbol{F}_x^{md} = \begin{pmatrix} 2\nu_t^h \dfrac{\partial u}{\partial x} \\ \nu_t^h \left(\dfrac{\partial u}{\partial x} + \dfrac{\partial v}{\partial y}\right) \\ \nu_t^h \dfrac{\partial w}{\partial x} \end{pmatrix} \quad \boldsymbol{F}_y^{md} = \begin{pmatrix} \nu_t^h \left(\dfrac{\partial u}{\partial y} + \dfrac{\partial v}{\partial x}\right) \\ 2\nu_t^h \dfrac{\partial v}{\partial y} \\ \nu_t^h \dfrac{\partial w}{\partial y} \end{pmatrix} \quad \boldsymbol{F}_z^{md} = \begin{pmatrix} \nu_t^v \dfrac{\partial u}{\partial z} \\ \nu_t^v \dfrac{\partial v}{\partial z} \\ \nu_t^v \dfrac{\partial w}{\partial z} \end{pmatrix} \tag{2.16}$$

$$\boldsymbol{S}_h = \begin{pmatrix} fv \\ -fu \\ 0 \end{pmatrix} \qquad \boldsymbol{S}_q = -\frac{1}{\rho_0} \begin{pmatrix} \dfrac{\partial q}{\partial x} \\ \dfrac{\partial q}{\partial y} \\ \dfrac{\partial q}{\partial w} \end{pmatrix} \tag{2.17}$$

If the hydrostatic pressure assumption is applied, the non-hydrostatic pressure will be zero. With this assumption, a three-dimensional, hydrodynamic model can be significantly simplified because the momentum equation in the vertical direction (Eq. (2.4)) can be neglected.

2.1.2 Turbulence model

The turbulence is modelled using an eddy viscosity concept. The eddy viscosity can be described using empirical formula (see section 4.1) or solving a turbulence closure model. In the MIKE 3 Wave Model FM, there are two turbulence models available, namely the k-ε model and the k-ω model; both are two-equations models.

The k-epsilon model

The k-ε model presented here follows Rodi (1980,1984) and has an additional limiter from Larsen and Fuhrman (2018). The model describes k, the specific turbulent kinetic energy and ε, the dissipation rate of turbulent kinetic energy (turbulent dissipation). The eddy viscosity, ν_t, is defined as

$$\nu_t = c_\mu \frac{k^2}{\tilde{\varepsilon}} \tag{2.18}$$

where c_μ is an empirical constant and $\tilde{\varepsilon}$ is a limited version of ε. Solving a system of equations for k and ε results in the eddy viscosity in eq. (2.18) and this value can be used in the momentum equations for the horizontal and/or vertical eddy viscosity, ν_t^h and ν_t^v.

The turbulent kinetic energy, k, and the turbulent dissipation, ε, are obtained from the following transport equations.

$$\frac{\partial k}{\partial t} + \frac{\partial uk}{\partial x} + \frac{\partial vk}{\partial y} + \frac{\partial wk}{\partial z} = F_k + \frac{\partial}{\partial z}\left(\frac{\nu_{t0}^v}{\sigma_k^v}\frac{\partial k}{\partial z}\right) + P_k - \varepsilon \tag{2.19}$$

$$\frac{\partial \varepsilon}{\partial t} + \frac{\partial u\varepsilon}{\partial x} + \frac{\partial v\varepsilon}{\partial y} + \frac{\partial w\varepsilon}{\partial z} = F_\varepsilon + \frac{\partial}{\partial z}\left(\frac{\nu_{t0}^v}{\sigma_\varepsilon^v}\frac{\partial \varepsilon}{\partial z}\right) + P_\varepsilon - c_{2\varepsilon}\frac{\varepsilon^2}{k} \tag{2.20}$$

Here, P_k and P_ε are shear production terms and F_k and F_ε are horizontal diffusion terms. The details of the various terms are presented in the following.

The shear production terms are given as

$$P_k = \nu_t p_0 \tag{2.21}$$

$$P_\varepsilon = c_{1\varepsilon} c_\mu k p_0 \tag{2.22}$$

where, $c_{1\varepsilon}$ is a closure coefficient. Furthermore,

$$p_0 = 2\sum_{i=1}^{3}\sum_{j=1}^{3} S_{ij} S_{ij} \tag{2.23}$$

where S_{ij} is the mean strain rate tensor defined as

$$S_{ij} = \frac{1}{2}\left(\frac{\partial u_i}{\partial x_j} + \frac{\partial u_j}{\partial x_i}\right), \quad \text{for} \quad i,j = 1,2,3 \tag{2.24}$$

Here, is used the following notation

$$u_1 = u\,, \qquad u_2 = v\,, \qquad u_3 = w \tag{2.25}$$

$$x_1 = x\,, \qquad x_2 = y\,, \qquad x_3 = z \tag{2.26}$$

The vertical diffusion terms are given directly in the transport equations for k and ε. The horizontal diffusion terms have a similar form and are given by

$$F_k = \frac{\partial}{\partial x}\left(\frac{\nu_{t0}^h}{\sigma_k^h}\frac{\partial k}{\partial x}\right) + \frac{\partial}{\partial y}\left(\frac{\nu_{t0}^h}{\sigma_k^h}\frac{\partial k}{\partial y}\right) \tag{2.27}$$

$$F_\varepsilon = \frac{\partial}{\partial x}\left(\frac{\nu_{t0}^h}{\sigma_\varepsilon^h}\frac{\partial \varepsilon}{\partial x}\right) + \frac{\partial}{\partial y}\left(\frac{\nu_{t0}^h}{\sigma_\varepsilon^h}\frac{\partial \varepsilon}{\partial y}\right) \tag{2.28}$$

The coefficients σ_k^h, σ_k^v, σ_ε^h and σ_ε^v are closure coefficients. For the diffusion terms is used an unlimited version of the eddy viscosity

$$\nu_{t0}^h = c_\mu \frac{k^2}{\varepsilon}, \qquad \nu_{t0}^v = c_\mu \frac{k^2}{\varepsilon} \tag{2.29}$$

If the momentum equations use an empirical formula for either the horizontal or vertical eddy viscosity, that value is also used in the diffusion terms in the turbulence model. This means, that $\nu_{t0}^h = \nu_t^h$ or $\nu_{t0}^v = \nu_t^v$ is used instead of the corresponding expression in eq. (2.29).

To limit the eddy viscosity in regions with nearly-potential flow and stabilize the model, Larsen and Fuhrman (2018) introduced a limited value of the turbulent dissipation ε,

$$\tilde{\varepsilon} = \max\left[\varepsilon, \lambda_2 \frac{c_{2\varepsilon}}{c_{1\varepsilon}} \frac{p_0}{p_\Omega}\, \varepsilon\right] \tag{2.30}$$

Here, $\lambda_2 = 0.05$ is a limiter coefficient and

$$p_\Omega = 2\sum_{i=1}^{3}\sum_{j=1}^{3}\Omega_{ij}\Omega_{ij} \tag{2.31}$$

where Ω_{ij} is the rotation tensor,

$$\Omega_{ij} = \frac{1}{2}\left(\frac{\partial u_i}{\partial x_j} - \frac{\partial u_j}{\partial x_i}\right), \quad \text{for} \quad i,j = 1,2,3 \tag{2.32}$$

Several carefully calibrated empirical coefficients enter the k-ε turbulence model. In the standard k-ε model (Rodi (1984)), they are

$$c_\mu = 0.09, \qquad c_{1\varepsilon} = 1.44, \qquad c_{2\varepsilon} = 1.92 \tag{2.33}$$

$$\sigma_k^h = \sigma_k^v = 1.0, \qquad \sigma_\varepsilon^h = \sigma_\varepsilon^v = 1.3 \tag{2.34}$$

In matrix form, the transport equations for k and ε may be written

$$\frac{\partial \boldsymbol{U}}{\partial t} + \nabla \cdot \boldsymbol{F} = \boldsymbol{S} \tag{2.35}$$

where $\boldsymbol{U} = (k,\ \varepsilon)^T$ and $\boldsymbol{F} = \boldsymbol{F^c} - \boldsymbol{F^d} = (\boldsymbol{F}_x, \boldsymbol{F}_y, \boldsymbol{F}_z)^T$. The flux components and the source terms can be written

$$\boldsymbol{F}_x^c = \begin{pmatrix} uk \\ u\varepsilon \end{pmatrix}, \quad \boldsymbol{F}_y^c = \begin{pmatrix} vk \\ v\varepsilon \end{pmatrix}, \quad \boldsymbol{F}_z^c = \begin{pmatrix} wk \\ w\varepsilon \end{pmatrix} \tag{2.36}$$

$$\boldsymbol{F}_x^d = \begin{pmatrix} \frac{\nu_{t0}^h}{\sigma_k^h}\frac{\partial k}{\partial x} \\ \frac{\nu_{t0}^h}{\sigma_\varepsilon^h}\frac{\partial \varepsilon}{\partial x} \end{pmatrix}, \quad \boldsymbol{F}_y^d = \begin{pmatrix} \frac{\nu_{t0}^h}{\sigma_k^h}\frac{\partial k}{\partial y} \\ \frac{\nu_{t0}^h}{\sigma_\varepsilon^h}\frac{\partial \varepsilon}{\partial y} \end{pmatrix}, \quad \boldsymbol{F}_z^d = \begin{pmatrix} \frac{\nu_{t0}^v}{\sigma_k^v}\frac{\partial k}{\partial z} \\ \frac{\nu_{t0}^v}{\sigma_\varepsilon^v}\frac{\partial \varepsilon}{\partial z} \end{pmatrix} \tag{2.37}$$

$$\boldsymbol{S} = \begin{pmatrix} P_k - \varepsilon \\ P_\varepsilon - c_{2\varepsilon}\frac{\varepsilon^2}{k} \end{pmatrix} \tag{2.38}$$

The k-omega model

The k-ω model presented here is following Larsen and Fuhrman (2018). It extends the model in Wilcox (2008) with an additional limiter. The model describes the specific turbulent kinetic energy, k, and the specific dissipation rate, ω. The eddy viscosity, ν_t, is defined as

$$\nu_t = \frac{k}{\tilde{\omega}} \tag{2.39}$$

where $\tilde{\omega}$ is a limited version of ω. This value of the eddy viscosity can be used in the momentum equations for the horizontal and/or vertical eddy viscosity, ν_t^h and ν_t^v.

The transport equations for the turbulent kinetic energy, k, and the specific dissipation rate, ω, reads

$$\frac{\partial k}{\partial t}+\frac{\partial uk}{\partial x}+\frac{\partial vk}{\partial y}+\frac{\partial wk}{\partial z}=F_k+\frac{\partial}{\partial z}\left(\frac{\nu_{t0}^v}{\sigma_k^v}\frac{\partial k}{\partial z}\right)+P_k-\beta_k\omega k \tag{2.40}$$

$$\frac{\partial \omega}{\partial t}+\frac{\partial u\omega}{\partial x}+\frac{\partial v\omega}{\partial y}+\frac{\partial w\omega}{\partial z}=F_\omega+\frac{\partial}{\partial z}\left(\frac{\nu_{t0}^v}{\sigma_\omega^v}\frac{\partial \omega}{\partial z}\right)+F_{\omega c}+P_\omega-\beta_\omega\omega^2 \tag{2.41}$$

Here, F_k and F_ω are horizontal diffusion terms, $F_{\omega c}$ is a cross-diffusion term and P_k and P_ω are production terms. The details of the various terms are presented in the following.

The production terms are given by

$$P_k=\nu_t p_0 \tag{2.42}$$

$$P_\omega=\alpha\frac{\omega}{\widehat{\omega}}p_0 \tag{2.43}$$

where $\widehat{\omega}$ is a limited version of the specific dissipation rate, ω, α is a closure coefficient and p_0 was defined in eq. (2.23).

The vertical diffusion terms are given directly in the transport equations for k and ω. The horizontal diffusion terms have a similar form and are given by

$$F_k=\frac{\partial}{\partial x}\left(\frac{\nu_{t0}^h}{\sigma_k^h}\frac{\partial k}{\partial x}\right)+\frac{\partial}{\partial y}\left(\frac{\nu_{t0}^h}{\sigma_k^h}\frac{\partial k}{\partial y}\right) \tag{2.44}$$

$$F_\omega=\frac{\partial}{\partial x}\left(\frac{\nu_{t0}^h}{\sigma_\omega^h}\frac{\partial \omega}{\partial x}\right)+\frac{\partial}{\partial y}\left(\frac{\nu_{t0}^h}{\sigma_\omega^h}\frac{\partial \omega}{\partial y}\right) \tag{2.45}$$

The coefficients σ_k^h, σ_k^v, σ_ω^h and σ_ω^v are closure coefficients. For the diffusion terms is used an unlimited version of the eddy viscosity

$$\nu_{t0}^h=\frac{k}{\omega}\,,\qquad \nu_{t0}^v=\frac{k}{\omega} \tag{2.46}$$

If the momentum equations use an empirical formula for either the horizontal or vertical eddy viscosity, that value is also used in the diffusion terms in the turbulence model. This means, that $\nu_{t0}^h=\nu_t^h$ or $\nu_{t0}^v=\nu_t^v$ is used instead of the corresponding expression in eq. (2.46). The cross-diffusion term in the equation for ω reads

$$F_{\omega c}=\frac{\sigma_{do}}{\omega}\max\left\{0,\frac{\partial k}{\partial x}\frac{\partial \omega}{\partial x}+\frac{\partial k}{\partial y}\frac{\partial \omega}{\partial y}+\frac{\partial k}{\partial z}\frac{\partial \omega}{\partial z}\right\} \tag{2.47}$$

To limit the eddy viscosity in regions with nearly-potential flow and stabilize the model, Larsen and Fuhrman (2018) introduced an additional limiter for ω on top of the limiter already present in the k-ω model from Wilcox (2008). The limited versions of ω are defined as

$$\widehat{\omega}=\max\left[\omega,\lambda_1\sqrt{\frac{p_0-p_b}{\beta_k}}\right] \tag{2.48}$$

$$\widetilde{\omega}=\max\left[\widehat{\omega},\lambda_2\frac{\beta_\omega}{\beta_k\alpha}\frac{p_0}{p_\Omega}\omega\right] \tag{2.49}$$

The values of the limiter coefficients are $\lambda_1 = 0.875$ and $\lambda_2 = 0.05$ and p_Ω was defined in eq. (2.31).

The system contains several empirically determined closure coefficients which have the following values,

$$\sigma_k^h = \sigma_k^v = \frac{5}{3}\,, \qquad \sigma_\omega^h = \sigma_\omega^v = 2\,, \qquad \sigma_{do} = \frac{1}{8} \tag{2.50}$$

$$\alpha = 0.52 \tag{2.51}$$

$$\beta_k = 0.09\,, \qquad \beta_\omega = \beta_0 f_\beta\,, \qquad \beta_0 = 0.0708 \tag{2.52}$$

$$f_\beta = \frac{1 + 85\chi_\omega}{1 + 100\chi_\omega}\,, \qquad \chi_\omega = \left|\frac{\sum_{i=1}^{3}\sum_{j=1}^{3}\sum_{k=1}^{3}\Omega_{ij}\Omega_{jk}S_{ki}}{(\beta_k\omega)^3}\right| \tag{2.53}$$

These values are from Larsen and Fuhrmann (2018), except f_β which is from Wilcox (2008). Larsen and Fuhrman (2018) use $f_\beta = 1$, consistent with two-dimensional flow. Note that β_k corresponds to c_μ in the k-ε model. The mean strain rate tensor S_{ij} and the rotation tensor Ω_{ij} were defined in eq. (2.24) and (2.32).

In matrix form, the transport equations for k and ω may be written as

$$\frac{\partial \boldsymbol{U}}{\partial t} + \nabla \cdot \boldsymbol{F} - \boldsymbol{G} = \boldsymbol{S} \tag{2.54}$$

where $\boldsymbol{U} = (k,\ \omega)^T$ and $\boldsymbol{F} = \boldsymbol{F^c} - \boldsymbol{F^d} = (\boldsymbol{F}_x, \boldsymbol{F}_y, \boldsymbol{F}_z)^T$. The flux components $\boldsymbol{F}$, the cross-diffusion $\boldsymbol{G}$ and the source terms $\boldsymbol{S}$ can be written

$$\boldsymbol{F}_x^c = \begin{pmatrix} uk \\ u\omega \end{pmatrix}, \qquad \boldsymbol{F}_y^c = \begin{pmatrix} vk \\ v\omega \end{pmatrix}, \qquad \boldsymbol{F}_z^c = \begin{pmatrix} wk \\ w\omega \end{pmatrix} \tag{2.55}$$

$$\boldsymbol{F}_x^d = \begin{pmatrix} \frac{\nu_{t0}^h}{\sigma_k^h}\frac{\partial k}{\partial x} \\ \frac{\nu_{t0}^h}{\sigma_\omega^h}\frac{\partial \omega}{\partial x} \end{pmatrix}, \qquad \boldsymbol{F}_y^d = \begin{pmatrix} \frac{\nu_{t0}^h}{\sigma_k^h}\frac{\partial k}{\partial y} \\ \frac{\nu_{t0}^h}{\sigma_\omega^h}\frac{\partial \omega}{\partial y} \end{pmatrix}, \qquad \boldsymbol{F}_z^d = \begin{pmatrix} \frac{\nu_{t0}^v}{\sigma_k^v}\frac{\partial k}{\partial z} \\ \frac{\nu_{t0}^v}{\sigma_\omega^v}\frac{\partial \omega}{\partial z} \end{pmatrix} \tag{2.56}$$

$$\boldsymbol{G} = \begin{pmatrix} 0 \\ \frac{\sigma_d}{\omega}\max\left[0, \frac{\partial k}{\partial x}\frac{\partial \omega}{\partial x} + \frac{\partial k}{\partial y}\frac{\partial \omega}{\partial y} + \frac{\partial k}{\partial z}\frac{\partial \omega}{\partial z}\right] \end{pmatrix} \tag{2.57}$$

$$\boldsymbol{S} = \begin{pmatrix} P_k - \beta_k\omega k \\ P_\omega - \beta_\omega\omega^2 \end{pmatrix} \tag{2.58}$$

Boundary conditions at the surface and the seabed

At boundaries where there is a friction, the boundary conditions for k, ε and ω can be modelled with wall functions, Wilcox (1998),

$$k = \frac{1}{\sqrt{\beta_k}}U_\tau^2\,, \qquad \varepsilon = \frac{U_\tau^3}{\kappa\Delta y}\,, \qquad \omega = \frac{U_\tau}{\sqrt{\beta_k}\kappa\Delta y} \tag{2.59}$$

Here, U_τ is the friction velocity associated with the boundary and Δy is the distance from the boundary to the point where the conditions are employed. Furthermore, $\kappa = 0.41$ is the von Kármán constant.

At the seabed, $z = -d$, if there is a bed resistance, the boundary conditions are the wall functions in eq. (2.59) where $\Delta y = \Delta z_b$ is the distance to the bottom and $U_\tau = U_{\tau b}$ is the friction velocity associated with the bottom stress, see section 4.2.

At the surface, $z = \eta$, it is assumed there is no friction, and the boundary conditions are

at $z = \eta$

$$\frac{\partial k}{\partial z} = 0, \qquad \varepsilon = \frac{\left(k\sqrt{c_\mu}\right)^{3/2}}{\alpha_s \kappa h}, \qquad \omega = \frac{\sqrt{k}}{\alpha_s \beta_k^{1/4} \kappa h} \tag{2.60}$$

where $\alpha_s = 0.07$ is an empirical constant.

2.2 Governing equations in a sigma coordinate system

The equations are solved using a vertical σ-transformation

$$t' = t, \qquad x' = x, \qquad y' = y, \qquad \sigma = \frac{z + d}{h} \tag{2.61}$$

where σ varies between 0 at the bottom and 1 at the surface. The chain rule is applied to obtain partial derivatives of the function $f = f(t, x, y, z)$

$$\frac{\partial f}{\partial t} = \frac{\partial f}{\partial t'} + \frac{\partial f}{\partial \sigma}\frac{\partial \sigma}{\partial t} \tag{2.62}$$

$$\frac{\partial f}{\partial x} = \frac{\partial f}{\partial x'} + \frac{\partial f}{\partial \sigma}\frac{\partial \sigma}{\partial x} \tag{2.63}$$

$$\frac{\partial f}{\partial y} = \frac{\partial f}{\partial y'} + \frac{\partial f}{\partial \sigma}\frac{\partial \sigma}{\partial y} \tag{2.64}$$

$$\frac{\partial f}{\partial z} = \frac{\partial f}{\partial \sigma}\frac{\partial \sigma}{\partial z} \tag{2.65}$$

where

$$\frac{\partial \sigma}{\partial t} = -\sigma\frac{1}{h}\frac{\partial h}{\partial t} \equiv A_t \tag{2.66}$$

$$\frac{\partial \sigma}{\partial x} = -\frac{1}{h}\left(\sigma\frac{\partial h}{\partial x} - \frac{\partial d}{\partial x}\right) \equiv A_x \tag{2.67}$$

$$\frac{\partial \sigma}{\partial y} = -\frac{1}{h}\left(\sigma\frac{\partial h}{\partial y} - \frac{\partial d}{\partial y}\right) \equiv A_y \tag{2.68}$$

$$\frac{\partial \sigma}{\partial z} = \frac{1}{h} \equiv A_z \tag{2.69}$$

2.2.1 Navier-Stokes equations

In the sigma coordinate system, the governing equations are given as

$$\frac{\partial h}{\partial t'}+\frac{\partial hu}{\partial x'}+\frac{\partial hv}{\partial y'}+\frac{\partial h\omega}{\partial \sigma}=0 \tag{2.70}$$

$$\frac{\partial hu}{\partial t'}+\frac{\partial hu^2}{\partial x'}+\frac{\partial hvu}{\partial y'}+\frac{\partial h\omega u}{\partial \sigma}= fhv-\frac{h}{\rho_0}\left(\frac{\partial q}{\partial x'}+\frac{\partial q}{\partial \sigma}\frac{\partial \sigma}{\partial x}\right)-gh\frac{\partial \eta}{\partial x'}+hF_u+\frac{\partial}{\partial \sigma}\left(\frac{\nu_t^v}{h}\frac{\partial u}{\partial \sigma}\right) \tag{2.71}$$

$$\frac{\partial hv}{\partial t'}+\frac{\partial huv}{\partial x'}+\frac{\partial hv^2}{\partial y'}+\frac{\partial h\omega v}{\partial \sigma}= -fhu-\frac{h}{\rho_0}\left(\frac{\partial q}{\partial y'}+\frac{\partial q}{\partial \sigma}\frac{\partial \sigma}{\partial y}\right)-gh\frac{\partial \eta}{\partial y'}+hF_v+\frac{\partial}{\partial \sigma}\left(\frac{\nu_t^v}{h}\frac{\partial v}{\partial \sigma}\right) \tag{2.72}$$

$$\frac{\partial hw}{\partial t'}+\frac{\partial huw}{\partial x'}+\frac{\partial hvw}{\partial y'}+\frac{\partial h\omega w}{\partial \sigma}=-\frac{1}{\rho_0}\frac{\partial q}{\partial \sigma}+hF_w+\frac{\partial}{\partial \sigma}\left(\frac{\nu_t^v}{h}\frac{\partial w}{\partial \sigma}\right) \tag{2.73}$$

The modified vertical velocity, ω, in the sigma coordinate system is given by

$$\omega=\frac{1}{h}\left(w+u\frac{\partial d}{\partial x}+v\frac{\partial d}{\partial y}-\sigma\left(\frac{\partial h}{\partial t}+u\frac{\partial h}{\partial x}+v\frac{\partial h}{\partial y}\right)\right) \tag{2.74}$$

The modified vertical velocity is the velocity across a level of constant σ. The horizontal diffusion terms are approximated by

$$hF_u\approx\frac{\partial}{\partial x}\left(2h\nu_t^h\frac{\partial u}{\partial x}\right)+\frac{\partial}{\partial y}\left(h\nu_t^h\left(\frac{\partial u}{\partial y}+\frac{\partial v}{\partial x}\right)\right) \tag{2.75}$$

$$hF_v\approx\frac{\partial}{\partial x}\left(h\nu_t^h\left(\frac{\partial u}{\partial y}+\frac{\partial v}{\partial x}\right)\right)+\frac{\partial}{\partial y}\left(2h\nu_t^h\frac{\partial v}{\partial y}\right) \tag{2.76}$$

$$hF_w\approx\frac{\partial}{\partial x}\left(h\nu_t^h\frac{\partial w}{\partial x}\right)+\frac{\partial}{\partial y}\left(h\nu_t^h\frac{\partial w}{\partial y}\right) \tag{2.77}$$

The surface and bottom boundary conditions for u, v and ω are

at $z = \eta$

$$\omega=0,\qquad\left(\frac{\partial u}{\partial \sigma},\frac{\partial v}{\partial \sigma}\right)=(0,0) \tag{2.78}$$

at $z = -d$

$$\omega=0,\qquad\left(\frac{\partial u}{\partial \sigma},\frac{\partial v}{\partial \sigma}\right)=\frac{\mathrm{h}}{\rho_0\nu_t^v}(\tau_{bx},\tau_{by}) \tag{2.79}$$

The depth-averaged continuity equation becomes

$$\frac{\partial h}{\partial t'}+\frac{\partial h\bar{u}}{\partial x'}+\frac{\partial h\bar{v}}{\partial y'}=0 \tag{2.80}$$

where $\bar{u}$ and $\bar{v}$ are the depth–averaged velocities

$$\bar{u}=\int_0^1 u d\sigma, \quad \bar{v}=\int_0^1 v d\sigma=0 \tag{2.81}$$

In matrix form the continuity equations and the momentum equations may be written

$$\frac{\partial h}{\partial t'}+\nabla\cdot\boldsymbol{F}^c=0 \tag{2.82}$$

$$\frac{\partial \boldsymbol{U}}{\partial t'}+\nabla\cdot\boldsymbol{F}^m=\boldsymbol{S}_h+\boldsymbol{S}_q \tag{2.83}$$

where $\boldsymbol{F}^c=\left(F_x^c,\ F_y^c\right)^T=(h\bar{u},h\bar{v})^T$, $\boldsymbol{U}=(hu,hv,hw)^T$ and $\boldsymbol{F}^m=\boldsymbol{F}^{mc}-\boldsymbol{F}^{md}=(\boldsymbol{F}_x^m,\boldsymbol{F}_y^m,\ \boldsymbol{F}_\sigma^m)^T$.

The flux components and the source terms can be written

$$\boldsymbol{F}_x^{mc}=\begin{pmatrix} huu+\frac{1}{2}g(\eta^2+2\eta d)\\ huv\\ huw\end{pmatrix}\quad \boldsymbol{F}_y^{mc}=\begin{pmatrix} huv\\ hvv+\frac{1}{2}g(\eta^2+2\eta d)\\ hvw\end{pmatrix}\quad \boldsymbol{F}_\sigma^{mc}=\begin{pmatrix} hu\omega\\ hv\omega\\ hw\omega\end{pmatrix} \tag{2.84}$$

$$\boldsymbol{F}_x^{md}=\begin{pmatrix} 2h\nu_t^h\frac{\partial u}{\partial x}\\ h\nu_t^h\left(\frac{\partial u}{\partial y}+\frac{\partial v}{\partial x}\right)\\ h\nu_t^h\frac{\partial w}{\partial x}\end{pmatrix}\quad \boldsymbol{F}_y^{md}=\begin{pmatrix} h\nu_t^h\left(\frac{\partial u}{\partial y}+\frac{\partial v}{\partial x}\right)\\ 2h\nu_t^h\frac{\partial v}{\partial y}\\ h\nu_t^h\frac{\partial w}{\partial y}\end{pmatrix}\quad \boldsymbol{F}_\sigma^{md}=\begin{pmatrix} \frac{\nu_t^v}{h}\frac{\partial u}{\partial \sigma}\\ \frac{\nu_t^v}{h}\frac{\partial v}{\partial \sigma}\\ \frac{\nu_t^v}{h}\frac{\partial w}{\partial \sigma}\end{pmatrix} \tag{2.85}$$

$$\boldsymbol{S}_h=\begin{pmatrix} g\eta\frac{\partial d}{\partial x'}+fhv\\ g\eta\frac{\partial d}{\partial y'}-fhu\\ 0\end{pmatrix}\quad \boldsymbol{S}_q=-\frac{1}{\rho_0}\begin{pmatrix} h\left(\frac{\partial q}{\partial x'}+\frac{\partial q}{\partial \sigma}\frac{\partial \sigma}{\partial x}\right)\\ h\left(\frac{\partial q}{\partial y'}+\frac{\partial q}{\partial \sigma}\frac{\partial \sigma}{\partial y}\right)\\ \frac{\partial q}{\partial \sigma}\end{pmatrix} \tag{2.86}$$

To give a conservative formulation, the gravity surface terms are split into two terms (see Chippada (1998), Rogers (2001), Quecedo (2002), Liang or Borthwick (2009))

$$gh\frac{\partial \eta}{\partial x'}=\frac{1}{2}g\frac{\partial(h^2-d^2)}{\partial x'}-g\eta\frac{\partial d}{\partial x'}=\frac{1}{2}g\frac{\partial(\eta^2+2\eta d)}{\partial x'}-g\eta\frac{\partial d}{\partial x'} \tag{2.87}$$

$$gh\frac{\partial \eta}{\partial y'}=\frac{1}{2}g\frac{\partial(h^2-d^2)}{\partial y'}-g\eta\frac{\partial d}{\partial y'}=\frac{1}{2}g\frac{\partial(\eta^2+2\eta d)}{\partial y'}-g\eta\frac{\partial d}{\partial y'} \tag{2.88}$$

It is easily seen that if η is constant, the two terms cancel exactly. In the discrete case, this is also true if the two derivatives are calculated using the same scheme.

2.2.2 Turbulence model

The k-epsilon model

In the sigma coordinate system, the transport equations for the k-ε model are given as

$$\frac{\partial hk}{\partial t'}+\frac{\partial huk}{\partial x'}+\frac{\partial hvk}{\partial y'}+\frac{\partial h\omega k}{\partial \sigma}=hF_k+\frac{\partial}{\partial \sigma}\left(\frac{\nu_{t0}^v}{h\sigma_k^v}\frac{\partial k}{\partial \sigma}\right)+h(P_k-\epsilon) \tag{2.89}$$

$$\frac{\partial h\varepsilon}{\partial t'}+\frac{\partial hu\varepsilon}{\partial x'}+\frac{\partial hv\varepsilon}{\partial y'}+\frac{\partial h\omega\varepsilon}{\partial \sigma}=hF_\varepsilon+\frac{\partial}{\partial \sigma}\left(\frac{\nu_{t0}^v}{h\sigma_\varepsilon^v}\frac{\partial \varepsilon}{\partial \sigma}\right)+h\left(P_\varepsilon-c_{2\varepsilon}\frac{\varepsilon^2}{k}\right) \tag{2.90}$$

The horizontal diffusion terms are defined as

$$hF_k\approx\frac{\partial}{\partial x}\left(\frac{h\nu_{t0}^h}{\sigma_k^h}\frac{\partial k}{\partial x}\right)+\frac{\partial}{\partial y}\left(\frac{h\nu_{t0}^h}{\sigma_k^h}\frac{\partial k}{\partial y}\right) \tag{2.91}$$

$$hF_\varepsilon\approx\frac{\partial}{\partial x}\left(\frac{h\nu_{t0}^h}{\sigma_\varepsilon^h}\frac{\partial \varepsilon}{\partial x}\right)+\frac{\partial}{\partial y}\left(\frac{h\nu_{t0}^h}{\sigma_\varepsilon^h}\frac{\partial \varepsilon}{\partial y}\right) \tag{2.92}$$

In matrix form, the transport equations for *k* and *ε* may be written

$$\frac{\partial \boldsymbol{U}}{\partial t'}+\nabla\cdot\boldsymbol{F}=\boldsymbol{S} \tag{2.93}$$

where $\boldsymbol{U}=(hk,h\varepsilon)^T$ and $\boldsymbol{F}=\boldsymbol{F}^c-\boldsymbol{F}^d=(\boldsymbol{F}_x,\boldsymbol{F}_y,\boldsymbol{F}_\sigma)^T$. The flux components and the source terms can be written

$$\boldsymbol{F}_x^c=\begin{pmatrix}huk\\ hu\varepsilon\end{pmatrix},\quad \boldsymbol{F}_y^c=\begin{pmatrix}hvk\\ hv\varepsilon\end{pmatrix},\quad \boldsymbol{F}_\sigma^c=\begin{pmatrix}h\omega k\\ h\omega\varepsilon\end{pmatrix} \tag{2.94}$$

$$\boldsymbol{F}_x^d=\begin{pmatrix}\frac{h\nu_{t0}^h}{\sigma_k^h}\frac{\partial k}{\partial x}\\ \frac{h\nu_{t0}^h}{\sigma_\varepsilon^h}\frac{\partial \varepsilon}{\partial x}\end{pmatrix},\quad \boldsymbol{F}_y^d=\begin{pmatrix}\frac{h\nu_{t0}^h}{\sigma_k^h}\frac{\partial k}{\partial y}\\ \frac{h\nu_{t0}^h}{\sigma_\varepsilon^h}\frac{\partial \varepsilon}{\partial y}\end{pmatrix},\quad \boldsymbol{F}_\sigma^d=\begin{pmatrix}\frac{\nu_{t0}^v}{h\sigma_k^v}\frac{\partial k}{\partial \sigma}\\ \frac{\nu_{t0}^v}{h\sigma_\varepsilon^v}\frac{\partial \varepsilon}{\partial \sigma}\end{pmatrix} \tag{2.95}$$

$$\boldsymbol{S}=\begin{pmatrix}h(P_k-\varepsilon)\\ h\left(P_\varepsilon-c_{2\varepsilon}\frac{\varepsilon^2}{k}\right)\end{pmatrix} \tag{2.96}$$

The k-omega model

In this section, the modified vertical velocity in the sigma coordinate system is called w_s (instead of ω). This is to distinguish it from the specific dissipation rate, ω, of turbulent kinetic energy which was introduced in section 2.1.2. In the sigma coordinate system, the transport equations for the k-ω model are given as

$$\frac{\partial hk}{\partial t'}+\frac{\partial huk}{\partial x'}+\frac{\partial hvk}{\partial y'}+\frac{\partial hw_sk}{\partial \sigma}=hF_k+\frac{\partial}{\partial \sigma}\left(\frac{\nu_{t0}^v}{h\sigma_k^v}\frac{\partial k}{\partial \sigma}\right)+h(P_k-\beta_k\omega k) \tag{2.97}$$

$$\frac{\partial h\omega}{\partial t'}+\frac{\partial hu\omega}{\partial x'}+\frac{\partial hv\omega}{\partial y'}+\frac{\partial hw_s\omega}{\partial \sigma}=hF_\omega+\frac{\partial}{\partial \sigma}\left(\frac{\nu_{t0}^v}{h\sigma_\omega^v}\frac{\partial \omega}{\partial \sigma}\right)+hF_{\omega c}+h(P_\omega-\beta_\omega\omega^2) \tag{2.98}$$

The horizontal diffusion terms are defined as

$$hF_k\approx\frac{\partial}{\partial x}\left(\frac{h\nu_{t0}^h}{\sigma_k^h}\frac{\partial k}{\partial x}\right)+\frac{\partial}{\partial y}\left(\frac{h\nu_{t0}^h}{\sigma_k^h}\frac{\partial k}{\partial y}\right) \tag{2.99}$$

$$hF_\omega\approx\frac{\partial}{\partial x}\left(\frac{h\nu_{t0}^h}{\sigma_\omega^h}\frac{\partial \omega}{\partial x}\right)+\frac{\partial}{\partial y}\left(\frac{h\nu_{t0}^h}{\sigma_\omega^h}\frac{\partial \omega}{\partial y}\right) \tag{2.100}$$

In matrix form, the transport equations for k and ω may be written

$$\frac{\partial \boldsymbol{U}}{\partial t'}+\nabla\cdot\boldsymbol{F}-\boldsymbol{G}=\boldsymbol{S} \tag{2.101}$$

where $\boldsymbol{U}=(hk,h\omega)^T$ and $\boldsymbol{F}=\boldsymbol{F}^c-\boldsymbol{F}^d=(\boldsymbol{F}_x,\boldsymbol{F}_y,\boldsymbol{F}_\sigma)^T$. The flux components $\boldsymbol{F}$, the cross-diffusion $\boldsymbol{G}$ and the source terms $\boldsymbol{S}$ can be written

$$\boldsymbol{F}_x^c=\begin{pmatrix}huk\\hu\omega\end{pmatrix},\quad \boldsymbol{F}_y^c=\begin{pmatrix}hvk\\hv\omega\end{pmatrix},\quad \boldsymbol{F}_\sigma^c=\begin{pmatrix}hw_sk\\hw_s\omega\end{pmatrix} \tag{2.102}$$

$$\boldsymbol{F}_x^d=\begin{pmatrix}\frac{h\nu_{t0}^h}{\sigma_k^h}\frac{\partial k}{\partial x}\\\frac{h\nu_{t0}^h}{\sigma_\omega^h}\frac{\partial \omega}{\partial x}\end{pmatrix},\quad \boldsymbol{F}_y^d=\begin{pmatrix}\frac{h\nu_{t0}^h}{\sigma_k^h}\frac{\partial k}{\partial y}\\\frac{h\nu_{t0}^h}{\sigma_\omega^h}\frac{\partial \omega}{\partial y}\end{pmatrix},\quad \boldsymbol{F}_\sigma^d=\begin{pmatrix}\frac{\nu_{t0}^v}{h\sigma_k^v}\frac{\partial k}{\partial \sigma}\\\frac{\nu_{t0}^v}{h\sigma_\omega^v}\frac{\partial \omega}{\partial \sigma}\end{pmatrix} \tag{2.103}$$

$$\boldsymbol{G}=\begin{pmatrix}0\\hF_{\omega c}\end{pmatrix} \tag{2.104}$$

$$\boldsymbol{S}=\begin{pmatrix}h(P_k-\varepsilon)\\h(P_\omega-\beta_\omega\omega^2)\end{pmatrix} \tag{2.105}$$

3 Numerical method

The discretization in solution domain is performed using a cell-centered finite volume method (CCFV). The spatial domain is discretized by subdivision of the continuum into non-overlapping control volumes and by evaluating the field equations in integral form on these cells.

3.1 Mesh and discretization scheme

3.1.1 Mesh

The computational mesh is based on the unstructured meshes approach, which gives the maximum degree of flexibility. Control of node distribution allows for optimal usage of nodes and adaptation of mesh resolution to the relevant physical scales. The use of unstructured meshes also makes it possible to handle problems characterized by computational domains with complex boundaries.

The 3D mesh is a layered mesh. In the horizontal domain an unstructured mesh is used while in the vertical domain a structured mesh is used (see Figure 3.1). The elements are prisms with either a 3-sided or 4-sided polygonal base. Hence, the horizontal faces are either triangles or quadrilateral elements. The elements are perfectly vertical, and all layers have identical horizontal topology.

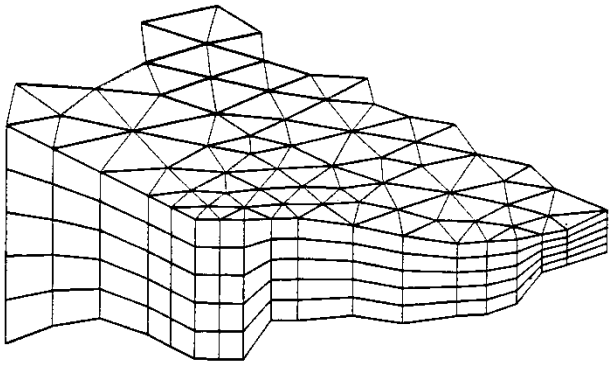


Figure 3.1 Principle of meshing

For the vertical discretization both a standard sigma discretization and a combined sigma/z-level discretization can be used. For the hybrid sigma/z-level discretization, sigma coordinates are used from the free surface to a specified depth, z_0, and z-level coordinates are used below. The different types of vertical discretization are illustrated in Figure 3.2. At least one sigma layer is needed using the sigma/z-level discretization to allow changes in the surface elevation.

Sigma

In the sigma domain a constant number of layers, $N_{\sigma,}$, is used, and the height of each sigma layer is a fixed fraction of the total depth of the sigma domain, h_σ, where $h_\sigma = \eta - \max(z_b, z_\sigma)$. The discretization in the sigma domain is given by a number of discrete σ-levels $\{\sigma_i,\ \ i = 1, (N_\sigma + 1)\}$. Here σ varies from $\sigma_1 = 0$ at the bottom interface of the lowest sigma layer to $\sigma_{N_\sigma+1} = 1$ at the free surface.

Variable sigma coordinates can be obtained using a discrete formulation of the general vertical coordinate (s-coordinate) system proposed by Song and Haidvogel (1994). First an equidistant discretization in an s-coordinate system *(-1≤ s ≤0*) is defined

$$s_i = -\frac{N_\sigma + 1 - i}{N_\sigma} \qquad i = 1, (N_\sigma + 1) \tag{3.1}$$

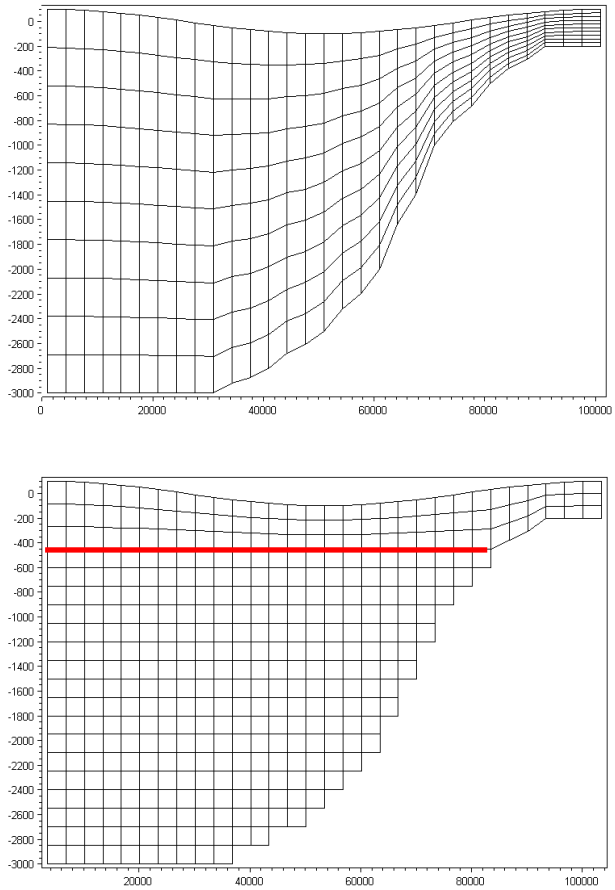


Figure 3.2 Illustrations of the different vertical grids. Upper: sigma mesh, Lower: combined sigma/z-level mesh with simple bathymetry adjustment. The red line shows the interface between the z-level domain and the sigma-level domain

The discrete sigma coordinates can then be determined by

$$\sigma_i = 1 + \sigma_c s_i + (1 - \sigma_c) c(s_i) \qquad i = 1, (N_\sigma + 1) \tag{3.2}$$

where

$$c(s) = (1 - b)\frac{\sinh(\theta s)}{\sinh(\theta)} + b\frac{\tanh\left(\theta\left(s + \frac{1}{2}\right)\right) - \tanh\left(\frac{\theta}{2}\right)}{2\tanh\left(\frac{\theta}{2}\right)} \tag{3.3}$$

Here σ_c is a weighting factor between the equidistant distribution and the stretch distribution, θ is the surface control parameter, and b is the bottom control parameter. The

range for the weighting factor is $0 < \sigma_c \leq 1$ where the value 1 corresponds to equidistant distribution, and 0 corresponds to stretched distribution. A small value of σ_c can result in linear instability. The range of the surface control parameter is $0 < \theta < 20$, and the range of the bottom control parameter is $0 \leq b \leq 1$. If $\theta \ll 1$ and $b = 0$, an equidistant vertical resolution is obtained. By increasing the value of θ, the highest resolution is achieved near the surface. If $\theta > 0$ and $b = 1$, a high resolution is obtained both near the surface and near the bottom.

Examples of a mesh using variable vertical discretization are shown in Figure 3.3 and Figure 3.4.

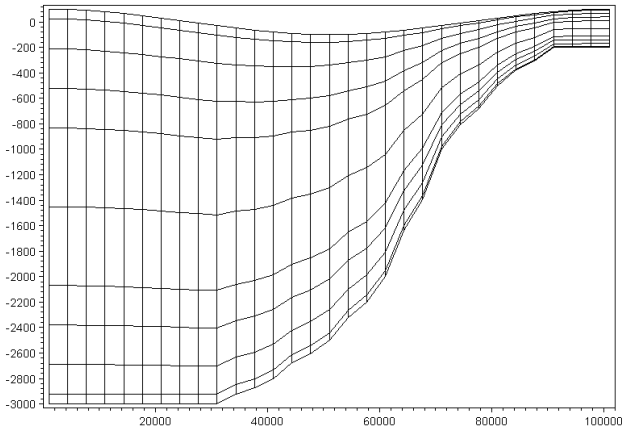


Figure 3.3 Example of vertical distribution using layer thickness distribution. Number of layers: 10, thickness of layers 1 to 10: .025, 0.075, 0.1, 0.01, 0.02, 0.02, 0.1, 0.1, 0.075, 0.025

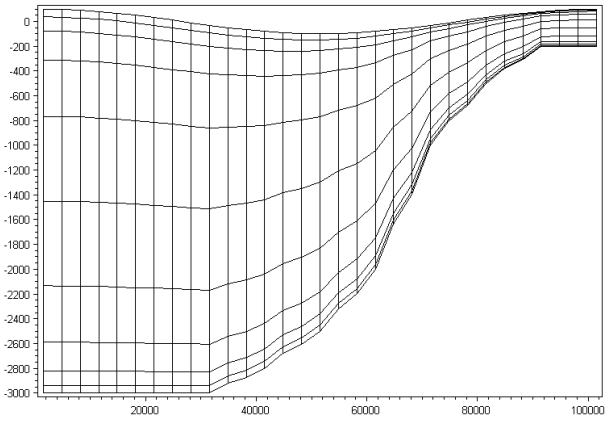


Figure 3.4 Example of vertical distribution using variable distribution. Number of layers: 10, σ_c = 0.1, θ = 5, b = 1

Combined sigma/z-level

In the z-level domain the discretization is given by a number of discrete z-levels $\{z_i,\ i = 1, (N_z + 1)\}$, where N_z is the number of layers in the z-level domain. z_1 is the minimum z-level, and z_{N_z+1} is the maximum z-level, which is equal to the sigma depth, z_σ. The corresponding layer thickness is given by

$$\Delta z_i = z_{i+1} - z_i \qquad i = 1, N_z \tag{3.4}$$

The discretization is illustrated in Figure 3.5 and Figure 3.6.

Using standard z-level discretization the bottom depth is rounded to the nearest z-level. Hence, for a cell in the horizontal mesh with the cell-averaged depth, z_b, each cell in the corresponding column in the z-domain is only included if the following criterion is satisfied

$$z_{i+1} - z_b \geq \frac{1}{2}(z_{i+1} - z_i) \qquad i = 1, N_z \tag{3.5}$$

The cell-averaged depth, z_b, is calculated as the mean value of the depth at the vertices of each cell in the horizontal mesh. To take into account the correct depth for the case where the bottom depth is below the minimum z-level ($z_1 > z_b$) a bottom fitted approach is used. Here, a correction factor, f_1, for the layer thickness in the bottom cell is introduced. The correction factor is used in the calculation of the volume and vertical face integrals. The correction factor for the bottom cell is calculated by

$$f_1 = \frac{(z_2 - z_b)}{\Delta z_1} \tag{3.6}$$

The corrected layer thickness is given by $\Delta z_1^* = f_1 \Delta z_1$. The simple bathymetry adjustment approach is illustrated in Figure 3.5.

For a more accurate representation of the bottom depth an advanced bathymetry adjustment approach can be used. For a cell in the horizontal mesh with the cell-averaged depth, z_b, each cell in the corresponding column in the z-domain is included if the following criterion is satisfied

$$z_{i+1} > z_b \qquad i = 1, N_z \tag{3.7}$$

A correction factor, f_i, is introduced for the layer thickness for these cells

$$f_i = min\left(max\left(\frac{(z_{i+1} - z_b)}{\Delta z_i}, \frac{z_{min}}{\Delta z_i}\right), 1\right) \qquad i = 2, N_z$$

$$f_i = max\left(\frac{(z_{i+1} - z_b)}{\Delta z_i}, \frac{z_{min}}{\Delta z_i}\right) \qquad i = 1 \tag{3.8}$$

A minimum layer thickness, Δz_{min}, is introduced to avoid very small values of the correction factor. The correction factor is used in the calculation of the volume and vertical face integrals. The corrected layer thicknesses are given by $\{\Delta z_i^* = f_i \Delta z_i,\ i = 1, N_z\}$. The advanced bathymetry adjustment approach is illustrated in Figure 3.6.

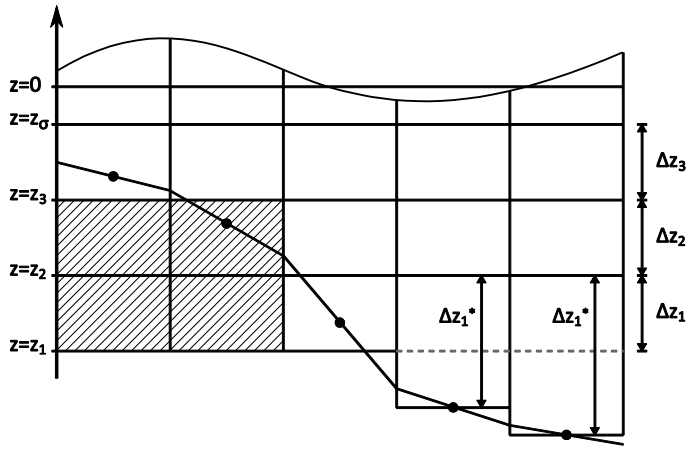


Figure 3.5 Simple bathymetry adjustment approach

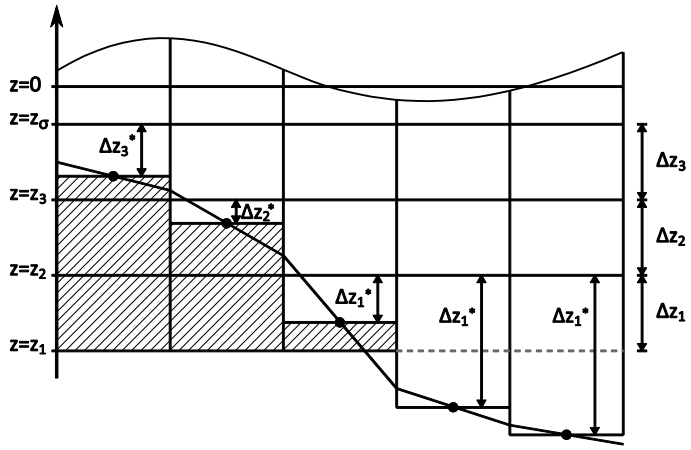


Figure 3.6 Advanced bathymetry adjustment approach

3.1.2 Discretization scheme

The discrete solution for the water depth, *h*, is defined at the centroid of the elements of the 2D horizontal mesh. The discrete solutions for the velocity components, u, v and w, and the turbulent variables, k and ε, are defined at the centroid of the elements of the 3D mesh. The non-hydrostatic pressure, q, is positioned in the centroid of the horizontal cell faces as shown in Figure 3.7. The location of the discrete non-hydrostatic pressure secures an exact representation of the surface boundary condition. The modified vertical velocity, ω, is also positioned in the centroid of the horizontal cell faces. The coordinates of the centroids are the averages of the coordinates of the cells vertices.

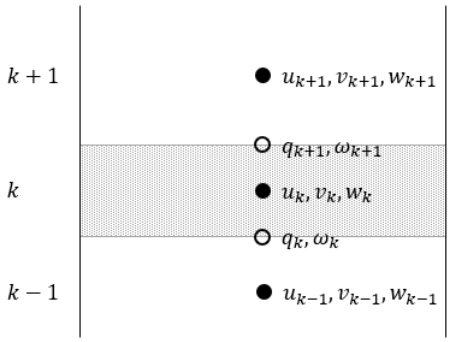


Figure 3.7 Vertical variable arrangement around layer k. Velocity components, u, v and w, are located in cell centers; non-hydrostatic pressure, q, is located in cell interfaces

3.2 Finite volume method

The matrix form of the governing equations presented in Chapter 2 can be written as

$$\frac{\partial \boldsymbol{W}}{\partial t} + \nabla \cdot \boldsymbol{F}(\boldsymbol{W}) = \boldsymbol{S} \tag{3.9}$$

Integrating Eq. (3.9) over the *i*th cell and using Gauss's theorem to rewrite the flux integral gives

$$\int_{V_i} \frac{\partial \boldsymbol{W}}{\partial t} d\Omega + \int_{\Gamma_i} (\boldsymbol{F}(\boldsymbol{W}) \cdot \boldsymbol{n})\, d\Gamma = \int_{V_i} \boldsymbol{S}(\boldsymbol{W}) d\Omega \tag{3.10}$$

where V_i is the volume of the *i*th cell, Ω is the integration variable defined on V_i, Γ_i is the boundary of the *i*th cell and Γ is the integration variable along the boundary. $\boldsymbol{n} = (n_x, n_y, n_z)^T$ is the unit outward normal vector along the boundary. Evaluating the volume integrals by a one-point quadrature rule, the quadrature point being the centroid of the cell, and evaluating the boundary integral using a mid-point quadrature rule, Eq. (3.10) can be written

$$\frac{\partial \boldsymbol{W}_i}{\partial t} + \frac{1}{V_i} \sum_{j}^{NF} \boldsymbol{F} \cdot \boldsymbol{n}_{ij} \Delta\Gamma_{ij} = \boldsymbol{S}_i \tag{3.11}$$

Here $\boldsymbol{W}_i$ and $\boldsymbol{S}_i$, respectively, are average values of $\boldsymbol{W}$ and $\boldsymbol{S}$ over the *i*th cell and stored at the cell centre. NF is the number of faces of the cell and the face ij is common to the cells associated with $\boldsymbol{W}_i$ and $\boldsymbol{W}_j$. $\Delta\Gamma_{ij}$ is the area of the face ij, and $\boldsymbol{n}_{ij}$ is the restriction of $\boldsymbol{n}$ to the face ij.

The normal flux $\boldsymbol{F}_n(\boldsymbol{W}_L, \boldsymbol{W}_R) = \boldsymbol{F}(\boldsymbol{W}_L, \boldsymbol{W}_R) \cdot \boldsymbol{n}_{ij}$ is determined from the variables, $\boldsymbol{W}_L$ and $\boldsymbol{W}_R$, to the left and right of the face ij. Using a first order scheme $\boldsymbol{W}_L = \boldsymbol{W}_i$ and $\boldsymbol{W}_R = \boldsymbol{W}_j$. Second-order spatial accuracy is achieved by employing a linear gradient-reconstruction technique. The face value at the vertical faces for the variable W in cell i is obtained by

$$W(x, y) = W_i + \nabla W_i \cdot \boldsymbol{r} \tag{3.12}$$

where (x,y) is the point where the value is required, $\boldsymbol{r}$ is the distance vector from the cell centre to the point (x,y) and ∇W_i is the gradient vector. For estimation of the gradient vector the Green-Gauss gradient approach is utilized. Here the procedure proposed by

Jawahar and Kamath (2000) is used. This procedure is based on a wide computational stencil to improve accuracy also for meshes with poor connectivity. The vertex (node) value is computed using the pseudo-Laplacian procedure proposed by Holmes and Connell (1989).

3.3 Numerical solution of the Navier-Stokes equations

3.3.1 Time integration

The time integration of the Navier-Stokes equations is performed using a semi-implicit scheme. The vertical convective and diffusive terms are discretized using an implicit scheme to remove the stability limitations associated with the vertical resolution. Here a second order implicit trapezoidal method is used (see Lambert (1973) and Hirsch (1990)). The remaining terms are discretized using a two-stage explicit second-order Runge-Kutta scheme (the midpoint method). The non-hydrostatic pressure is treated by a fractional step approach developed by Chorin (1968) called the projection method which is based on the Helmholtz-Hodge decomposition. In the sigma coordinate system, the integration procedure is

Stage 1:

$$\frac{h^{n+1/2}-h^n}{\Delta t/2} = -\left(\frac{\partial F_x^c}{\partial x'} + \frac{\partial F_y^c}{\partial y'}\right)^n \tag{3.13}$$

$$\frac{\boldsymbol{U}^* - \boldsymbol{U}^n}{\Delta t/2} = -\left(\frac{\partial \boldsymbol{F}_x^m}{\partial x'} + \frac{\partial \boldsymbol{F}_y^m}{\partial y'}\right)^n - \frac{1}{2}\left(\left(\frac{\partial \boldsymbol{F}_\sigma^m}{\partial \sigma}\right)^* + \left(\frac{\partial \boldsymbol{F}_\sigma^m}{\partial \sigma}\right)^n\right) + \boldsymbol{S}_h^n + \boldsymbol{S}_q^n \tag{3.14}$$

$$\frac{\boldsymbol{U}^{n+1/2} - \boldsymbol{U}^\star}{\Delta t/2} = \boldsymbol{S}_q^* \tag{3.15}$$

Stage 2:

$$\frac{h^{n+1}-h^n}{\Delta t} = -\left(\frac{\partial F_x^c}{\partial x'} + \frac{\partial F_y^c}{\partial y'}\right)^{n+1/2} \tag{3.16}$$

$$\frac{\boldsymbol{U}^* - \boldsymbol{U}^n}{\Delta t} = -\left(\frac{\partial \boldsymbol{F}_x^m}{\partial x'} + \frac{\partial \boldsymbol{F}_y^m}{\partial y'}\right)^{n+1/2} - \frac{1}{2}\left(\left(\frac{\partial \boldsymbol{F}_\sigma^m}{\partial z}\right)^* + \left(\frac{\partial \boldsymbol{F}_\sigma^m}{\partial z}\right)^n\right) + \boldsymbol{S}_h^{n+1/2} + \boldsymbol{S}_q^{n+1/2} \tag{3.17}$$

$$\frac{\boldsymbol{U}^{n+1} - \boldsymbol{U}^\star}{\Delta t} = \boldsymbol{S}_q^* \tag{3.18}$$

Calculating $\boldsymbol{S}_q^*$ requires knowledge of the non-hydrostatic pressure, q. The pressure is calculated solving a Poisson equation. The modified vertical velocity is calculated after the update of the water depth from Eq. (2.74).

Due to the explicit scheme, the time step interval, Δt, is restricted by the Courant-Friedrichs-Lewy (CFL) condition

$$C = \Delta t \frac{\left(\sqrt{gh} + |u|\right) + \left(\sqrt{gh} + |v|\right)}{\Delta l} \leq C_{max} \tag{3.19}$$

where C is the Courant number and Δl is a characteristic length. C_{max} is the maximum Courant number and must be less than or equal to 1. A variable time step interval is used in the time integration of the Navier-Stokes equations and determined so that the Courant number is less than a maximum Courant number in all computational nodes. The characteristic length for a prism, where the horizontal face is a quadrilateral element, is determined as the area of the element divided by the longest edge length of the element. If the horizontal face is a triangular element, the characteristic length is two times the area divided by the longest edge length.

3.3.2 Poisson equation

The Poisson equation is derived by differentiating the three components of the vector Eq. (3.15) and (3.18) by x', y' and σ and substituting the resulting expressions back into the continuity equation

$$\frac{\partial u}{\partial x'}+\frac{\partial u}{\partial \sigma}\frac{\partial \sigma}{\partial x}+\frac{\partial v}{\partial y'}+\frac{\partial v}{\partial \sigma}\frac{\partial \sigma}{\partial y}+\frac{1}{h}\frac{\partial w}{\partial \sigma}=0 \tag{3.20}$$

The resulting Poisson equation in sigma coordinates reads

$$\frac{\partial^2 q}{\partial x'^2}+\frac{\partial^2 q}{\partial y'^2}+\left(A_x^2+A_y^2+A_z^2\right)\frac{\partial^2 q}{\partial \sigma^2}+2A_x\frac{\partial^2 q}{\partial x'\partial \sigma}+2A_y\frac{\partial^2 q}{\partial y'\partial \sigma}+\left(\frac{\partial A_x}{\partial x'}+\frac{\partial A_y}{\partial y'}\right)\frac{\partial q}{\partial \sigma}=\frac{\rho_0}{\Delta t^*}\left(\frac{\partial u^\star}{\partial x'}+\frac{\partial v^\star}{\partial y'}+A_x\frac{\partial u^\star}{\partial \sigma}+A_y\frac{\partial v^\star}{\partial \sigma}+A_z\frac{\partial w^\star}{\partial \sigma}\right) \tag{3.21}$$

In the first stage $\Delta t^*=\Delta t/2$, and in the second stage $\Delta t^*=\Delta t$. The Poisson equation in Cartesian coordinate reads

$$\frac{\partial^2 q}{\partial x^2}+\frac{\partial^2 q}{\partial y^2}+\frac{\partial^2 q}{\partial z^2}=\frac{\rho_0}{\Delta t^*}\left(\frac{\partial u^\star}{\partial x}+\frac{\partial v^\star}{\partial y}+\frac{\partial w^\star}{\partial z}\right) \tag{3.22}$$

The surface and bottom boundary conditions for the non-hydrostatic pressure, q, in the sigma coordinate system are

at $z=\eta$

$$q=0 \tag{3.23}$$

$at\ z=-d$

$$\frac{\partial q}{\partial \sigma}=0 \tag{3.24}$$

For applications where the still water depth, d, is changing in time the following bottom boundary condition is used

$$\frac{\partial q}{\partial \sigma}=\rho_0 h\frac{\partial^2 d}{\partial t^2} \tag{3.25}$$

In a Cartesian coordinate system, the boundary condition at the bottom is

$$\frac{\partial \mathrm{q}}{\partial \mathrm{z}}=0 \tag{3.26}$$

3.3.3 Space discretization

The space discretization is performed using the finite volume method as described in Section 3.2. In this section the focus is on the discretization for the equations in the sigma coordinate system.

The normal convective flux $\boldsymbol{F}_n(\boldsymbol{U}) = \left(f_1, f_2, f_3, f_4\right)$ at the vertical faces in the sigma domain can be written

$$\boldsymbol{F}_n(\boldsymbol{U}) = \begin{pmatrix} hu_\perp \\ huu_\perp + \frac{1}{2}g(\eta^2 + 2\eta d)n_x \\ hvu_\perp + \frac{1}{2}g(\eta^2 + 2\eta d)n_y \\ hwu_\perp \end{pmatrix} \tag{3.27}$$

where $\boldsymbol{U} = (h, hu, hv, hw)^T$ is the solution vector, and $u_\perp = un_x + vn_y$ is the velocity perpendicular to the cell face. Here f_1 is the contribution to the continuity equation, and f_2, f_3 and f_4 are the contributions to the three momentum equations. This flux is reconstructed at cell-interfaces using the HLLC scheme introduced by Toro et al. (1994) for solving the Euler equations. The shock-capturing scheme enables robust and stable simulation of flows involving shocks or discontinuities such as bores and hydraulic jumps. This is essential for modelling of waves in the breaking zone or porous structures. The interface flux is computed as follows (see Toro (2001))

$$\boldsymbol{F}(\boldsymbol{U}_L, \boldsymbol{U}_R) \cdot \boldsymbol{n} = \begin{cases} \boldsymbol{F}_L & if\ S_L \geq 0 \\ \boldsymbol{F}_{*L} & if\ S_L < 0 \leq S_* \\ \boldsymbol{F}_{*R} & if\ S_* < 0 \leq S_R \\ \boldsymbol{F}_R & if\ S_R \leq 0 \end{cases} \tag{3.28}$$

where $\boldsymbol{F}_L = \boldsymbol{F}_n(\boldsymbol{U}_L)$ and $\boldsymbol{F}_R = \boldsymbol{F}_n(\boldsymbol{U}_R)$ are calculated from Eq. (3.27), and the middle region fluxes, $\boldsymbol{F}_{*L}$ and $\boldsymbol{F}_{*R}$ are given by

$$\boldsymbol{F}_{*L} = \begin{pmatrix} e_1 \\ e_2 n_x - u_{\parallel L} e_1 n_y \\ e_2 n_y + u_{\parallel L} e_1 n_x \\ e_3 \end{pmatrix} \tag{3.29}$$

$$\boldsymbol{F}_{*R} = \begin{pmatrix} e_1 \\ e_2 n_x - u_{\parallel R} e_1 n_y \\ e_2 n_y + u_{\parallel R} e_1 n_x \\ e_3 \end{pmatrix} \tag{3.30}$$

Here $u_\parallel = -un_y + vn_x$ is the velocity tangential to the cell face, and (e_1, e_2, e_3) is the component of the normal flux which is calculated using the HLL solver proposed by Harten et al. (1983)

$$\boldsymbol{E} = \frac{S_R \widehat{\boldsymbol{E}}_L - S_L \widehat{\boldsymbol{E}}_R + f_{HLLC} S_L S_R \left(\widehat{\boldsymbol{U}}_R - \widehat{\boldsymbol{U}}_L\right)}{S_R - S_L} \tag{3.31}$$

Here $\widehat{\boldsymbol{U}} = (h, hu_\perp, h\omega)^T$ and $\widehat{\boldsymbol{E}} = \left(hu_\perp, hu_\perp u_\perp + \frac{1}{2}g(\eta^2 + 2\eta d), h\omega\right)^T$. To be able to scale the damping introduced by the HLLC solver a scaling factor f_{HLLC} has been introduced, where the factor must be in the interval [0,1]. The scaling factor, $f_{HLLC} = 1$, corresponds to the standard HLLC solver.

An appropriate method for approximating the wave speeds is essential for the efficiency of the HLLC solver. Different approximations can be found in the literature, e.g. Fraccarollo and Toro (1994). Here the approach used by Song et al. (2011) is used

$$S_L = \begin{cases} u_{\perp R} - 2\sqrt{gh_R} & h_L = 0 \\ min\left(u_{\perp L} - \sqrt{gh_L}, u_{\perp *} - \sqrt{gh_*}\right) & h_L > 0 \end{cases} \tag{3.32}$$

and

$$S_R = \begin{cases} u_{\perp L} + 2\sqrt{gh_L} & h_R = 0 \\ max\left(u_{\perp R} + \sqrt{gh_R}, u_{\perp *} + \sqrt{gh_*}\right) & h_R > 0 \end{cases} \tag{3.33}$$

where the Roe-averaged quantities

$$u_{\perp *} = \frac{u_{\perp L}\sqrt{h_L} + u_{\perp R}\sqrt{h_R}}{\sqrt{h_L} + \sqrt{h_R}} \tag{3.34}$$

$$h_* = \frac{1}{2}(h_L + h_R) \tag{3.35}$$

The speed S_* is given by the

$$S_* = \frac{S_L h_R(u_{\perp R} - S_R) - S_R h_L(u_{\perp L} - S_L)}{h_R(u_{\perp R} - S_R) - h_L(u_{\perp L} - S_L)} \tag{3.36}$$

The convective flux at the horizontal faces is calculated using a second-order upwinding scheme. The diffusive flux at the cell interfaces is approximated by a central scheme. This vertical discretization results in a linear five-diagonal system which has to be solved for each column of the discrete momentum equation.

Discretization of the Poisson pressure equation is performed by integrating over the individual control volumes. The procedure results in a large sparse linear system that needs to be solved in each of the two stages in the time integration procedure. This sparse linear system of equations is solved using an iteractive solver from the PETSc library, Balay (2017). More specifically, the iterative solver is the restarted Generalized Minimal Residual method (GMRES), which for single-subdomain simulations is preconditioned with a two-level incomplete LU factorization, ILU(2). For multi-subdomain simulations the Block Jacobi preconditioner is used, where each block is solved with ILU(2). Each block coincides with the division of variables over the processors. See Chapter 5 for further details on single- and multi-subdomain simulations.

3.3.4 Flooding and drying

The approach for treatment of the moving boundaries (flooding and drying fronts) problem is based on the work by Zhao et al. (1994) and Sleigh et al. (1998). When the depths are small the problem is reformulated, and only when the depths are very small the elements/cells are removed from the calculation. The reformulation is made by setting the momentum fluxes to zero and only taking the mass fluxes into consideration.

The depth in each element is monitored and the elements are classified as dry, partially dry or wet. Also, the element faces are monitored to identify flooded element faces.

- An element face is defined as flooded if the water depth at one side of a face is less than a tolerance depth, h_{dry}, and the water depth at the other side of the face is larger than a tolerance depth, h_{wet}.
- An element is dry if the water depth is less than a tolerance depth, h_{dry}, and none of the element faces are flooded faces. The element is removed from the calculation.
- An element is partially dry if the water depth is larger than h_{dry} and less than a tolerance depth, h_{wet}, or when the depth is less than h_{dry}, and one of the element faces is a flooded face. The momentum fluxes are set to zero, and only the mass fluxes are calculated.
- An element is wet if the water depth is bigger than h_{wet}. Both the mass flux and the momentum flux are calculated.

A non-physical flow across the face will be introduced for a flooded face when the surface elevation in the wet element on one side of the face is lower than the bed level in the partially wet element on the other side. To overcome this problem the face will be treated as a closed boundary (Section 3.3.7).

In case the water depth becomes negative, the water depth is set to zero, and the water is subtracted from the adjacent elements to maintain mass balance. When this occur the water depth at the adjacent elements may become negative. Therefore, an iterative correction of the water depth is applied (max. 100 iterations). Normally only one or a few correction steps are needed.

3.3.5 Sponge layer

Sponge (or absorbing) layers can be used as efficient numerical wave absorbers in wave simulations. These could be set up along model boundaries to provide radiation boundary conditions, which absorb wave energy propagating out of the model area.

The implemented method is based on the sponge layer technique introduced by Larsen and Dancy (1983). In the sponge layer the calculated surface elevation, η, and the velocities u, v and w, are corrected at every time step as

$$\eta = \frac{\eta - \eta^{ref}}{c} + \eta^{ref} \qquad u = \frac{u}{c} \qquad v = \frac{v}{c} \qquad w = \frac{w}{c} \tag{3.37}$$

where c is the sponge coefficient, and η^{ref} is the reference level.

To minimize reflections, the values of the sponge layer coefficient, c, should be close to unity along the front edge of the sponge layer and should increase smoothly towards the closed/land boundary. When selecting the sponge layer coefficient, c, the following formula has been found to work well

$$c = a^{r^{s/\Delta s}}, \quad 0 \le s \le w \tag{3.38}$$

where w is the width of the sponge layer, and a and r are assigned constant values. s is the distance from the closed boundary, and Δs is the characteristic size of the elements in the sponge layer area. Depending on ratio $w/\Delta s$ you may use the values listed in Table 3.1.

Table 3.1 Recommended values for sponge layer coefficients

w/Δs	a	r
10	5	0.5
20	7	0.7
50	10	0.85
100	10	0.92
200	10	0.95

3.3.6 Internal wave generation

The relaxation zone technique is applied for wave generation and absorption. Here a relaxation function is applied to introduce the analytical solution for the incoming waves smoothly into the calculation domain. The analytical solution is the target solution and contains values from the chosen wave theory for the surface elevation, the velocities and the pressure. The relaxation zone is defined as the area to the right of the polyline when positioned at the starting point and looking forward along the line (see Figure 3.8). The target and the computed solution are weighted in the relaxation zone after each step in the time integration

$$\theta = \alpha\theta_{Computed} + (1-\alpha)\theta_{Target} \tag{3.39}$$

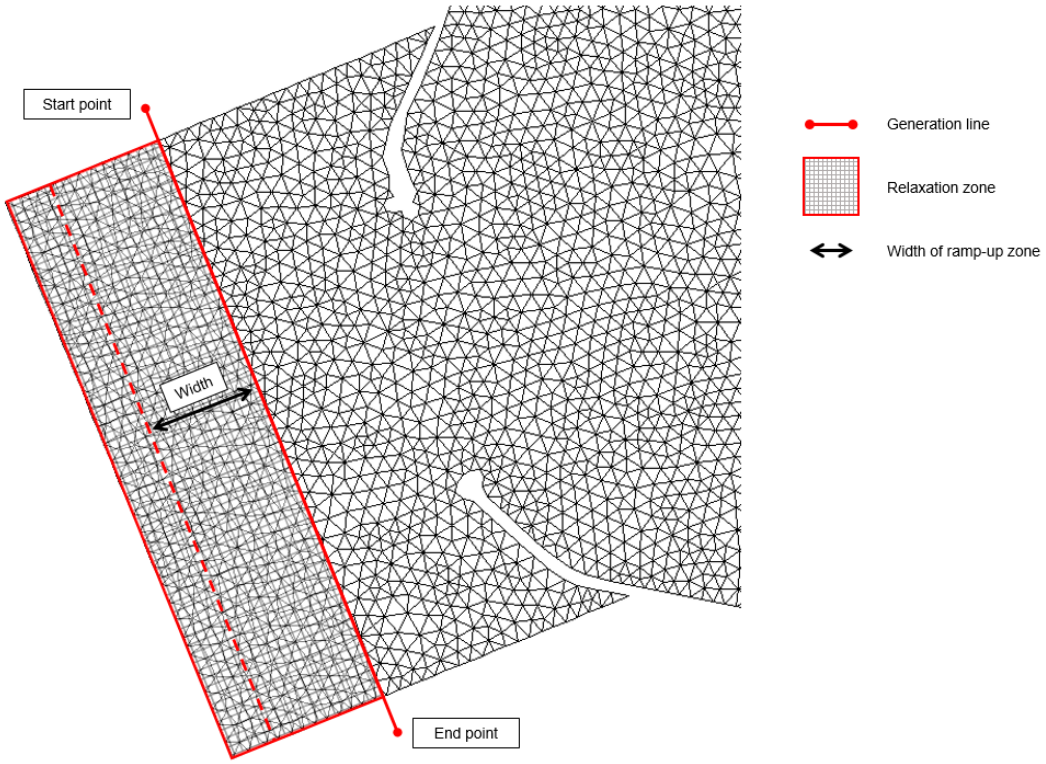


Figure 3.8 The relaxation zone is the area to the right of the generation line when looking forward along the line from the starting point. The width of the ramp-up zone is specified by the width parameter.

where θ represents the surface elevation, velocity component and non-hydrostatic pressure. For the surface elevation and velocities the ramp up factor, α, is given as

$$\begin{aligned} \alpha &= 1 - \frac{exp(s^f)-1}{\exp(1)-1} && 0 \le s \le 1 \\ \alpha &= 0 && s > 1 \end{aligned} \tag{3.40}$$

Here, s is the distance from the polyline divided by the width of the ramp up zone, and f is the ramp up factor. The value $f = 3.5$ is applied. For the non-hydrostatic pressure, q, the target value is applied as a Dirichlet condition for $s > 1$. Hence, here the ramp up factor is given by

$$\begin{aligned} \alpha &= 1 && 0 \le s \le 1 \\ \alpha &= 0 && s > 1 \end{aligned} \tag{3.41}$$

For unidirectional regular waves Stokes theory (1th and 5th order) and stream function theory (Fenton (1988)) can be applied. For irregular waves the single summation method is applied. Here a single direction is assigned to each discrete frequency. A range of standard formulations for the frequency spectrum and the directional distribution are applied.

3.3.7 Boundary conditions

At the lateral closed (solid) boundaries, either a condition of zero velocity or a condition of zero normal velocity is imposed. A condition of zero velocity, $u = v = w = 0$, is also called a no-slip condition. For a condition with zero normal velocity, $u_\perp = 0$, the normal flux vector is

$$\boldsymbol{F}_n(\boldsymbol{U}) = \begin{pmatrix} 0 \\ \frac{1}{2} g(\eta^2 + 2\eta d) n_x \\ \frac{1}{2} g(\eta^2 + 2\eta d) n_y \\ 0 \end{pmatrix} \tag{3.42}$$

For the zero normal velocity condition, a wall friction can be applied, see section 4.3. If the normal velocity is zero and there is no wall friction, the tangential stress is set to zero and this boundary condition is sometimes called a full-slip condition. At the lateral closed boundaries, the normal pressure gradient is zero.

3.4 Numerical solution of the Transport equations

3.4.1 Time integration

The time integration is performed using either a first order explicit Euler method or a second-order explicit Runge-Kutta scheme (the midpoint method). However, to overcome the severe time step restriction due to small vertical grid spacing, the vertical convective and diffusive terms are treated implicitly. The vertical diffusion term is treated using a second order implicit trapezoidal method. The vertical convective term is treated either using the explicit method or an implicit Euler method, and the same method is used for all discrete equations in a column of the 3D mesh. The explicit method is used when the following criteria are satisfied

Sigma domain

$$\frac{\omega_i \Delta t}{\Delta \sigma_i} < \frac{1}{2} \tag{3.43}$$

z-level domain

$$\frac{w_i \Delta t}{\Delta z_i} < \frac{1}{2} \tag{3.44}$$

for all elements in the column. Here ω_i is the modified vertical velocity and $\Delta\sigma_i$ the vertical grid spacing in the sigma domain. w_i is the vertical velocity and Δz_i the vertical grid spacing in the z-level domain. Finally, Δt is the discrete time step interval. For details of the time integration methods, see Lambert (1973) and Hirsch (1990).

The transport equations for the turbulence model are solved using the same time step as used for solving the Navier-Stokes equations.

3.4.2 Spatial discretization

The normal flux due to the convective terms at the vertical faces is calculated using simple upwinding. It is calculated as the mass flux times the values in the upwind direction. Both a first order and a second order scheme can be applied for the spatial discretization. The second order version approximates the horizontal gradients to obtain second order accurate values at the vertical faces (see Section 3.2). To provide stability and minimize oscillatory effects, an ENO (Essentially Non-Oscillatory) type procedure is applied to limit the horizontal gradients in combination with a simple min-max face value limiter. When the explicit time integration approach is used for the vertical convective terms, the calculation of the normal flux due to the convective terms at the horizontal faces is performed using a 3rd order ENO procedure (Shu, 1997). When the implicit time integration approach is used for the vertical convective terms the normal flux is calculated using a first-order upwinding scheme.

3.4.3 Boundary conditions

Solving the transport equations for the turbulence model, the lateral closed boundary conditions depend on the boundary conditions for the flow equations. In case of no-slip condition or in case of zero normal velocity where wall friction is applied, a Dirichlet boundary condition is applied. The values in the elements at the wall are calculated using the wall functions in eq. (2.59) . In this case, $\Delta y = \Delta y_w$ is the distance to the wall from the center of the elements and $U_\tau = U_{\tau w}$ is the friction velocity associated with the wall stress, see section 4.3. In case of zero normal velocity without wall friction, the normal convective flux is zero, and the normal gradient of the transport variables is zero.
zero.

3.5 Time stepping procedure

The solution is determined at sequence of discrete times

$$t^k = t^0 + k\Delta t_{overall} \qquad k = 0, 1, 2, 3 \ldots \tag{3.45}$$

where $\Delta t_{overall}$ is the overall time step interval. The time steps for the hydrodynamic calculations are dynamic.

At the actual time t in the interval $t^{k-1} < t \leq t^k$ the new time step interval is determined using the following procedure

$$\Delta t^* = C_{max} min\left(\frac{\Delta l}{\left(\sqrt{gh_i} + |u_i|\right) + \left(\sqrt{gh_i} + |v_i|\right)}\right) \tag{3.46}$$

$$\Delta t^{**} = min\left(max(\Delta t, \Delta t_{min}), \Delta t_{max}\right) \tag{3.47}$$

$$\Delta t = \frac{t^k - t}{int\left(\frac{(t^k - t)}{\Delta t^{**}}\right) + 1} \tag{3.48}$$

Here Δt_{min} and Δt_{max} are the minimum and maximum time steps, respectively, and int is the whole number of $(t^k - t)/\Delta t$. This procedure secures that the time steps for the hydrodynamic calculations are synchronized at the overall discrete time steps.

4 Physics

4.1 Eddy viscosity

Both the vertical and horizontal eddy viscosity can be derived solving a turbulence closure model (see section 2.1.2). In that case the eddy viscosity is calculated using eq. (2.18) or (2.39). In some applications, a constant eddy viscosity can be used for the horizontal eddy viscosity. Alternatively, Smagorinsky (1963) proposed to express sub-grid scale transports by an effective eddy viscosity related to a characteristic length scale. The sub-grid scale eddy viscosity is given by

$$\nu_t^h = c_s^2 l^2 \sqrt{2\left(S_{xx}S_{xx} + 2S_{xy}S_{xy} + S_{yy}S_{yy}\right)} \tag{4.1}$$

where c_s is a constant, l is a characteristic length and the deformation rate is given by

$$S_{xx} = \frac{\partial u}{\partial x} \quad S_{xy} = \frac{1}{2}\left(\frac{\partial u}{\partial y} + \frac{\partial v}{\partial x}\right) \quad S_{yy} = \frac{\partial v}{\partial y} \tag{4.2}$$

For more details on this formulation, the reader is referred to Lilly (1967), Leonard (1974), Aupoix (1984), and Horiuti (1987).

4.2 Bed resistance

The bottom stress, $\boldsymbol{\tau}_b = (\tau_{bx}, \tau_{bx})$ is determined by a quadratic friction law

$$\frac{\boldsymbol{\tau}_b}{\rho_0} = c_f \boldsymbol{u}_b |\boldsymbol{u}_b| \tag{4.3}$$

where c_f is the drag coefficient, and, $\boldsymbol{u}_b = (u_b, v_b)$ is the flow velocity at a distance Δz_b above the seabed, and the drag coefficient is determined by assuming a logarithmic profile between the seabed and a point Δz_b above the seabed

$$c_f = \frac{1}{\left(\frac{1}{\kappa}\ln\left(\max\left(\frac{\Delta z_b}{z_0}, 2\right)\right)\right)^2} \tag{4.4}$$

where $\kappa = 0.41$ is the von Kármán constant, and z_0 is the bed roughness length scale. When the boundary surface is rough, z_0 depends on the roughness height, k_s, trough

$$z_0 = m k_s \tag{4.5}$$

where m is approximately 1/30.

The friction velocity associated with the bottom stress is given by

$$U_{\tau b} = \sqrt{c_f |\boldsymbol{u}_b|^2} \tag{4.6}$$

A semi-implicit discretization is used to get a stable solution for small water depths, which for element i reads

First stage:

$$\frac{\boldsymbol{\tau}_{bi}^{n+1/2}}{\rho_0} = c_f^n |\boldsymbol{u}_i^n| \boldsymbol{u}_i^* \tag{4.7}$$

Second stage:

$$\frac{\boldsymbol{\tau}_{bi}^{n+1}}{\rho_0} = c_f^n \left|\boldsymbol{u}_i^{n+1/2}\right| \boldsymbol{u}_i^* \tag{4.8}$$

Here the $*$ indicates the provisional value of the velocity.

4.3 Wall friction

For closed lateral boundary with zero normal velocity and wall friction, the stress $\boldsymbol{\tau}_w$ tangential to the wall is determined by a quadratic friction law

$$\boldsymbol{\tau}_w = \rho_0 c_f \boldsymbol{u}_{wall} |\boldsymbol{u}_{wall}| \tag{4.9}$$

Here, c_f is the drag coefficient and $\boldsymbol{u}_{wall}$ is the velocity tangential to the wall at a distance Δy_w to the wall; $\boldsymbol{u}_{wall}$ and Δy_w are evaluated at the cell center. The drag coefficient is given by

$$c_f = \frac{1}{\left(\frac{1}{\kappa}\ln\left(\max\left(\frac{\Delta y_w}{y_0}, 2\right)\right)\right)^2} \tag{4.10}$$

where $\kappa = 0.41$ is the von Kármán constant and y_0 is the wall roughness length scale given by

$$y_0 = m k_s \tag{4.11}$$

The parameter k_s is a wall roughness height and $m \approx 1/30$. Furthermore, the friction velocity $U_{\tau w}$ at the wall is determined as follows (Fuhrman et. al. (2014)).

$$U_{\tau w} = \sqrt{c_f |\boldsymbol{u}_{wall}|^2} \tag{4.12}$$

For a closed lateral boundary with zero velocity (i.e., a no-slip condition), the friction velocity can be determined using the law of the wall (Bredberg (2008), Wilcox (1998))

$$\frac{|\boldsymbol{u}_{wall}|}{U_{\tau w}} = \frac{1}{\kappa}\ln\left(\frac{U_{\tau w}\Delta y_w}{\nu}\right) + B \tag{4.13}$$

Here, ν is the kinematic viscosity of water and $B = 5.1$ is an empirically determined constant. Eq. (4.13) is solved iteratively to find $U_{\tau w}$, the friction velocity at the wall, and this value can be used in the boundary conditions of the turbulence models described in section 2.1.2.

4.4 Porosity

For wave simulations, the governing equations have been modified to include porosity and the effects of non-Darcy flow through porous media. In this way, it is possible to model partial reflection, absorption and transmission of wave energy at porous structures such as rubble mound breakwaters.

The main effects of porosity are introduced by additional laminar and turbulent friction terms for describing losses due to flow through a porous structure. In most practical cases the pore sizes are relatively large (typically 0.1m to 1.0m), and the turbulent losses will dominate. The laminar loss term has also been included to allow the simulation of small scale physical model tests.

The flow resistance inside the porous structure is described by the linear and non-linear resistance forces expressed as

$$\boldsymbol{F} = \rho a \boldsymbol{u} + \rho b |\boldsymbol{u}| \boldsymbol{u} \tag{4.14}$$

where a and b are resistance coefficients accounting for the laminar and turbulent friction loss, respectively, $\boldsymbol{u} = (u, v, w)$ is the velocity vector, and the magnitude of the flow velocity is defined by $|\boldsymbol{u}| = \sqrt{u^2 + v^2 + w^2}$. a and b are determined by the empirical expressions formulated by van Gent (1995) and Liu et al. (1999)

$$a = \alpha \frac{(1-n)^2}{n^3} \frac{\vartheta}{D_{50}^2} \tag{4.15}$$

$$b = \beta \left(1 + \frac{7.5}{KC}\right) \frac{(1-n)}{n^2} \frac{1}{D_{50}} \tag{4.16}$$

Where n is the porosity, α and β are user specified coefficients, ϑ is the kinematic viscosity and D_{50} is the grain diameter of the porous materials. KC is the Keulegan-Carpenter number defined as

$$KC = \frac{u_m T}{n D_{50}} \tag{4.17}$$

where u_m is the maximum oscillating velocity, and T is the period of the oscillation. u_m is approximated by the magnitude of the flow velocity.

In the momentum equations the time derivative terms are multiplied by a factor $(1 + C_m)$ where C_m is the added mass coefficient to take transient interaction between grains and water into account. van Gent (1995) gave C_m as

$$c_m = \gamma \frac{1-n}{n} \tag{4.18}$$

where γ is an empirical coefficient, which takes the value 0.34.

In the transport equations for the k-ε model additional production terms are included for porous media flow following the approach by Nakayama and Kuwahara (1999) and Hsu et al. (2002).

In the sigma domain the z-coordinate (in the physical domain) of the element centers is varying in time. Therefore the porosity has to be updated at each calculation step. Here, a

bilinear interpolation is applied for mapping the specified porosity map onto the calculation mesh.

5 Parallelization

The MIKE 3 Wave Model FM is parallelized for shared-memory multiprocessor/multicore computers using OpenMP. This parallelization is performed by adding compiler directives to the code. To improve performance and to be able to perform simulations on large massively parallel distributed-memory computers and clusters, MIKE 3 Wave Model FM has also been parallelized using domain decomposition concept and Message Passing Interface (MPI). Given the number of processor cores allocated to a simulation, the computational mesh is partitioned into subdomains, and the workload associated with each domain is distributed between the allocated cores. The data exchange between domains is performed by message passing using the Intel MPI Library, which has multi fabric message passing capabilities. It allows the use of mixed communication between the domains. Thus, domains will exchange data via the fastest communication interface – in ranked order: shared memory, InfiniBand, Ethernet, etc.. The implementation uses a hybrid approach (OpenMP and MPI).

5.1 The domain decomposition

The domain partitioning is performed using the METIS graph partitioning library (Karypis and Kumar, (1998, 1999)). The computational mesh is converted into a graph, and then METIS uses a multi-level graph partitioning scheme to split the graph into subgraphs, representing the partitioned subdomains, which are distributed among the allocated cores. METIS computes a balanced partitioning that minimizes the connectivity of the subdomains. This partitioning is performed based on the 2D (horizontal) mesh. Using a 2D mesh to partition a 3D domain can cause unbalanced partitioning. When combined sigma/z-level discretization is used in 3D flow calculations, the number of vertical elements can vary significantly across the domain. This difference in the number of vertical elements can lead to an unbalanced partitioning. To get a balanced partitioning for a 3D mesh, weights corresponding to the actual number of vertical elements associated to each vertex of the graph are used. The partitioning is then made so that the sum of vertex-weights is the same for all subdomains. Hence, with both 2D and 3D meshes, the partitioning strategy ensures that the difference in the number of elements in all subdomains is minimized.

The chosen numerical scheme for the discretization in the spatial domain requires an overlapping domain decomposition. It is based on the halo-layer (“ghost”-cells) approach, where each subdomain contains elements from connected subdomains. This overlap is needed, because calculations require values from the connecting elements. Thus, calculations of some elements at the border between subdomains require values from the connected subdomains.

5.2 Data exchange

The data exchange between processes is based on the aforementioned halo-layer (“ghost”-cells) approach with overlapping elements. The extension of the halo-layer area depends on the numerical scheme used for the discretization in the spatial domain and which variables are chosen to be exchanged between subdomains. Here a two-element wide halo-layer is applied. The data exchanges are performed via asynchronous communication when possible, and synchronous communications are used in different parts of the system to ensure correct execution. The MIKE 3 Wave Model FM uses a dynamic time step in the time integration scheme. To ensure that the calculations are performed with the same time step in all subdomains, time step information is exchanged between processes and thereby synchronizing the processes of each time step. Several

special features require additional data exchange. These special interest points cause synchronization of two or more subdomains during the data exchange. The case of input and output data exchange is mentioned in the next subsection. Finally, information is exchanged between subdomains in connection with error handling. When the system encounters an error in the model, the error is distributed to the other processes when the time step is finished and the simulation is stopped.

5.3 Input and output

The input and output (I/O) is handled using a parallel I/O approach. The master process reads the global mesh information, performs the partitioning of the mesh and distributes the information about the individual subdomains to the slave processes. Each process then reads the additional input specifications using the generic specification file. The input data (porosity maps, sponge layer maps, etc.) are read by each process using the global data files. Since the individual processes perform I/O locally, the simulation data files must be accessible by each process. This access could be through a network-attached storage system or locally on each computer. The output data files from the simulations are written to private files for each subdomain. At the end of the simulation, the data files are merged to obtain data files containing global information.

6 References

/1/ Aupoix, B. (1984), Eddy Viscosity Subgrid Scale Models for HomogeneousTurbulence, in Macroscopic Modelling of Turbulent Flow, Lecture Notes in Physics, Proc. Sophie-Antipolis, France.

/2/ Balay, S. K. (2017), *PETSc User Manual*, Tech. Rep. ANL-95/11-Revision 3.8, Mathematics and Computer Science Division., Argonne National Lab.

/3/ Bredberg, J. (2000). On the wall boundary condition for turbulence models. *Chalmers University of Technology, Department of Thermo and Fluid Dynamics. Internal Report 00/4. G oteborg*, 8-16.

/4/ Chippada, S., Dawson, C.N., Martinez, M.L. and Wheeler, M.F. (1998), *A Godunov-type finite volume method for the system of Shallow Water Equations*, Computational Methods in Applied Mechanics and Engineering, 151, 105-129.

/5/ Chorin, A. J. (1968), *Numerical Solution of the Navier-Stokes Equations*, Math. Comp., 22.

/6/ Fenton, J. D. (1988), *The numerical solution of steady water wave problems*, Computers & Geosciences, Vol. 14, No. 3, pp 357-368.

/7/ Fraccarollo I., Toro E.F. (1994), *Experimental and numerical assessment of the shallow water model for two-dimensional dam-break type problems*, Journal of Hydraulic Research 33, 951-979.

/8/ Fuhrman, D. R., Baykal, C., Sumer, B. M., Jacobsen, N. G., & Fredsøe, J. (2014). Numerical simulation of wave-induced scour and backfilling processes beneath submarine pipelines. *Coastal engineering*, *94*, 10-22.

/9/ Harten A., Lax P.D., Van Leer B. (1983), *On upstream differencing and Godunov-type schemes for hyperbolic conservation-laws*, SIAM Rev 25(1), 54-74.

/10/ Hirsch, C. (1990). *Numerical Computation of Internal and External Flows,* Volume 2: Computational Methods for Inviscid and Viscous Flows, Wiley.

/11/ Holmes, D. G. and Connell, S. D. (1989), *Solution of the 2D Navier-Stokes on unstructured adaptive grids*, AIAA Pap. 89-1932 in Proc. AIAA 9th CFD Conference.

/12/ Horiuti, K. (1987), Comparison of Conservative and Rotational Forms in Large Eddy Simulation of Turbulent Channel Flow, Journal of Computational Physics, 71, pp 343-370.

/13/ Hsu T.-J., Sakakiyama T., Liu P.L.-F. (2002), *A numerical model for wave motions ad turbulent flows in front of a composite breakwater*, Coastal Eng. 55, 1148-1158.

/14/ Jawahar P. and Kamath H. (2000), *A high-resolution procedure for Euler and Navier-Stokes computations on unstructured grids*, Journal of Computational Physics, 164, 165-203.

/15/ Karypis G., Kumar .V. (1998), *METIS: family of multilevel partitioning algorithms*, Available from: http://glaros.dtc.umn.edu/gkhome/views/metis

/16/ Karypis G., V. Kumar (1999), *A Fast and Highly Quality Multilevel Scheme for Partitioning Irregular Graphs*, SIAM Journal on Scientific Computing, Vol. 20, No. 1, 1999, pp. 359—392.

/17/ Lambert J.D. (1973), *Computational Methods in ordinary Differential Equations*, John Willey & Sons.

/18/ Larsen, B. E., & Fuhrman, D. R. (2018). On the over-production of turbulence beneath surface waves in Reynolds-averaged Navier–Stokes models. *Journal of Fluid Mechanics*, *853*, 419-460.

/19/ Larsen, J., & Dancy, H. (1983), *Open Boundaries in Short-wave Simulations - A New Approach*, Coastal Engineering, 7, 285-297.

/20/ Leonard, A. (1974), Energy Cascades in Large-Eddy Simulations of Turbulent Fluid Flows, Advances in Geophysics, 18, pp 237-247.

/21/ Song, L. Zhou J., Guo J., Zou Q., and Liu Y. (2011), *A robust well-balanced finite volume model for shallow water flows with wetting and drying over irregular terrain*, Advances in Water Resources, vol. 34, no. 7, 915–932.

/22/ Liang Q., Borthwick A.G.L, (2009), *Adaptive quadtree simulation of shallow flows with wet-dry fronts over complex topography*, Computers and Fluids 38, 221-234.

/23/ Lilly, D.K. (1966), On the Application of the Eddy Viscosity Concept in the Inertial Subrange of Turbulence, NCAR Manuscript No. 123, National Center for Atmospheric Research, Boulder, Colorado.

/24/ Nakayama A., Kuwahara F. (1999), *A Macroscopic Turbulence Model for Flow in a Porous Medium*, Journal of Fluid Eng., 121, 427-422

/25/ Quecedo, M. and Pastor, M. (2002), *A reappraisal of Taylor-Galerkin algorithm for drying-wetting areas in shallow water computations*, International Journal for Numerical Methods in Fluids, 38, 515-531.

/26/ Rodi, W. (1984), *Turbulence models and their applications in hydraulics,* IAHR, Delft, the Netherlands.

/27/ Rodi, W. (1980), *Turbulence Models and Their Application in Hydraulics – A State of the Art Review*, Special IAHR Publication.

/28/ Rogers, B., Fujihara, M. and Borthwick, A.G.L. (2001), *Adaptive Q-tree Godunov-type scheme for shallow water equations*, International Journal for Numerical Methods in Fluids, 35, 247-280.

/29/ Shu C.W. (1997), *Essentially Non-Oscillatory and Weighted Essentially Non-Oscillatory Schemes for Hyperbolic Conservation Laws*, NASA/CR-97-206253, ICASE Report No. 97-65, NASA Langley Research Center, pp. 83.

/30/ Sleigh, P.A., Gaskell, P.H., Bersins, M. and Wright, N.G. (1998), *An unstructured finite-volume algorithm for predicting flow in rivers and estuaries*, Computers & Fluids, Vol. 27, No. 4, 479-508.

/31/ Smagorinsky J. (1963), *General Circulation Experiment with the Primitive Equations*, Monthly Weather Review, 91, No. 3, 99-164.

/32/ Song, Y and Haidvogel D. (1994), *A semi-implicit ocean circulation model using a generalized topography-following coordinate system*, Journal of Comp. Physics, 115, pp. 228-244.

/33/ Toro, E.F. (2001), *Shock-capturing methods for free-surface flows*, Chichester, John Wiley & Sons.

/34/ Toro, E.F., Spruce, M., Speares, W. (1994). Restoration of the contact surface in the HLL-Riemann solver. Shock Waves 4, 25–34.

/35/ van Gent, M. R. A. (1995), *Wave Interaction with Permeable Coastal Structures*, (Ph.D. thesis), Delft University.

/36/ Wilcox, D. C. (1998). *Turbulence modeling for CFD* (Vol. 2, pp. 103-217). La Canada, CA: DCW industries.

/37/ Wilcox, D. C. (2008). Formulation of the kw turbulence model revisited. *AIAA journal*, *46*(11), 2823-2838.

/38/ Zhao, D.H., Shen, H.W., Tabios, G.Q., Tan, W.Y. and Lai, J.S. (1994), *Finite volume 2-dimensional unsteady-flow model for river basins*, Journal of Hydraulic Engineering, ASCE, 1994, 120, No. 7, 863-833.

APPENDICES

APPENDIX A – Governing equations in spherical coordinates

A Governing equations in spherical coordinates

In spherical coordinates the independent variables in the horizontal domain are the longitude, λ , and the latitude, ϕ. The horizontal velocity field (u,v) is defined by

$$u = Rcos\phi\frac{d\lambda}{dt} \qquad v = R\frac{d\phi}{dt} \tag{A1.1}$$

where R is the radius of the earth.

A.1 Governing equations in spherical coordinate system and z-coordinates

A.1.1 Navier-Stokes equations

The continuity and momentum equations are given as

$$\frac{1}{Rcos\phi}\left(\frac{\partial u}{\partial\lambda}+\frac{\partial vcos\phi}{\partial\phi}\right)+\frac{\partial w}{\partial z}=0 \tag{A1.2}$$

$$\frac{\partial u}{\partial t}+\frac{1}{Rcos\phi}\left(\frac{\partial u^2}{\partial\lambda}+\frac{\partial vucos\phi}{\partial\phi}\right)+\frac{\partial wu}{\partial z}= \left(f+\frac{u}{R}tan\phi\right)v-\frac{1}{Rcos\phi}\left(\frac{1}{\rho_0}\frac{\partial q}{\partial\lambda}+g\frac{\partial\eta}{\partial\lambda}\right)+F_u+\frac{\partial}{\partial z}\left(\nu_t^v\frac{\partial u}{\partial z}\right) \tag{A1.3}$$

$$\frac{\partial v}{\partial t}+\frac{1}{Rcos\phi}\left(\frac{\partial uv}{\partial\lambda}+\frac{\partial v^2cos\phi}{\partial\phi}\right)+\frac{\partial wv}{\partial z}= -\left(f+\frac{u}{R}tan\phi\right)u-\frac{1}{Rcos\phi}\left(\frac{1}{\rho_0}\frac{\partial q}{\partial\phi}+g\frac{\partial\eta}{\partial\phi}\right)+F_v+\frac{\partial}{\partial z}\left(\nu_t^v\frac{\partial v}{\partial z}\right) \tag{A1.4}$$

$$\frac{\partial w}{\partial t}+\frac{1}{Rcos\phi}\left(\frac{\partial uw}{\partial\lambda}+\frac{\partial vwcos\phi}{\partial\phi}\right)+\frac{\partial w^2}{\partial z}=-\frac{1}{\rho_0}\frac{\partial q}{\partial z}+F_w+\frac{\partial}{\partial z}\left(\nu_t^v\frac{\partial w}{\partial z}\right) \tag{A1.5}$$

A.1.2 Transport equations

The transport equations for the k-ε model are given as

$$\frac{\partial k}{\partial t}+\frac{1}{Rcos\phi}\left(\frac{\partial uk}{\partial\lambda}+\frac{\partial vkcos\phi}{\partial\phi}\right)+\frac{\partial wk}{\partial z}=F_k+\frac{\partial}{\partial z}\left(\frac{\nu_{t0}^v}{\sigma_k^v}\frac{\partial k}{\partial z}\right)+P_k-\varepsilon \tag{A1.6}$$

$$\frac{\partial\varepsilon}{\partial t}+\frac{1}{Rcos\phi}\left(\frac{\partial u\varepsilon}{\partial\lambda}+\frac{\partial v\varepsilon cos\phi}{\partial\phi}\right)+\frac{\partial w\varepsilon}{\partial z}=F_\varepsilon+\frac{\partial}{\partial z}\left(\frac{\nu_{t0}^v}{\sigma_\varepsilon^v}\frac{\partial\varepsilon}{\partial z}\right)+P_\varepsilon-c_{2\varepsilon}\frac{\varepsilon^2}{k} \tag{A1.7}$$

The transport equations for the k-ω model are given as

$$\frac{\partial k}{\partial t}+\frac{1}{Rcos\phi}\left(\frac{\partial uk}{\partial \lambda}+\frac{\partial vkcos\phi}{\partial \phi}\right)+\frac{\partial wk}{\partial z}=F_k+\frac{\partial}{\partial z}\left(\frac{\nu_{t0}^v}{\sigma_k^v}\frac{\partial k}{\partial z}\right)+P_k-\beta_k\omega k \quad \text{(A1.8)}$$

$$\frac{\partial \omega}{\partial t}+\frac{1}{Rcos\phi}\left(\frac{\partial u\omega}{\partial \lambda}+\frac{\partial v\omega cos\phi}{\partial \phi}\right)+\frac{\partial w\omega}{\partial z}=F_\omega+\frac{\partial}{\partial z}\left(\frac{\nu_{t0}^v}{\sigma_\omega^v}\frac{\partial \omega}{\partial z}\right)+F_{\omega c}+P_\omega-\beta_\omega\omega^2 \quad \text{(A1.9)}$$

A.2 Governing equations in spherical coordinate system and sigma coordinates

A.2.1 Navier-Stokes equations

The continuity and momentum equations are given as

$$\frac{\partial h}{\partial t'}+\frac{1}{Rcos\phi}\left(\frac{\partial hu}{\partial \lambda'}+\frac{\partial hvcos\phi}{\partial \phi'}\right)+\frac{\partial \omega}{\partial \sigma}=0 \quad \text{(A1.10)}$$

$$\frac{\partial hu}{\partial t'}+\frac{1}{Rcos\phi}\left(\frac{\partial hu^2}{\partial \lambda'}+\frac{\partial hvucos\phi}{\partial \phi'}\right)+\frac{\partial h\omega u}{\partial \sigma}= \quad \text{(A1.11)}$$

$$\left(f+\frac{u}{R}tan\phi\right)hv-\frac{1}{Rcos\phi}\left(\frac{h}{\rho_0}\left(\frac{\partial q}{\partial \lambda}+\frac{\partial q}{\partial \sigma}\frac{\partial \sigma}{\partial \lambda}\right)+gh\frac{\partial \eta}{\partial \lambda}\right)+hF_u+\frac{\partial}{\partial \sigma}\left(\frac{\nu_t^v}{h}\frac{\partial u}{\partial \sigma}\right)$$

$$\frac{\partial hv}{\partial t'}+\frac{1}{Rcos\phi}\left(\frac{\partial huv}{\partial \lambda'}+\frac{\partial hv^2cos\phi}{\partial \phi'}\right)+\frac{\partial h\omega v}{\partial \sigma}= \quad \text{(A1.12)}$$

$$-\left(f+\frac{u}{R}tan\phi\right)hu-\frac{1}{R}\left(\frac{h}{\rho_0}\left(\frac{\partial q}{\partial \phi}+\frac{\partial q}{\partial \sigma}\frac{\partial \sigma}{\partial \phi}\right)+gh\frac{\partial \eta}{\partial \phi}\right)+hF_v+\frac{\partial}{\partial \sigma}\left(\frac{\nu_t^v}{h}\frac{\partial v}{\partial \sigma}\right)$$

$$\frac{\partial hw}{\partial t'}+\frac{1}{Rcos\phi}\left(\frac{\partial huw}{\partial \lambda'}+\frac{\partial hvwcos\phi}{\partial \phi'}\right)+\frac{\partial h\omega w}{\partial \sigma}= \quad \text{(A1.13)}$$

$$-\frac{1}{\rho_0}\frac{\partial q}{\partial \sigma}+hF_w+\frac{\partial}{\partial \sigma}\left(\frac{\nu_t^v}{h}\frac{\partial w}{\partial \sigma}\right)$$

The vertical velocity, ω, is given by

$$\omega=\frac{1}{h}\left(w+\frac{u}{Rcos\phi}\frac{\partial d}{\partial \lambda}+\frac{v}{R}\frac{\partial d}{\partial \phi}-\sigma\left(\frac{\partial h}{\partial t}+\frac{u}{Rcos\phi}\frac{\partial h}{\partial \lambda}+\frac{v}{R}\frac{\partial h}{\partial \phi}\right)\right) \quad \text{(A1.14)}$$

A.2.2 Transport equations

The transport equations for the k-ε model are given as

$$\frac{\partial hk}{\partial t'}+\frac{1}{Rcos\phi}\left(\frac{\partial huk}{\partial \lambda'}+\frac{\partial hvkcos\phi}{\partial \phi'}\right)+\frac{\partial h\omega k}{\partial \sigma} \quad \text{(A1.15)}$$

$$=hF_k+\frac{\partial}{\partial \sigma}\left(\frac{\nu_{t0}^v}{h\sigma_k^v}\frac{\partial k}{\partial \sigma}\right)+h(P_k-\varepsilon)$$

$$\frac{\partial h\varepsilon}{\partial t'} + \frac{1}{Rcos\phi}\left(\frac{\partial hu\varepsilon}{\partial \lambda'} + \frac{\partial hv\varepsilon cos\phi}{\partial \phi'}\right) + \frac{\partial h\omega\varepsilon}{\partial \sigma}$$
$$= hF_\varepsilon + \frac{\partial}{\partial \sigma}\left(\frac{\nu_{t0}^v}{h\sigma_\varepsilon^v}\frac{\partial \varepsilon}{\partial \sigma}\right) + h\left(P_\varepsilon - c_{2\varepsilon}\frac{\varepsilon^2}{k}\right) \quad \text{(A1.16)}$$

The transport equations for the k-ω model are given as

$$\frac{\partial hk}{\partial t'} + \frac{1}{Rcos\phi}\left(\frac{\partial huk}{\partial \lambda'} + \frac{\partial hvkcos\phi}{\partial \phi'}\right) + \frac{\partial hw_s k}{\partial \sigma}$$
$$= hF_k + \frac{\partial}{\partial \sigma}\left(\frac{\nu_{t0}^v}{h\sigma_k^v}\frac{\partial k}{\partial \sigma}\right) + h(P_k - \beta_k \omega k) \quad \text{(A1.17)}$$

$$\frac{\partial h\omega}{\partial t'} + \frac{1}{Rcos\phi}\left(\frac{\partial hu\omega}{\partial \lambda'} + \frac{\partial hv\omega cos\phi}{\partial \phi'}\right) + \frac{\partial hw_s \omega}{\partial \sigma}$$
$$= hF_\omega + \frac{\partial}{\partial \sigma}\left(\frac{\nu_{t0}^v}{h\sigma_\omega^v}\frac{\partial \omega}{\partial \sigma}\right) + hF_{\omega c} + h\,(P_\omega - \beta_\omega \omega^2) \quad \text{(A1.18)}$$

Note that in eqs. (A1.17)-(A1.18), the modified vertical velocity in the sigma coordinate system is called w_s (instead of ω). This is to distinguish it from the specific dissipation rate, ω, of turbulent kinetic energy which was introduced in section 2.1.2.

ALLEGATO D

Littoral Process

DHI Software

DHI WATER & ENVIRONMENT

LITPACK

An Integrated Modelling System for Littoral Processes and Coastline Kinetics

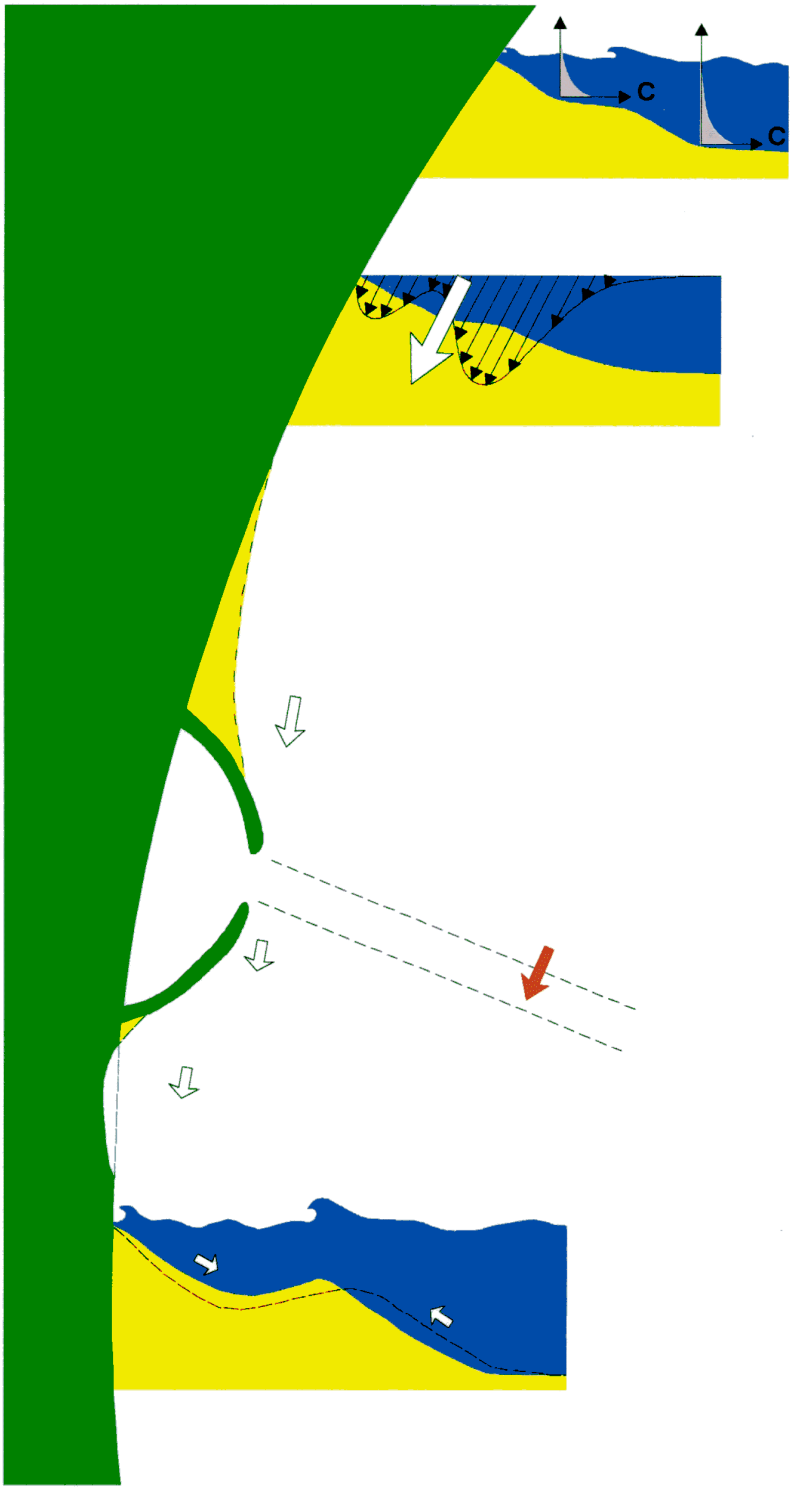


A Short Description

DHI
WATER & ENVIRONMENT

LITPACK

- FOR FOR MODELLING OF COASTAL PROCESSES



Noncohesive sediment transport in combined waves and current
STP

Littoral drift along a uniform beach with an arbitrary coastal profile
LITDRIFT

Coastline development due to changes in transport capacity
LITLINE

Channel backfilling due to nonequilibrium sediment transport mechanisms
LITTREN

Profile development due to cross-shore transport
LITPROF

LITPACK – LITTORAL TRANSPORT AND COASTLINE KINETICS

Introduction

LITPACK is a 'stand-alone' deterministic numerical modelling system, describing the major processes in the nearshore zone. LITPACK integrates DHI's proven numerical models for coastal sediment transport and coastline development, in a single package suitable for a wide range of coastal engineering applications.

The individual modules of LITPACK simulate particular coastal processes, with the linking between modules being performed by an automatic control module. This allows rapid simulation of complex coastal problems, without loss of detail in the individual modules.

All LITPACK modules apply a fully deterministic approach. This allows consideration of many, and sometimes dominating, factors which are not available to semi-empirical formulations. For example the simulation of a complex multi-barred profile, with varying grain size distribution, is prone to gross error when using an energy flux approach.

The processes covered by the individual modules can broadly be described as:

STP - Non-cohesive sediment transport in waves and currents

LITDRIFT - Longshore current and littoral drift

LITLINE - Coastline evolution

LITTREN - Trench sedimentation

LITPROF - Cross-shore profile development

General Overview

A short description of applications, basic equations and solution techniques for each of the LITPACK modules is presented on the following pages.

The Sediment Transport Module, STP

The computational module STP calculates the non-cohesive sediment transport in combined waves and currents.

The STP Module is integrated in the other LITPACK modules and forms the basis for all sediment transport calculations in LITPACK – and in DHI's 2D modelling system, MIKE 21, as well!

STP solves the vertical sediment diffusion equation on an intra-wave period grid to provide a detailed description of the non-cohesive sediment transport for breaking/non-breaking waves and current.

STP accounts for:

- Waves and currents at arbitrary angles
- Breaking/non-breaking waves
- Plane/ripple-covered bed
- Uniform/graded bed material
- Effect of bed slope
- Effect of streaming

Application Areas

STP is the basis for all sediment transport modelling within LITPACK, but can also be applied for investigating harbour siltation and intake problems.

Basic Equations

The 'intra-wave period' sediment transport model STP forms the basic sediment transport description for combined wave and current action in all the LITPACK modules.

In combined waves and current the turbulent interaction in the near bed boundary layer is of importance for the bed shear stresses as well as for the eddy viscosity distribution. The basis for the sediment transport description is the model for turbulent wave-current boundary layers of Fredsøe (1984). The boundary layer is composed of two regions:

Close to the bed the turbulence and the shear stress in the wave boundary layer vary within the wave period, giving rapidly changing bed concentration and turbulent diffusion coeffi-cients.

Outside the wave boundary layer the mean velocity is described by a log-profile. The increased turbulence level in the wave boundary layer retards the mean current, an effect which is expressed through an apparent wave roughness, k_w, which is larger than the natural bed roughness k.

The total sediment load is split into bed load and suspended load, which are calculated separately. The transport of non-cohesive material as bed load is calculated according to the model presented by Engelund and Fredsøe (1976). Through subsequent developments this model has been extended to cover combined waves and current, and conditions in the surf zone. The bed load transport is determined as a function of the bed shear stress through the dimensionless bed shear stress, θ:

$$\theta = \frac{U_f^{\,2}}{(s-1)\,gd}$$

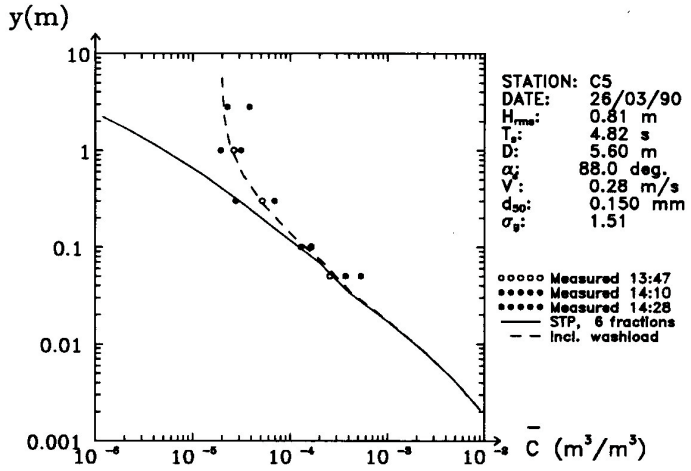
The bed load transport is assumed to correspond to the instantaneous bed shear stress under unsteady conditions, e.g. under wave action.

The suspended load transport, q_s, is described through the sediment concentration C, which is determined from the vertical turbulent diffusion equation:

$$\frac{\partial C}{\partial t} = \frac{\partial}{\partial z}\left[\varepsilon_s \frac{\partial C}{\partial z}\right] + w\frac{\partial C}{\partial z}$$

ε_s is taken to be equal to the turbulent eddy viscosity of the flow field. The near-bed boundary condition is given as bed concen-tration C_b at the level z = 2d. C_b is determined as a function of θ using the dynamic con-siderations of Bagnold (1954), that a certain sediment concentration is required near the bed in order to transfer the shear stress to the bed through grain-grain interaction.

The bed concentration, C_b, is only valid for the plane bed case, i.e. sheet flow, which is found for θ larger than about 0.8. At smaller θ-values the bed is covered by wave ripples. The sediment transport model by Fredsøe et. al (1985) has been modified to take the effect of wave ripples into account. The modification involves the bed concentration, turbulent diffusion and the bed roughness. The values of C_b and ε are based directly on the laboratory measurements of Nielsen (1979). The rough-ness is expressed through the ripple dimensions as given by Raudkivi (1988). The sediment transport model converges gradually towards a plane bed description with increasing bed shear stress or mean current velocity.



Vertical mean sediment concentration profile calculated by STP, compared to full scale field measurements

Inside the surf zone, the wave energy is dissipated due to breaking, and the production of turbulence is very intense. This has been taken into account by use of a one-equation turbulence model (Deigaard et. al. (1986)).

STP also has the possibility to solve the intra-wave period vertical sediment diffusion equation for asymmetric waves, including the effects of Lagrangian drift, induced streaming and density driven currents. Inside the breaker zone, the undertow profile is also dependent on the shoreward flux of water in the surface roller.

The suspended sediment transport q_s is calculated as the product of sediment concentration and the mean circulation current averaged over the wave period T (Hedegaard et al. (1988)):

$$q_s = \frac{1}{T}\int_0^T \int_{2d}^{D} C\, U_{mean}\, dydt$$

The suspended sediment follows the water, and the sediment transport shall be based on the Lagrangian flow velocity.
U_{mean} is thus taken as the sum of the Eulerian circulation current U and the Lagrangian drift velocity U_D obtained from the flow model.

Symbol List

s	:	relative sediment density
g	:	acceleration of gravity
d	:	grain size
U_f	:	shear velocity
t	:	time
z	:	vertical coordinate (zero at the bed)
ε_s	:	turbulent diffusion coefficient
w	:	settling velocity of the sediment.

Solution Technique

The equations are solved using interpolation and finite difference techniques with time-variables defined on an intra-wave period staggered grid and space-variables defined on a non-equidistant vertical grid.

Input

The following basic input is required in STP:

- Water depth and bed slope
- Wave properties; height, period and angle
- Current velocity and direction
- Sediment properties; size, gradation, fall velocity.

Output

The following output can be obtained from STP:

- Time averaged values of the profiles of eddy viscosity, concentration, velocity and the suspended sediment transport in two directions
- Total bed load and suspended load in two directions
- Time-varying profiles of eddy viscosity, concentration and velocity in two directions
- Time-varying values of bed velocity, friction velocity, Shields parameter and bed concentration.

References

Bagnold, R.A., "Experiments on a gravity-free dispersion of large solid spheres in a Newtonian fluid under shear". Proceeding Royal Society, London (A), 49, 1954.

Deigaard, R., Fredsøe, J. and Hedegaard, I.B. (1986a) "Suspended sediment in the surf zone". J. of Waterway, Port, Coastal and Ocean Engineering, ASCE, Vol. 112, No. 1.

Engelund, F. and Fredsøe, J. (1976) "A sediment transport model for straight alluvial channels", Nordic Hydrology, 7.

Fredsøe, J. (1984) "The turbulent boundary layer in combined wave-current motion". J. of Hydraulic Engineering, ASCE, Vol. 110, No. HY8.

Fredsøe, J., Andersen, O.H. and Silberg, S. (1985) "Distribution of suspended sediment in large waves", J. of Waterway, Port, Coastal and Ocean Engineering, ASCE, Vol. 111, No. 6.

Hedegaard, I.B. (1985) "Wave generated ripples and resulting sediment transport in waves". Inst. Hydrodynamics and Hydraulic Engng., Tech. Univ. of Denmark, Ser. Paper 36.

Nielsen, P. (1970) "Some basic concepts of wave sediment transport". Int. Hydrodynamics and Hydraulic Engineering. Tech. Univ. of Denmark. Ser. Paper 20.

Raudkivi, Arved J. (1988) "The roughness heights under waves". J. Hydraulic Research, Vol. 26, No. 5.

Svendsen, I.A., Schäffer, H.A. and Buhr Hansen, J. (1987) "The interaction between the undertow and the boundary layer flow on a beach". J. Geophysical Research Vol. 92, No. C11.

Zyserman, J. and Fredsøe, J. (1988) "The effect of rip-currents on the longshore sediment transport". 2nd Int. Symp. On Wave Research and Coastal Engng., Hannover.

THE LONGSHORE CURRENT AND LITTORAL DRIFT MODULE, LITDRIFT

The LITDRIFT Module combines STP with a coastal hydrodynamic module to give a deterministic description of the littoral drift.

LITDRIFT provides a powerful tool for sediment budget analysis, which is of paramount importance to all coastal morphology studies.

The LITDRIFT Module simulates the cross-shore distribution of wave height, set-up and longshore current for an arbitrary coastal profile. It provides a detailed deterministic description of the cross-shore distribution of the longshore sediment transport for an arbitrary bathymetry for both regular and irregular sea states.

LITDRIFT accounts for:

- Regular/irregular waves
- Water levels
- Tidal currents
- Wind shear stresses
- Non-uniform bottom friction
- Wave refraction and shoaling
- Breaking
- Non-uniform sediment distribution.

LITDRIFT has the possibility to transfer a wave climate from deeper waters to a point in the profile, generating the output as a normal database for input in LITDRIFT or STP.

Application Areas

LITDRIFT can be applied to the study of coastal processes, e.g.:

- Littoral transport distribution
- Bypass of sediments
- Annual drift calculations.

Basic Equations

The hydrodynamic model LITDRIFT includes a description of propagation, shoaling and breaking of waves, calculation of the driving forces due to radiation stress gradients, momentum balance for the cross-shore and longshore direction giving the wave set-up and the longshore current velocities. The model can be applied on complex coastal profiles with longshore bars. In the case of a longshore bar the broken waves can reform in the trough onshore of the bar. The waves can be treated as regular or irregular, and the effect of directional spreading can be included in the description.

It is assumed in the model that the conditions are uniform along the straight coast.

The equation for shore-parallel momentum balance determines the longshore current velocity profile:

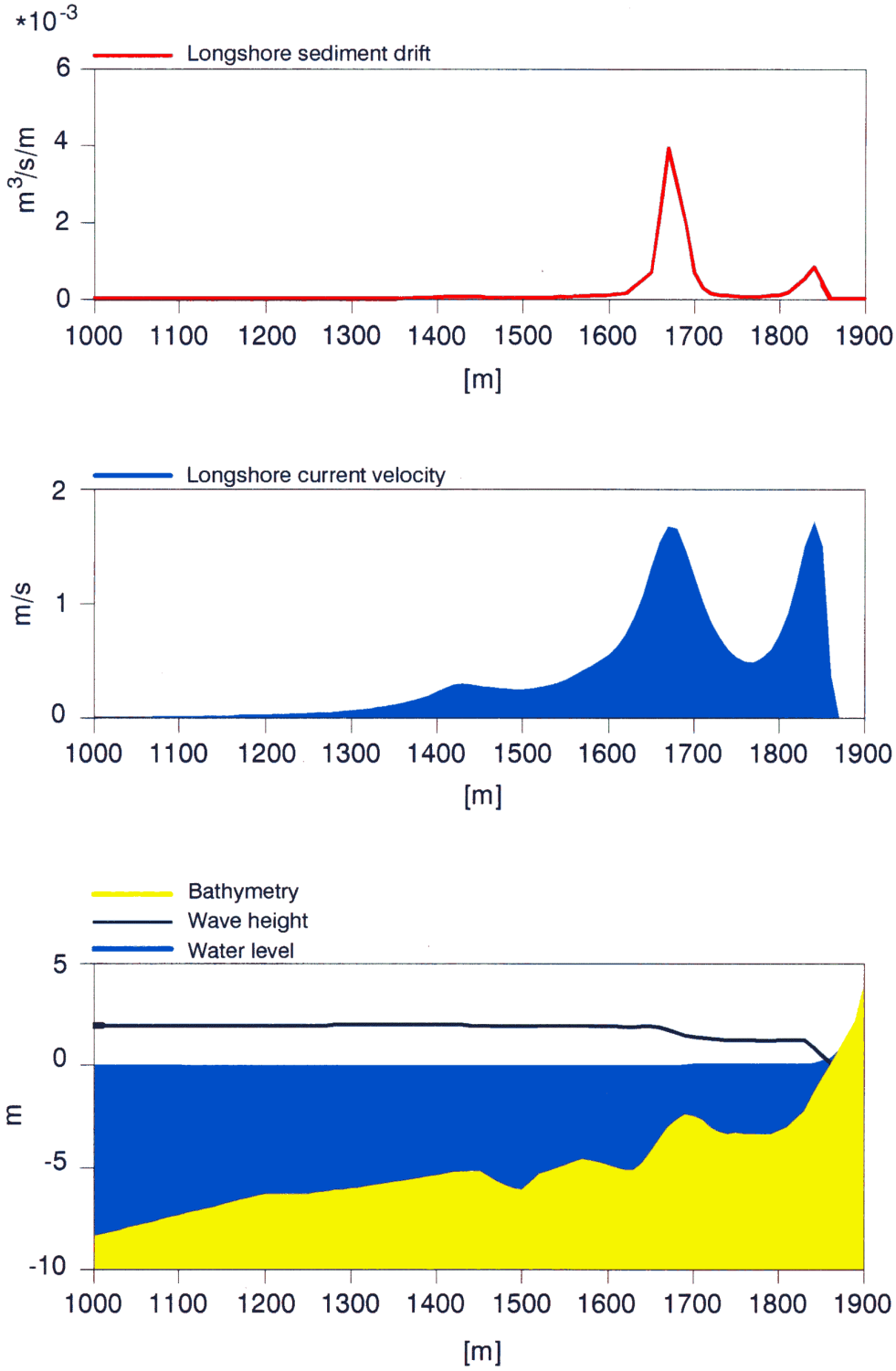
$$\tau_b - \frac{d}{dy}\left[\rho E D \frac{du}{dy}\right] = -\frac{ds_{xy}}{dy} + \tau_w + \tau_{cur}$$

The relation between u and τ_b is established by the model of Fredsøe (1984).

Having computed the longshore current points are selected which are representative for the littoral drift. The sediment transport calculations automatically carried out by the STP-module, are made to reflect the local conditions with respect to the energy dissipation, the percentage of non-breaking waves and the rms of the wave heights, cf. Deigaard et al. (1988).

The total sediment transport is dominated by transport contributions from areas where wave breaking occurs. The point selection procedure therefore gives preference to points in this area. In case of a bar-profile, the sediment calculation points will thus be located on the bars, where waves are breaking.

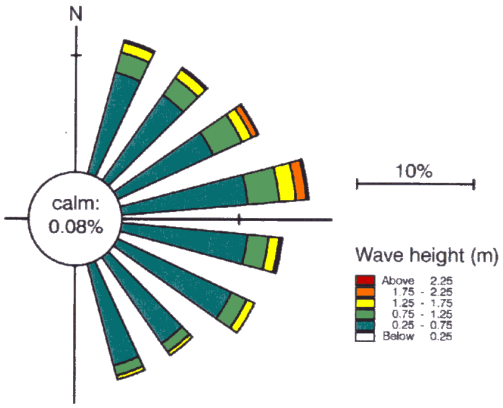
LITDRIFT gives the distribution of sediment transport across the profile, which is integrated



Calculated Sediment Transport, Velocity, Wave Height and Water Level along a Profile

to obtain the total longshore sediment transport rate.

By including a hydrodynamic database, LITDRIFT calculates the net/gross littoral transport for a section of coastline over a specific design period. Important factors, such as the linking of the water level and the profile to the incident sea state are included.



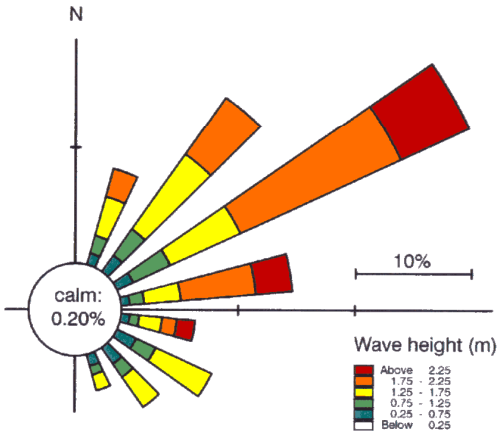
Annual Wave Climate

Symbol List

τ_b : bed shear stress due to the longshore current
ρ : density of water
E : momentum exchange coefficient
D : water depth
u : longshore current velocity
y : shore-normal coordinate
s_{xy} : shear component of the radiation stress
τ_w and
$\tau_{cur.}$: driving forces due to wind and coastal current.

Solution Technique

The equations are solved using finite difference techniques with variables defined on a space-staggered equidistant horizontal grid.



Corresponding Littoral Drift Scaled by Gross Climate

Input

The following basic input is required in LITDRIFT:

- Cross-shore profile bathymetry with the values of bed roughness and grain properties (size, fall- velocity and gradation) given at each grid point
- Water level
- Wave properties; height, period and angle
- Tidal current velocity.

Output

The following output can be obtained from LITDRIFT:

- Cross-shore distribution of water level, longshore current, wave height and wave angle, water flux, bed load and suspended transport, total load and cumulative total load transport
- Cross-shore distribution of total annual littoral drift
- Total net- and gross transport rates.

References

Deigaard, R., Fredsøe, J., Hedegaard, I.B., Zyserman, J.A., Andersen, O.H., (1988) "Littoral Drift Model for Natural Environments", 21st Int. Conf. On Coastal Engng., Málaga.

Foster, T., Mangor, K. and Skou, A. "Controlling Parameters on Littoral Transport and Coastline Development". The 7th Symposium on Coastal and Ocean management, California, July 8-12, 1991.

Foster, T.M. and Skou, A.J. "LITPACK on Integrated Modelling System for Littoral Processes and Coastline Kinetics". 3rd International Software Exhibition for Environmental Science & Engineering, Como, Italy, September 1992.

Skou, A., Hedegaard, I.B., Fredsøe, J., and Deigaard, R. "Applications of Mathematical Models for Coastal Sediment Transport and Coastline Development". Proceedings of COPEDEC III, Mombasa, Kenya, September 16-20, 1991.

THE COASTLINE EVOLUTION MODULE, LITLINE

LITLINE is a powerful and reliable tool for the design and optimisation of many coastal engineering projects.

Based upon the results from LITDRIFT, LITLINE simulates the coastal response to gradients in the longshore sediment transport capacity resulting from natural features and a wide variety of coastal structures.

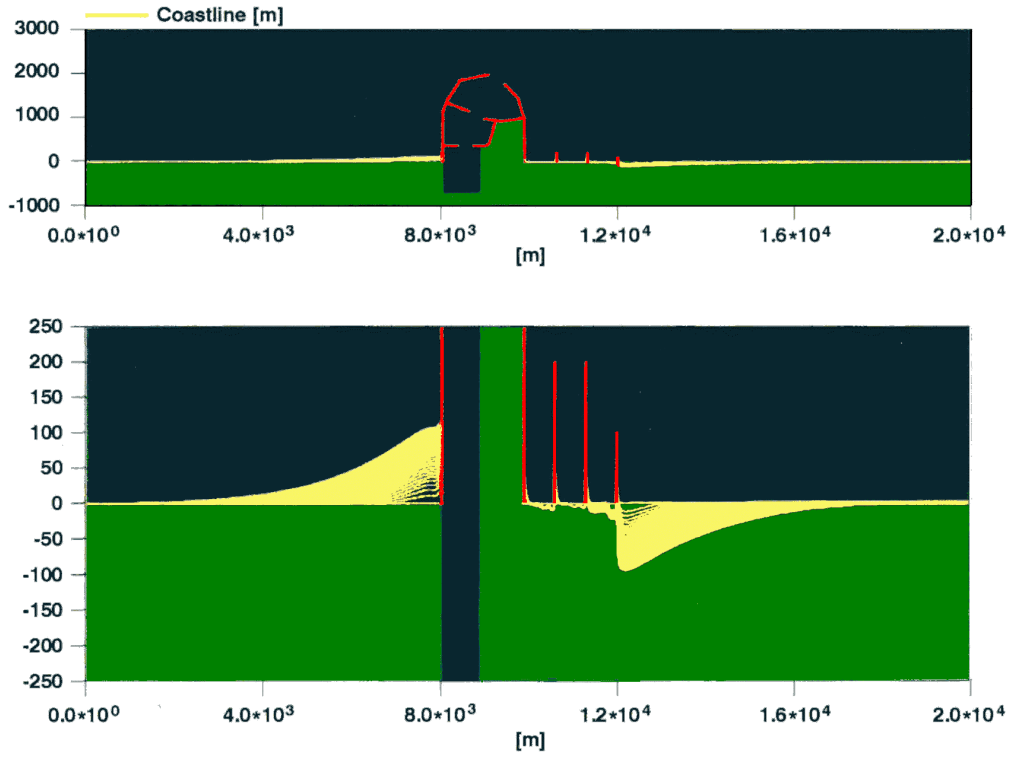
LITLINE calculates the coastline evolution by solving a continuity equation for the sediment in the littoral zone. The influence of structures, sources and sinks are included.

LITLINE accounts for

- Structures (groynes, jetties, revetments and offshore breakwaters)
- Sources and sinks
- Diffraction of waves
- Depth contours
- Active depth and dunes.

Application Areas

The evolution of the coastline can be calculated, either based on a yearly net littoral drift or from a time series of wave events. The latter option offers the capability of studying coastline movements during a winter season (for instance maximum retreat) or coastline changes on a coast with monsoon climate.



Development of coastline near harbour during 30 years
Upper Figure: True scale, Lower Figure: Dissorted scale

Basic Equations

Based upon the results from the LITDRIFT, LITLINE simulates the coastal response to gradients in the longshore sediment transport capacity resulting from natural features and a wide variety of coastal structures.

The model solves the continuity equation for the coastline:

$$\frac{\partial y_c}{\partial t} = -\frac{1}{h_{act}} \frac{\partial Q}{\partial x} + \frac{Q_{sou}}{h_{act} \Delta x}$$

The changes to the transport conditions caused by coastal structures are modelled by introducing appropriate internal boundary conditions. Besides blocking the transport, large structures change the transport relations close to the structure due to the sheltering effect from the structure itself. This effect is automatically included by introducing modified transport relations close to the structure.

With jetties and breakwaters the influence of diffraction on the wave climate is included.

Symbol List

y_c : distance from the baseline to the coastline
t : time
h_{act} : height of the active cross-shore profile
Q : long-shore transport of sediment expressed in volumes
x : long-shore position
Δx : long-shore discretization step
Q_{sou} : source/sink term expressed in volume/Δx.

Solution Technique

The equations are solved using finite difference techniques with variables defined on a space-staggered equidistant horizontal grid. The sediment transport rates are found by interpolation in a transport table previously generated for the particular site.

Input

The following basic input is required in LITLINE:

- Longshore relative coastline alignment together with dune properties, profile description, active depth and depth contour angles at each grid point
- Cross-shore profile bathymetries
- Data base with wave properties (wave height, -period and angle), tidal current and water levels
- Position and size of structures
- Position and magnitudes of sources/sinks
- Database of transport rates (previously generated)

Output

The results of the simulation are the coastline position, longshore sediment transport rates and the depth in front of revetments, if they are present. The accumulated volume of material deposited and bypassed is also given.

THE TRENCH SEDIMENTATION MODULE, LITTREN

LITTREN finds applications in areas where the suspended load is not in equilibrium with the local hydrodynamics, for example channel back-filling and intake intrusion problems.

LITTREN accounts for

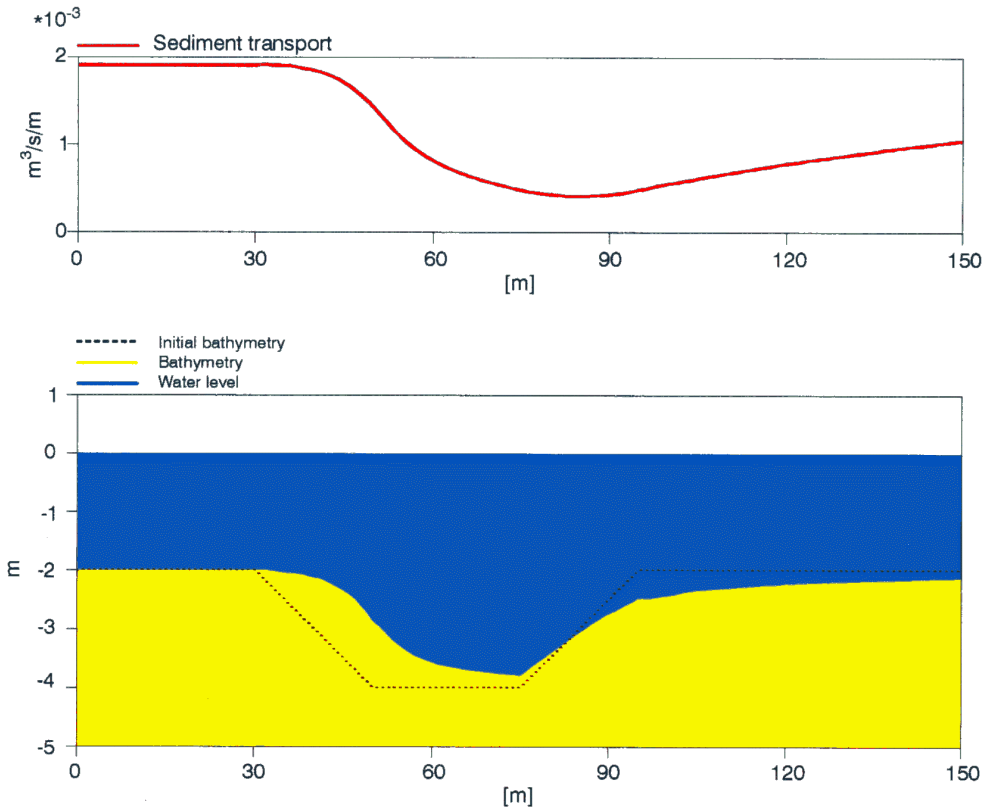
- Non-equilibrium sediment transport in combined waves and currents.
- Full morphological feed back between bed level change, waves, currents and sediment transport.
- Current and wave 'refraction' over the channel.

Basic Equations

Based upon the standard STP formulation, LITTREN links a one-dimensional wave – current model to a non-equilibrium formulation of the vertical sediment diffusion equation.

$$\frac{\partial c}{\partial t} = \frac{\partial}{\partial z}\left(\varepsilon_s \frac{\partial c}{\partial z}\right) + w\frac{\partial c}{\partial z}$$

Bed load transport and the near bed concentration include gravity effects, which are found to be important. In cases where the channel direction is similar to the persistent current direction, gravity effects are the dominating back-filling mechanism.



Example of Simulated Trench Sediment

The change in bed level is found by the bottom sediment continuity equation:

$$\frac{\partial z}{\partial t} = -\frac{1}{(1-n)}\frac{\partial q}{\partial x}$$

Solution Technique

The module includes a morphological subroutine using a modified Lax-Wendroff solution to the bottom sediment continuity equation.

This allows continuous interaction between the morphology and hydrodynamics, thereby avoiding an overly conservative solution based upon initial values.

Input

The following basic input is required in LITTREN:

- Bathymetry profile perpendicular to the trench alignment
- Arbitrary time series of wave/current magnitudes and directions and water levels
- Grain diameter and fall velocity.

Output

The outcome of the simulation is the bathymetry of the trench profile, total change in bed level and total-load transport rates along the trench profile.

List of Symbols

c : concentration of sediment
t : time
ε_s : eddy viscosity
w : sediment fall velocity
z : bed level
n : porosity of the bed
q : sediment flux
x : horizontal coordinate.

THE PROFILE DEVELOPMENT MODULE, LITPROF

LITPROF describes cross-shore profile changes by solving the bottom sediment continuity equation, based on the sediment transport rates calculated by STP.

LITPROF being a time-domain model, includes the effects of changing morphology on the wave climate and transport regime. This enables a simulation of profile development for a time-varying incident wave field.

LITPROF accounts for the following effects:

- Shoaling of waves
- Breaking waves
- Transport, including the effects of undertow, Lagrangrian drift, streaming and bed slope
- Structures (submerged breakwater and/or revetment).

Application Areas

LITPROF can be applied to investigate storm profile development and the response of beach nourishment to storm conditions. Furthermore, a profile envelope for various wave conditions may be obtained forming the basis for estimating burial depths for pipelines.

Basic Equations

A sediment transport table based on STP calculations are used as the basis for the morphological module (Hedegaard et al. (1988), describing the development of the coastal profile. The bed level change is described by the continuity equation for the sediment:

$$\frac{\partial h}{\partial t} = - \frac{1}{1-n} \frac{\partial q_s}{\partial x}$$

The boundary condition is that the sediment transport is zero at the coastline.

The morphological model cannot be based directly on the sediment transport rates calculated from the local wave parameters, because it is not physically correct to expect an immediate, local response of the sediment transport to varying hydrodynamic conditions (Roelvink and Stive (1988)). Today no theory exists that can describe the actual cross shore variation of the sediment transport, and a heuristic transformation of the sediment transport calculated from the local conditions has been applied. The transformation reflects that the circulation current does not adjust immediately to the driving forces, but develops gradually. The peak of sediment transport is therefore shifted shorewards relative to the maximum of the driving forces. The transformation, giving the sediment transport, q_{sl}, used for the profile modelling, is expressed as a response function:

$$\frac{\partial q_{sl}}{\partial x} = \frac{q_s - q_{sl}}{L}$$

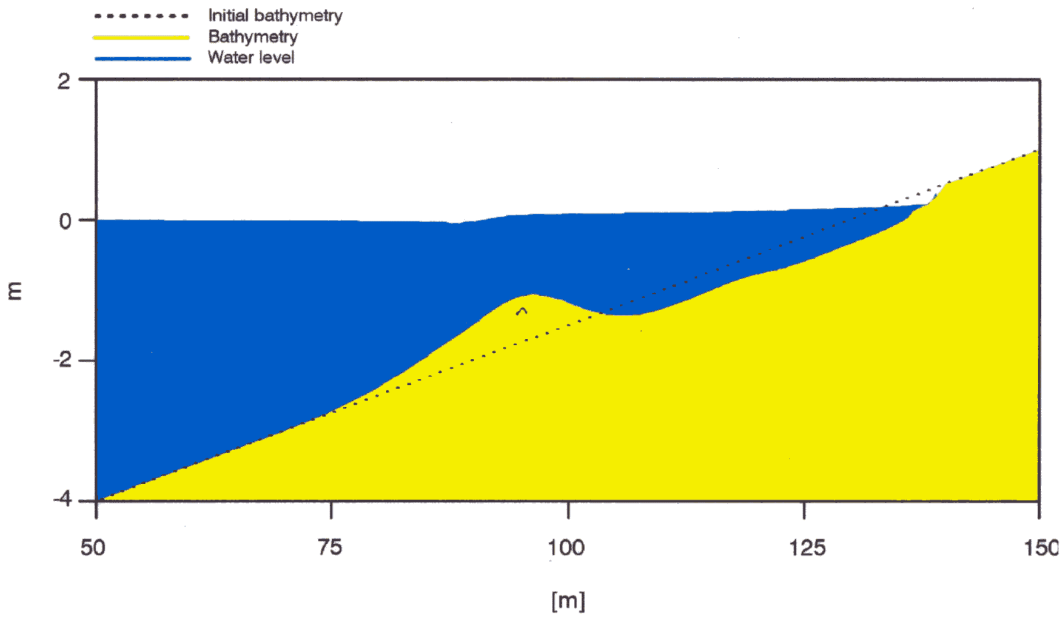
Symbol List

h : bed level
n : porosity of the bed material.

The length scale L is proportional to the local water depth.

Solution Technique

The equations are solved using finite difference techniques with variables defined on a space-staggered equidistant horizontal grid.



Example of Bar Development in Profile

Input

The following basic input is required in LITPROF:

- Cross-shore profile bathymetry
- Arbitrary time-series of wave height and water level
- Data base of transport rates (previously generated).

Output

The main results from LITPROF are

- Profile response to various conditions
- Fate of nourished material
- Profile response to structures
- Profile envelope.

1998-07-09/S:/LITPACK/LITPACK-SHORT.DOC.AJS.kin

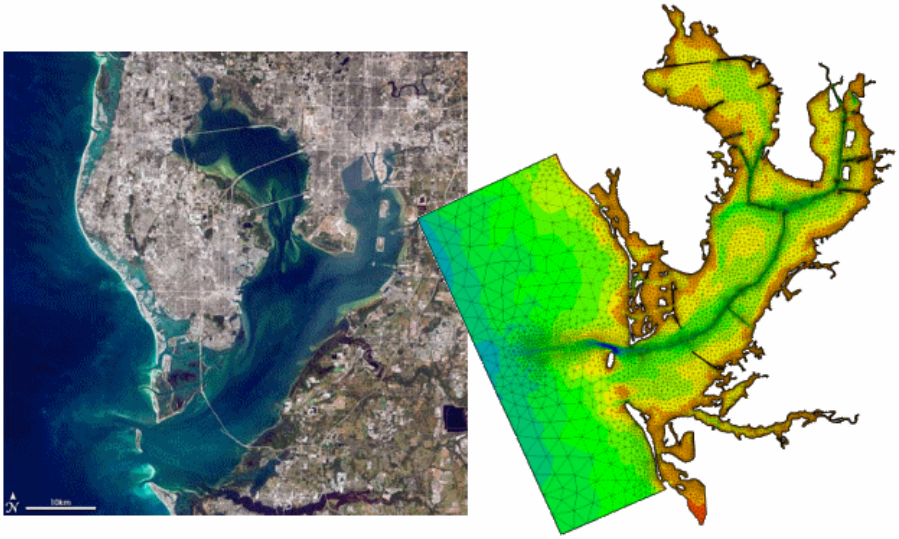
References

Hedegaard, I.B., Deigaard, R. (1988) "A model for cross-shore sediment transport and coastal profile development". Proc. IAHR. 2nd Int. Symp. On Wave Research and Coastal Engineering, Hannover.

Roelvink, J.A. and M.J.F. Stive (1988) "Large scale tests of cross-shore sediment transport on the upper shoreface". Proc. IAHR. Symposium on Mathematical Modelling of Sediment Transport in the Coastal Zone, Copenhagen.

ALLEGATO E

MIKE 21 Hydrodynamics (HD)



MIKE 21 & MIKE 3 Flow Model FM

Hydrodynamic Module

Short Description

The expert in WATER ENVIRONMENTS



DHI headquarters
Agern Allé 5
DK-2970 Hørsholm
Denmark

+45 4516 9200 Telephone
+45 4516 9333 Support
+45 4516 9292 Telefax

mike@dhigroup.com
www.mikepoweredbydhi.com

MIKE213_HD_FM_Short_Description_.docx / AJS/EBR/NHP / 2017-10-02

© DHI

MIKE 21 & MIKE 3 Flow Model FM

The Flow Model FM is a comprehensive modelling system for two- and three-dimensional water modelling developed by DHI. The 2D and 3D models carry the same names as the classic DHI model versions MIKE 21 & MIKE 3 with an 'FM' added referring to the type of model grid - Flexible Mesh.

The modelling system has been developed for complex applications within oceanographic, coastal and estuarine environments. However, being a general modelling system for 2D and 3D free-surface flows it may also be applied for studies of inland surface waters, e.g. overland flooding and lakes or reservoirs.



MIKE 21 & MIKE 3 Flow Model FM is a general hydrodynamic flow modelling system based on a finite volume method on an unstructured mesh

The Modules of the Flexible Mesh Series

DHI's Flexible Mesh (FM) series includes the following modules:

Flow Model FM modules

- Hydrodynamic Module, HD
- Transport Module, TR
- Ecology Modules, MIKE ECO Lab/AMB Lab
- Oil Spill Module, OS
- Mud Transport Module, MT
- Particle Tracking Module, PT
- Sand Transport Module, ST
- Shoreline Morphology Module, SM

Wave module

- Spectral Wave Module, SW

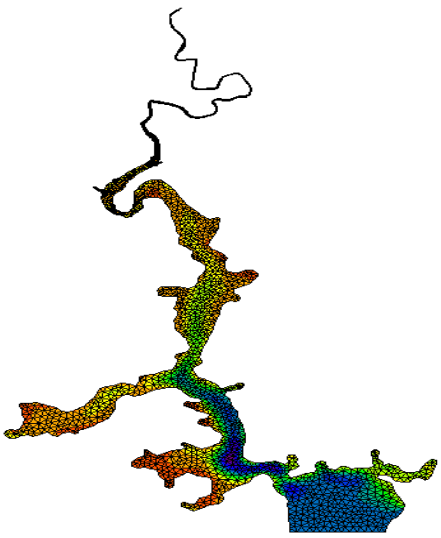
The FM Series meets the increasing demand for realistic representations of nature, both with regard to 'look alike' and to its capability to model coupled processes, e.g. coupling between currents, waves and sediments. Coupling of modules is managed in the Coupled Model FM.

All modules are supported by advanced user interfaces including efficient and sophisticated tools for mesh generation, data management, 2D/3D visualization, etc. In combination with comprehensive documentation and support, the FM series forms a unique professional software tool for consultancy services related to design, operation and maintenance tasks within the marine environment.

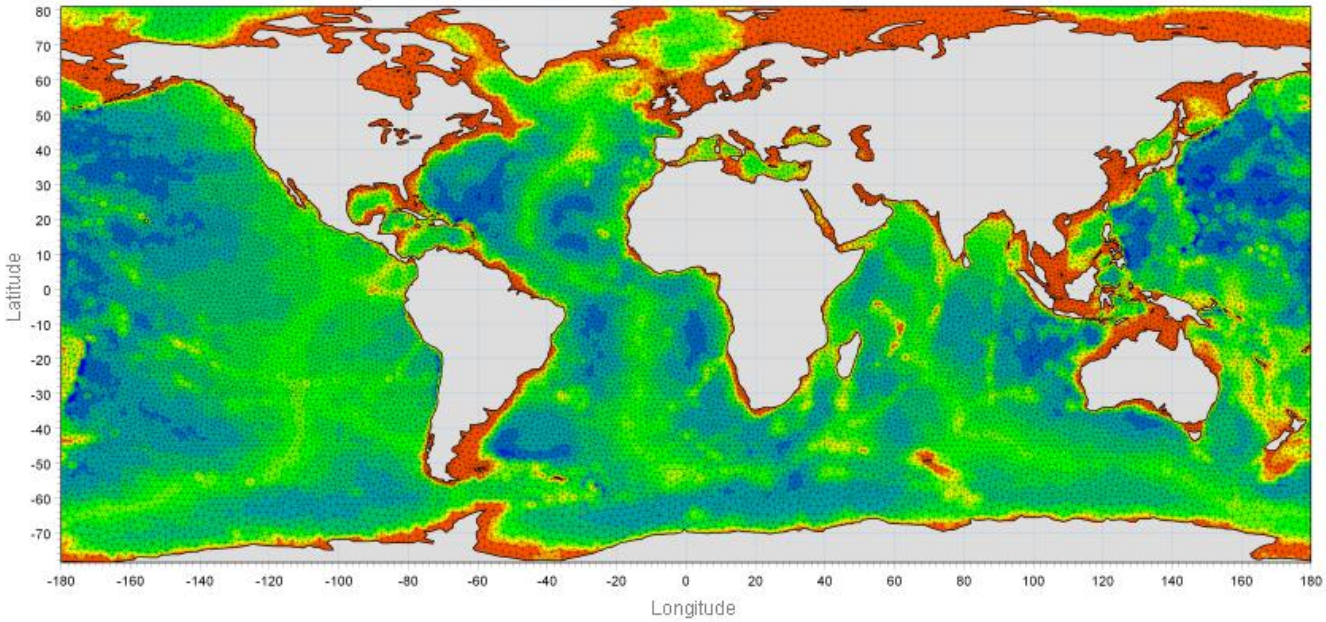
An unstructured grid provides an optimal degree of flexibility in the representation of complex geometries and enables smooth representations of boundaries. Small elements may be used in areas where more detail is desired, and larger elements used where less detail is needed, optimising information for a given amount of computational time.

The spatial discretisation of the governing equations is performed using a cell-centred finite volume method. In the horizontal plane, an unstructured grid is used while a structured mesh is used in the vertical domain (3D).

This document provides a short description of the Hydrodynamic Module included in MIKE 21 & MIKE 3 Flow Model FM.



Example of computational mesh for Tamar Estuary, UK



MIKE 21 & MIKE 3 FLOW MODEL FM supports both Cartesian and spherical coordinates. Spherical coordinates are usually applied for regional and global sea circulation applications. The chart shows the computational mesh and bathymetry for the planet Earth generated by the MIKE Zero Mesh Generator

MIKE 21 & MIKE 3 Flow Model FM - Hydrodynamic Module

The Hydrodynamic Module provides the basis for computations performed in many other modules, but can also be used alone. It simulates the water level variations and flows in response to a variety of forcing functions on flood plains, in lakes, estuaries and coastal areas.

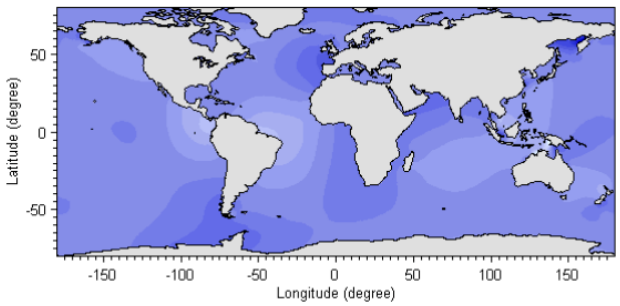
Application Areas

The Hydrodynamic Module included in MIKE 21 & MIKE 3 Flow Model FM simulates unsteady flow taking into account density variations, bathymetry and external forcings.

The choice between 2D and 3D model depends on a number of factors. For example, in shallow waters, wind and tidal current are often sufficient to keep the water column well-mixed, i.e. homogeneous in salinity and temperature. In such cases a 2D model can be used. In water bodies with stratification, either by density or by species (ecology), a 3D model should be used. This is also the case for enclosed or semi-enclosed waters where wind-driven circulation occurs.

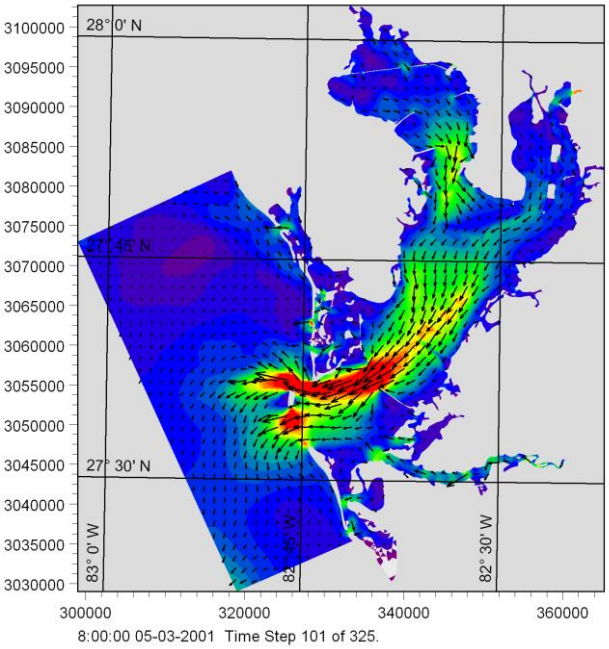
Typical application areas are

- Assessment of hydrographic conditions for design, construction and operation of structures and plants in stratified and non-stratified waters
- Environmental impact assessment studies
- Coastal and oceanographic circulation studies
- Optimization of port and coastal protection infrastructures
- Lake and reservoir hydrodynamics
- Cooling water, recirculation and desalination
- Coastal flooding and storm surge
- Inland flooding and overland flow modelling
- Forecast and warning systems

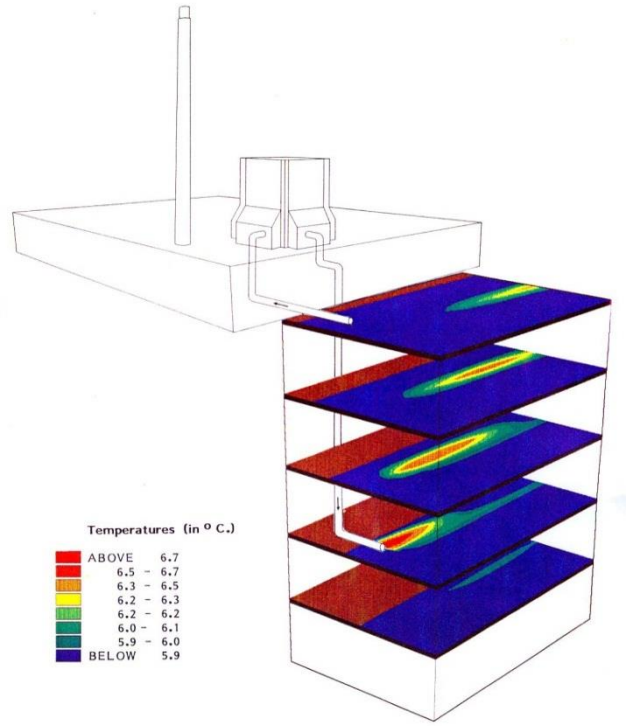


Example of a global tide application of MIKE 21 Flow Model FM. Results from such a model can be used as boundary conditions for regional scale forecast or hindcast models

The MIKE 21 & MIKE 3 Flow Model FM also support spherical coordinates, which makes both models particularly applicable for global and regional sea scale applications.



Example of a flow field in Tampa Bay, Florida, simulated by MIKE 21 Flow Model FM

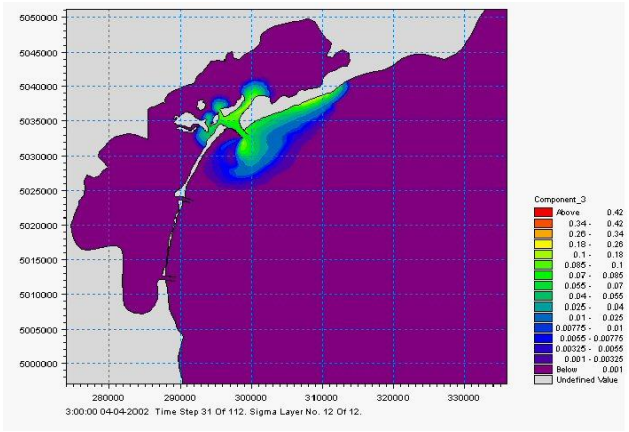


Study of thermal plume dispersion



Typical applications with the MIKE 21 & MIKE 3 Flow Model FM include cooling water recirculation and ecological impact assessment (eutrophication)

The Hydrodynamic Module is together with the Transport Module (TR) used to simulate the spreading and fate of dissolved and suspended substances. This module combination is applied in tracer simulations, flushing and simple water quality studies.



Tracer simulation of single component from outlet in the Adriatic, simulated by MIKE 21 Flow Model FM HD+TR



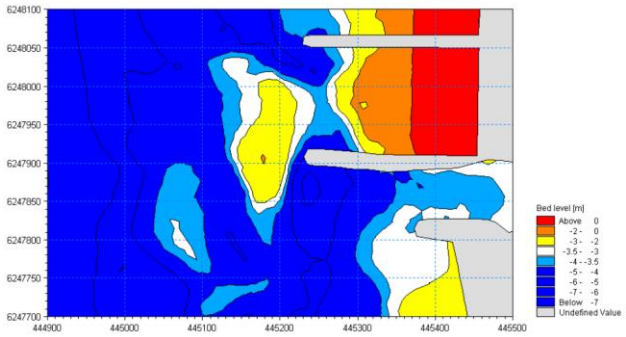
Prediction of ecosystem behaviour using the MIKE 21 & MIKE 3 Flow Model FM together with MIKE ECO Lab

The Hydrodynamic Module can be coupled to the Ecological Module (MIKE ECO Lab) to form the basis for environmental water quality studies comprising multiple components.

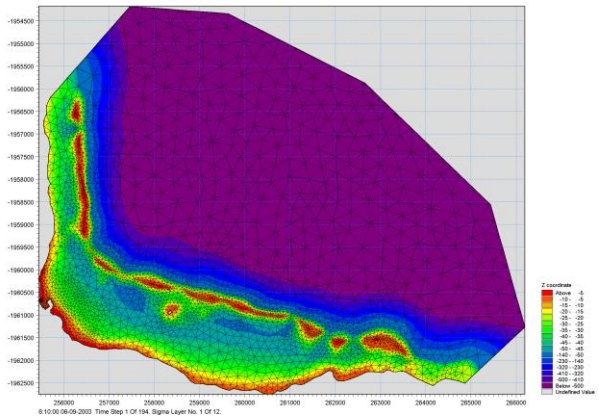
Furthermore, the Hydrodynamic Module can be coupled to sediment models for the calculation of sediment transport. The Sand Transport Module and Mud Transport Module can be applied to simulate transport of non-cohesive and cohesive sediments, respectively.

In the coastal zone the transport is mainly determined by wave conditions and associated wave-induced currents. The wave-induced currents are generated by the gradients in radiation stresses that occur in the surf zone. The Spectral Wave Module can be used to calculate the wave conditions and associated radiation stresses.

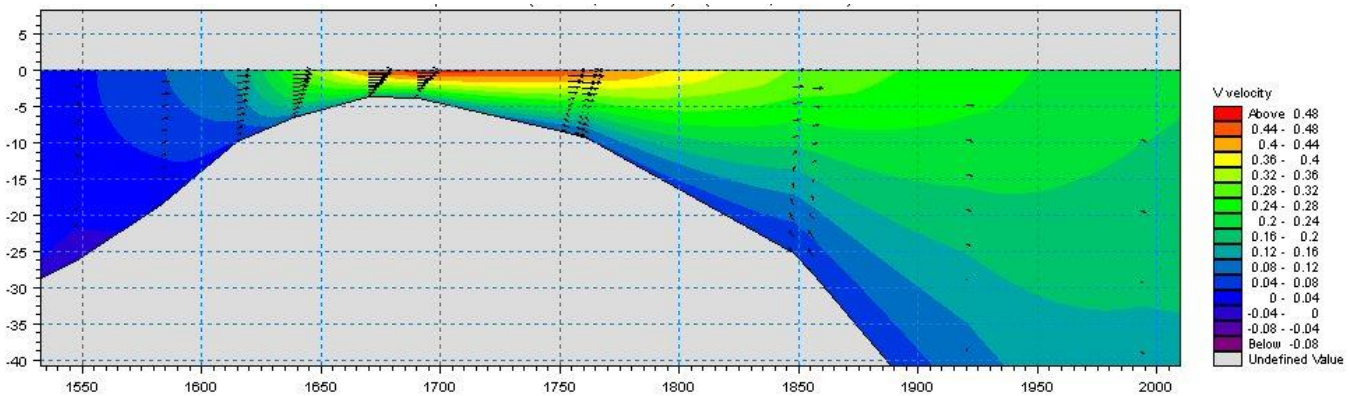




Coastal application (morphology) with coupled MIKE 21 HD, SW and ST, Torsminde harbour Denmark



Model bathymetry of Taravao Bay, Tahiti



Example of vertical profile of cross reef currents in Taravao Bay, Tahiti simulated with MIKE 3 Flow Model FM. The circulation and renewal of water inside the reef is dependent on the tides, the meteorological conditions and the cross reef currents, thus the circulation model includes the effects of wave induced cross reef currents

Computational Features

The main features and effects included in simulations with the MIKE 21 & MIKE 3 Flow Model FM – Hydrodynamic Module are the following:

- Flooding and drying
- Momentum dispersion
- Bottom shear stress
- Coriolis force
- Wind shear stress
- Barometric pressure gradients
- Ice coverage
- Tidal potential
- Precipitation/evaporation
- Infiltration
- Heat exchange with atmosphere
- Wave radiation stresses
- Sources and sinks, incl. jet
- Structures

Model Equations

The modelling system is based on the numerical solution of the two/three-dimensional incompressible Reynolds averaged Navier-Stokes equations subject to the assumptions of Boussinesq and of hydrostatic pressure. Thus, the model consists of continuity, momentum, temperature, salinity and density equations and it is closed by a turbulent closure scheme. The density does not depend on the pressure, but only on the temperature and the salinity.

For the 3D model, the free surface is taken into account using a sigma-coordinate transformation approach or using a combination of a sigma and z-level coordinate system.

Below the governing equations are presented using Cartesian coordinates.

The local continuity equation is written as

$$\frac{\partial u}{\partial x}+\frac{\partial v}{\partial y}+\frac{\partial w}{\partial z}=S$$

and the two horizontal momentum equations for the x- and y-component, respectively

$$\frac{\partial u}{\partial t}+\frac{\partial u^2}{\partial x}+\frac{\partial vu}{\partial y}+\frac{\partial wu}{\partial z}=fv-g\frac{\partial \eta}{\partial x}-\frac{1}{\rho_0}\frac{\partial p_a}{\partial x}-\frac{g}{\rho_0}\int_z^\eta \frac{\partial \rho}{\partial x}dz+F_u+\frac{\partial}{\partial z}\left(\nu_t\frac{\partial u}{\partial z}\right)+u_sS$$

$$\frac{\partial v}{\partial t}+\frac{\partial v^2}{\partial y}+\frac{\partial uv}{\partial x}+\frac{\partial wv}{\partial z}=-fu-g\frac{\partial \eta}{\partial y}-\frac{1}{\rho_0}\frac{\partial p_a}{\partial y}-\frac{g}{\rho_0}\int_z^\eta \frac{\partial \rho}{\partial y}dz+F_v+\frac{\partial}{\partial z}\left(\nu_t\frac{\partial v}{\partial z}\right)+v_sS$$

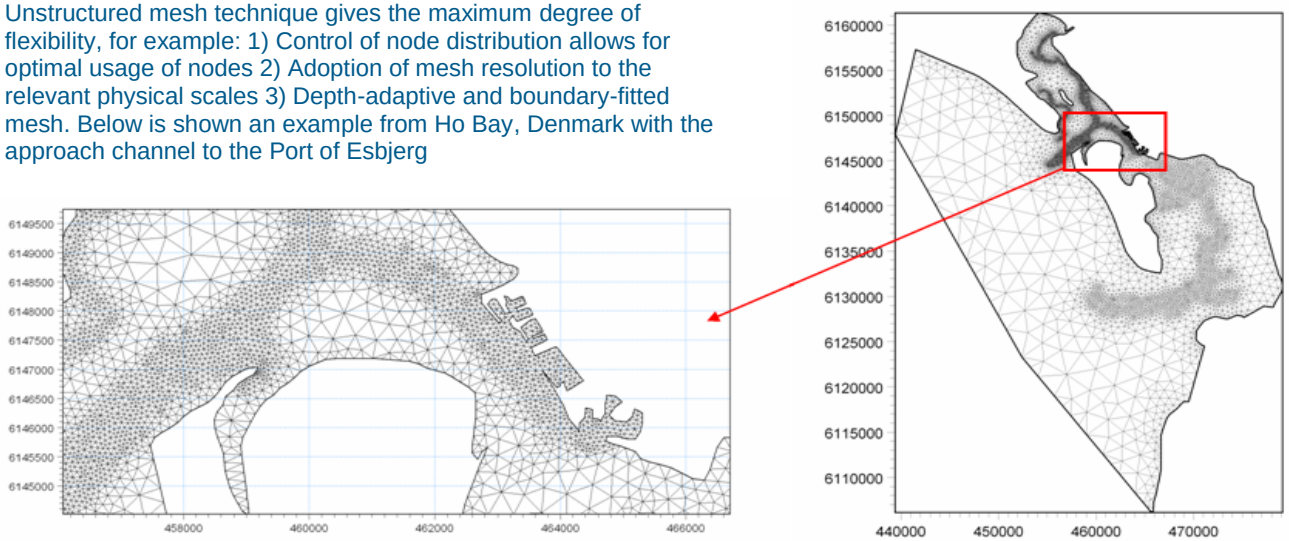
Temperature and salinity

In the Hydrodynamic Module, calculations of the transports of temperature, *T*, and salinity, *s* follow the general transport-diffusion equations as

$$\frac{\partial T}{\partial t}+\frac{\partial uT}{\partial x}+\frac{\partial vT}{\partial y}+\frac{\partial wT}{\partial z}=F_T+\frac{\partial}{\partial z}\left(D_v\frac{\partial T}{\partial z}\right)+\hat{H}+T_sS$$

$$\frac{\partial s}{\partial t}+\frac{\partial us}{\partial x}+\frac{\partial vs}{\partial y}+\frac{\partial ws}{\partial z}=F_s+\frac{\partial}{\partial z}\left(D_v\frac{\partial s}{\partial z}\right)+s_sS$$

Unstructured mesh technique gives the maximum degree of flexibility, for example: 1) Control of node distribution allows for optimal usage of nodes 2) Adoption of mesh resolution to the relevant physical scales 3) Depth-adaptive and boundary-fitted mesh. Below is shown an example from Ho Bay, Denmark with the approach channel to the Port of Esbjerg



The horizontal diffusion terms are defined by

$$(F_T, F_s) = \left[\frac{\partial}{\partial x}\left(D_h \frac{\partial}{\partial x}\right) + \frac{\partial}{\partial y}\left(D_h \frac{\partial}{\partial y}\right)\right](T, s)$$

The equations for two-dimensional flow are obtained by integration of the equations over depth.

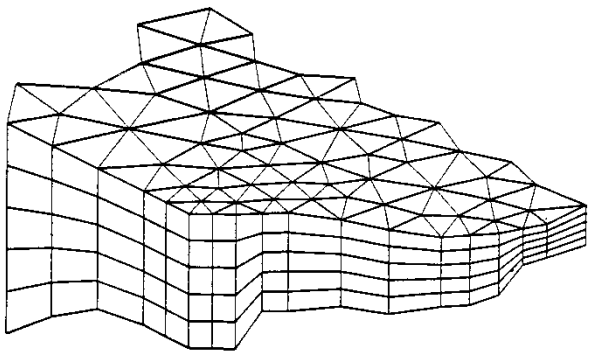
Heat exchange with the atmosphere is also included.

Symbol list

t	time
x, y, z	Cartesian coordinates
u, v, w	flow velocity components
T, s	temperature and salinity
D_v	vertical turbulent (eddy) diffusion coefficient
$\hat{H}$	source term due to heat exchange with atmosphere
S	magnitude of discharge due to point sources
T_s, s_s	temperature and salinity of source
F_T, F_s, F_c	horizontal diffusion terms
D_h	horizontal diffusion coefficient
h	depth

Solution Technique

The spatial discretisation of the primitive equations is performed using a cell-centred finite volume method. The spatial domain is discretised by subdivision of the continuum into non-overlapping elements/cells.



Principle of 3D mesh

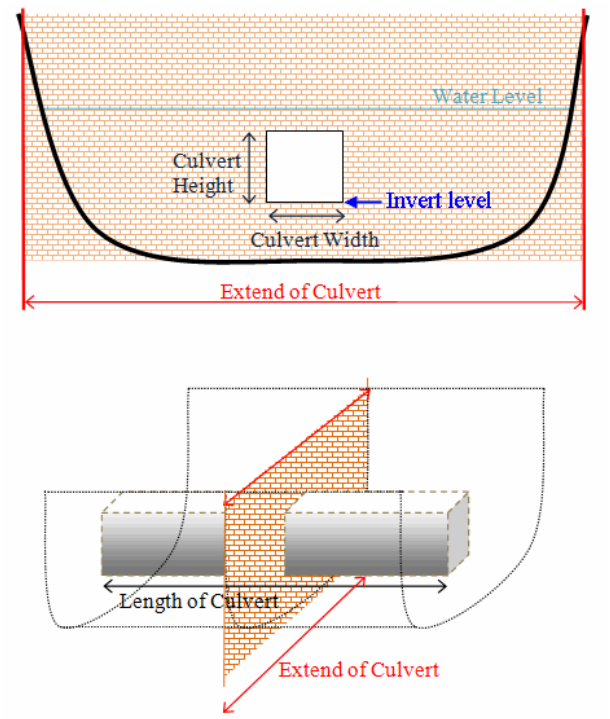
In the horizontal plane an unstructured mesh is used while a structured mesh is used in the vertical domain of the 3D model. In the 2D model the elements can be triangles or quadrilateral elements. In the 3D model the elements can be prisms or bricks whose horizontal faces are triangles and quadrilateral elements, respectively.

The effect of a number of structure types (weirs, culverts, dikes, gates, piers and turbines) with a horizontal dimension which usually cannot be resolved by the computational mesh is modelled by a subgrid technique.

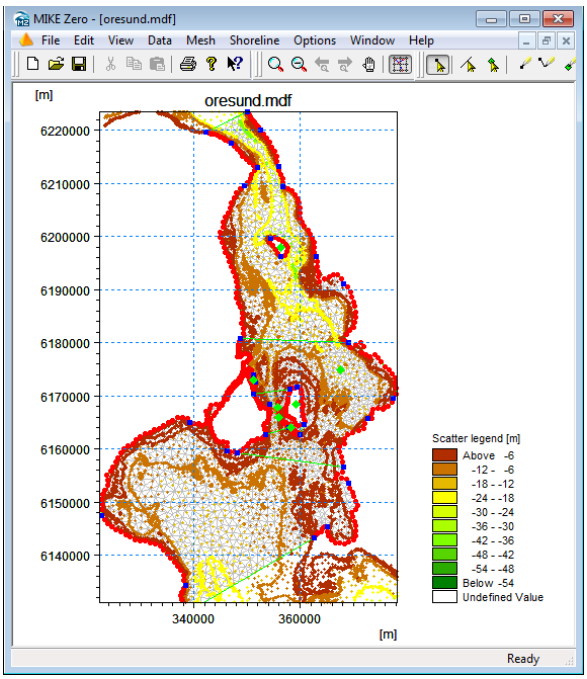
Model Input

Input data can be divided into the following groups:

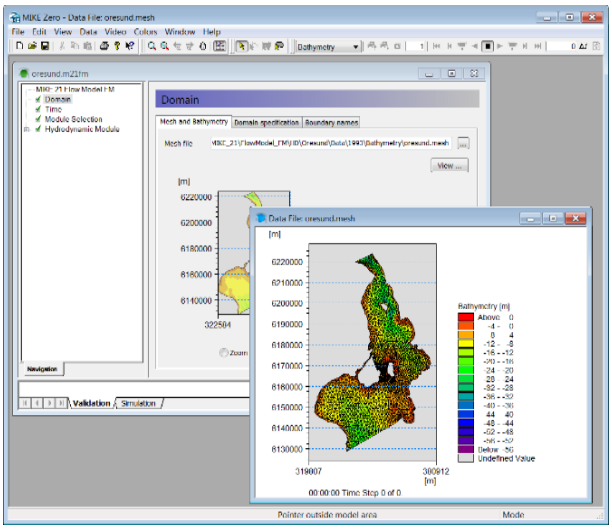
- Domain and time parameters:
  - computational mesh (the coordinate type is defined in the computational mesh file) and bathymetry
  - simulation length and overall time step
- Calibration factors
  - bed resistance
  - momentum dispersion coefficients
  - wind friction factors
  - heat exchange coefficients
- Initial conditions
  - water surface level
  - velocity components
  - temperature and salinity
- Boundary conditions
  - closed
  - water level
  - discharge
  - temperature and salinity
- Other driving forces
  - wind speed and direction
  - tide
  - source/sink discharge
  - wave radiation stresses
- Structures
  - Structure type
  - location
  - structure data



Setup definition of culvert structure



The Mesh Generator is an efficient MIKE Zero tool for the generation and handling of unstructured meshes, including the definition and editing of boundaries



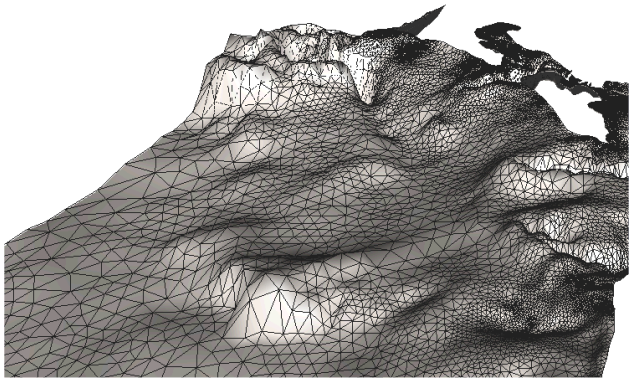
View button on all the GUIs in MIKE 21 & MIKE 3 FM HD for graphical view of input and output files

Providing MIKE 21 & MIKE 3 Flow Model FM with a suitable mesh is essential for obtaining reliable results from the models. Setting up the mesh includes the appropriate selection of the area to be modelled, adequate resolution of the bathymetry, flow, wind and wave fields under consideration and definition of codes for defining boundaries.



2D visualization of a computational mesh (Odense Estuary)

Bathymetric values for the mesh generation can e.g. be obtained from the MIKE Powered by DHI product MIKE C-Map. MIKE C-Map is an efficient tool for extracting depth data and predicted tidal elevation from the world-wide Electronic Chart Database CM-93 Edition 3.0 from C-MAP Norway.

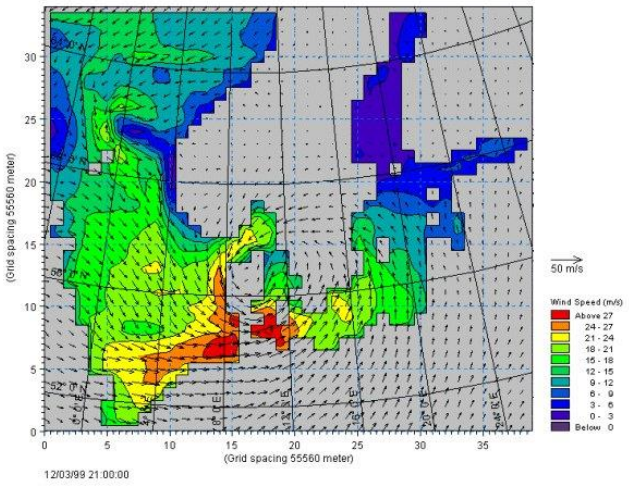


3D visualization of a computational mesh

If wind data is not available from an atmospheric meteorological model, the wind fields (e.g. cyclones) can be determined by using the wind-generating programs available in MIKE 21 Toolbox.

Global winds (pressure & wind data) can be downloaded for immediate use in your simulation. The sources of data are from GFS courtesy of NCEP, NOAA. By specifying the location, orientation and grid dimensions, the data is returned to you in the correct format as a spatial varying grid series or a time series. The link is:

http://www.waterforecast.com/hindcastdataproducts



The chart shows a hindcast wind field over the North Sea and Baltic Sea as wind speed and wind direction

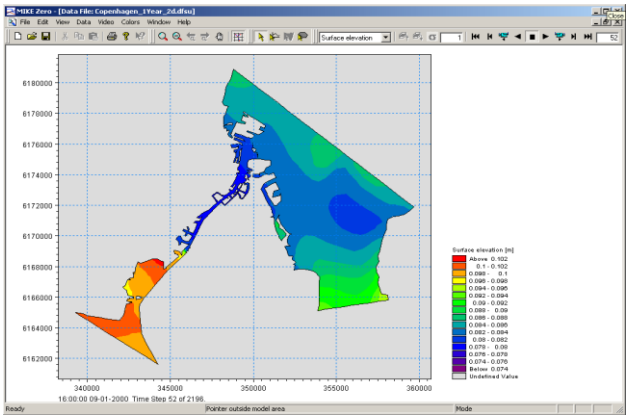
Model Output

Computed output results at each mesh element and for each time step consist of:

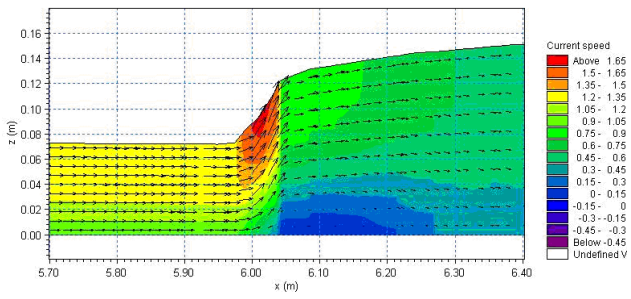
- Basic variables
  - water depths and surface elevations
  - flux densities in main directions
  - velocities in main directions
  - densities, temperatures and salinities
- Additional variables
  - Current speed and direction
  - Wind velocity
  - Air pressure
  - Drag coefficient
  - Precipitation/evaporation
  - Courant/CFL number
  - Eddy viscosity
  - Element area/volume

The output results can be saved in defined points, lines and areas. In the case of 3D calculations, the results are saved in a selection of layers.

Output from MIKE 21 & MIKE 3 Flow Model FM is typically post-processed using the Data Viewer available in the common MIKE Zero shell. The Data Viewer is a tool for analysis and visualization of unstructured data, e.g. to view meshes, spectra, bathymetries, results files of different format with graphical extraction of time series and line series from plan view and import of graphical overlays.



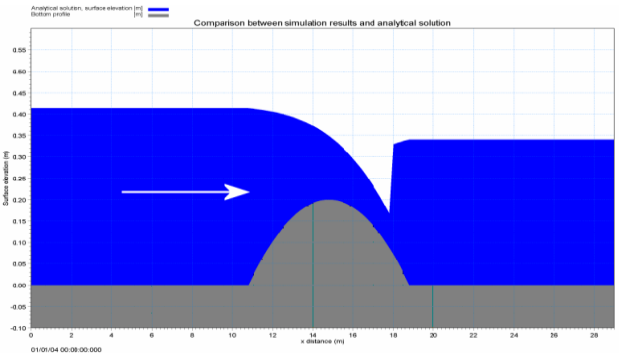
The Data Viewer in MIKE Zero – an efficient tool for analysis and visualization of unstructured data including processing of animations. Above screen dump shows surface elevations from a model setup covering Port of Copenhagen



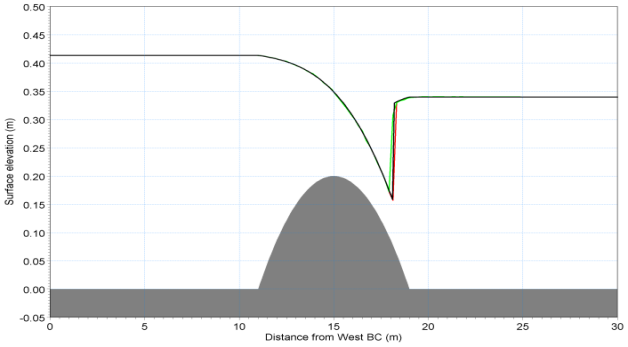
Vector and contour plot of current speed at a vertical profile defined along a line in Data Viewer in MIKE Zero

Validation

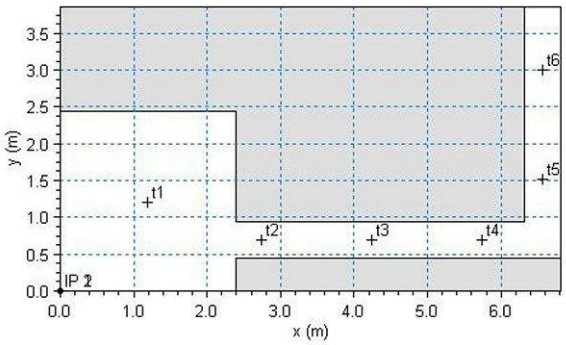
Prior to the first release of MIKE 21 & MIKE 3 Flow Model FM in year 19xx the model has successfully been applied to a number of basic idealized situations for which the results can be compared with analytical solutions or information from the literature.



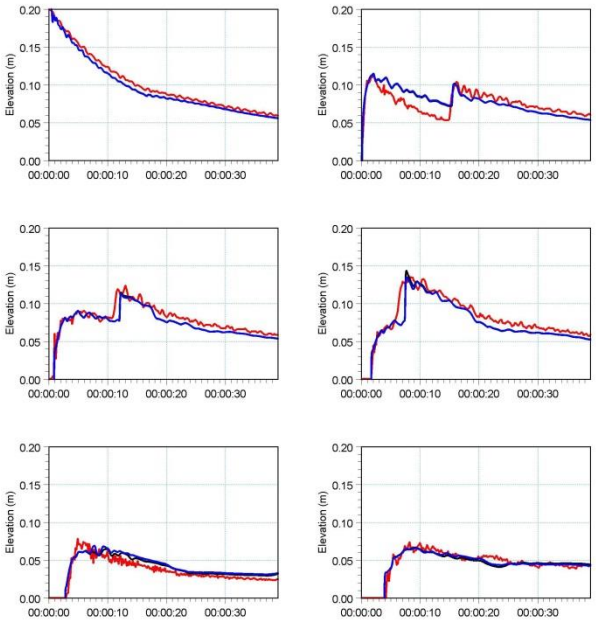
The domain is a channel with a parabola-shaped bump in the middle. The upstream (western) boundary is a constant flux and the downstream (eastern) boundary is a constant elevation. Below: the total depths for the stationary hydraulic jump at convergence. Red line: 2D setup, green line: 3D setup, black line: analytical solution



A dam-break flow in an L-shaped channel (a, b, c):

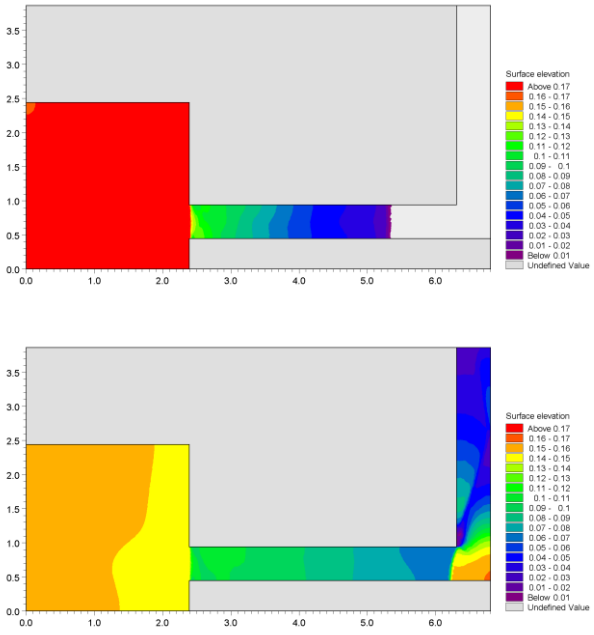


a) Outline of model setup showing the location of gauging points



b) Comparison between simulated and measured water levels at the six gauge locations.
(Blue) coarse mesh solution (black) fine mesh solution and (red) measurements

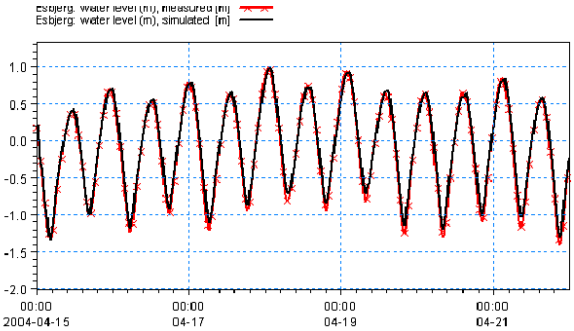
The model has also been applied and tested in numerous natural geophysical conditions; ocean scale, inner shelves, estuaries, lakes and overland, which are more realistic and complicated than academic and laboratory tests.



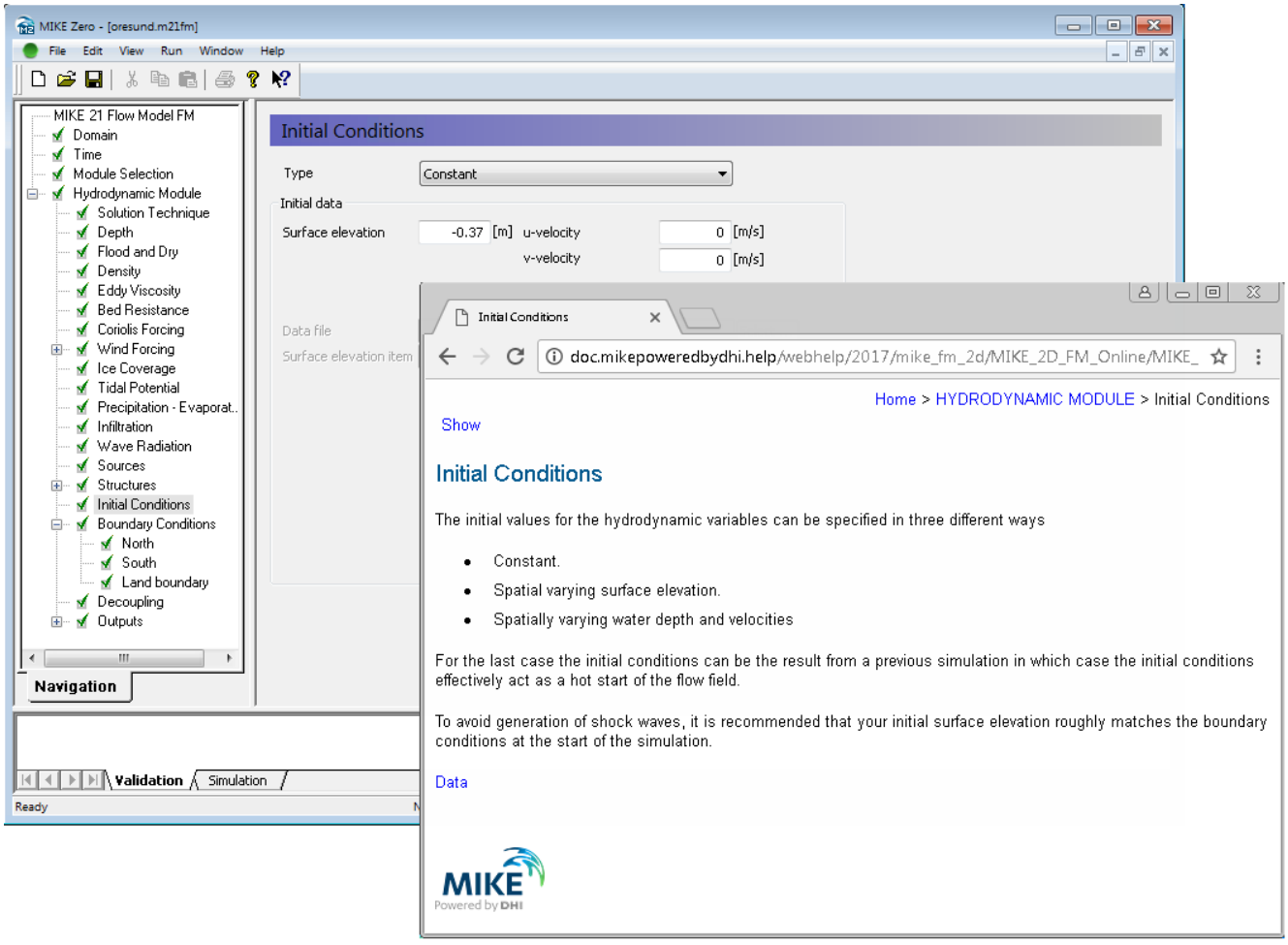
c) Contour plots of the surface elevation at T = 1.6 s (top) and T = 4.8 s (bottom)



Example from Ho Bay, a tidal estuary (barrier island coast) in South-West Denmark with access channel to the Port of Esbjerg.



Comparison between measured and simulated water levels

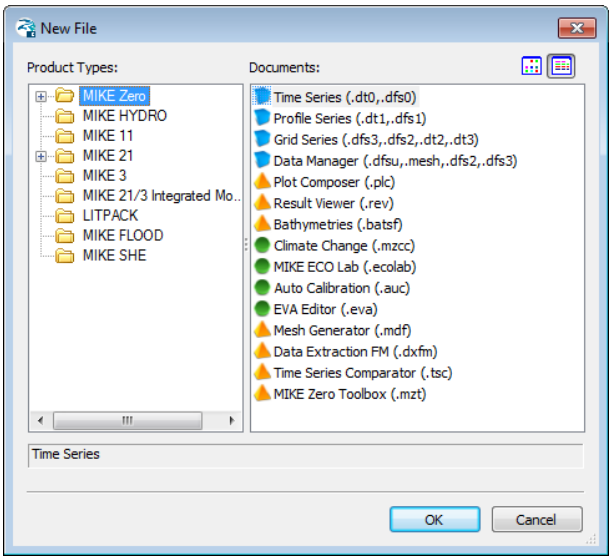


The user interface of the MIKE 21 and MIKE 3 Flow Model FM (Hydrodynamic Module), including an example of the extensive Online Help system

Graphical User Interface

The MIKE 21 & MIKE 3 Flow Model FM Hydrodynamic Module is operated through a fully Windows integrated graphical user interface (GUI). Support is provided at each stage by an Online Help system.

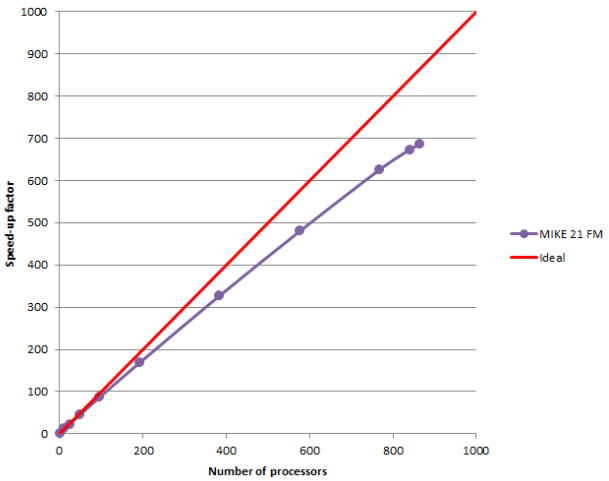
The common MIKE Zero shell provides entries for common data file editors, plotting facilities and utilities such as the Mesh Generator and Data Viewer.



Overview of the common MIKE Zero utilities

Parallelisation

The computational engines of the MIKE 21 & MIKE 3 FM series are available in versions that have been parallelised using both shared memory as well as distributed memory architecture. The latter approach allows for domain decomposition. The result is much faster simulations on systems with multiple cores. It is also possible to use a graphics card (GPU) to perform computational intensive hydrodynamic computations.



Example of MIKE 21 HD FM speed-up using a HPC Cluster with distributed memory architecture (purple)

Hardware and Operating System Requirements

The MIKE Zero Modules support Microsoft Windows 7 Professional Service Pack 1 (64 bit), Windows 10 Pro (64 bit), Windows Server 2012 R2 Standard (64 bit) and Windows Server 2016 Standard (64 bit).

Microsoft Internet Explorer 9.0 (or higher) is required for network license management. An internet browser is also required for accessing the web-based documentation and online help.

The recommended minimum hardware requirements for executing the MIKE Zero modules are:

Processor:	3 GHz PC (or higher)
Memory (RAM):	2 GB (or higher)
Hard disk:	40 GB (or higher)
Monitor:	SVGA, resolution 1024x768
Graphics card: (GUI and visualisation)	64 MB RAM (256 MB RAM or higher is recommended)
Graphics card: (for GPU computation)	1 GB RAM (or higher). requires a NVIDIA graphics card with compute capability 2.0 or higher

Support

News about new features, applications, papers, updates, patches, etc. are available here:

www.mikepoweredbydhi.com/Download/DocumentsAndTools.aspx

For further information on MIKE 21 and MIKE 3 Flow Model FM software, please contact your local DHI office or the support centre:

MIKE Powered by DHI Client Care
Agern Allé 5
DK-2970 Hørsholm
Denmark

Tel: +45 4516 9333
Fax: +45 4516 9292

mike@dhigroup.com
www.mikepoweredbydhi.com

Further Reading

Petersen, N.H., Rasch, P. “Modelling of the Asian Tsunami off the Coast of Northern Sumatra”, presented at the 3rd Asia-Pacific DHI Software Conference in Kuala Lumpur, Malaysia, 21-22 February, 2005

French, B. and Kerper, D. Salinity Control as a Mitigation Strategy for Habitat Improvement of Impacted Estuaries. 7th Annual EPA Wetlands Workshop, NJ, USA 2004.

DHI Note, “Flood Plain Modelling using unstructured Finite Volume Technique” January 2004 – download from

http://www.theacademybydhi.com/research-and-publications/scientific-publications

Documentation

The MIKE 21 & MIKE 3 Flow Model FM models are provided with comprehensive user guides, online help, scientific documentation, application examples and step-by-step training examples.

